SYNTHESIS AND CHARACTERIZATION OF HIGH OXYGEN STORAGE CAPACITY NANOPARTICLES DISPERSED DIESEL FOR THE EMISSION REDUCTION AND PERFORMANCE ENHANCEMENT OF A DIRECT INJECTION ENGINE

A thesis submitted in partial fulfillment of the requirements
for the award of the degree of

DOCTOR OF PHILOSOPHY

by

N. SHANMUGA PRIYA

(Roll No. 11610327)

Department of Mechanical Engineering

Indian Institute of Technology Guwahati

Guwahati – 781039

INDIA

December 2015

Department of Mechanical Engineering
Indian Institute of Technology Guwahati
Guwahati-781039, Assam, India

CERTIFICATE

It is certified that the work contained in the thesis entitled "**Synthesis and characterization of high oxygen storage capacity nanoparticles dispersed diesel for the emission reduction and performance enhancement of a direct injection engine**" submitted by **Mrs. N. Shanmuga Priya** to the Indian Institute of Technology Guwahati for the award of degree of Doctor of Philosophy has been carried out under our supervision in the department of Mechanical Engineering, Indian Institute of Technology Guwahati. This work has not been submitted elsewhere for the award of any other degree or diploma.

Dr. S. Kanagaraj
Associate professor
Department of Mechanical Engineering
Indian Institute of Technology Guwahati

Dr. Chandramohan Somayaji
Assistant professor
Department of Mechanical Engineering
Indian Institute of Technology Guwahati

Dedicated to

My Parents (Late) Mr.P.Natesan and Mrs.N.Vasavi

and

My Grand Parents (Late) Mr.M.Marappan and Mrs.M.Rangammal

Acknowledgement

I would like to express my gratitude to my supervisor Dr. S. Kanagaraj for his confidence, kindness, and patience with me for all these years. I would also thank my co-supervisor Dr.C. Somayaji for his timely suggestions. I would also thank my Doctoral committee members Prof. P. Mahanta, Dr. Amaresh Dalal, Dr. Anil Verma and Dr. K. Pakshirajan for continually reviewing the progress of my work with valuable suggestions and constructive criticism to improve the quality of the thesis. I also deeply acknowledge Prof. D. Chakraborty, Prof. P. Mahanta and A. K. Dass for extending various facilities in the department of mechanical engineering during the tenure of my research work.

I wish to express my sincere thanks to the technical staff from the department of Mechanical and Chemical Engineering, Department of physics and Central instruments facilities for their timely help. I am greatly indebted to Prof. D. K. Mahanta, The faculty in-charge of heat engine Lab, Mechanical department, Assam Engineering College, Guwahati, for his permission and cooperation to carryout engine related studies in ACE. I would like to acknowledge Assam pollution control board, Assam, for exhaust emission analyzer. I also thank Dr. Sakthivel, Postdoc fellow, Israel Institute of Technology, Israel, for the chemical stoichiometry calculation.

I would like to thank Dr. Sree Sree Shivakumara Swamiji Head of Sree Siddaganga Mutt, for his blessings with holiness for the completion of this thesis in addition with Dr. M.N. Channabasappa, Director of Siddaganga Institute of Technology, and Dr. Shivakumaraiah, Principal SIT, Tumkur for their kind help and support from the college. I also thank the staff members and colleagues for helping me in various fields.

The support received from the summer Internship students Petchammal, Balasubramaniam, wishely, Vishal and Hareesh at different stages of my work is also acknowledged. I would like to thank my labmates and friends Sreekanth, Vignesh, Avanish, Devarshi, Urmila, Saumes, Maharana, Barsha, Pushpendra, Naresh, Charan, Sridhar, Muthuraja, Jonney, Santosh, Manish, Suresh and Srevanthi who made my work memorable. A special thanks to Arun and Satheesh for their support during various experimentations.

I would like to thank my husband Shanmuga Sundaram and my son Deekshith Balaji for supporting me in the completion of this thesis in various ways by taking all the responsibility. Their unconditional love and support inspired me to do hard work with dedication. I am also thankful for my sisters Vadivu and Usha for their moral support. I extend my thanks to my cousins and relatives, who filled my absence in various needs.

Finally, I express my sincere thanks to all who helped me in whatever form during my stay at IIT Guwahati and successful completion of this thesis.

I gratefully thank the supreme Almighty God, who has showered his blessings on me in various ways to make me stand for what I am today.

N. Shanmuga Priya

19th December, 2014 IIT Guwahati

Abstract

In order to meet the increase in stringent regulation for exhaust gas emission from diesel vehicles, an exhaust-gas-after-treatment has become an essential process in most of the countries leading to use diesel particulate filters and catalytic converters as a treatment device. The effective utilization of the fuel is one of most essential requirements by considering the depletion of fossil fuel. Hence, there is a need to increase the effective utilization of different types of fuel in an engine without making any changes in the system. The objective of present work is to improve the performance and reduce the harmful emission of a diesel engine by homogenously dispersing the nanosized high oxygen storage capacity (OSC) materials of CZY (C=Ce; Z=Zr; Y= Al, Mn, Bi, La, Nd) oxides in diesel, named as a nanofuel. An attempt was made to synthesize nanoparticles having the improved OSC, which were homogenously dispersed in diesel with the help of oleic acid as a surfactant in order to meet the objectives. Cerium based solid solutions were prepared by sol-gel process and characterized. It is observed that the synthesized solid solutions had stable cubic fluorite structure, higher OSC, lattice defects and <10 nm crystallite size. The quantitative and qualitative studies on OSC of different solid solutions were done using suitable characterization techniques. It was observed that the cerium based solid solutions of $Ce_{0.6}Zr_{0.2}Al_{0.26}O_2$, $Ce_{0.6}Zr_{0.2}Al_{0.39}O_2$ and $Ce_{0.6}Zr_{0.2}Mn_{0.2}O_2$ were found to have the higher OSC in a decreasing order, where the CeO_2 and $Ce_{0.6}Zr_{0.4}O_2$ were considered as base materials. The OSC of base materials was increased if the doping element has lower ionic radius than the cerium. A tip sonicator, magnetic stirrer and a combination of both were used systematically to verify their versatility for the preparation of stable nanofuel. Though different types of surfactant based on anionic, cationic and nonionic were attempted, the ceria based nanofuel synthesized using Tween 80 as a surfactant and the combined preparation technique yielded a more stable nanofuel with the dispersion stability of 100 % for the period of 24 hrs and 99 % stability for 48 hrs. An accelerated sedimentation technique using centrifuge was also proposed to study the influence of ageing on the dispersion stability of nanofuel and it was found that the nanoparticles were settled completely after 620 hrs. The optimum concentration of nanoparticles to be dispersed in diesel was selected as 0.06 wt. % based on the performance enhancement study using CeO_2 based nanofuel, where the brake thermal efficiency and mechanical efficiency of an engine were increased by 12.8 and 9.2 %, respectively. In addition, the

brake specific fuel consumption and frictional power were decreased by 11.3 and 20.8 %, respectively. The relative stability of CeO_2, $Ce_{0.6}Zr_{0.4}O_2$, $Ce_{0.6}Zr_{0.2}Al_{0.26}O_2$, $Ce_{0.6}Zr_{0.1}Al_{0.39}O_2$ and $Ce_{0.6}Zr_{0.2}Mn_{0.2}O_2$ dispersed diesel was found to be 87, 88, 88, 91 and 89.5 %, respectively, at 0.06 wt. % after 168 hrs of synthesize. It was found that the properties of diesel were not varied significantly by dispersing different types of nanoparticle at 0.06 wt. %. When highest OSC material $Ce_{0.6}Zr_{0.2}Al_{0.26}O_2$ was dispersed in diesel and tested, it was observed that the brake thermal efficiency and mechanical efficiency of an engine were found to be increased by 20.7 and 8.2 %, respectively with respect to diesel at 100 % loading conditions and the brake specific fuel consumption and frictional power were decreased by 17.1 and 15.3 %, respectively. If only mechanical efficiency is considered, $Ce_{0.6}Zr_{0.4}O_2$ dispersed diesel was observed to show 11 % enhancement in comparison to that of diesel at 100 % loading condition. The highest reduction of NO_x, CO and hydrocarbon was found to be 68, 60 and 44 %, respectively, when 0.06 wt. % of $Ce_{0.6}Zr_{0.2}Al_{0.26}O_2$ based nanofuel was used in an IC engine at 100 % loading. A field study was also carried out with high OSC nanoaprticles dispersed diesel, where the utilization period of $Ce_{0.6}Zr_{0.2}Al_{0.26}O_2$ based nanofuel was increased by 25±1 % compared to that of pure diesel. In addition, the maximum utility time of CeO_2, $Ce_{0.6}Zr_{0.4}O_2$, $Ce_{0.6}Zr_{0.2}Mn_{0.2}O_2$ and $Ce_{0.6}Zr_{0.1}Al_{0.39}O_2$ dispersed diesel was noted to be 5±1, 17±1, 20±2 and 22 %, respectively. Thus, the $Ce_{0.6}Zr_{0.2}Al_{0.26}O_2$ based nanofuel is recommended to be effectively used in an IC engine in order to enhance the performance of an engine and to reduce its emission, which can be commercially explored.

CONTENTS

Page No.

ABSTRACT……..i

CONTENTS…….…….....iii

LIST OF FIGURES…….....vi

LIST OF TABLES…….....xi

Chapter 1. INTRODUCTION

1.1 Indian energy and emission scenario in world context 1

1.2 Emission and its standards 2

1.3 Effects of exhaust pollution..... 4

1.4 Solutions to meet energy demand and emission issues 4

1.5 Advantages and limitations of a diesel engine 4

1.6 Biodiesel and its limitations 5

1.7 Diesel additives and combustion catalysts 5

1.8 Ceria as an oxidation catalyst 7

1.9 Possible effects of nanoparticles deposition emission and environmental implications 8

1.9 Organization of thesis 10

Chapter 2. LITERATURE REVIEW

2.1 High oxygen storage capacity (OSC) materials 11

2.1.1 Ceria- zirconia solid solutions 12

2.1.2 Ceria – zirconia with other metals..... 16

2.1.3 Evaluation of OSC of a material 18

2.2. Nanoparticles characterization 25

2.2.1 Structural characterization 25

2.3 Synthesis of nanofluid..... 26

2.4 Quality characterization of nanofluid 28

2.4.1 Dispersion stability of nanofluid 29

2.4.2 Fuel properties..... 30

2.5 Experimental studies on engine performance and emission level..... 30

2.6 Technical gap 33

2.7 Objectives of the work 33

Chapter 3. MATERIALS AND METHODS

3.1 Raw materials 35
3.2 Synthesis of nanoparticles 36
3.3 Synthesis of nanofuel 38
3.4 Characterization of nanoparticles 41
3.4.1 Structural analysis - X-Ray diffractometer (XRD) 41
3.4.2 Lattice vibration studies- Raman spectroscopy 43
3.4.3 Image studies - Transmission electron microscope (TEM) 43
3.4.4 Oxygen storage capacity studies- Thermogravimetric analyzer (TGA) 44
3.4.5 Thermal expansion studies – Thermomechanical analyzer (TMA) 45
3.5 Quality characterization of nanofuel 46
3.5.1 Dispersion stability studies- UV-Vis Spectrophotometer 46
3.6 Characterization of nanofuel 48
3.6.1 Surface tension study - Tensiometer 48
3.6.2 Flash and Fire point temperature measurement - Pensky-Martens open type apparatus 49
3.6.3 Thermal conductivity measurement - KD 2 pro Thermal properties analyzer 50
3.6.4 Viscosity measurement- Rheometer 50
3.7 Performance and emission studies in an Internal Combustion Engine 51
3.7.1 IC engine Test rig 51
3.7.2 Emission studies - Gas Analyzer and emission monitor 52
3.8 Field Study 53

Chapter 4. RESULTS AND DISCUSSION

4.1 Synthesize of ceria based high oxygen storage capacity (OSC) materials 55
4.1.1 Selection of a suitable technique to synthesize $Ce_xZr_{1-x}O_2$ ($0.4 \leq x \leq 0.8$) solid solutions based on their OSC 55
4.1.2 Structural analysis of $Ce_{0.6}Zr_{0.4-x}Y_{1.3x}O_2$ (CZY) and $Ce_{0.6}Zr_{0.4-x}Mn_xO_2$ (CZM) (x=0.0, 0.1, 0.2, 0.3, 0.4; Y=Al, Bi, La, Nd) 59
4.1.3 Quantitative studies on oxygen storage capacity (OSC) of CZY and CZM solid solutions by thermogravimetric analysis 74

4.1.4. TEM studies on high OSC solid solutions 83
4.1.5 Qualitative confirmation of OSC 87
4.1.5.1 Lattice vibration studies 87
4.1.5.2 Studies on thermal expansion 91
4.1.5.3 Lattice defects confirmation 95
4.2 Optimization of surfactant and synthesis technique to prepare nanofuel 99
4.2.1 Influence of surfactant on the stability of nanofuel 99
4.2.2 Influence of preparation technique on the relative stability of nanofuel 103
4.2.3 Accelerated relative stability study 109
4.3 Optimization of ceria concentration for the performance enhancement of an IC engine 111
4.4 Studies on high OSC nanoparticles dispersed diesel 119
4.4.1 Studies on the dispersion stability of nanofuel 119
4.4.2 Characterization of nanofuel 122
4.5 Engine performance with high OSC nanoparticle (0.06 wt. %) dispersed diesel (Nanofuel) and emission studies 127
4.5.1 Engine performance studies 127
4.5.2 Exhaust gas analysis using high OSC nanoparticles (0.06 wt. %) dispersed diesel (Nanofuel) 135
4.6 Field trial on nanofuels 145

Chapter 5. CONCLUSIONS AND FUTURE SCOPE

5.1 Conclusions 149
5.2 Scope of future work 152
References 155
List of Publications 165
Annexure – I 168

List of Figures

Page No.

Figure 1.1 World energy consumption by region during 1990-2030 [source: EIA] 1
Figure 1.2 Global energy related emission as on 2009 [source: EIA] 2
Figure 1.3 Stringent Euro norms for automobile vehicle [source: EIA] 3
Figure 1.4 Dependence of Ceria toxicity on particle size [Shcherbakov et al. 2011] 9
Figure 3.1 Flow chart for the Co-precipitation preparation technique to synthesize $Ce_xZr_{1-x}O_2$ solid solutions 36
Figure 3.2 Flow chart for the sol-gel preparation technique to synthesize $Ce_xZr_{1-x}O_2$ 37
Figure 3.3 A setup to synthesize the nanoparticles as per COP and sol-gel technique (a) Microfluidics pump, b) Magnetic stirrer, c) pH meter 38
Figure 3.4 Tip sonicator 39
Figure 3.5 Different samples prepared using tip sonicator 40
Figure 3.6 Preparation of nanofuel using magnetic stirrer 41
Figure 3.7 Bruker D8 advance powder X-Ray diffractometer 42
Figure 3.8 Laser micro Raman spectroscopy 43
Figure 3.9 Transmission electron microscope 44
Figure 3.10 Thermogravimetric analyzer 45
Figure 3.11 Thermomechanical Analyzer 46
Figure 3.12 UV - Vis spectrophotometer 47
Figure 3.13 Tensiometer 48
Figure 3.14 Flash and Fire point temperature measuring instrument 49
Figure 3.15 KD 2 Pro - Thermal conductivity measuring instrument 50
Figure 3.16 Anton-Paar Rheometer 51
Figure 3.17 IC engine test rig 52
Figure 3.18 Exhaust gas analyzer and emission monitor 52
Figure 3.19 Suction and drained nanofuel line in the nanofuel reservoir 53
Figure 3.20 Three diesel generators used for field trial 54

Figure 4.1 XRD patterns of $Ce_xZr_{1-x}O_2$ ($0.4 \leq x \leq 0.8$) solid solutions prepared by (a) COP and (b) Sol-gel method 56
Figure 4.2 Raman spectra of $Ce_xZr_{1-x}O_2$ prepared by (a) COP and (b) Sol-gel method 58
Figure 4.3 TEM images of $Ce_{0.6}Zr_{0.4}O_2$ prepared by (a) COP and (b) Sol-gel method 58
Figure 4.4 XRD patterns of fresh $Ce_{0.6}Zr_{0.4-x}Al_{1.3x}O_2$ samples 60
Figure 4.5 XRD patterns of aged $Ce_{0.6}Zr_{0.4-x}Al_{1.3x}O_2$ solid solutions 61
Figure 4.6 XRD patterns of fresh $Ce_{0.6}Zr_{0.4-x}Mn_xO_2$ samples 63
Figure 4.7 XRD patterns of aged $Ce_{0.6}Zr_{0.4-x}Mn_xO_2$ samples 64
Figure 4.8 XRD patterns of fresh $Ce_{0.6}Zr_{0.4-x}Bi_{1.3x}O_2$ samples 66
Figure 4.9 XRD patterns of aged $Ce_{0.6}Zr_{0.4-x}Bi_{1.3x}O_2$ samples 67
Figure 4.10 XRD patterns of fresh $Ce_{0.6}Zr_{0.4-x}La_{1.3x}O_2$ samples 69
Figure 4.11 XRD patterns of aged $Ce_{0.6}Zr_{0.4-x}La_{1.3x}O_2$ samples 70
Figure 4.12 XRD patterns of fresh $Ce_{0.6}Zr_{0.4-x}Nd_{1.3x}O_2$ samples 72
Figure 4.13 XRD patterns of aged $Ce_{0.6}Zr_{0.4-x}Nd_{1.3x}O_2$ samples 72
Figure 4.14 Weight loss of the CZY and CZM solid solutions during the second heating cycle: (a) $Ce_{0.6}Zr_{0.4-x}Al_{1.3x}O_2$, (b) $Ce_{0.6}Zr_{0.4-x}Mn_xO_2$, (c) $Ce_{0.6}Zr_{0.4-x}Bi_{1.3x}O_2$, (d) $Ce_{0.6}Zr_{0.4-x}La_{1.3x}O_2$, (e) $Ce_{0.6}Zr_{0.4-x}Nd_{1.3x}O_2$ 76
Figure 4.15 OSC of $Ce_{0.6}Zr_{0.4-x}Y_{1.3x}O_2$ and $Ce_{0.6}Zr_{0.4-x}Mn_xO_2$ (Y= Al, Nd, La, Bi; $0 \leq x \leq 0.04$) samples 80
Figure 4.16 Comparison of OSC and specific surface area (SSA) of different solid solutions with respect to $Ce_{0.6}Zr_{0.4}O_2$ 82
Figure 4.17 (i-iv) TEM images of fresh $Ce_{0.6}Zr_{0.2}Al_{0.26}O_2$ at different magnification 84
Figure 4.18 (i-iv) TEM images of fresh $Ce_{0.6}Zr_{0.2}Mn_{0.2}O_2$ at different magnification 85
Figure 4.19 (i-ii) TEM images of fresh $Ce_{0.6}Zr_{0.2}Bi_{0.39}O_2$ 85
Figure 4.20 TEM image of fresh $Ce_{0.6}Zr_{0.2}La_{0.26}O_2$ 86
Figure 4.21 TEM image of fresh $Ce_{0.6}Zr_{0.2}Nd_{0.13}O_2$ 87
Figure 4.22 Raman spectra of fresh $Ce_{0.6}Zr_{0.4-x}Al_{1.3x}O_2$ solid solutions 88
Figure 4.23 Raman spectra of aged $Ce_{0.6}Zr_{0.4-x}Al_{1.3x}O_2$ solid solution 89
Figure 4.24 Raman spectra of fresh $Ce_{0.6}Zr_{0.4-x}Mn_xO_2$ samples 90

Figure 4.25 Raman spectra of aged $Ce_{0.6}Zr_{0.4-x}Mn_xO_2$ samples 91
Figure 4.26 Thermal expansion behavior of $Ce_{0.6}Zr_{0.4-x}Al_{1.3x}O_2$ samples..... 92
Figure 4.27 A schematic representation about transverse thermal vibration of M-O-M Bond, Evans et al. [1998]..... 92
Figure 4.28 Coefficient of thermal expansion (CTE) of $Ce_{0.6}Zr_{0.4-x}Al_{1.3x}O_2$ at different temperature range..... 93
Figure 4.29 Thermal expansion behavior of $Ce_{0.6}Zr_{0.4-x}Mn_xO_2$ samples 94
Figure 4.30 Coefficient of thermal expansion of $Ce_{0.6}Zr_{0.4-x}Mn_xO_2$ at different temperature range..... 94
Figure 4.31 HRTEM image and filtered image of CeO_2 without significant lattice defect 95
Figure 4.32 HRTEM images of $Ce_{0.6}Zr_{0.4}O_2$, (i) filtered image without lattice defect, (ii) Filtered image with lattice defect-edge dislocation and (iii) Filtered image with lattice defect- edge dislocation..... 96
Figure 4.33 HRTEM images of $Ce_{0.6}Zr_{0.2}Al_{0.26}O_2$ (i) - (v) Filtered image with lattice defects .. 97
Figure 4.34 HRTEM image of $Ce_{0.6}Zr_{0.2}Mn_{0.2}O_2$ (i-iv) Filtered image with lattice defects..... 98
Figure 4.35 Influence of different surfactants on the relative stability of nanofuel having 0.06 wt. % of CeO_2 100
Figure 4.36 Electrostatic stabilization mechanism of (a) CTAB and (b) SDS surfactant on Nanofuel 101
Figure 4.37 Steric stabilization mechanism of Non-ionic surfactant..... 102
Figure 4.38 Relative stability of nanofuel prepared by magnetic stirrer for 72 hrs..... 104
Figure 4.39 Relative stability of nanofuel prepared by tip sonicator for 168 hrs 105
Figure 4.40 Comparison of relative stability of 0.06 wt. % nanofuel..... 106
Figure 4.41 XRD patterns of derived CeO_2 nanoparticle from nanofuel 108
Figure 4.42 TEM images of nanofuel drop synthesized by the a) Magnetic stirring, b) Tip sonication, c) Combined technique in 20nm scale, d) Combined technique in 50nm scale 109
Figure 4.43 Predicted relative stability of nanofuel up to 620 hrs period of time- nanofuel synthesized by combined technique..... 110

Figure 4.44 Accelerated relative stability with curve fitting for CeO_2 nanofuel at 0.06 wt. % 110
Figure 4.45 Effect of ceria concentration and load on BTE of an IC engine 113
Figure 4.46 Increase in BTE while nanofuel usage compared to diesel in an IC engine at different concentration of CeO_2 nanoparticles 114
Figure 4.47 Effect of concentration of ceria nanoparticles on BSFC of an engine 114
Figure 4.48 Decrease in BSFC compared to diesel with respect to CeO_2 concentration..... 115
Figure 4.49 Effect of CeO_2 concentration on frictional power of an IC engine 116
Figure 4.50 Decrease in frictional power of an engine with respect to diesel..... 117
Figure 4.51 Effect of CeO_2 concentration on mechanical efficiency of an IC engine..... 118
Figure 4.52 Increase in mechanical efficiency compared to diesel with respect to CeO_2 concentration..... 118
Figure 4.53 Relative stability studies on nanofuel based on (a) CeO_2, (b) $Ce_{0.6}Zr_{0.4}O_2$, (c) $Ce_{0.6}Zr_{0.2}Al_{0.26}O_2$, (d) $Ce_{0.6}Zr_{0.1}Al_{0.39}O_2$, (e) $Ce_{0.6}Zr_{0.2}Mn_{0.2}O_2$..... 120
Figure 4.54 Effect of concentration and duration on relative stability of high OSC nanoparticle dispersed diesel 122
Figure 4.55 Effect of high OSC nanoparticles on the surface tension of diesel 123
Figure 4.56 Effect of high OSC nanoparticles on the flash point temperature of diesel 124
Figure 4.57 Effect of high OSC nanoparticles on the fire point temperature of diesel 124
Figure 4.58 Effective thermal conductivity of nanofuel having different concentration of nanoparticles 125
Figure 4.59 Effect of 0.06 wt. % OSC nanoparticles on viscosity of nanofuel at room temperature 126
Figure 4.60 Effect of high OSC nanoparticles in diesel at 0.06 wt. % on BSFC 128
Figure 4.61 Decrease in BSFC of an engine using 0.06 wt. % nanofuel with respect to diesel..... 129
Figure 4.62 Effect of high OSC nanoparticles in diesel at 0.06 wt. % on BTE of an engine 130
Figure 4.63 Increase in BTE of an engine using 0.06 wt. % nanofuel with respect to diesel 130

Figure 4.64 Effect of high OSC nanoparticles in diesel at 0.06 wt. % on frictional power of an engine 131
Figure 4.65 Effect of high OSC nanoparticles in diesel at 0.06 wt. % on mechanical efficiency of an engine 132
Figure 4.66 Increase in mechanical efficiency of an engine using 0.06 wt. % nanofuel with respect to diesel 133
Figure 4.67 Effect of nanoparticles in diesel at 0.06 wt. % on CO emission 135
Figure 4.68 Decrease in CO emission with different types of nanofuel at 0.06 wt. % in comparison with diesel 136
Figure 4.69 Effect of nanoparticles in diesel at 0.06 wt. % on hydrocarbon emission 137
Figure 4.70 Decrease in hydrocarbon emission with different nanofuel at 0.06 wt. % in comparison with diesel 138
Figure 4.71 Effect of nanoparticles in diesel at 0.06 wt. % on NO_x emission 139
Figure 4.72 Decrease in NO_x emission with different types of nanofuel at 0.06 wt. % in comparison with diesel 140
Figure 4.73 Effect of nanoparticles in diesel at 0.06 wt. % on CO_2 emission 141
Figure 4.74 Increase in CO_2 emission with different types of nanofuel at 0.06 wt. % in comparison with diesel 142
Figure 4.75 Effect of nanofuel at 0.06 wt. % on running time of different capacity of diesel generators at no load condition 146
Figure 4.76 Increase in running time of different capacity of diesel generators using nanofuel at 0.06 wt. % compared to diesel 147

List of Tables

Page No.

Table 2.1 Influence of preparation methods and precursors on the size of Ce-Zr solid solution 14

Table 2.2 Comparative studies on different OSC measurement techniques 19

Table 2.3 Influence of different catalysts and specific surface area on OSC from selected literatures 24

Table 4.1 Structural parameters and OSC of $Ce_xZr_{1-x}O_2$ solid solutions prepared by COP and sol-gel (SOL) method..... 57

Table 4.2 Crystallite size, d-spacing and lattice constant of fresh and aged $Ce_{0.6}Zr_{0.4-x}Al_{1.3x}O_2$ (CZA) solid solutions 62

Table 4.3 Crystallite size, d-spacing and lattice constant of fresh and aged $Ce_{0.6}Zr_{0.4-x}Mn_xO_2$ (CZM) solid solutions 65

Table 4.4 Crystallite size, d-spacing and lattice constant of fresh and aged $Ce_{0.6}Zr_{0.4-x}Bi_{1.3x}O_2$ (CZB) solid solutions 68

Table 4.5 Crystallite size, d-spacing and lattice constant of fresh and aged $Ce_{0.6}Zr_{0.4-x}La_{1.3x}O_2$ (CZL) solid solutions..... 71

Table 4.6 Crystallite size, d-spacing and lattice constant of fresh and aged $Ce_{0.6}Zr_{0.4-x}Nd_{1.3x}O_2$ (CZN) solid solutions 73

Table 4.7 BET specific surface area for high OSC nanoparticles 83

Table 4.8 Relative stability of nanofuel based on the synthesis technique 107

Table 4.9 One week relative stability studies on nanofuels 121

Table 4.10 Engine performance parameters of an engine and their changes with respect to diesel using high OSC nanoparticles at 0.06 wt. % 134

Table 4.11 Engine exhaust emission of high OSC nanoparticles dispersed diesel against loading and different type of nanofuel 144

Chapter 1

Introduction

1.1 Indian energy and emission scenario in world context

Energy is the main source of human civilization and its requirement increased enormously to have a comfortable life in addition to have an industrial revolution to make the people comfort. Institutions such as the International energy agency (IEA), the U.S energy information administration (EIA), and the European environment agency record and publish world consumption energy data periodically. Figure 1.1 shows the world total primary energy consumption by region from 1990 to 2030. According to EIA, India was the fifth-largest consumer of energy after China, US, Canada, and Russia as an individual country. In developing countries, particularly those that are sub-tropical or tropical such as India, the energy consumption per capita was closer to 700 W, whereas it was 11400, 6000 and 1600 W for the US, Germany and China energy, respectively, Goyal [2009].

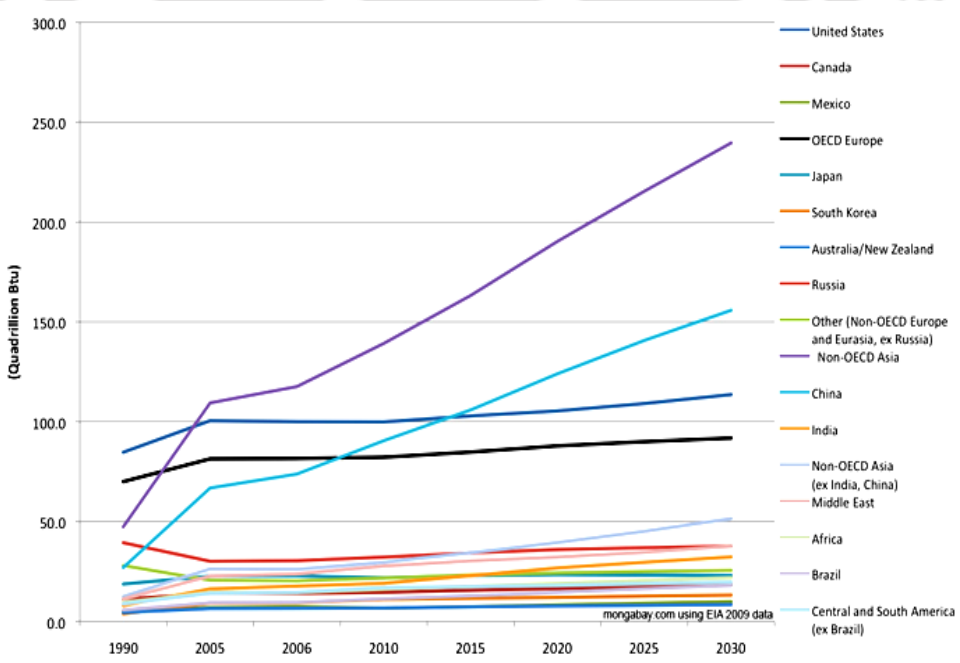

Figure 1.1 World energy consumption by region during 1990-2030 [source: EIA]

In case of global energy related emissions, India was the fifth largest emitter by region as on 2009, which is shown in Figure 1.2. The developed countries like Japan, Canada and Australia stood after India in energy related emission. In India, nearly 29.5% of energy was produced from crude oil source after the coal source. According to EIA, as on 2013, the oil consumption by India was around 3.7 million barrels per day, whereas the total oil production was less than 1 million barrels per day. The increased gap between production and consumption led to energy imbalance in India, which is one of the most important developing countries in the world.

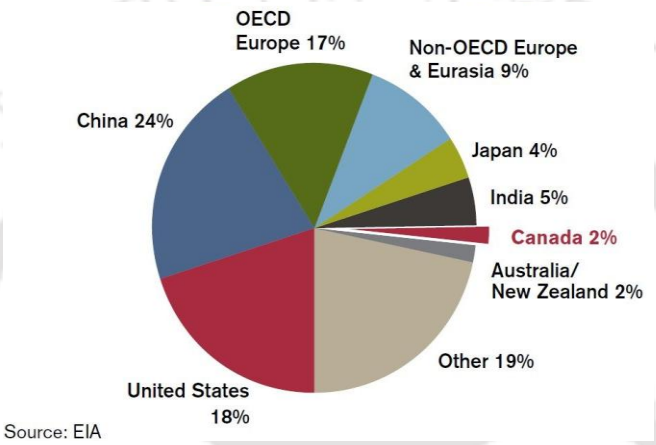

Figure 1.2 Global energy related emission as on 2009 [source: EIA]

1.2 Emission and its standards

The environmental protection agency of USA designates size criteria pollutants for determining the air quality. These are carbon monoxide (CO), nitrogen oxides ($NO/NO_2/NO_x$), sulfur dioxide (SO_2), ground level ozone (O_3), and a particulate matter. Petroleum-fueled vehicles, engines and industrial processes directly produce the majority of CO and NO_x in the atmosphere. They are also principal sources of gases such as hydrocarbon, which combine with NO_x in sunlight to create O_3. Petroleum- fueled transportation and coal-burning power plants are considered to be the main causes of global warming. Excess amounts of carbon dioxide, methane and NO_x, among other gases trap the heat in the atmosphere and create the green house effect. The emission target protocol was adopted at Kyoto in 1997 and came into force in 2005. According to Kyoto protocol, carbon dioxide, methane, nitrous oxide, fluorinated gases, hydrofluorocarbon (HFC), perfluorocarbon (PFC) and sulphur hexafluoride (SF_6) were named as green house gases. Carbon dioxide (CO_2) is a main constituent of petroleum fuel exhaust. As it is not toxic, it is not

classified as a pollutant. About one-third of CO_2 emitted into the atmosphere every year comes from the vehicle exhaust. Methane (CH_4), although usually associated with natural gas, is also emitted whenever crude oil is extracted, transported, refined, or stored. Under Kyoto protocol, 37 industrialized and developed countries accepted to cap carbon production from power stations and industrial installation, while developing countries such as India and China were mandated to take measures but without caps. As per Kyoto protocol, the countries must reduce total green house gas emission by 2012 in comparison to 1990 level.

European emission standards define the acceptable limits for exhaust emission from vehicles. The emission standards are defined as a series of European Union directives staging the progressive introduction of increasingly stringent standards. For each vehicle type, different standards were applicable according Euro norms. For diesel vehicle, as per Euro V standards, the CO, particulates, nitrogen oxides and combined emission of hydrocarbon and nitrogen oxides were 500, 5 (80 % reduction of emission in comparison to the Euro IV standard), 180 (20 % reduction of emission in comparison to the Euro IV standard), 230 mg/km, respectively. Figure 1.3 shows the stringent emission standards started from Euro I to Euro VI. According to the Euro VI norms, the combined emission of hydrocarbon and nitrogen oxide was found to be reduced completely.

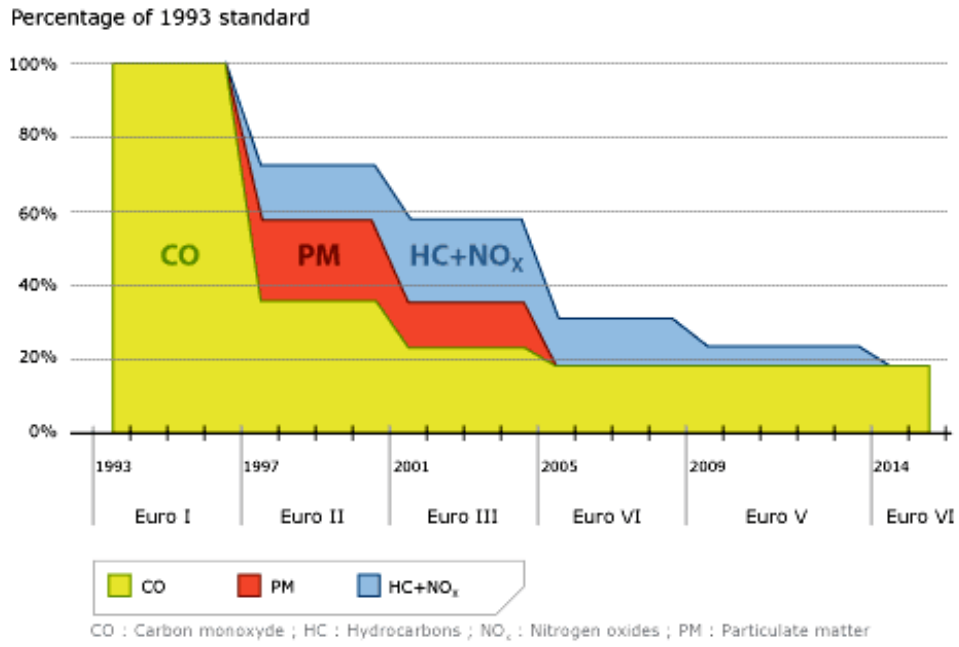

Figure 1.3 Stringent Euro norms for automobile vehicle [source: EIA]

1.3 Effects of exhaust pollution

Problems generated due to engine exhaust can be divided as follows:

1. Local effects - e.g. poisoning human breathing air
2. Regional effects - fallout from airborne pathogens-infection, particles, chemicals
3. Global effects - changing the interaction among the atmosphere, ocean and sun, weather effects, effects on plants and the ocean biosphere.

For human, the exhaust pollution contributes to an increased risk of death, non-allergic respiratory symptoms and disease. Hydrocarbon has the potential to cause cancer. NO_x forms nitric acid, and irritates the eyes, throat and respiratory system. Carbon monoxide reduces the flow of oxygen in the blood stream and is particularly dangerous to persons with heart disease. However, carbon dioxide does not directly impair human health, but it is a green house gas that traps the earth heat and contributes to the potential for global warming.

1.4 Solutions to meet energy demand and emission issues

The awareness is increased by the public and government towards human health hazards presented by the atmospheric pollution from the combustion products of fossil fuels. Added to the pollution caused by the automobile industries, stringent emission norms and the increase in crude oil prices due to rapid industrial growth are forced to think about the energy efficient, environmental friendly and combustion enhanced fuel in terms of bio fuel and/or the fuel added with additives and catalysts.

1.5 Advantages and limitations of a diesel engine

The major use of a diesel engine is found in the area of power production, commercial transportation, industrial sectors and agricultural machineries due to its ease of operation and more power per unit of fuel i.e. higher fuel economy. Added to the above, the diesel engine has several advantages over other fuel engines, which are as follows:

1. The specific fuel consumption of a diesel engine is better than the petrol engine.
2. The cost of diesel is lower than the petrol, which is helpful to have reduced running cost.
3. Due to low vapour pressure, the fuel is considered to be safer than the petrol in many applications including marine engines, and it is immune to vapor lock.

4. Waste heat through the cooling water jacket and exhaust is less

Though the diesel engine has the above advantages in addition to high thermal efficiency, rigidity, simplicity in structures and fuel economy, its use in an automobile industry is limited due to the generation of high emission level compared to that of a petrol engine. It has motivated the researchers to come up with new technologies to control the emission generated from a diesel engine in different possible ways.

1.6 Biodiesel and its limitations

Though one of the major alternatives for above discussed problems is the biofuel, its acceptance level is very low because of different factors including the lack of supply, economic constraints, etc. As an alternative to diesel or diesel blend, the biodiesel is expected to meet the present and future energy demand. Biodiesel is derived from the renewable domestic sources such as vegetable oil and animal fat, which are non-toxic, biodegradable, eco-friendly and more reliable compare to fossil fuel as it forms low level of carbon and smoke, which are responsible for the global warming. On the other hand, biodiesel has higher molecular weight, density, viscosity, cold flow and pour point than the conventional diesel. The characteristics of biodiesel cause low volatility, poor fuel atomization, injector choking, piston ring sticking and incomplete combustion. The characteristics and properties of biodiesel limit its use in cold or chill weather. Depending on the blend ratio of biodiesel in diesel, NO_x emission is reported to be higher with respect to pure diesel.

1.7 Diesel additives and combustion catalysts

A large variety of fuel additives is added to the diesel to improve the engine efficiency and reduce the emission. The various fuel characteristics such as the volatility and sulfur content in the fuel, which affect the particulate emission can be altered by the use of fuel additives. It helped to reduce the high temperature leading to short ignition delay in a diesel engine. Many research activities on the influence of fuel additives on the performance of an engine and its emission level were focused, Keskin et al. [2008]. The emission of NO_x was also controlled by adding suitable additives in the fuel.

There are two groups of catalysts such as metal containing catalysts and ash free catalysts being studied in a diesel engine. Metal containing compounds are claimed to be more effective than the

ash free catalysts, which are used as combustion catalysts for hydrocarbon fuels. These are proved to be most effective not only for reducing the CO or hydrocarbon but also adsorption of particulate matter and reduction of NO_x.

The metal based catalysts are manganese, iron, sodium, copper, barium, cerium, calcium and platinum, which have the high catalytic activity in combustion process. The metal based catalysts reduced the diesel engine emission and fuel consumption. The reason for emission reduction is that the metal based catalyst reacted with water to produce hydroxyl radicals to enhance the soot oxidation or it reacted with the carbon atoms in the soot lowering its oxidation temperature, Yang et al. [1998]. In order to perform the above required functions, the catalysts are required to have the following characteristics, Zhu et al. [2012]:

1) They must be soluble or insoluble in diesel homogenously without settling or agglomeration during its application, storage, and on-board consumption.
2) They must have excellent catalytic activity to promote the hydrocarbon combustion.
3) The characteristics of fuel should not change significantly and it should not generate the secondary pollution by adding the catalysts in fuel.

The metal based catalysts are either manufactured in the form of the organometallic compounds or nanoparticles. The nanoparticles are in the range of 0.1 to 100 nm, which are small enough to approach molecular dimension, and their properties are significantly different from those of larger, and micrometer sized particles. At such dimension, the surface area to volume ratio of the particles increased considerably and using of them enhanced the contact between the fuel and oxidizer, Luca et al. [2005]. One of the major reasons for the efficiency improvement of an engine is the high surface area to volume ratio of nanoparticles compared to conventional powder, as the catalytic reaction is essentially a surface phenomenon. As the nanoparticles affect the rate of chemical reactions, the ignition delay period is expected to decrease. It has also been reported that dispersing nanoparticles in diesel increased the ignition probability of the mixture, Tyagi et al. [2008] and it was proposed to disperse them in the high temperature zone for direct oxidation reaction, rapid energy release and enhanced propulsive performance with increased density impulse. In addition to that the nanoparticles enhanced the thermal conductivity and mass diffusivity, Shafii et al. [2011].

1.8 Ceria as an oxidation catalyst

In recent years, a special attention has been given to synthesize and characterize the solid solutions based on cerium oxide (CeO_2) for the cleaning of automotive emission including diesel exhaust, because the redox properties of the catalysts can contribute to lower the emission, Masui et al. [2006]. CeO_2 is found to be widely used as an automotive three-way catalyst (TWC) for exhaust gas treatment device because of its attractive characteristics such as low temperature reduction, large specific surface area and cubic structure. It enables to operate the after-combustion-device more efficiently irrespective of the fuel mixture in an IC engine, Kaspar et al. [2003]. Because of its redox and acido-basic surface characteristics, it is also employed in fluid catalytic cracking, Trovarelli et al. [2001], SO_x removal, Cao et al. [2010], ethylbenzene dehydro-generation, Hirano [1986] and the water gas shift reaction, Wang et al. [2006]. Due to wide range of applications of rare-earth metal oxides like ceria, more emphasis is being given by many research scientists in the related area of research. The inherent attractive characteristics such as an elevated oxygen transport capacity, which is also called as oxygen storage capacity (OSC), associated with the ability of changing the valency state from Ce^{3+} to Ce^{4+}or vice versa made ceria for the many different applications, Egchi et al. [2011]. The redox characteristics of ceria were more effective when the particles were in the range of nanosize, Yetter et al. [2009]. The main role of ceria in catalytic applications is to provide oxygen buffering capacity during the rich/lean oscillation of exhaust gases. Ceria has the ability to donate its oxygen for the oxidation of CO and hydrocarbon during the oxygen deficient portion and absorb excess oxygen for the reduction of NO_x. The required oxygen for complete combustion of the fuel can be supplied by the ceria when it was used during the combustion stage.

Ceria nanoparticles dispersed in biodiesel increased the total combustion heat, while the concentration of smoke and NO_x was decreased in the exhaust of a diesel engine, Sajith et al. [2010]. Another important advantage of nanoparticles in liquid fuel is their size, because there is no chance for fuel injector and filter clogging as in the case of micron sized particles, Ganesh et al. [2011]. Addition of low boiling point component in diesel also promoted the spray evaporation and mixture formation processes, Li et al. [2009a]. The dispersion of ceria in diesel caused significant changes in light-off temperature, and kinetics of oxidation. The oxidation rate was also increased with the addition of ceria in diesel, Jung et al. [2005]. In order to ensure the same characteristics of ceria dispersed diesel and pure diesel, the nanoparticles are always

dispersed in tiny amounts at ppm level in diesel. It was found that the use of ceria as a TWC was explored in automobile applications. In order to reduce the engine exhaust emission and improve its enhanced performance, an attempt is being made to enhance the oxygen storage capacity of ceria and its application in engine performance as a nanofuel, nanoparticles dispersed diesel.

1.9 Possible effects of nanoparticles deposition emission and environmental implications

Humans have been exposed to nanoparticles throughout their evolutionary phases; however, this exposure has been increased to a great extent in the past century because of the industrial revolution. Nanoparticles constitute a part of particulate matter (PM). Epidemiological studies have shown that urban pollution with airborne PM deriving from combustion sources such as motor vehicle and industrial emissions contributes to respiratory and cardiovascular morbidity and mortality [Pope et al. 2001, Peters et al. 2002, Brook et al. 2004). Thus, combustion-derived nanoparticles and their characteristics have been largely by Medina et al. [2007]. In addition, the relevance of health effects of those particles is as follows:

- Size – In addition to being able to cross cell membranes, they can reach the blood and various organs because of their very small size. Due to their high surface area to volume ratio, more molecules of the chemicals are expected to present on the surface. It may be one of the reasons why nanoparticles are generally more toxic than larger particles of the same composition.

- Chemical composition and surface characteristics – The toxicity of nanoparticles depends on the chemical composition of nanoparticles and the composition of chemicals adsorbed on their surfaces. However, the surfaces of nanoparticles can be modified in order to make them less harmful to health.

- Shape – Although there is little definitive evidence, the health effects of nanoparticles are likely to depend also on their shape. A significant example is nanotubes, which may be of a few nanometres in diameter but with a length that could be several micrometres. A recent study showed a high toxicity of carbon nanotubes which seemed to produce harmful effects by an entirely new mechanism, different from the normal model of toxic dusts

However the ceria based nanoparticles dispersed in diesel were found to reduce the particulate matter (PM) from the engine exhaust. Cassee et al. [2012] exposed the Atherosclerosis-prone apolipo protein E knockout ($APOE^{-/-}$) mice in the CeO_2 engine exhaust and observed that addition of CeO_2 nanoparticles to fuel decreased the number of particles in exhaust and may reduce atherosclerotic burden associated with exposure to standard diesel fuel. From the extensive assessment of biological parameters performed, the only concerning effect of cerium addition was a slightly raised level of cytokines in a region of the central nervous system.

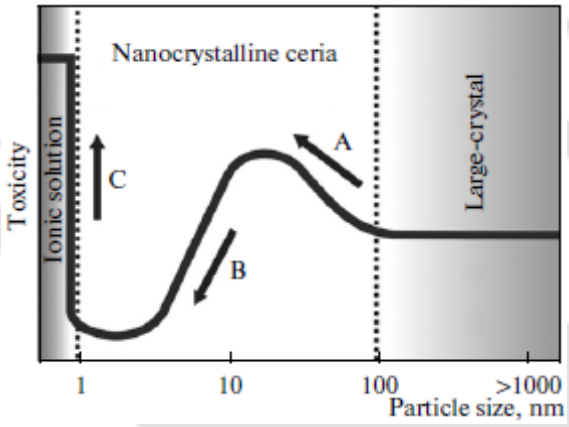

Figure1.4 Dependence of Ceria toxicity on particle size [Shcherbakov et al. 2011]

Shcherbakov et al. [2011] studied the physical and chemical properties of CeO_2, which was suggested to be a highly bioactive material. Fig. 1 indicates the dependence of Ceria toxicity on particle size. As it is observed from Fig. 1.4, the dependence of toxicity of ceria on particle size must have a nonmonotonic character. With decreasing the size of nanocrystalline ceria nanoparticles below an anomalous decrease of toxicity of ceria nanoparticles was observed. The given fact is connected with a sharp increase in the oxygen nonstoichiometry of particles and growth of the content of Ce^{3+} in its composition. The decrease in toxicity of ceria particles and growth of antioxidant (reductive) activity continue up to particles of subnanometer sizes.

Overall, the use of cerium as a fuel catalyst is potentially useful way to limit the health effects of vehicle exhaust. However, further testing is required to ensure that such an approach is not associated with a chronic inflammatory response which may eventually cause long-term health effects.

1.10 Organization of thesis

The present thesis is organized into five chapters. Chapter 1 gives an idea about the energy requirement for India, the stringent pollution norms, human health issues due to pollution and global environment issues. The solution was explored in detail and presented its feasibility to use as an alternate for diesel fuel. Fuel additives and fuel catalyst in the form of metal were introduced along with their advantages. Metal based ceria catalyst and its various applications are also briefly described. The overall organization of thesis was also described.

Chapter 2 presents a literature review in the field of ceria as high oxygen storage materials and its limitation. The literature was also given in support to the high OSC ceria based material, OSC evaluation techniques, nanoparticles characterization, synthesis of nanofluid, quality characterization of nanofluid, and experimental studies on engine performance and emission reduction.

Chapter 3 gives the detailed description of the techniques involved in the nanoparticles and nanofuel preparation and their characterization. It also gives the methodology to measure OSC, thermal expansion studies, engine performance and field study. All the methodologies were explained with the help of pictorial views of the relevant equipments / instruments.

Chapter 4 describes the results and discussion on the optimization of ceria based solid solution composition through quantitative and qualitative studies. Reasons for the enhanced fuel characteristics, performance and reduced emission were also presented. Field study using diesel generators and their enhanced performance were discussed with the help of experimental findings.

Chapter 5 presents a gist of overall work, prominent results obtained and salient findings from the thesis work. A conclusion note and the future direction for the present work were also briefed.

Chapter 2

Literature review

Metals in combustion received large interest as a result of the ability to produce oxygen while heating. The ability of a material to reversibly accept or contribute oxygen to its surrounding is the basis of use of a metal or its solid solution in catalytic applications, and it is referred as the oxygen storage capacity (OSC). It is the notable and highly desirable characteristic of nanosized metals during the heating.

The OSC of Three-way catalyst (TWC) enables great reduction of more harmful products of exhaust emission such as unburned hydrocarbon, CO, NO_x and CO_2. The TWC provides oxygen to CO and hydrocarbon under rich fuel conditions and extract oxygen from NO_x under lean fuel conditions. Though the use of TWC in the exhaust manifold has been explored significantly, the use of cerium based oxides as a catalyst in fuel to improve its combustion efficiency and reduce the emission level is yet to be explored in detail.

2.1 High oxygen storage capacity (OSC) materials

Cerium based oxides continue to attract researchers and industries, because of their potential use in catalytic applications in various fields. Ceria is especially interesting among the rare earth metal oxides because of its ability to change the valency state from Ce^{4+} to Ce^{3+} or vice versa. In cerium based oxides, the electronic re-configuration is associated with loss or addition of oxygen, which can be triggered at relatively low temperature in the range of 300-800 °C by the changes in the partial pressure of oxygen in gas with solid contact, Ozawa et al. [2000] and Crozier et al. [2008]. When oxygen vacancies are present in a metal, these ions can move through the lattice easily giving rise to oxygen ion conductivity. It plays an important role in the catalytic applications because the oxygen vacancies can move rapidly from surface to bulk or vice versa.

When ceria is used as a catalyst, it stores excess oxygen during the reduction process of NO_x and releases oxygen for the oxidation of CO and unburned hydrocarbon, which was due to its ability to switchover between Ce^{4+} and Ce^{3+} oxidation states depending on the partial pressure of

oxygen in the exhaust gas composition. The redox property of ceria is more effective if it is in the range of nanometer size, Sayle et al. [2005].

Hirano et al. [1999] synthesized the ultrafine CeO_2 (cerium (IV) oxide) powder in the range of 10-25 nm under hydrothermal condition in the presence of urea with a precursor of cerium (IV) sulfate and cerium (IV) ammonium sulfate. They investigated the effect of concentration of urea and hydrothermal treatment temperature on the morphology and crystallite size of the synthesized particles and reported that the crystallinity and particle size of ceria were observed to be decreased with an increase of urea concentration.

Hirano et al. [2000] prepared the crystalline cerium (IV) oxide nanoparticles by thermal hydrolysis with cerium di-ammonium nitrate as a precursor. The prepared nanoparticles were mixed with H_2SO_4 or $(NH_4)_2SO_4$ to find the effect of SO_4^{2-} on the ceria particles. The obtained nanoparticles were in the range of 10 nm size. In the presence of H_2SO_4, the nanosized crystals were found to be agglomerated into large spherical particles of 150-180 nm.

Rao et al. [2003] studied the structural and redox properties of ceria and ceria based materials. It was reported that the fluorite structure of ceria was retained up to 900 K under reduced atmosphere. The lattice constant was found to be increased with reduction temperature indicating the lattice expansion of its crystal structure, which was attributed to the reduction of Ce^{4+} ions into Ce^{3+}.

Though the low temperature reduction, large specific surface area and cubic structure are the inherent attractive characteristics of ceria for the higher OSC, the change of cubic structure of CeO_2 into hexagonal Ce_2O_3 and the reduction of specific surface area observed in the temperature range of 1017-1170 K are the major limitations of using CeO_2 as a fuel catalyst.

2.1.1 Ceria- zirconia solid solutions

In order to overcome the inherent limitations of CeO_2 as discussed above, the Zr^{4+} was doped in the cubic CeO_2 structure resulting the enhanced thermal stability, redox property and catalytic activity. It was observed that the reducible Ce^{4+} and its thermal stability were increased with Zr/Ce ratio, Vlaic et al. [1997].

Ceria- zirconia solid solution exits in three different structures namely monoclinic, tetragonal, and cubic. Cubic and monoclinic structure are thermally stable below 1300 K, whereas the tetragonal phase is a metastable structure and it is prepared by high temperature ceramic method, which is a solid state reaction in the composition range of 10-50 mol% of ceria. It was also observed that the kinetics of redox process was favorable for the cubic phase compared to tetragonal and monoclinic, Vlaic et al. [1999].

Rossignol et al. [1999] compared the OSC of synthesized $Ce_xZr_{1-x}O_2$ material by co-precipitation and sol-gel method using different precursors and it was confirmed that the maximum value of OSC was not obtained for the same composition prepared by sol-gel and co-precipitation technique. Sol-gel prepared $Ce_xZr_{1-x}O_2$ had the highest OSC in case of $0.75 \leq x \leq 0.98$, whereas co-precipitated oxides showed a plateau at $x \geq 0.5$.

Deshpande et al. [2004] synthesized highly stable $Ce_{1-x}Zr_xO_2$ nanoparticle solid solutions (x= 0.0, 0.1, 0.2, 0.3... 1) by hydroxide co-precipitation method with cerium ammonium nitrate and zirconyl chloride as precursors. The size of the nanoparticles obtained from their study was 3.5 nm for CeO_2 and 2.5 nm for ZrO_2. Dhage et al. [2004] synthesized $Ce_{0.75}Zr_{0.25}O_2$ at 100 °C by the sol-gel technique with the precursors of ceric nitrate and zirconium oxychloride, where the particle size was observed to be 5 nm whereas the same obtained from glycine nitrate process and microwave hydrothermal technique was noted to be 35 and 6 nm, respectively. They also suggested that the microstructural stability of the sample could be improved by doping suitable cations such as Zr^{4+}, Al^{3+} and Si^{4+}.

Wang et al. [2006] synthesized $Ce_{0.5}Zr_{0.5}O_2$ by spray freezing method and calcined at different temperature. It was observeded that the crystallite size and reduction temperature of the sample were increased from 6 to 12 nm and 486 to 731 °C, respectively, when the calcination temperature of the sample was increased from 500 to 1000 °C. Gateshki et al. [2007] synthesized CeO_2-ZrO_2 by sol-gel technique with the starting precursor of ammonium cerium nitrate and zirconyl chloride.

Table 2.1 gives the information about different preparation techniques, types of precursor used and the particle size of Ce-Zr solid solutions. Since the size of the solid solution depends on the preparation technique and its starting precursor, various synthesize routes were explored.

Table 2.1 Influence of preparation methods and precursors on the size of Ce-Zr solid solution

Synthesize method	Material composition	Starting Precursors	Size (nm)	Remarks	Reference
Combustion Emulsion Method	ZrO_2-CeO_2	Nitrates of zirconium and cerium	10	A single phase solid solution of ZrO_2-CeO_2 with wide range of composition	Takatori et al. [1999]
Direct precipitate - hydrothermal condition	CeO_2-ZrO_2	Ammonium cerium nitrate, zirconium oxy chloride	8-10	Decrease in crystallite size and increase in specific surface area with an increase of Zr/Ce ratio	Hirano et al. [2003]
Sol- gel	$Ce_{0.7}$ $Zr_{0.3}O_2$	Nitrates of cerium and zirconium	7.3	Solid solution provided more active oxygen species	Ping et al. [2008]
Sol- gel	ZnO:CeO_2	Ethanolic suspension of $Zn(CH_3COO)_2$. $2H_2O$, Cerium nitrate	-	Ultrafine material for optical UV filters	Lima et al. [2009]
Co-precipitation	Mesostructured $Ce_{0.6}$ $Zr_{0.4}O_2$	zirconium n-propoxide, ammonium cerium (IV) nitrate	4	Mesostructure collapsed after 1000 °C	Changlin et al. [2009 a]
Ultrasonic-assisted membrane reaction	$Ce_{1-x}Zr_xO_2$ (x= 0.4, 0.5, 0.6, 0.8)	Nitrates of cerium and zirconium	4.7 - 6	Lower Ce/Zr ratio showed better texture characteristics and high OSC	Meng et al. [2010]

Modeshia et al. [2007] studied cerium titanate pyrochlore $(Na_{1/3}Ce_{2/3})_2Ti_2O_7$ prepared by hydrothermal precipitation reaction. It was observed that the prolonged exposure of the sample at above ambient temperature was attributed to the growth of the particle size, which was not having any influence on the reduction temperature of the sample. They confirmed that the fluorite type structure was largely responsible for low temperature reduction rather than the high specific surface area of nanocrystalline material.

Zhang et al. [2007] synthesized $Ce_{0.6}Zr_{0.4}O_2$ by co-precipitation, sol-gel, solution combustion and surfactant-assistant method. It was concluded that (i) $Ce_xZr_{1-x}O_2$ obtained by co-precipitation technique had high specific surface area which was decreased with temperature, (ii) $Ce_xZr_{1-x}O_2$ prepared by solution combustion technique had highest activity, and the particle size was increased by thermal treatment at 900 °C.

OSC was influenced by textural, morphological and structural modification of CeO_2-ZrO_2, Xiaodong et al. [2007]. A thin zirconia coated ceria was not promoting or degrading the OSC of the enveloped ceria core. Ceria-zirconia solid solution prepared by co-precipitation technique showed better OSC than the physical preparation or ceria coating on zirconium or vice versa.

Prasad et al. [2009] reported that the replacement of cerium ions by cations modified the ion mobility, and the change in lattice resulted the formation of a defective fluorite structured solid solution. Such modifications in the defect structure of ceria are able to confer new properties to the material, such as better resistance to sintering at high temperature. They synthesized $Ce_xZr_{1-x}O_2$ (x= 1, 0.7, 0.4, 0.2, 0) solid solution using nitrates of cerium and zirconium by sol-gel method. The obtained nanoparticles had the cubic fluorite structure, a mixture of monoclinic and tetragonal phases and size of 15-30 nm diameter. They also suggested that the stabilization of cubic structure at intermediate composition was achieved with decrease in particle size of the mixed oxide.

From the above literature, it is concluded that the ceria doped with Zr^{4+} ions enhanced the oxygen mobility, OSC and the reduction or oxidation at low temperature. The method of preparation of the sample also influenced the dispersion/incorporation of Zr^{4+} in ceria. It was observed that the thermal stability of CeO_2-ZrO_2 was increased with Zr/Ce ratio. The cubic structure, which favored for high oxygen mobility in CeO_2-ZrO_2 was maintained at high Zr/Ce ratio.

2.1.2 Ceria – zirconia with other metals

From the recent studies, it is observed that the formation of mixed oxides of ceria with 3^+ vacancy element increased the oxygen mobility, Trovarelli [1999]. Jia et al. [2008] suggested that the doping of Al^{3+} and Zr^{4+} with ceria lattice enhanced the OSC and thermal stability.

Chang et al. [1996] observed that MnO_x supported $LaAlO_3$ had good O_2 uptake (oxidation) and O_2 release (reduction) rate at temperature below 600 °C, which was confirmed by the temperature program reduction (TPR) studies and it was significantly better than the ceria-stabilized alumina.

Kozlov et al. [2002] observed the effect of different synthesize method on the redox properties of CeO_2-ZrO_2-Al_2O_3. They prepared $ZrO_2/CeO_2/Al_2O_3$, ZrO_2-CeO_2/Al_2O_3 and ZrO_2-CeO_2-Al_2O_3 by sequential impregnation technique, co-impregnation technique and sol-gel technique, respectively. It was concluded that the sol-gel technique was found to be the most effective method to facilitate the intimate interaction, which resulted in Zr-rich cubic mixed oxide, and it was thermally stable upto 900 °C without segregation of the components.

When Pd supported Ce-Zr mixed oxide was used as a catalyst, the sintering process was expected to reduce the number of active sites, Arias et al. [2002]. It was observed that the catalytic activity of the test material was influenced by the ageing process. They also found the superior catalytic activity of Pd supported $(Ce, Zr)O_x/Al_2O_3$.

Masui et al. [2006] prepared CeO_2-ZrO_2-Bi_2O_3 by co-precipitation method and confirmed that the OSC of the catalysts was increased with Bi^{3+}content. The reduction temperature of CeO_2-ZrO_2-Bi_2O_3 catalysts was reduced considerably by 52% compared to that of $Ce_{0.86}Zr_{0.14}O_2$. Furthermore, the OSC of CeO_2-ZrO_2-Bi_2O_3 catalysts was more than twice that of the conventional CeO_2-ZrO_2 catalysts (482 µmol O_2/g) at 350 °C. The reason was that Bi_2O_3 was reduced to Bi ions easily and both Ce^{4+} and Bi^{3+} were reduced simultaneously. The low temperature reduction behavior was promoted by the addition of silver to the lattice and the deposition on the surface of CeO_2-ZrO_2-Bi_2O_3 solid solution and formed the $0.84Ce_{0.68}Zr_{0.18}Bi_{0.14}O_{1.93}$ -0.16AgCl.

Mikulova et al. [2006] prepared cerium-zirconium with neodymium ions and praseodymium ions by sol-gel and co-precipitation method. It was concluded that the praseodymium ions were

able to promote the oxygen mobility. The solubility of Sm^{3+} and Nd^{3+} ions in $Ce_{1-x}M_xO_2$ (M= Sm, Pr, Nd) was limited to x= 0.4, whereas the same was found to be 0.75 for Pr^{4+} (praseodymium). Moreover, the coefficient of thermal expansion of the solid solution was increased with the substitution concentration of the dopant, which is expected to create greater formation of oxygen vacancy.

Xiaodong et al. [2006] synthesized manganese doped ceria-zirconia mixed oxides by co-precipitation method and found that Mn doped CeO_2-ZrO_2 sample has increased OSC compared to CeO_2-ZrO_2 sample. Jia et al. [2008] synthesized $Mn_{0.1}Ce_{0.9}O_x$ (MC) and $Mn_{0.1}Ce_{0.6}Zr_{0.9}O_x$ (MCZ) by sol-gel method. It was concluded that the manganese doped with cerium and zirconium was found to have good redox and structural properties at higher temperature. The fresh MC sample had more absorbed oxygen species than the MCZ samples. Though the crystallite size of MC (5 nm) was lower than that of MCZ (5.6 nm), the increase in particle size for MCZ catalysts was less than that of MC, when the temperature was raised.

Zhang et al. [2009] prepared the CeO_2-ZrO_2-La_2O_3-Al_2O_3 catalyst by co-precipitation method which was found to have high thermal sintering effect, OSC improvement and reduction temperature. Introducing La^{3+} in CeO_2-ZrO_2-Al_2O_3 catalysts created more defective structure and enhanced the mobility of bulk oxygen, where the OSC of the test sample was found to be increased from 100.5 to 118.4 μmol/g at 1000 °C.

Hongmei et al. [2010] suggested that the CeO_2-ZrO_2-Al_2O_3 solid solution was expected to maintain the excellent textural properties, and thermal stability in addition to its attractive OSC, when the sample was prepared by co-precipitation method. It was observed that the CeO_2-ZrO_2-Al_2O_3 catalysts with 10 – 75 wt.% of Al_2O_3 had excellent structural stability and improved OSC.

Ming et al. [2010] confirmed that the OSC of ceria was increased with concentration of ZrO_2 in $Ce_{0.4}Zr_{0.5-x}Y_{0.1}Mn_{0.1}O_2$ and $Ce_{0.4}Zr_{0.5-x}Y_{0.1}Mn_{x-0.025}O_2$ mixed oxide. The reversible reduction of ceria was significantly modified by the addition of ZrO_2 with 0.025 mol%, which increased the OSC of CeO_2-ZrO_2-Y_2O_3 compounds. Doping a small amount of Mn ion in the $Ce_{0.4}Zr_{0.5}Y_{0.1}O_2$ sample increased the OSC, and decreased the reduction temperature. The $Ce_{0.4}Zr_{0.5-x}Y_{0.1}Mn_{0.1}O_2$ and $Ce_{0.4}Zr_{0.5-x}Y_{0.1}Mn_{x-0.025}O_2$ formed the cubic structure of CeO_2-ZrO_2 solid solution. It is observed that Mn ions were incorporated into the ceria-zirconia lattice, which created more defectives leading to higher mobility and diffusion ability of bulk oxygen. When Mn content in

cerium- zirconium-yttrium (CZYM) was 0.025%, the OSC and the particle size of the sample were observed to be 561 μmol/gram, and 5.5 nm, respectively.

From the above discussion, it is concluded that the selection of an appropriate precursor, the preparation method, composition, and textural properties played an important role in the success of the preparation of the high OSC material.

2.1.3 Evaluation of OSC of a material

The OSC was indicated by denoting the amount of O_2 absorption/release per unit weight of the catalyst, (O_2) μmol/g of catalyst, Gupta et al. [2010]. The valency change of Ce^{4+} to Ce^{3+} or vice versa and the O_2 release mostly occurred on the surface at relatively low temperature and it was possible at moderate temperature that could be observed from the temperature reduction program (TPR) profiles. Suitable redox property, i.e, the reduction at low temperature, is the desirable characteristics for oxygen storage materials, and it was supported by Wang et al. [2006].

Xiaodong et al. [2006] introduced CO step pulses in place of H_2 and O_2 to study the OSC. The total production of CO_2 per gram of catalyst in the first ten CO pulses was calculated and it provided the information on complete OSC of the catalyst. Jia et al. [2008] also proposed H_2 or CO pulse injection method for the measurement of OSC of a catalytic material.

Zhang et al. [2009] indicated that the ceria has two reduction peaks at 500 and 830 °C during TPR, which are associated with the release of surface oxygen and bulk oxygen, respectively. In case of CeO_2-ZrO_2 mixed oxide, only one peak was observed, which was ascribed to the simultaneous release of oxygen from the surface and bulk owing to its high oxygen mobility.

Meng et al. [2010] obtained the OSC of ceria-zirconia by the integrated area of up-take H_2 before reaching 600 °C in TPR. The average H_2 consumption peak area of two TPR profiles was used to calculate the OSC of a catalyst. Hongmei et al. [2010] measured the OSC by injecting pulses of oxygen into the sample bed until no oxygen consumption was detected by a thermal conductivity detector. Table 2.2 shows the different OSC measurement techniques noted from various literatures.

Table 2.2 Comparative studies on different OSC measurement techniques

Sl. No	Method of measurement of OSC	Methodology followed	Material used	Reference
1	TPR	Thermal decomposition of cerium-zirconyl oxalate under Ar flow at 1273 K and subsequent reoxidation at 673 K. H_2 reduction at 1273 K and subsequent reoxidation at 873 K. The TPR was carried out up to 1173 K at 10 K/min. under H_2 environment	CeO_2 –ZrO_2 powder	Masui et al. [2000]
2	H_2-TPR for redox treatment	Heating the sample from 30 to 300 °C (30 min. O_2, 70 ml/min.); cooling from 300 – 30 °C and purge Ar for 20 min. TPR heating 30-980 °C (10 °C/min. H_2-Ar mixture 30 ml/min.)	CeO_2-ZrO_2-Al_2O_3, CeO_2-ZrO_2/Al_2O_3 CeO_2-ZrO_2-Al_2O_3	Kozlov et al. [2002]
3	TPR–re oxidation O_2–H_2	Pretreated the sample from 30 to 500 °C (1 hr, 50% O_2- 50% N_2, 50 ml/min.); purged with N_2 for 0.5 hr; cooling to 30 °C (N_2); TPR-reoxidation heating up to 850 °C (1 hr, 50% O_2-50% N_2). The above cycle was repeated for 4 times	$RE_{0.6}Zr_{0.4-x}Y_xO_2$ (RE= Ce, Pr)	He et al. [2003]
4	TPR	Reduction in H_2 at 450 °C for 1 hr (30 ml/min.). After purging reducing gas with Helium, a stream of 5% O_2/He at 30 ml/min. was admitted in the reactor at 350 °C. The oxygen consumption was monitored by an on-line quadrupole mass spectrometer.	CeO_2–ZrO_2	Letichevsky et al. [2005]

5	TPR	Samples were heated from RT to 600 °C in TPR (10 K/min under flowing 5% H_2/Ar gas). Hold for 20 min., & switch the flow of Ar, (20 min.). The OSC was measured by injecting impulse O_2 gas at 600 °C. The amount of consumed O_2 was identified as OSC	CeO_2-Al_2O_3 powder	Ozawa et al. [2008]
6	TPR	5.49% H_2/Ar with 30 sccm flow rate and the heating rate of 10 °C/ min. up to 600 °C over 100 mg sample. Volume of H_2 intake by the sample was calibrated against CuO standard using an online thermal conductivity detector.	$Ce_{1-x}M_xO_{2-\delta}$ (M = Mn, Fe, Co, Ni, Cu, Pd, Pt, Ru, La, Y),	Gupta et al. [2010]
7	TPR/ OSC - injecting pulses of Oxygen	Reduction of the sample (200 mg) at 550 °C under H_2 flow (40 ml/min) and then the sample was cooled down to 200 ºC under N_2 at the flow rate of 20 ml/min.	CeO_2-ZrO_2-Al_2O_3 Co- precipitation	Hongmei et al. [2010]
8	TPR/pulse injection of O_2 technique	Sample was reduced with a flow rate of 10 ml/min. H_2 at 550 °C for 1 h, and then cooled to RT under Helium. The oxygen storage capacity complete (OSCC) was measured by pulse injection of O_2 until no consumption of O_2 was detected. The amount of O_2 consumed during the re-oxidation stage is referred as OSCC.	Ceria–zirconia–neodymia ternary solid solution coprecipitation method	Wang et al. [2011a]
9	TPR/ Oxygen-pulsing technique	Pulse reaction system equipped with a mass spectrometer used as a detector.	$Ce_{0.7}Zr_{0.3}O_2$	Du et al. [2011]

10	CO oxidation	Alternate pulses of O_2 and CO were injected every minute in order to simulate lean and rich operating conditions of the engine working cycle coupled with a TWC	$Ce_{1-x}Nd_xO_2$ - Co-precipitation $Zr_{0.10}(Ce_{1-x}M_x)_{0.90}O_2$ (M = Pr or Nd) - sol-gel method	Mikulova et al. [2006]
11	CO reduction	Rapid introduction of CO and He (CO pulse) or CO and O_2 (CO-O_2 cycle)	Mn doped CeO_2-ZrO_2 mixed oxides	Xiaodong et al. [2006]
12	CO reduction	Inlet gas flow sequence CO (5S)-tO_2 (5S)+ CO+ O_2 at a flow rate of 300 ml/min.	$Ce_{1-x}Zr_xO_2$	Meiqing et al. [2007]
13	CO reduction	The sample was purged in pure He for 10 min. to remove O_2 from the system and then exposed to 4% CO/He at 500 °C. CO_2 concentration was monitored as a function of time, and the OSC was obtained by integrating the amount of CO_2 formed during the first 2 min.	Ce-Zr-Pr (CZP), Ce-Zr-Nd (CZN) mixed oxides by co-precipitation	Wu et al. [2007]
14	CO oxidation reaction	Alternately pulsing: 4% CO/1% Ar/He (5s) → 2%O_2/1% Ar/He (5s)→4% CO/1% Ar/He (5s) for 5 cycles. The gas at 300 ml/min. over 25 mg sample was supplied to prevent the back mixing of reactants (CO and O_2).	$Mn_{0.1}Ce_{0.9}O_x$ and $Mn_{0.1}Ce_{0.6}Zr_{0.3}O_x$ prepared by sol-gel	Jia et al. [2008]
15	CO oxidation reaction-	CO (2 vol.%)/N_2 and O_2 (1.0 vol. %)/N_2 were fed into the reactor alternately for 60 s each. (O_2 storage and release behavior)	Pt/CeO_2.ZrO_2. Y_2O_3	Dong et al. [2008]
16	CO oxidation	CO and O_2 were introduced into a catalyst every 3 min.	Co-precipitated-Al_2O_3/CeO_2/ZrO_2	Morikawa et al. [2008]

17	CO oxidation reaction	Alternated $CO–O_2–CO–O_2–CO–O_2$ pulses. The OSC was determined based on the CO uptake during the first CO pulse from the alternated series	$La_{1-y}Ce_yCo_{1-x}Fe_xO$	Levasseur et al. [2009]
18	CO oxidation	CO and O_2 switch gas	$Pt/CeO_2–ZrO_2$	Kondratenko et al. [2009]
19	TGA	First heating cycle from 30 to 800 °C then cooling down to 150 °C, second heating cycle from 150 to 800 °C. Weight loss obtained during second heating cycle was used to calculate the OSC	Wet impregnated CeO_2-ZrO_2/Al_2O_3	Ozawa et al. [2000]
20	TGA	The weight change observed during the TGA was monitored under N_2 or dry air in the temperature from RT to 723 K	$Pt/Ce_xZr_{1-x}O_2$ solids	Bazin et al. [2009]
21	TGA	The weight change observed during the TGA was monitored under N_2 or dry air in the temp. range of 573–1073 K.	$Ce_xZr_{1-x}O_2$, $Ce_xHf_{1-x}O_2$ and $Ce_xTb_{1-x}O_{2-\delta}$	Reddy et al. [2011]
22	TGA	Sample was heated up to 600 °C (N_2, 50 ml/min.) in order to release the O_2. After 10 min., the synthetic air was introduced resulting to an increase in sample weight due the uptake of O_2 from air. The said weight change was considered as OSC of the sample	Ceria–zirconia	Ghom et al. [2011]

From the above information based on Table 2.2, it is noted that the OSC of nanoparticles has been studied using different techniques. Thermogravimetric analysis was used to find the redox temperature of the catalysts. When ceria was doped with zirconia, the reduction temperature was

decreased from 757 to 486 °C corresponding to the diminution of 36%. The doping of ZrO_2 in the CeO_2 lattice could create oxygen vacancies leading to increase the channel diameter for oxygen migration in the lattice, which caused the bulk oxygen release at low temperature. It was associated with the ZrO_2 ability to modify the sublattice oxygen in the CeO_2-ZrO_2 mixed oxides for generating defective structures, Wang et al. [2006].

Jia et al. [2008] suggested that the dynamic OSC, which is a measure of OSC at a continuous oxidation and reduction state, could be used to simulate the real operating condition, where the exhaust gas composition rapidly oscillated between the reducing and oxidizing environment.

Chung et al. [2009] used TGA technique to characterize the OSC by monitoring the changes in weight under cyclic heating in air environment. The heating cycle consisted of the following: (i) first heating up to 900 °C, (ii) cooling down to 150 °C and (iii) second heating up to 900 °C. The heating and cooling rates were maintained at 5 °C/min. The weight loss of the sample (Al_2O_3-$Ce_{0.5}Zr_{0.5}O_2$) in the second heating cycle was used to calculate the oxygen release characteristics of the catalyst between 300 and 800 °C. They also measured the OSC of sample at static condition using H_2/CO pulse injection technique.

Morikawa et al. [2008] measured the OSC of Al_2O_3-CeO_2-ZrO_2 using TGA with the pretreatment at 500 °C for 15 min. under O_2/N_2 and H_2/N_2 atmosphere. The change in atmosphere was repeated until the weight reduction under H_2 (20%)/N_2 (balance) environment and the weight gain under O_2 (20%)/N_2 (balance) environment became almost the same.

Table 2.3 shows the influencing parameters and characteristic features on OSC of different catalysts. It was observed that the OSC of CeO_2-ZrO_2 solid solution was influenced by the Ce/Zr ratio. Higher specific surface area was observed for higher OSC materials within the same composition and synthesis technique.

Table 2.3 Influence of different catalysts and specific surface area on OSC from selected literatures

Samples		Particle size (nm)	Specific surface area (m^2/g)	Volume (ml/g)	OSC (μmol/g)	Remarks
$Ce_{0.84}Zr_{0.16}O_2$		-	3.1	-	482	Co-precipitation technique of preparation. OSC was measured by injecting pulses of oxygen in the sample bed, Masui et al. [2006]
$Ce_{0.73}Zr_{0.17}Bi_{0.10}O_{1.95}$		-	2.9	-	647	
$Ce_{0.68}Zr_{0.18}Bi_{0.14}O_{1.93}$		-	1.7	-	696	
$Ce_{0.64}Zr_{0.16}Bi_{0.20}O_{1.9}$		-	0.8	-	1036	
$0.84Ce_{0.68}Zr_{0.18}Bi_{0.14}O_{1.93}$-0.16AgCl		-	1.3	-	951	
Ce/Zr= 1/3	CeO_2-ZrO_2	-	79/19	-	1383*	Co-precipitation technique of preparation. Wu et al. [2007]
	CeO_2-ZrO_2-Pr_6O_{11}	-	78/41	-	1197*	
	CeO_2-ZrO_2-Nd_2O_3	-	76/28	-	1215*	
	*Total OSC in μmol					
$Mn_{0.1}Ce_{0.9}O_x$		5	70.745	-	0.9534	Sol-gel technique of preparation Dynamic OSC was measured using TPR technique, Jia et al. [2008]
$Mn_{0.1}Ce_{0.6}Zr_{0.3}O_x$		5.6	55.056	-	0.8152	
CeO_2-ZrO_2-Al_2O_3		5.1	149	0.36	182.2	Co-precipitation technique of preparation, Zhang et al. [2009].
CeO_2-ZrO_2-$La_2O_3Al_2O_3$		3.8	189	0.43	195.8	

$Ce_x Zr_{0.5-x}$ $Al_{0.5}O_{1.75}$	Ce/Zr=1/9	-	143	0.41	130	Co-precipitation technique of preparation. OSC was measured by injecting pulses of oxygen in the sample bed. Hongmei et al. [2010]
	Ce/Zr=3/7	-	168	0.40	183	
	Ce/Zr=5/5	-	212	0.40	395	
	Ce/Zr=7/3	-	189	0.35	361	
	Ce/Zr=9/1	-	99	0.25	428	
$Ce_{0.4} Zr_{0.5} Y_{0.1}O_2$		4.4	121.2	0.26	466	Co-precipitation technique of preparation, Ming et al. [2010]
$Ce_{0.4}Zr_{0.49}Y_{0.1} Mn_{0.01} O_2$		4.5	109.8	0.24	526	
$Ce_{0.4}Zr_{0.475}Y_{0.1}Mn_{0.025}O_2$		4.3	117.6	0.25	561	
$Ce_{0.4}Zr_{0.45}Y_{0.1} Mn_{0.05}O_2$		4.9	98.3	0.23	515	
$Ce_{0.4} Zr_{0.4} Y_{0.1} MN_{0.1}O_2$		5.5	87.9	0.21	546	

2.2. Nanoparticles characterization

As the particle size, structure and specific surface area are found to have a great influence on OSC of a catalyst, the characterization of nanoparticles has significant role to play in many applications.

2.2.1 Structural characterization

In order to have a structural identification of the catalyst, X-ray diffraction analysis was performed. The average crystallite size was calculated from the full width at half maximum (FWHM) using the line profiles and Scherrer's equation and the lattice constant of the crystal was calculated using Bragg's law.

Hirano et al. [2000] confirmed that the crystallite size of CeO_2 was increased with hydrolysis temperature, and the crystal was found to have the cubic fluorite structure along with single

phase. Dhage et al. [2004] obtained the particle size of $Ce_{0.75}Zr_{0.25}O_2$ from XRD data and confirmed the mesoporous structure, which was collapsed on heating at 500 °C for 4 hrs.

Dutta et al. [2006] observed the fluorite structure of $Ce_{1-x}Zr_xO_2$ from XRD pattern and the Zr substitution in ceria led to broader width of XRD pattern compared to pure CeO_2. Wei et al. [2008] synthesized CeO_2 - ZrO_2 - Al_2O_3 mixed oxides with 10-75 wt.% Al_2O_3. However, the individual phases of Al_2O_3 and ZrO_2 were not detected by XRD, which confirmed that alumina and zirconia were well dispersed in CeO_2 crystal lattice and CeO_2 - ZrO_2 - Al_2O_3 was a homogenous solid solution.

Ming et al. [2010] observed that the XRD peaks of $Ce_{0.4}Zr_{0.5-x}Y_{0.1}Mn_xO_2$ ($0<x<0.1$) showed the cubic fluorite structure and no peaks for MnO_x and Y_2O_3 phases. It is suggested that the MnO_x and Y_2O_3 species might be incorporated into the CeO_2-ZrO_2 lattice forming a homogeneous solid solution with highly dispersed state. In addition, the samples showed broad symmetric peaks confirming the small crystallites. With an increase of Mn content, the peak intensities of $Ce_{0.4}Zr_{0.5-x}Y_{0.1}Mn_xO_2$ samples were found to be high indicating the increase of crystal size.

Hongmei et al. [2010] observed the peaks for $Ce_xZr_{0.5-x}Al_{0.50}O_{1.75}$ ($0.05\leq x\leq 0.45$) which were identical to the cubic fluorite structure of $Ce_{1-x}Zr_xO_2$ solid solution (Joint Committee on powder diffraction standards- JCPDS -28- 271) and it is confirmed that Zr^{4+} doped into CeO_2 crystal lattice during the solid solution formation by co-precipitation and sol-gel methods. From Ming et al. [2010] studies, it was observed that the crystallite size of $Ce_{1-x}Zr_xO_2$ was increased with Ce/Zr ratio. The decrease of (111) spacing could be attributed to Zr^{4+} doping which shrunk for the smaller lattice (ionic radius 0.084 nm) than the Ce^{4+} (ionic radius 0.097 nm).

2.3 Synthesis of nanofluid

The nanofluid is obtained by dispersing the nanoparticles in the base fluid. Because of the high specific surface area and Van der Waals force of attraction, the nanoparticles are expected to agglomerate in the liquid leading to sedimentation, and clogging. Thus, the utilization of nanofluid for commercial application is yet to be realized. Simple techniques such as ultrasonic agitation, tip sonication, magnetic stirring or the addition of surfactant to the fluids are often used to minimize the particles aggregation and improve the dispersion behavior of them in the fluid.

Garg et al. [2009] suggested two methods such as mechanical method including ultrsonication using a probe or a bath and chemical method including the use of surfactants to disperse multi wall carbon nanotubes in base fluids. They synthesized the nanofluid with de-ionized water, where gum arabic was used as a surfactant. The mixture was sonicated for 5 min. at 100% amplitude using 130 W, 20 kHz ultrasonication probe. As the probe sonicated with a limited conic volume, the sonication was followed by 5 min. of magnetic stirring in order to facilitate the uniform dispersion. The ultrasonication and magnetic stirring process were used alternatively for every 5 min. until the sample was sonicated for the desired period of time. Based on the processing time, a certain amount of energy was transferred to the sample. The samples prepared by the above techniques were found to be stable for a month with no visible sedimentation.

Ultrosonication is a common tool used to break the agglomeration of nanoparticles in solution based processing techniques. Ultrasonication can be done by different ways: direct by sonotrode in the solvent and indirect by the ultrasonic bath. The tip of ultrasonic sonotrode oscillates at a fixed frequency and produces a conical field of high energy in the fluid. The solvent undergoes nucleate boiling which produces infinite number of micro bubbles, which produces large amount of energy during their collapse that is the primary mechanism by which ultrasonic energy disperses the nanoparticles, Krause et al. [2010].

Sonawane et al. [2011] prepared the nanofluid which was found to be very stable even after 24 hrs independent of sonication time used to prepare the nanofluid. With an appropriate concentration of polyoxyethylene (20) sorbitan Monolaurate (Tween 20) and oleic acid as surfactants, the nanofluids were prepared by suspending different volume concentration (0.1-1%) of Al_2O_3 nanoparticles in Aviation Turbine Fluid. Gan et al. [2012] prepared a nanofluid with boron nanoparticles in n-decane and ethanol as a liquid medium. The nanofluid was prepared by vigorously mixing the liquid and nanoparticles by hand and then the ultrasonic disruptor was used to prevent the agglomeration.

In order to get the homogeneous dispersion of nanoparticles in a fluid, different surfactants were used during synthesis of nanofluid. Cetyl trimethylammonium bromide (CTAB) has been used by Luo et al. [2006] to get an optimum and stable slurry by 10 mol% Gd_2O_3-doped CeO_2 nanoparticles. Ashok et al. [2007] used sorbitan monooleate (span 80) as a surfactant and diethyl ether as an additive to improve the performance of a fuel in a diesel engine.

Changlin et al. [2009] synthesized mesostructured $Ce_{0.6}Zr_{0.4}O_2$ by co-precipitation method with different surfactants namely pluronic Triblock co polymer P123 (MW: 5800, $EO_{20}PO_{70}EC_{20}$), Brij 56 ($C_{16}EO_{10}$) and CTAB. It was concluded that the surfactants had little influence on the mesoporous structure of the nanoparticles. Ganesh et al. [2011] used CTAB for biodiesel in order to disperse Magnalium to control the particle sedimentation.

Aqueous tetramethyl ammonium hydroxide was used as a surfactant in order to cover the magnetic particles with hydroxide anion where tetramethyl ammonium cation was used to create electrostatic inter-particle repulsion in an aqueous environment, Shafii et al. [2011]. Gan et al. [2011a] reported that an overlap of the surfactant layer was expected to produce repulsive forces to overcome the Van der Waals force of attraction, thus the stability of the nanofluid was maintained. It is also noted that a sufficient amount of surfactant was required to be added to form a layer around the particles to produce the required repulsive forces.

Some examples of previously used surfactants are sodium lauryl sulfate (SDS), sodium dodecyl benzentsulfonate (SDBS), cetyltrimethyl ammonium chloride (CTAC) and CTAB. From the literature, it was found that SDBS failed at elevated temperature, Sadri et al. [2014].

2.4 Quality characterization of nanofluid

Nanofluids are not a simple mixture of liquid and solid particles. The nanoparticles tend to aggregate with time due to their high surface activity. The agglomeration of nanoparticles results not only the settlement and clogging, it also affects the physical and thermal properties of nanofluids. Thus, the investigation on stability of nanofluids is a key issue that influenced the properties of them for different applications. The factors affecting the stability of suspension are the nanoparticles concentration, dispersant, viscosity of base fluid, temperature, surfactants and pH value. The type, dimension and density of the nanoparticles and the technique used for the preparation of nanofluid also influence its stability. Few techniques such as sedimentation, UV vis spectrophotometer and zeta potential analyzer are being used to study the dispersion stability of nanofluid.

2.4.1 Dispersion stability of nanofluid

Sedimentation method is the most simple and reliable technique to study the dispersion stability of nanofluids. In this method, the variation of concentration or particle size of suspended medium with sedimentation time was obtained by sedimentation photograph of nanofluids.

Zhu et al. [2007] measured the stability of graphite suspension by a sedimentation balance method. The weight of sedimented nanoparticles during a certain period of time was measured from which the suspension fraction was calculated. It was observed that the stability of suspension was increased with the pH value of the fluid where the maximum dispersion was noticed at a pH value of 9-10. A further increase in the pH value resulted in unstable suspension. Long period of observation is the limitation of sedimentation method compared to any other method, Li et al. [2009b].

Jana et al. [2007] studied the stability of water based nanofluid dispersed with Au and Cu nanoparticles using UV spectrophotometer and it was observed that the stability of nanofluid was influenced by various forces such as (i) gravitational force on the particle, (ii) electrostatic force and (iii) Van der Waals forces between the particles.

Hwang et al. [2007] used CuO_2 and SiO_2 nanoparticles to prepare nanofluid with deionized water, ethylene glycol and oil. They studied the dispersion stability of a test sample using a UV-spectrophotometer. They reported the influence of type of nanoparticles and base fluid on the dispersion stability of nanofluids. Kumar et al. [2009] characterized the copper nanoparticles dispersed elthylene glycol using an UV spectrophotometer, where a good dispersion was noticed against time.

Zeta potential of nanofluid was measured using a zeta potential analyzer by electrophoresis light scattering method. This method has the limitation of viscosity and concentration of nanofluid. Zhu et al. [2009] measured the absorbency of alumina nanoparticles in a liquid medium with SDBS dispersant. According to electrostatic stabilization theory, a high absolute value of zeta potential increased the electrostatic repulsion among the nanoparticles in a suspension leading to their higher stability in a base fluid. Lin et al. [2011] obtained the concentration of Al_2O_3 nanoparticles against time in the nanofluid using the light absorbance data compiled by the

spectrophotometer. The variation in weight concentration of the nanoparticles in the nanofluid for a given period of time was determined as a precipitation rate of the Al_2O_3 nanofluid.

2.4.2 Fuel properties

Surface tension and viscosity are the important influencing properties of fuel during the injection process. A highly viscous nanofluid could also result in increasing the pumping power during the application of fuel.

Sajith et al. [2010] reported that the viscosity of nanofluid was found to be increased with the addition of ceria nanoparticles in Jatropha based biodiesel. It was suggested to limit the dosing of cerium oxide by 20-80 ppm, where the viscosity was reported to increase with particle concentration resulting to increased frictional power. Das et al. [2003a] performed the rheological studies on alumina based nanofluids. With an increase of particle volume fraction, the viscosity of nanofluid showed higher values than that of water. Surface tension of nanofluid was found to have a slight deviation from the base fluid. It was concluded that the change of surface tension of nanofluid against water was observed to have a negligible effect on the heat transfer characteristics.

Kim et al. [2007] measured the surface tension of Laponite, silver and Fe_2O_3 nanoparticles dispersed water using a tensiometer and it was found that the surface tension of nanofluid was differed negligibly from that of pure water. Golubovic et al. [2009] measured the surface tension of Al_2O_3 and Bi_2O_3 nanoparticles dispersed water to study the critical heat flux. The surface tension of nanofluid as a function of nanoparticles concentration was not changed significantly.

2.5 Experimental studies on engine performance and emission level

The performance of a compression ignition engine is generally characterized by several key parameters including the brake specific fuel consumption (BSFC), brake thermal efficiency (BTE) and the mechanical efficiency.

By knowing the cylinder pressure and rate of heat release, the typical combustion characteristics including the rate of increase of cylinder pressure, ignition delay and total combustion duration can be determined. The injection timing, which is the start of fuel injection, was determined at the crank angle where the injector needle raised abruptly. The ignition timing, which is the start

of combustion, was determined at a point when the heat was released. The time lag between ignition timing and injection timing is referred as the ignition delay. The end of a combustion process in a cycle was taken as a point where 90% of the cumulative heat release was completed. The time lag between end of the combustion and the ignition timing was taken as the total combustion duration.

Kao et al. [2008] reported that an addition of aqueous aluminum nanofluid in diesel increased the total combustion heat in addition to the reduction of smoke and nitrogen oxides in the exhaust emission. Tyagi et al. [2008] presented the ignition characteristics of alumina and aluminum nanoparticles dispersed diesel without any surfactant. It was concluded that adding nanoparticle to the fuel caused significant improvements in the radiative and heat / mass transfer characteristics and hence the droplet was ignited at a much lower temperature, which has the potential of reducing the evaporation and ignition time of droplets in a diesel engine.

Huang et al. [2009] reported that the melting temperature of a 1 nm aluminum particle could be as low as 127 °C, one fifth of its bulk material, which had a significant influence on the ignition and combustion mechanisms. Tyagi et al. [2008] reported that the high specific surface area to volume ratio of the nanoparticles allowed more fuel in contact with the oxidizer. Because of the small interparticle distance, the time scale of the chemical reactions was very much different than the reactions associated with large sized particles and thus, the ignition delay time for nanosized particles would be reduced.

Gan et al. [2011b] compared the burning behavior of nano and micron suspension of aluminum in the fuel. The results showed the characteristics and structure of particle agglomeration formed during the droplet evaporation and the combustion behavior. It was concluded that the burning behavior of nano suspension was better than the micron suspension.

Kao et al. [2011] dispersed aqueous aluminum nanoparticles in diesel and the results showed the decrease in BSFC and increase in BTE compared to that of diesel. Zhu et al. [2011] used ferrous picrate catalyst in diesel and reported the reduction of smoke by 26.2% at full load condition.

Shafii et al. [2011] carried out the performance study of a four-stroke diesel engine using water based ferrofluid mixed diesel. Water based ferrofluid has two advantages: the diesel can be diluted, which can reap the benefits of water diesel emulsion; the magnetic nanoparticles can be

collected at the exhaust of an engine. By adding a 0.4% ferrofluid to diesel, the BSFC was decreased by 3.2 - 6.5% and BTE was increased by 3.3 - 6.9%. The emission of NO_x and CO was decreased by 9 - 15 ppm and 3.33 - 6.89%, respectively. Zhu et al. [2012] used ferrous picrate catalyst for diesel engines, where the reduction in BSFC and the increase in BTE were observed with an addition of the catalyst. At the catalyst dosing ratio of 1:10000, the BSFC was reduced by 3.3 - 4.2% at light engine load of 0.12 MPa and 2.0 - 2.4% at heavy engine load of 0.4 MPa. From the in-cylinder pressure and heat release rate analysis, it was found that the catalyst reduced the ignition delay and the combustion duration resulting the higher peak cylinder pressure and faster rate of heat release.

Ganesh et al. [2011] observed the reduction of BSFC and increase of BTE, when magnalium and cobalt oxide were dispersed in biodiesel. Sajith et al. [2010] reported that the cerium oxide supplied the oxygen for oxidizing the hydrocarbon and soot and it got converted into cerous oxide. As cerium oxide acts as an oxidation catalyst, it lowered the activation temperature of carbon combustion and enhanced the hydrocarbon oxidation promoting the complete combustion of fuel. An average reduction of 25 to 40% in the hydrocarbon emission was obtained for the catalyst dosing level ranging from 40 to 80 ppm. They have obtained a 30% reduction in NO_x and 25 to 40% reduction in hydrocarbon emission, when cerium oxide nanoparticles were dispersed with Jatropha based biodiesel. Ganesh et al. [2011] also reported that the fuel evaporation time was reduced by metal oxide nanoparticles leading to the reduction of physical delay. In addition to that a 70% reduction in hydrocarbon, 41% reduction in CO and 30% reduction of NO_x emission at 75% load were also observed.

From the above literature, it was clearly understood that the nanoparticles dispersed diesel enhanced the performance of an internal combustion engine in terms of BSFC and BTE. It helped to reduce the smoke, NO_x and unburned hydrocarbon, which ensured its complete combustion. In general, the ignition delay and ignition temperature are the two critical parameters that influence the performance of a diesel engine. Both thermal efficiency and the reduction of emission level of an engine are improved by optimizing those parameters. Though there are many advantages of dispersing the nanoparticles in fuel including reduced ignition delay, increased energy density, high burning rate and reduced emission, a few works has been reported till date on the effect of dispersing the nanoparticles in diesel.

2.6 Technical gap

Based on the deliberation on several topics, the following technical gaps were identified.

- A suitable synthesis technique to prepare the high OSC ceria based homogeneous solid solution is not identified.
- The influencing parameters on the OSC of nanoparticles such as the crystallite size, surface area, structure, redox property and thermal stability are yet to be studied in detail.
- A suitable combination of materials and their effective stoichiometric ratio to have the highest possible OSC of ceria based nanomaterial is still to be identified clearly.
- Most of the studies on OSC of ceria based solid solution are done either by the complex method or expensive characterization techniques.
- Ageing studies on TWC materials are observed to be inadequate in order to find their thermal stability.
- Synthesis of highly stable nanoparticle dispersed fuel, studies on its dispersion stability and the selection of a suitable surfactant using feasible technique are yet to be explored in detail.
- Identification of suitable surfactants and synthesis technique are needed to be explored in order to get the highly stable nanofluid.
- Performance and exhaust emission studies on nanoparticle dispersed fuel in an IC engine are not studied in detail.

2.7 Objectives of the work

In this work, an attempt is proposed to improve the performance and reduce the harmful emission of a diesel engine by homogenously dispersing the nanosized high OSC materials of CZA and CZM (C=Ce; Z=Zr; M=Mn; Y= Al, Bi, La, Nd) oxides in diesel. The detailed objectives of the thesis work are as follows:

- To synthesize a homogeneous solid solution of nanoparticles (CZY and CZM oxides) using an appropriate technique and their characterization.

- To optimize the composition of CZY and CZM oxides based on their oxygen storage capacity and qualitative confirmation of the same.
- To synthesize highly stable nanoparticle dispersed fuel by selecting a suitable surfactant and a method of preparation.
- Dispersion stability studies on nanoparticle dispersed fuels and their characterization.
- Studies on the effect of nanoparticles type at an optimum concentration in diesel on the performance parameters and the reduction of different harmful emission in the exhaust gas of an engine.
- Field studies on the nanoparticle dispersed fuels.

Chapter 3

Materials and methods

This chapter is focused on discussing various techniques used and different methods employed for the preparation of nanoparticles beginning with materials used, methods followed to synthesize the nanoparticles and nanofuel, procedure adopted to test the nanofuel in an IC engine and field trial in the commercial diesel generators. The studies on nanoparticles and nanofuels involve several analytical tools and experimental techniques in order to confirm their characteristics. A series of different analytical instruments and techniques is used at various stages of development and testing of the nanoparticles and nanofuel, which are discussed below in detail.

3.1 Raw materials

To synthesize a solid solution of $Ce_xZr_{1-x}O_2$ (x= 0.2, 0.4, 0.6, 0.8), $Ce_{0.6}Zr_{0.4-x}Y_{1.3x}O_2$ (Y= Al, Bi, La, Nd) and $Ce_{0.6}Zr_{0.4-x}Mn_xO_2$ ($0.0 \leq x \leq 0.4$), Cerium (III) nitrate hexahydrate ($Ce(NO_3)_3.6H_2O$) (Aldrich, 99% and Alfa Aesar), Zirconium oxychloride ($ZrOCl_2$) (Lobachemie, 99%), Zirconyl (IV) oxynitrate hydrate powder ($ZrO(NO_3)_3.H_2O$) (Otto), Aluminum nitrate $Al(NO_3)_3.9H_2O$ (Merck), Manganese (II) nitrate hydrate $Mn(NO_3)_2.XH_2O$ (Aldrich), Bismuth nitrate penta hydrate $Bi(NO_3)_3.5H_2O$ (Merck), Lanthanum (III) nitrate hexa hydrate $La(NO_3)_3.6H_2O$ (Alfa Aesar) and Neodymium (III) nitrate hexa hydrate ($Nd(NO_3)_3.6H_2O$) (Alfa Aesar) were used as precursors. Ammonium hydroxide (NH_4OH) (Merck, 30% GR) was used as a precipitant in co-precipitation technique and Citric acid ($C_6H_8O_7$) (lobachemie) was used as a gel forming agent in sol-gel technique. Hexadecyl-trimethyl-ammonium bromide (CTAB) (Merck), Sodium lauryl sulfate (SDS) (Merck), Oleic acid (Merck), Polyoxyethylene (20) sorbitan monolaurate (Tween 20) (Merck), Polysorbate 80 (Tween 80) (Merck), Sorbitan monolaurate (span 20) (Merck) and Polyoxyethylene (20) sorbitan monooleate (span 80) (Merck) were used as surfactants during synthesis of the nanofuel. All the reagents were used without further treatment. Diesel was procured from the commercial outlet of Indian Oil Corporation Limited, Guwahati, India.

3.2 Synthesis of nanoparticles

In order to select a suitable method to prepare high OSC Ceria based nanoparticles, $Ce_xZr_{1-x}O_2$ (x= 0.2, 0.4, 0.6, 0.8) solid solution was synthesized by two techniques: (a) Co-precipitation (COP) method and (b) Sol-gel method, which are briefly discussed here.

As suggested by Zhang et al. [2007], $Ce_xZr_{1-x}O_2$ (x= 0.2, 0.4, 0.6, 0.8) solid solution was synthesized by COP technique and the methodology used for the same is shown in Figure 3.1. The aqueous solutions of $Ce(NO_3)_3.6H_2O$ (0.2mol/lit) and $ZrOCl_2$ having the desired Ce:Zr molar ratio were mixed thoroughly for 30 min. using a magnetic hot plate stirrer at room temperature. The molar ratio calculation is appended in Annexure – I. Then, the mixed solution was added 0.1ml/min into NH_4OH having the concentration of 2 mol/lit under vigorous stirring at 70 °C, where the pH value of the solution was maintained to be more than 10. The obtained precipitate was kept at room temperature for 48 hrs and then filtered. It was followed by washing with deionized water until no pH change was detected. The yellow colored precipitate was dried under ventilated condition at room temperature over night. Finally, the precipitate was calcinated at 200 °C for 2 hrs in a muffle furnace. The precipitate was agitated with a mortar and pestle to get the fine powder of $Ce_xZr_{x-1}O_2$ (x = 0.2, 0.4, 0.6, 0.8).

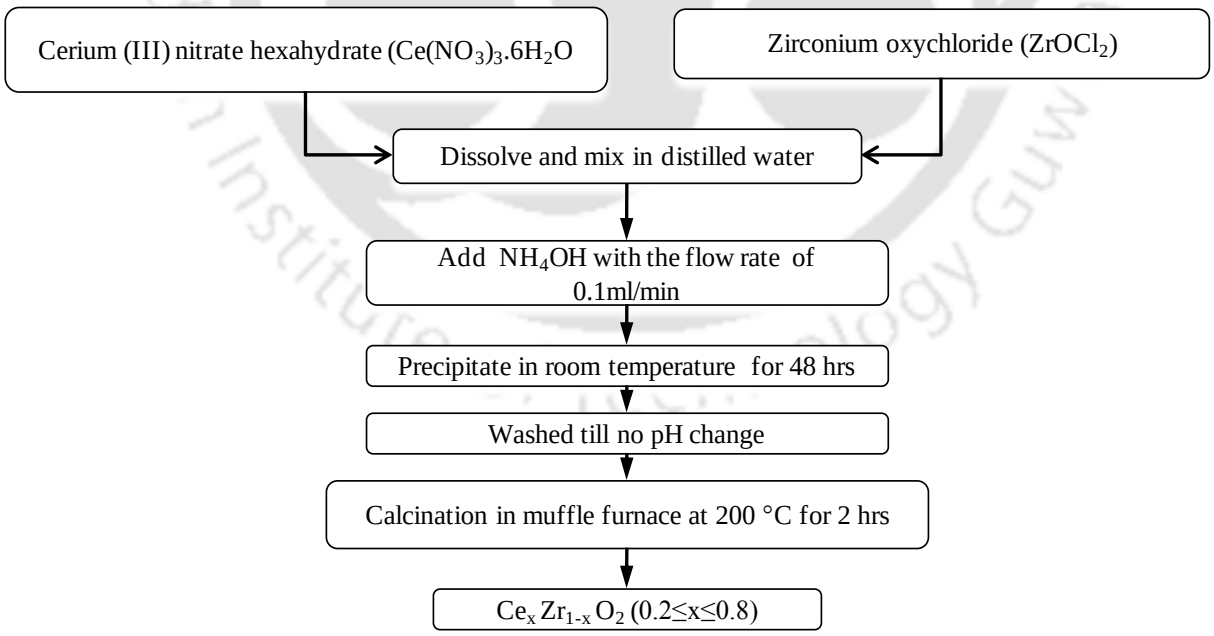

Figure 3.1 Flow chart for the Co-precipitation preparation technique to synthesize $Ce_xZr_{1-x}O_2$ solid solutions

$Ce_xZr_{1-x}O_2$ (x=0.2, 0.4, 0.6, 0.8) was also synthesized by sol-gel method, as suggested by Zhang et al. [2007] and the procedure adopted for the same is presented as a flow chart shown in Figure 3.2. The cerium (III) nitrate hexahydrate ($Ce(NO_3)_3.6H_2O$) and zirconium oxychloride ($ZrOCl_2$) with desired molar ratio, and the required quantity of citric acid were taken and all were mixed well in distilled water using a magnetic hot plate stirrer for 30 min. The pH value of the solution was increased up to 6 by dropping NH_4OH using the microfluidics pump with the flow rate of 0.5 ml/min. at room temperature. The mixture was heated at 60 °C for 30 min. and then heated further to 70 °C with continuous stirring. A transparent gel was formed at the end of the process, which was ignited and cooled in a muffle furnace in the static air environment at 350 °C. Then, the product was collected and agitated using a mortar and pestle to get the fine powder of $Ce_xZr_{1-x}O_2$ (x=0.2, 0.4, 0.6, 0.8). Figure 3.3 shows the setup used to synthesize the nanoparticles based on sol-gel / COP technique.

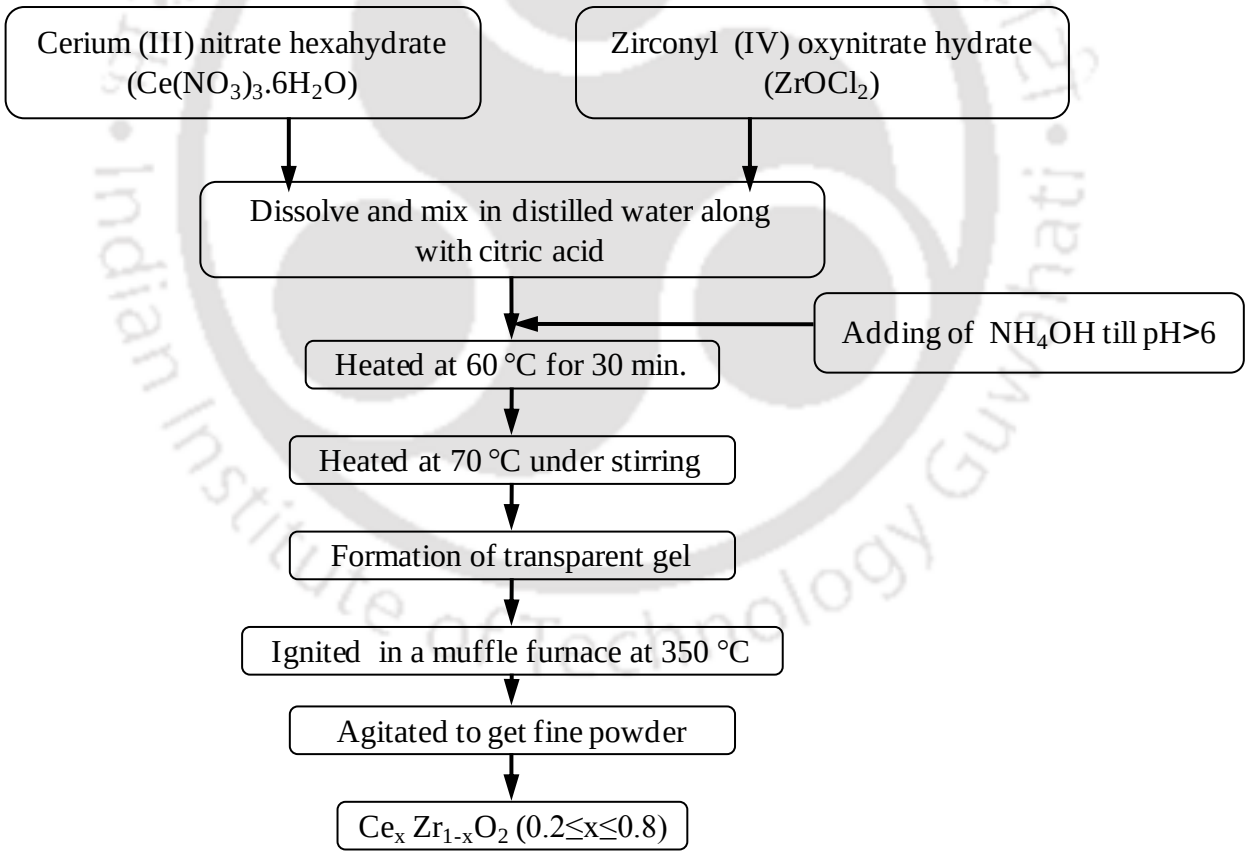

Figure 3.2 Flow chart for the sol-gel preparation technique to synthesize $Ce_xZr_{1-x}O_2$ solid solutions

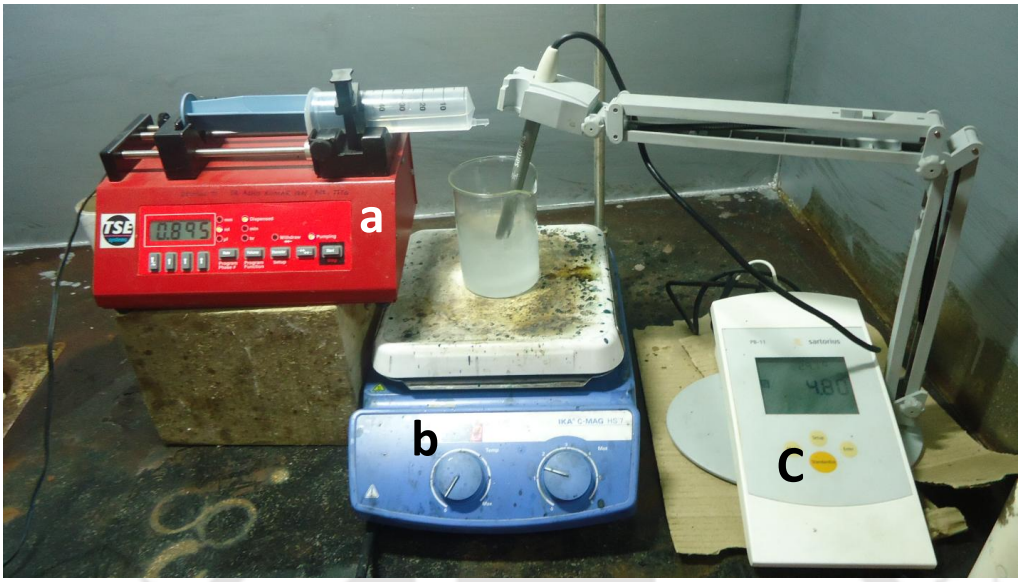

Figure 3.3 A setup to synthesize the nanoparticles as per COP and sol-gel technique
(a) Microfluidics pump, b) Magnetic stirrer, c) pH meter

Based on the OSC data of the nanoparticles synthesized by the above discussed techniques, sol-gel technique was followed for further studies. To synthesize $Ce_{0.6}Zr_{0.4-x}Y_{1.3x}O_2$ and $Ce_{0.6}Zr_{0.4-x}Mn_xO_2$ (where Y= Al, Bi, La and Nd; x= $0.0 \leq x \leq 0.4$) samples, the same procedure as discussed above for $Ce_xZr_{1-x}O_2$ by sol-gel technique was followed except the muffle furnace temperature, where it was maintained at 500 °C and the sample was called as fresh samples. Further, the samples were calcinated in a muffle furnace at 800 °C for 7 hrs, which were called as aged samples. The calcination temperature was selected based on the exhaust gas temperature passing through the catalytic converter used in an automobile system. The samples were designated as follows: $Ce_{0.4}Zr_{0.6}O_2$-CZ1, $Ce_{0.5}Zr_{0.5}O_2$-CZ2, $Ce_{0.6}Zr_{0.4}O_2$-CZ3, $Ce_{0.7}Zr_{0.3}O_2$-CZ4, $Ce_{0.8}Zr_{0.2}O_2$-CZ5, $Ce_{0.6}Zr_{0.3}Y_{0.13}O_2$-CZY1, $Ce_{0.6}Zr_{0.2}Y_{0.26}O_2$-CZY2, $Ce_{0.6}Zr_{0.1}Y_{0.39}O_2$-CZY3 and $Ce_{0.6}Zr_{0.0}Y_{0.52}O_2$-CZY4. In case of $Ce_{0.6}Zr_{0.4-x}Mn_xO_2$, the samples were designated as $Ce_{0.6}Zr_{0.3}Mn_{0.1}O_2$-CZM1, $Ce_{0.6}Zr_{0.2}Mn_{0.2}O_2$-CZM2, $Ce_{0.6}Zr_{0.1}Mn_{0.3}O_2$-CZM3 and $Ce_{0.6}Zr_{0.0}Mn_{0.4}O_2$-CZM4.

3.3 Synthesis of nanofuel

The nanofuel was synthesized by dispersing the desired type and quantity of nanoparticles in diesel. Due to high specific surface area of nanoparticles used for the nanofuel synthesize, the agglomeration of the same was expected to occur due to Van der Waals force of attraction,

which are required to overcome in order to produce a stable nanofuel using a suitable surfactant at 1:2 ratio as suggested by Sharif et al. [2009]. Different types of nanofuel synthesize techniques namely tip sonication, magnetic stirring and combination of both were explored for the same. In case of a tip-sonicator assisted nanofuel synthesis technique, a tip-sonicator make: M/s Sonics, USA, model: VCX 750, was used for the same, where the sample temperature was maintained at 35 °C and the setup used to prepare the nanofuel is shown in Figure 3.4. The sample container was kept in an ice bath in order to maintain the required sample temperature during the sonication period. The different concentration of nanoparticles was dispersed in diesel along with a suitable surfactant to prepare the nanofuel. The conical field of high energy was formed in diesel due to the oscillation of ultrasonic sonorod tip at 20 kHz frequency. The fluid undergoes nucleate boiling which produces infinite number of micro bubbles. When these bubbles collapse, it produces large amount of energy, which disperses the nanoparticles and avoiding the formation of agglomeration, Krause et al. [2010]. During the selection of suitable surfactant for further studies, the sonication period was selected as 1 hour based on our earlier results, Mandal et al. [2012]. The samples prepared using tip sonicator is shown in Figure 3.5.

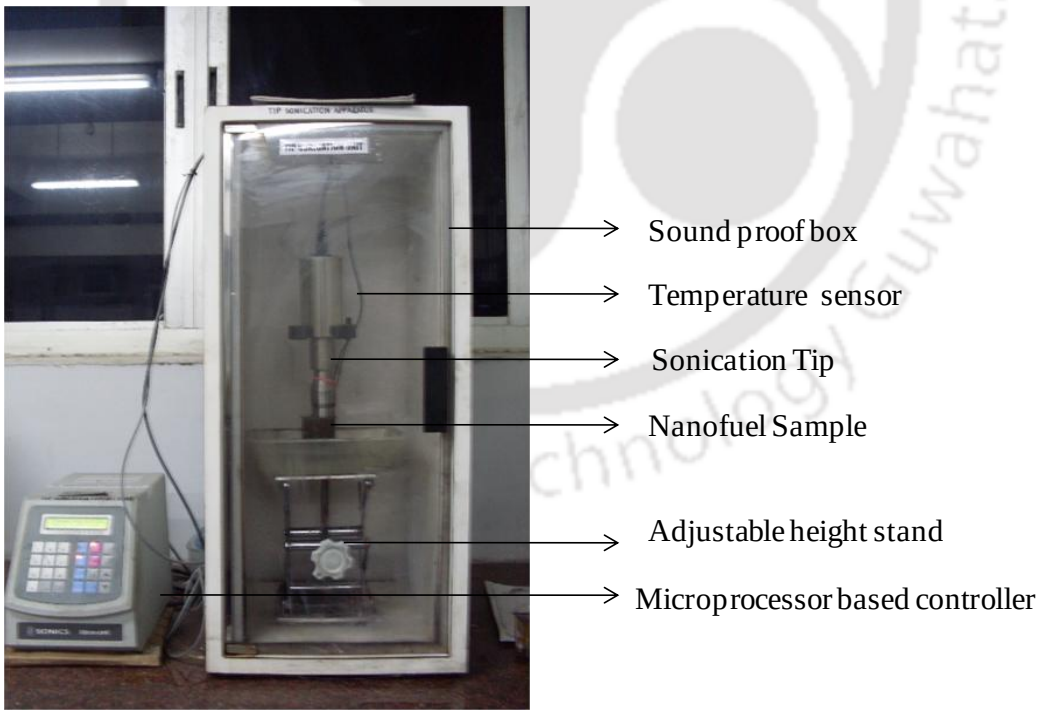

Figure 3.4 Tip sonicator

Figure 3.5 Different samples prepared using tip sonicator

In case of magnetic stirring technique to synthesize the nanofuel, a magnetic stirrer make: IKA C-Mag, model: HS7 was used. Figure 3.6 shows the pictorial view of nanofuel preparation using the magnetic stirrer. The required concentration of nanoparticles was added in diesel with suitable surfactant at 1:2 ratio and stirred for 2 hrs using the magnetic stirrer at room temperature, Das et al. [2008]. The magnetic field created on plate was changed its polarity by AC supply. In order to respond the change in magnetic field, the magnetic bead, which was placed inside the beaker also changed its direction, makes the vortex rotation within the fluid field in such a way that the bead rotates continuously leading to the dispersion of nanoparticles in diesel.

In case of combined technique to synthesize the nanofuel, the combination of tip sonicator and magnetic stirrer was used alternatively for 30 min. each for 2 hrs to disperse the nanoparticles in diesel. As the probe sonicates within the limited conic volume, tip-sonication was followed by magnetic stirring in order to facilitate the uniform dispersion of nanoparticles in diesel.

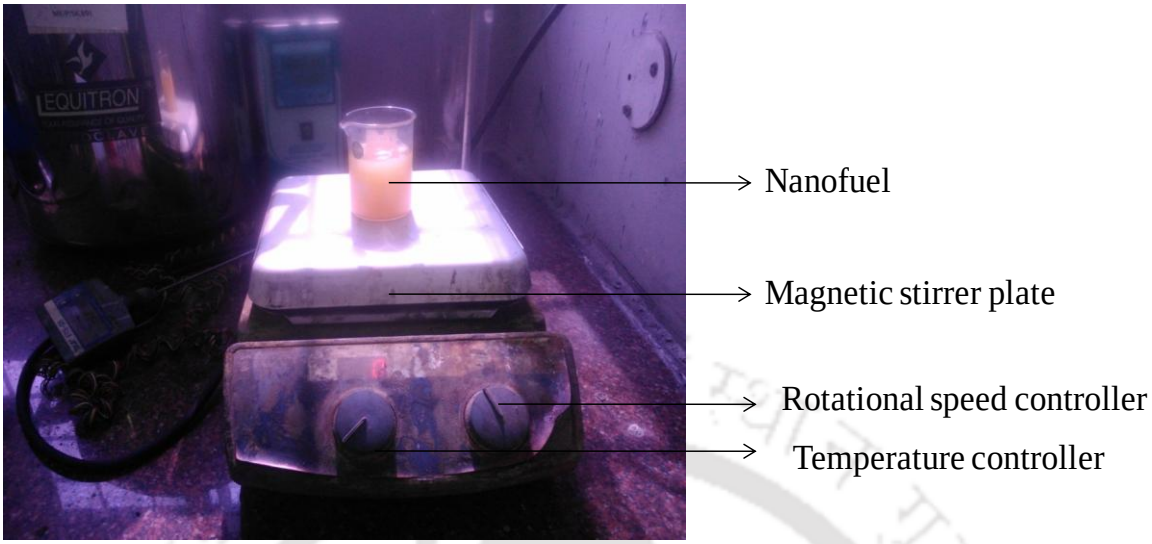

Figure 3.6 Preparation of nanofuel using magnetic stirrer

3.4 Characterization of nanoparticles

The synthesized nanoparticles were studied using different characterization techniques which are explained below.

3.4.1 Structural analysis - X-Ray diffractometer (XRD)

The X-ray diffractogram patterns of $Ce_{0.6}Zr_{0.4-x}Y_{1.3x}O_2$ (CZY; Y=Al, Bi, La, Nd) and $Ce_{0.6}Zr_{0.4-x}Mn_xO_2$ solid solutions were studied using a Bruker D8 advance powder diffractometer using a diffracted monochromated beam Cu-Kα (1.5406 Å) radiation source. A pictorial view of X-Ray diffractometer used in this study is shown in Figure 3.7. The samples were loaded on a zero back ground quartz plate and the intensity data were collected over the 2θ range from 10 to 70˚ with the scanning rate of 0.02˚ and the step time of 1 s. The crystalline phases of the sample were identified by comparing the reference data obtained from the JCPDS file. Three diffraction data were collected per sample in order to calculate the mean crystallite size and the lattice constant of the solid solution, which were calculated using the Scherrer's equation and Bragg's Law, respectively.

Scherrer's equation

$$d = \frac{\kappa\lambda}{\beta \cos\theta} \qquad \text{... (3.1)}$$

d = Crystallite size (nm)

κ = Particle shape factor - 0.894

λ = Wavelength of the X-ray used (1.5405 Å for Cu K α)

β = Full width at half maximum (radians)

θ = Diffracted angle of X-ray beam with the lattice plane (radians)

Bragg's Law

$$2d \sin\theta = n\lambda \quad \text{... (3.2)}$$

d = Interplanar spacing between the diffracting adjacent planes

θ = Angle of the X-ray beam with the lattice plane

n = Order of diffraction (1)

λ = Wavelength of the X-ray used (1.5405 Å for Cu Kα)

In addition to the above, the strain developed in the nanoparticles due to the processing technique followed to synthesize nanofuel was also calculated using X-ray diffractogram and the details of which are given below:

$$Strain = \frac{\beta}{\tan\theta} \quad \text{… (3.3)}$$

β = Full width at half maximum (radians)

θ = Diffracted angle of X-ray beam with the lattice plane

Figure 3.7 Bruker D8 advance powder X-Ray diffractometer

3.4.2 Lattice vibration studies- Raman spectroscopy

The oxygen storage capacity band of a material was confirmed by the Raman spectra using a laser micro Raman (Jovin Yvon, Triax 550) in the backscattering mode equipped with 514 nm green laser (Argon) and a CCD detector coupled with a monochromator having the XY step resolution of 0.1 μm, wave number accuracy of ± 1 cm^{-1} and its resolution of 0.5 cm^{-1}. The equipment was also used to confirm the crystallite phase and solid solution formation. The Figure 3.8 shows the pictorial view of the laser Raman spectroscopy.

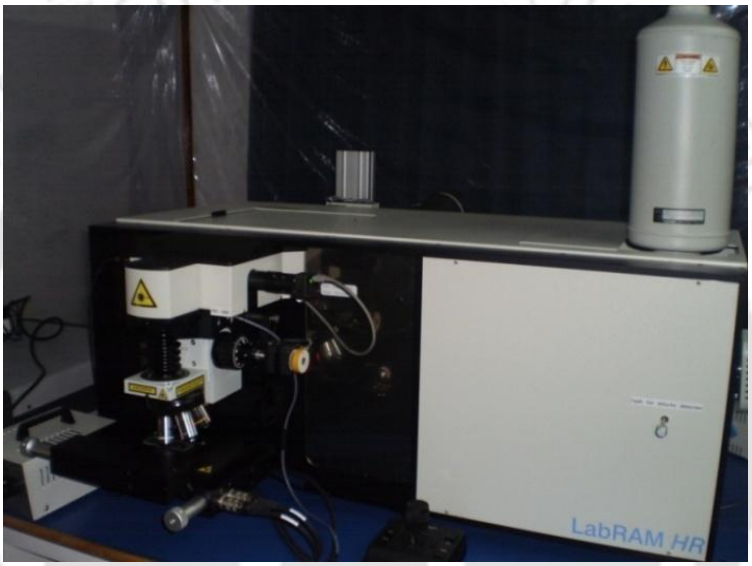

Figure 3.8 Laser micro Raman spectroscopy

3.4.3 Imaging studies - Transmission electron microscope (TEM)

A 200 kV Transmission Electron Microscope, JEOL JEM 2100, was used to confirm the crystallite size and shape of the solid solution. High resolution TEM and selective area electron diffraction (SAED) pattern were used to study the crystal defects in the solid solution. The homogenous dispersion of nanoparticles in nanofuel was also confirmed through TEM studies. Figure 3.9 shows the pictorial view of TEM.

Figure 3.9 Transmission electron microscope

3.4.4 Oxygen storage capacity studies- Thermogravimetric analyzer (TGA)

The oxygen storage capacity (OSC) of $Ce_xZr_{1-x}O_2$ ($0.2 \leq x \leq 0.8$), $Ce_{0.6}Zr_{0.4-x}Y_{1.3x}O_2$ and $Ce_{0.6}Zr_{0.4-x}Mn_xO_2$ (where Y= Al, Bi, La, Nd; $0.0 \leq x \leq 0.4$) was evaluated using the thermogravimetry analyzer under cyclic heating in the temperature range of 573–1073 K. The heating and cooling rate were maintained at 15 °C/min. and the initial weight of the sample was kept in the range of 500 mg. The samples were initially heated from room temperature to 800 °C in N_2 environment and cooled down to 150 °C in air environment followed by heating the sample up to 800 °C, as suggested by Ozawa et al. [2000]. The weight loss of the sample during second heating cycle was used to calculate the OSC of solid solution. The sample holder, made of Alumina, was heated in a muffle furnace up to 1200 °C to remove the contaminants from the pan, if any, later it was sonicated in an ultrasonic bath and dried in an oven to ensure the contaminant and moisture free sample holder. A Netzsch (STA 449F3, Germany) TG-DSC analyzer was employed for the same. The TGA used in the present study is shown in Figure 3.10.

Figure 3.10 Thermogravimetric analyzer

3.4.5 Thermal expansion studies – Thermomechanical analyzer (TMA)

Thermomechanical analyser (TMA/SS6000, Seiko Instruments) was used to measure the thermal expansion of the sample in the temperature range varying from 30 to 1000 °C at a heating rate of 10 °C/min. The test samples for TMA analysis were prepared by uniaxial compaction having the sample thickness and diameter of 5.50 ± 0.05 and 8.00 ± 0.05 mm, respectively. The density of test sample was observed to be varied within 10 % deviation from the theoretical density. A 'R'-type thermocouple was used to measure the sample temperature with an accuracy of 0.1 °C. To ensure proper contact between the probe and sample, a load of 100 mN was applied on the sample. A change in length of the sample against temperature was measured using a linear variable differential transformer (LVDT) technique having the sensitivity of 0.1 µm. The samples were pretreated in the TMA instrument to remove the absorbed moisture and the process induced residual stresses. The pictorial view of TMA is shown in Figure 3.11.

Figure 3.11 Thermomechanical Analyzer

3.5 Quality characterization of nanofuel

3.5.1 Dispersion stability studies- UV-Vis Spectrophotometer

The impact of high OSC nanoparticles on toxic emission can be achieved if the nanoparticles are homogeneously dispersed in diesel for a long period of time. Thus, it is expected that the nanoparticles would be continuously injected into the combustion chamber along with diesel. The dispersion stability of nanofuel was studied using a UV-Vis spectrophotometer model M/s Shimadzu, UVmini-1240, Japan, where the light was passed through the sample cell, and the detector records the intensity of the incidental and transmitted light and then the concentration of sample was calculated using the Beer-Lambert's equation, Pavia et al. [2007], which is expressed in eq. 3.4.

$$A = -\log\left(\frac{I}{I_0}\right) \quad \text{... (3.4)}$$

where I and I_0 are the intensity (power per unit area) of the incident and transmitted radiation, respectively. A is the intensity ratio.

$$\text{Relative stability} = \frac{A_i - A_c}{A_i} * 100 \quad \text{... (3.5)}$$

where A_i and A_c are the absorbance value of the nanofuel soon after its synthesize, and the absorbance value of nanofuel after the required period of time, respectively.

The relative stability of nanofuels was studied continually up to 168 hours (7 days). The duration of the relative stability test was selected on the basis of refilling the fuel tank in any automobile system. As the nanoparticles aggregate and sedimentation takes place concurrently, the relative stability of nanofuel changes continuously and thus it was studied on hour basis initially and then by day-basis in order to find the rate of sedimentation of nanoparticles in the fluid. As the prepared nanofuel has high absorbance value in the UV range, i.e. beyond the absorbance range of the instrument, ±3.9, the samples were diluted with Heptane in order to bring down the absorbance value to the measurable range of the spectrophotometer. It was chosen because the electrons might undergo several possible transitions of different energy in all compounds other than alkanes. The pictorial view of UV-Vis spectrophotometer is shown in Figure 3.12.

Figure 3.12 UV - Vis spectrophotometer

3.6 Characterization of nanofuel

In order to study the influence of CeO_2 based nanoparticles in diesel, the properties of nanofuel such as surface tension, flash and fire point temperature, thermal conductivity and viscosity were studied in detail.

3.6.1 Surface tension study - Tensiometer

Surface tension of nanofuel was measured against the concentration and the type of nanoparticles dispersed in it using a tensiometer. The surface tension between a liquid and the air was measured by placing a platinum ring below the surface of the liquid. The test was performed by pulling the ring upward by rotating a hand screw. When the ring just came out of the upper surface of the liquid, it was not detached abruptly from the liquid surface. Because of the surface tension, a hemispherical bubble was formed between the ring and the upper surface of the liquid. The ring was further pulled up very carefully. When the bubble just got detached from the ring, it showed the surface tension of the liquid. The pictorial view of tensiometer used to measure the surface tension of nanofuel is shown in Figure 3.13.

Figure 3.13 Tensiometer

3.6.2 Flash and Fire point temperature measurement - Pensky-Martens open type apparatus

The Flash and Fire point temperature of nanofuel were measured by using Pensky-Martens open type apparatus, which is shown in Figure 3.14. The flash point temperature of a volatile liquid is the lowest temperature at which it can vaporize to form an ignitable mixture in air. At the flash point, the vapor may cease to burn when the source of ignition was removed. The volatile liquid suddenly ignited from the heat received by the ignition source from which heat was given for a specific interval. The fire point temperature, a slightly higher than the flash point, is defined as the temperature at which the vapor continues to burn after being ignited. The sample contained in an open cup was heated and after some specific interval of time, a flame was brought over the surface. The measured flash point varied with the height of the flame above the liquid surface, and the measured flash point temperature coincides with the fire point at sufficient height. As the liquid vaporizes from the top surface of the diesel, the gas flame easily catches the hot vapor and suddenly it becomes ignited and immediately the fire goes away. The fire point temperature is assumed to be about 10 ºC higher than the flash point temperature.

Figure 3.14 Flash and Fire point temperature measuring instrument

3.6.3 Thermal conductivity measurement - KD 2 pro Thermal properties analyzer

The KD2-Pro Thermal Properties Analyzer, which is based on transient hot wire technique, was used to measure the thermal conductivity of nanofuel against the concentration and type of nanoparticles. The platinum wire serves the purpose of both heater and temperature sensor. The heat dissipated through the wire is used to increase the temperature of the sample. The accuracy of the thermal conductivity measurements was ± 2.5% in the range of 0.02 and 2 W/mK in the temperature range of 5 to 40 °C. The pictorial view of KD 2-Pro is shown in Figure 3.15.

Figure 3.15 KD 2 Pro - Thermal conductivity measuring instrument

3.6.4 Viscosity measurement- Rheometer

The Anton Paar Rheometer Model MCR 101 was used to study the viscosity of the nanofuel using the cone and plate geometry of the instrument. The upper plate was cone geometry (CP 50-1) with diameter of 49.964 mm, angle of 0.998˚ and the truncation of 99 µm. The sample was placed above the bottom plate, which was fixed on the base of the instrument. The viscosity of nanofuel was measured against different concentration and type of nanoparticles at 35 °C, which is the storage temperature and the maximum possible temperature in the fuel line till it reaches the combustion chamber. The tests were conducted under rotational mode with constant shear rate of 10 sec^{-1}. The pictorial representation of Rheometer is shown in Figure 3.16.

Figure 3.16 Anton-Paar Rheometer

3.7 Performance and emission studies in an Internal Combustion Engine

3.7.1 IC engine Test rig

The experimental setup used to study the performance characteristics of nanofuel is shown in Figure 3.17, which encompasses a Kirloskar stationary diesel engine having a single cylinder and water cooled rope brake dynamometer which is used for agricultural and industrial applications. The engine develops a power of 5 HP and it is operated at a constant speed of 1500 rpm. The operating conditions of an engine were kept as per the catalogue of the manufacturer. Initially, the engine was made to run with diesel for 30 min. to attain warm up condition and subsequently, the engine was tested using different concentrations of nanofuel without having any modifications in the system. The engine performance on pure diesel was also conducted as a basis for comparison. During the engine testing, the brake power was varied by changing the load through a rope brake dynamometer with the help of a spring balance.

Figure 3.17 IC engine test rig

3.7.2 Emission studies - Gas Analyzer and emission monitor

Figure 3.18 Exhaust gas analyzer and emission monitor

Exhaust emission such as hydrocarbon, CO, CO_2 and NO_x was measured using a portable gas Analyzer and emission monitor (Kane Quintox, KM9106), which is shown in Figure 3.18. The flue gas compositions were analyzed using a multi-component analyzer based on infrared and chemical cell technique. The apparatus was purged using fresh air before using it to study the

emission. The exhaust sample to be evaluated was passed through a cold trap (moisture separator) and filter element to prevent water vapor and particulates from entering into the analyzer. The hydrocarbon, CO and NO_x emission were measured in ppm (parts per million), and CO_2 emission was measured in terms of percentage.

3.8 Field Study

Field study of nanofuel was carried out in three different diesel generators having the capacity of 15, 25 and 30 kW. The diesel supply from the fuel tank to injection filter was disconnected and the fuel supply was directly taken from the nanofuel reservoir, as shown in Figure 3.19. The fuel line was drained through the suction pump and it was inserted in the nanofuel reservoir. In order to replace the residual diesel present in the fuel pump, nanofuel was filled in it using hydraulic suction pump. The same arrangement was followed for 25 and 30 kW capacity diesel generators. In order to calculate the fuel consumption, the time taken to consume 1 lit. of nanofuel was noted and compared with diesel. The pictorial view of all the generators tested for field trials are shown in Figure 3.20.

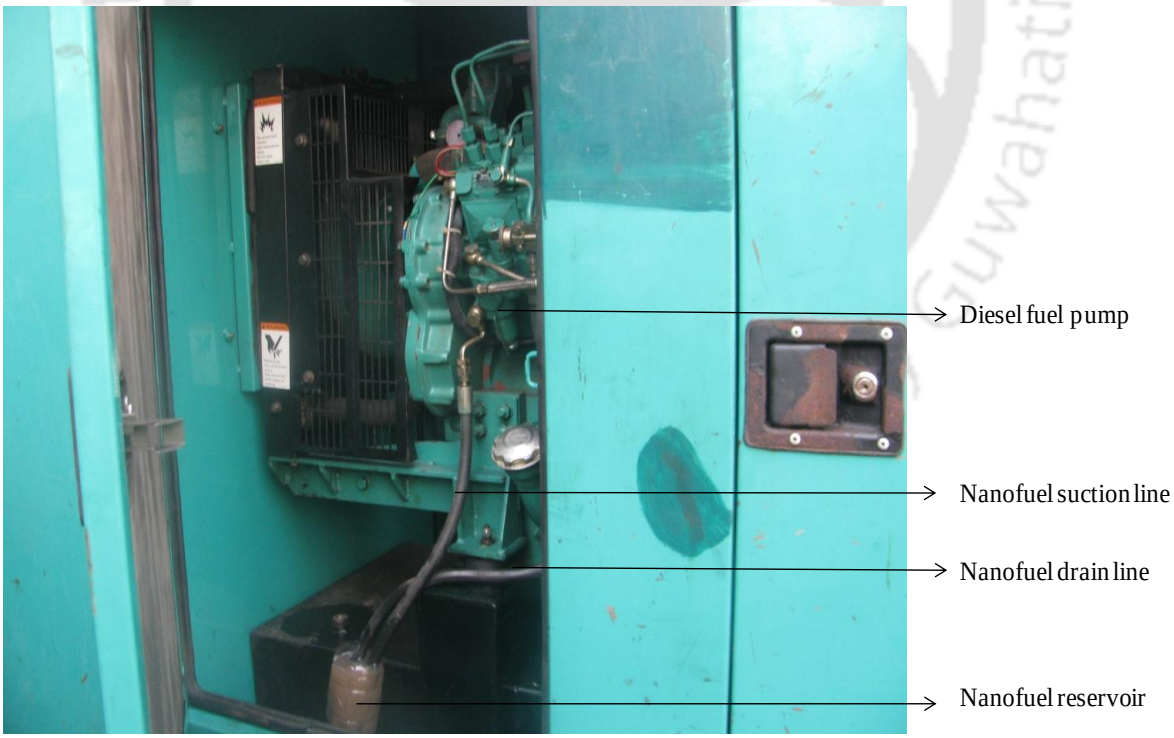

Figure 3.19 Suction and drained nanofuel line in the nanofuel reservoir

Figure 3.20 Three diesel generators used for field trial

Chapter 4

Results and Discussion

The results and discussion section gives a detailed technical insight into the various experimental outcomes in a sequential order as mentioned below:

4.1 Synthesize of ceria based high oxygen storage capacity (OSC) materials
4.2 Selection of a suitable surfactant and a synthesis technique to prepare nanofuel
4.3 Optimization of ceria concentration for the performance of an IC engine
4.4 Dispersion stability studies on nanoparticle dispersed fuels and their characterization
4.5 Engine performance with high OSC nanoparticle dispersed diesel (0.06 wt. % CZY solid solution / diesel - Nanofuel) and emission studies
4.6 Field trial on nanofuels

4.1 Synthesize of ceria based high oxygen storage capacity (OSC) materials

A ceria based high OSC nanomaterials is essential in order to have a higher catalytic effect in a three-way catalytic converter. The desirable characteristics of high OSC materials are the cubic structure and their stability at higher temperature. This section discusses about the selection of a suitable technique to synthesize high OSC nanoparticles, which will have the above requirements. The structural stability and formation of a solid solution of nanomaterials were confirmed by the X-ray diffractometric technique. The thermogravimetric technique was used to calculate the OSC of a nanomaterial, which were qualitatively confirmed by the Raman spectroscopy, HRTEM and TMA studies.

4.1.1 Selection of a suitable technique to synthesize $Ce_xZr_{1-x}O_2$ ($0.4 \leq x \leq 0.8$) solid solutions based on their OSC

In order to select a suitable technique to synthesize the $Ce_xZr_{1-x}O_2$ ($0.4 \leq x \leq 0.8$) solid solutions, the co-precipitation (COP) and sol-gel methods were followed. The nanomaterials were studied by different characterization techniques in order to confirm the homogeneous solid solution, OSC band, thermal stability, OSC and lattice defects. Figure 4.1a and 4.1b shows the X-ray

diffractrogram patterns of the $Ce_xZr_{1-x}O_2$ (CZ) solid solutions prepared by co-precipitation (COP) and sol-gel method, respectively. In both cases, four intense peaks corresponding to (111), (200), (220) and (311) planes were observed at around 28, 33, 47 and 57˚, respectively, in all the 5 combinations of the nanomaterials. These peaks confirmed the presence of homogeneous solid solution having the cubic fluorite structure, which is also confirmed by Meng et al. [2010]. It is also observed that there was a small peak shift towards the lower angle in both cases, which is due to increase of Ce/Zr ratio. The obtained peaks were found to be shifted from the Joint committee on Powder Diffraction Standards (JCPDS) 34-0394 of cubic CeO_2 structure, which is also shown in Figure 4.1 and it is confirmed that Zr^{4+} ions were doped on the lattice of CeO_2,

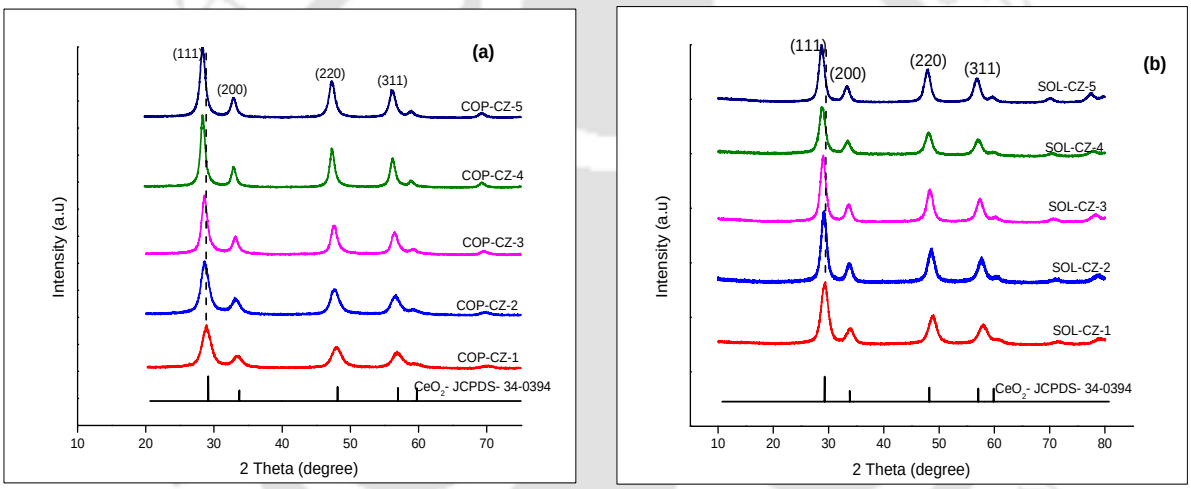

Figure 4.1 XRD patterns of $Ce_xZr_{1-x}O_2$ ($0.4 \leq x \leq 0.8$) solid solutions prepared by (a) COP and (b) Sol-gel method

Table 4.1 shows the average crystallite size, d-spacing, lattice constant, and OSC of $Ce_xZr_{1-x}O_2$ solid solutions prepared by COP and sol-gel synthesis technique. It was observed that the crystallite size of $Ce_xZr_{1-x}O_2$ solid solutions prepared by sol-gel technique was less than that of the COP synthesis technique. It was also noted that the lattice constant of $Ce_xZr_{1-x}O_2$ solid solutions was found to be less than that of CeO_2 (5.420Å). It is due to the fact that the radius of Zr^{4+} ions (0.84 Å) is smaller than the Ce^{4+} ions (0.97Å). The d-spacing was found to be in the range of 3.11 to 3.12 Å for COP sample and 3.04 to 3.09 Å for sol-gel sample. It is also confirmed that the strain induced in the ceria due to the substitution of Zr ions was found to be significantly less.

Table 4.1 also shows the OSC of $Ce_xZr_{1-x}O_2$ solid solutions prepared by COP and sol-gel methods. In general, the OSC of sample synthesized by sol-gel technique was observed to be higher than that of the same synthesized by COP technique. The OSC of $Ce_{0.6}Zr_{0.4}O_2$ prepared by COP and sol-gel technique was calculated to be 0.140 and 0.147 mol. of O_2/mol. of CeO_2, respectively, which is the highest among their own group of synthesized materials, and the sample prepared by sol-gel technique has the highest OSC among $Ce_xZr_{1-x}O_2$ solid solutions. It was due to the higher lattice expansion and high significant of OSC band in sol-gel samples than the COP synthesized samples.

Table 4.1 Structural parameters and OSC of $Ce_xZr_{1-x}O_2$ solid solutions prepared by COP and sol-gel (SOL) method

	$Ce_{0.4}Zr_{0.6}O_2$ (CZ1)		$Ce_{0.5}Zr_{0.5}O_2$ (CZ2)		$Ce_{0.6}Zr_{0.4}O_2$ (CZ3)		$Ce_{0.7}Zr_{0.3}O_2$ (CZ4)		$Ce_{0.8}Zr_{0.2}O_2$ (CZ5)	
	COP	SOL	COP	SOL	COP	SOL	COP	SOL	COP	SOL
Crystallite size (nm)	6.0	5.6	6.0	5.7	9.8	7.5	9.0	6.0	10.0	7.5
d-spacing (Å)	3.11	3.06	3.12	3.06	3.11	3.07	3.12	3.09	3.12	3.04
Lattice constant (Å)	5.27	5.34	5.28	5.38	5.39	5.34	5.39	5.40	5.39	5.31
OSC-(δ) (mol of O_2/mol of CeO_2)	0.024	0.043	0.067	0.121	0.140	0.147	0.102	0.131	0.079	0.102

Figure 4.2 (a) and (b) shows the Raman spectra of $Ce_xZr_{1-x}O_2$ solid solutions prepared by COP and sol-gel methods, respectively, where the corresponding major peaks were observed at 470 and 478 cm^{-1} confirming the cubic fluorite structure of the sample. The OSC band observed in the range of 610 to 640 cm^{-1} in both COP and sol-gel synthesized samples confirmed the presence of oxygen vacancies in solid solutions, which is also supported by Deshpande et al. [2000]. The OSC band of sol-gel synthesized samples was observed to be more significant than the COP prepared samples.

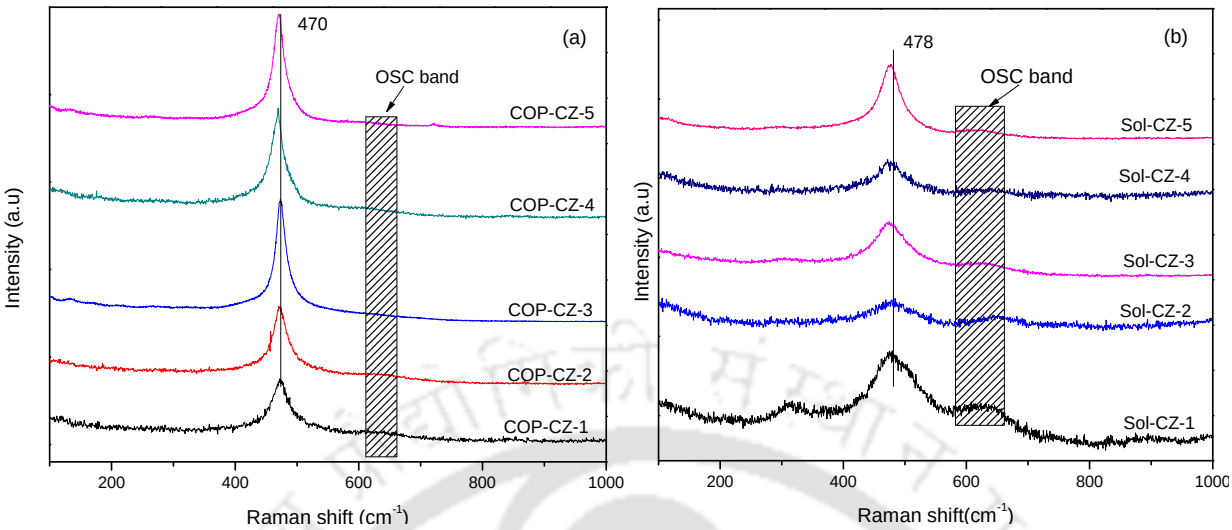

Figure 4.2 Raman spectra of $Ce_xZr_{1-x}O_2$ prepared by (a) COP and (b) Sol-gel method

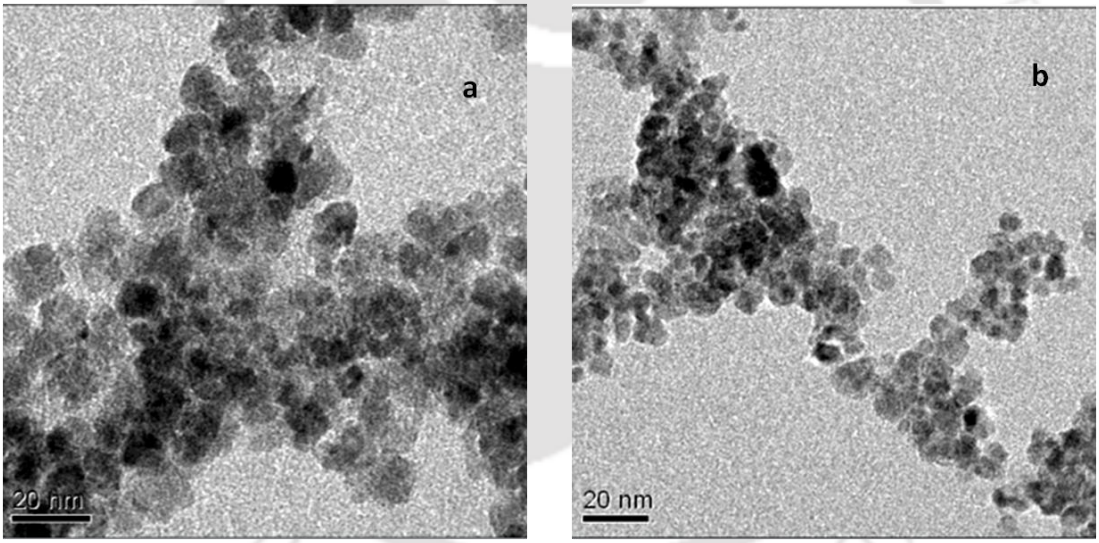

Figure 4.3 TEM images of $Ce_{0.6}Zr_{0.4}O_2$ prepared by (a) COP and (b) Sol-gel method

As the OSC of $Ce_{0.6}Zr_{0.4}O_2$ was found to be the highest among $Ce_xZr_{1-x}O_2$ solid solutions irrespective of the synthesize technique, TEM images were obtained for the same. Figure 4.3 (a) and (b) shows the TEM images of $Ce_{0.6}Zr_{0.4}O_2$ samples synthesized by COP and sol-gel synthesize technique, respectively, where the shape and size of the samples were observed to be uniform in each synthesize technique. The particles were found to be spherical in shape and the size was observed to be less than 8 and 10 nm in sol-gel and COP synthesize technique, respectively. It was also noted that the size of crystallites in sol-gel technique was found to be

less than that of COP technique and the particle size obtained from the TEM images was in good agreement with the XRD results.

It is noted from the above studies that the $Ce_{0.6}Zr_{0.4}O_2$ (CZ3) solid solution was observed to be the best composition having the highest OSC, 0.147 mol. of O_2 /mol. of CeO_2, among other types of solid solutions in $Ce_xZr_{1-x}O_2$. Incorporating an appropriate concentration of Zr ions in CeO_2 lattice increased the mobility of lattice oxygen and OSC. It is observed from the crystallite size and OSC of the $Ce_{0.6}Zr_{0.4}O_2$ solid solution that the sol-gel method was found to be the best technique to synthesize the high OSC nanoparticles compared to COP method. Hence, the $Ce_{0.6}Zr_{0.4}O_2$ solid solutions prepared by sol-gel technique were taken for further studies, where a 25, 50, 75 and 100 % of Zr^{4+} ions were replaced with 3rd component in ceria lattice, such as Al, Mn, Bi, La and Nd in order to further improve the OSC of $Ce_{0.6}Zr_{0.4}O_2$.

4.1.2 Structural analysis of $Ce_{0.6}Zr_{0.4-x}Y_{1.3x}O_2$ (CZY) and $Ce_{0.6}Zr_{0.4-x}Mn_xO_2$ (CZM) (x=0.0, 0.1, 0.2, 0.3, 0.4; Y=Al, Bi, La, Nd)

In order to confirm the formation of a solid solution, the XRD patterns of CZY and CZM fresh and aged solid solutions were studied. The crystallinity and crystal structure of the test sample were studied and confirmed using full width at half maximum (FWHM) and JCPDS files, respectively, through the XRD pattern. The structural stability of CZY and CZM solid solutions were also confirmed by studying the XRD pattern of aged samples.

Figure 4.4 shows the XRD patterns of fresh $Ce_{0.6}Zr_{0.4-x}Al_{1.3x}O_2$ ($0 \leq x \leq 0.4$) (CZA) solid solution. The diffractograms of cubic ZrO_2 and Al_2O_3 were also plotted for comparison purpose, where the respective data were obtained from JCPDS file 49-1642 and 10-0425. It is noted that the major peak of fresh CZA solid solutions was observed in the range of 28 - 29˚ for (111) plane and a shoulder peak was noted at 33˚ for (200) plane. An additional shoulder peak was also spotted in $Ce_{0.6}Zr_{0.4}O_2$ (CZ3) at 60˚. It is well known that the cubic CeO_2 exhibits a peak at 28.54˚ (JCPDS 34-0394), the monoclinic ZrO_2 reveals the peak at 28.218˚ (JCPDS 83-0944) and the most stable phase of γ-Al_2O_3 showed the peak at 66.8˚, Kozlov et al. [2002]. In case of all the fresh samples of CZA, as shown in Figure 4.4, the peaks corresponding to monoclinic ZrO_2 and γ-Al_2O_3 were not observed, which confirmed the uniform doping of Zr^{4+} and Al^{3+} in the ceria lattice to form a homogeneous solid solution of CZA. It is also confirmed by the formation of cubic fluorite structure of CZA, Peng et al. [2011]. The X-ray diffractograms of $Ce_{0.6}Zr_{0.4-}$

$_xAl_{1.3x}O_2$ solid solution samples showed that the peaks were relatively broadened compared to that of $Ce_{0.6}Zr_{0.4}O_2$ with an increase of Al^{3+} concentration, which indicated that the crystallite size of CZA was observed to be less compared to that of $Ce_{0.6}Zr_{0.4}O_2$ solid solution. In case of $Ce_{0.6}Zr_{0.4}O_2$, there was a slight shift from the cubic CeO_2 and monoclinic ZrO_2, which confirmed the incorporation of Zr^{4+} in cubic lattice forming the homogeneous solid solution having the cubic fluorite structure. It is consistent with the fact that the ionic radius of Zr^{4+} (0.84 Å) is smaller than that of Ce^{4+} (0.97 Å), Wang et al. [2011c].

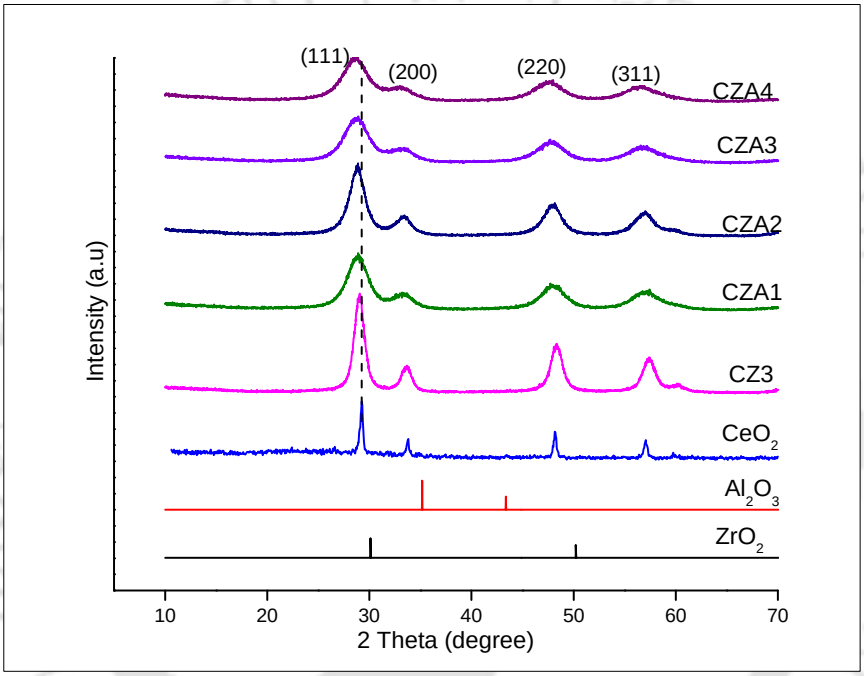

Figure 4.4 XRD patterns of fresh $Ce_{0.6}Zr_{0.4-x}Al_{1.3x}O_2$ samples

Figure 4.5 shows the diffractogram of aged CeO_2, $Ce_{0.6}Zr_{0.4}O_2$ and $Ce_{0.6}Zr_{0.4-x}Al_{1.3x}O_2$ samples. The major peaks were observed around 28, 33, 47 and 57˚ for all the samples of $Ce_{0.6}Zr_{0.4-x}Al_{1.3x}O_2$ composition for the plane of (111), (200), (220) and (311), respectively. It is observed that a decrease in FWHM in CZA aged samples compared to that of fresh samples confirmed the crystal size growth. The same trend was observed in case of all CZA1–CZA4 solid solutions suggesting the growth of crystallite size of the particles. In general, the peaks of CZA solid solution were found to be broadened with an increase of Al^{3+} concentration. The peak broadening in XRD is accounted for decrease in crystallite size [Wang et al. 2011b], strain effect [Fitzsimmons et al. 1991] and reduced crystallinity [Suhonen et al. 2001]. However, an increase

of crystallite size after ageing was less in CZA sample compared to CZ3 sample. The FWHM was observed to be reduced without any peak shift when Al^{3+} ions were introduced into CZ3 confirming the relief of stress from the CZA aged samples. In addition to that the ageing of sample at 800 °C led to rearrangement of crystal orientation, which is expected to reduce the crystal defects in the material, and it could be inferred from the peak narrowing as compared to fresh samples. The XRD patterns observed for all the aged CZA samples matched with JCPDS 34-0394 data, and it is confirmed that the CZA solid solution had a homogeneous structure and thus the highly dispersed Al^{3+} could not be detected in it. It is inferred that the insertion of Zr^{4+} and Al^{3+} has not changed the crystalline phase of CeO_2 but improved its structural integrity.

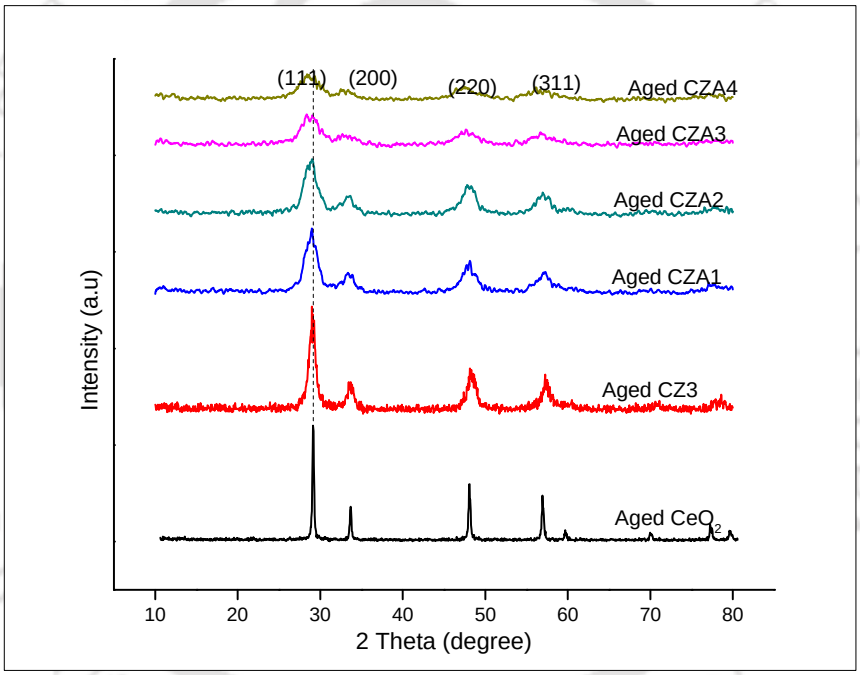

Figure 4.5 XRD patterns of aged $Ce_{0.6}Zr_{0.4-x}Al_{1.3x}O_2$ solid solutions

It is observed from Table 4.2 that the average crystallite size of fresh samples of $Ce_{0.6}Zr_{0.4-x}Al_{1.3x}O_2$ solid solutions varied from 2.7 to 4.7 nm, where the crystallite size of fresh sample was observed to be decreased initially with an increase of Al^{3+} concentration and then it was started to increase when 100 % replacement of Zr^{4+} was done with Al^{3+}. The crystallite size of all the samples was observed to be lower than that of $Ce_{0.6}Zr_{0.4}O_2$ (CZ3). Due to ageing of the sample at high temperature (800 °C for 7 hrs), the aggregation of the crystals was expected to take place leading to increased crystallite size by 45, 20 and 38 % for CZ3, CZA1 and CZA3

solid solutions, respectively. However, there was no influence of ageing on CZA2 and CZA4. It was noticed that the d- spacing of fresh CZA was increased slightly with Al^{3+} substitution in all the samples. The lattice constant of $Ce_{0.6}Zr_{0.4}O_2$ was found to be 5.31 Å, which is comparatively less than that of pure ceria i.e. 5.41 Å [Wang et al. 2011c]. The lattice shrinkage of ceria was caused by the introduction of Zr^{4+} (0.84 Å), which substitutes a part of Ce^{4+} (0.97 Å) in the CeO_2 structure. In case of $Ce_{0.6}Zr_{0.4-x}Al_{1.3x}O_2$, the lattice constant was found to be increased due to the increase of Ce/Zr ratio [Hongmei et al. 2010], which is caused by the replacement of Zr^{4+} by Al^{3+} though the ionic radius of Al^{3+} was reported to be 0.51 Å [Chong et al. 2004], which is lower than that of Ce^{4+} and Zr^{4+}. It could lead to the lattice defects and improved lattice oxygen mobility. Thus, the lattice constant of CZA was slightly higher than that of CZ3, which was also supported by Guo et al. [2008]. It is also observed that there was no appreciable increase in lattice constant of CZA due to ageing. Cerium ions were replaced by aluminium ions in the CeO_2 structure, which played a key role on inhibiting the diffusion of ions. The introduction of Al^{3+} in CZ3 suppressed its grain growth leading to a stable structure.

Table 4.2 Crystallite size, d-spacing and lattice constant of fresh and aged $Ce_{0.6}Zr_{0.4-x}Al_{1.3x}O_2$ (CZA) solid solutions

Sample	Fresh samples			Aged Samples			% increase of crysta -llite size*
	Crysta -llite size (nm)	d-spacing (Å)	Lattice constant (Å)	Crysta -llite size (nm)	d-spacing (Å)	Lattice constant (Å)	
$Ce_{0.6}Zr_{0.4}O_2$ -CZ3	7.5± 0.3	3.07± 0.03	5.31± 0.05	10.8± 0.9	3.09± 0.01	5.34± 0.04	45
$Ce_{0.6}Zr_{0.3}Al_{0.13}O_2$ -CZA1	4.7± 0.5	3.07± 0.08	5.36± 0.07	5.6± 0.7	3.09± 0.08	5.34± 0.04	20
$Ce_{0.6}Zr_{0.2}Al_{0.26}O_2$ -CZA2	4.7± 0.7	3.08± 0.03	5.33± 0.06	4.7± 0.6	3.07± 0.08	5.31± 0.02	0.2
$Ce_{0.6}Zr_{0.1}Al_{0.39}O_2$ -CZA3	2.7± 0.8	3.10± 0.06	5.49± 0.03	3.7± 0.5	3.07± 0.08	5.31± 0.05	38
$Ce_{0.6}Al_{0.52}O_2$ - CZA4	3.7± 0.7	3.23± 0.03	5.59± 0.04	3.7± 0.3	3.12± 0.04	5.39± 0.03	0.5
*% increase of crystallite size of aged samples with respect to fresh samples							

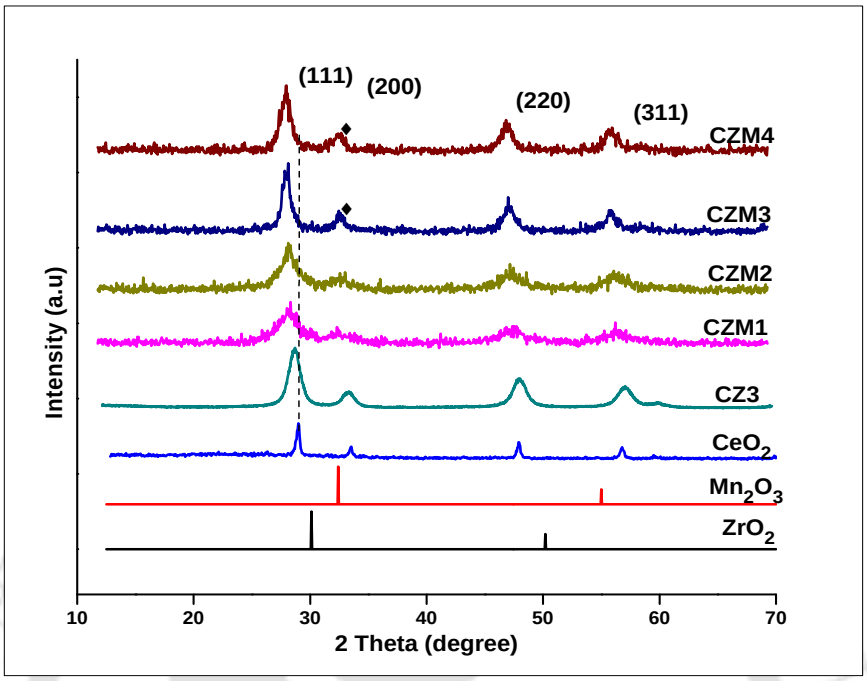

Figure 4.6 XRD patterns of fresh $Ce_{0.6}Zr_{0.4-x}Mn_xO_2$ samples

The XRD patterns of freshly prepared $Ce_{0.6}Zr_{0.4-x}Mn_xO_2$ ($0 \leq x \leq 0.4$) (CZM) are shown in Figure 4.6. The diffractograms of cubic ZrO_2 and Mn_2O_3 were also plotted for comparison purpose, where the respective data were obtained from JCPDS file 49-1642 and 02-0896. It was noted that ZrO_2 and Mn_2O_3 peaks were not observed in the freshly prepared CZM1 and CZM2 samples. Four strong peaks corresponding to $Ce_{0.6}Zr_{0.4-x}Mn_xO_2$ were observed to be around 28.55, 33.08, 47.48 and 56.33˚ for the plane of (111), (200), (220) and (311), respectively, which confirmed the presence of cubic fluorite structure as per JCPDS 34-0394. Though all the samples of $Ce_{0.6}Zr_{0.4-x}Mn_xO_2$ composition exhibited major peaks similar to that of CeO_2, a peak shift towards the lower angle side was observed with an increase of Mn ions substitution in place of Zr^{4+}, which is due to the smaller ionic radius of Zr^{4+} (0.84 Å), Mn^{3+} (0.62 Å) and Mn^{2+} (0.83 Å) compared to Ce^{4+}(0.97 Å) and Ce^{3+}(1.14 Å). The above observation is an indication of the changes in the lattice constant and confirmation of the formation of a homogeneous solid solution. An increasing trend observed for the d-spacing of CZM confirmed the above finding, which is presented in Table 4.3. A change in the d-spacing was due to induced uniform strain by doping smaller ionic radius metals like Zr^{4+} and Mn^{3+} in the ceria lattice and it is also supported by Atkinson et al. [2000]. The strain induced in the material is expected to increase the d-spacing

leading to a peak shift towards a lower angle side. It is also noted that the tetragonal zirconia peaks corresponding to 34.5 and 35.3˚, as referred by Hori et al. [1998], were not found in CZM even at higher concentration of Zr. A peak observed at 32.2˚ proved the presence of α-Mn_2O_3 in CZM3 and CZM4, which is due to the saturation of solubility limit of Mn ions in ceria- zirconia solid solutions.

Figure 4.7 shows the XRD patterns of $Ce_{0.6}Zr_{0.4-x}Mn_xO_2$ ($0 \leq x \leq 0.4$) aged samples. The peaks were observed to be around 28.80, 33.55, 47.80 and 56.84˚ for the respective plane of (111), (200), (220) and (311). A continuous peak shift towards lower angle side was observed in all aged samples. These results revealed that the aged samples continued to have the cubic fluorite structure similar to that of fresh samples, even though the samples were heated till 800 °C for 7 hrs. A decrease in FWHM in aged sample compared to that of fresh samples confirmed the crystal growth. No XRD peaks pertaining to ZrO_2 and Mn_2O_3 were observed in the samples except CZM3 and CZM4.

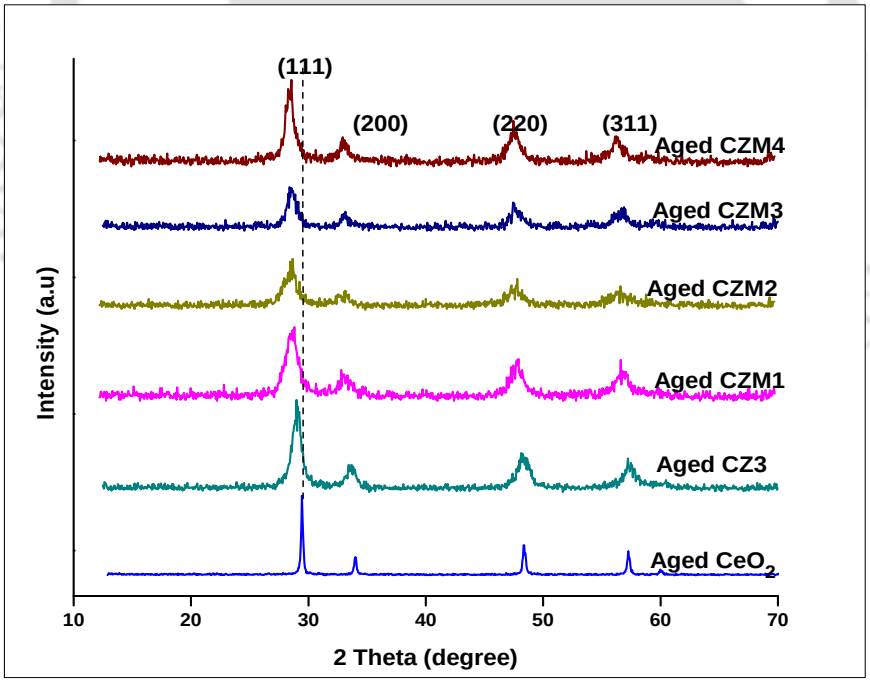

Figure 4.7 XRD patterns of aged $Ce_{0.6}Zr_{0.4-x}Mn_xO_2$ samples

Table 4.3 Crystallite size, d-spacing and lattice constant of fresh and aged $Ce_{0.6}Zr_{0.4-x}Mn_xO_2$ (CZM) solid solutions

Samples	Fresh samples			Aged samples			% increase of crysta -llite size*
	Crysta -llite size (nm)	d-spacing (Å)	Lattice constant (Å)	Crysta -llite size (nm)	d-spacing (Å)	Lattice constant (Å)	
$Ce_{0.6}Zr_{0.4}O_2$ -CZ3	7.5± 0.3	3.07± 0.03	5.31± 0.05	10.8± 0.9	3.09± 0.01	5.34± 0.04	45
$Ce_{0.6}Zr_{0.3}Mn_{0.1}O_2$ -CZM1	3.3± 0.5	3.07± 0.04	5.29± 0.03	3.6± 0.7	3.09± 0.05	5.29± 0.05	9
$Ce_{0.6}Zr_{0.2}Mn_{0.2}O_2$ -CZM2	2.7± 0.4	3.07± 0.09	5.28± 0.05	3.4± 0.7	3.09± 0.03	5.29± 0.02	26
$Ce_{0.6}Zr_{0.1}Mn_{0.3}O_2$ -CZM3	3.4± 0.2	3.09± 0.02	5.32± 0.04	3.8± 0.4	3.12± 0.02	5.35± 0.03	12
$Ce_{0.6}Mn_{0.4}O_2$ - CZM4	3.6± 0.2	3.11± 0.06	5.34± 0.02	3.9± 0.7	3.13± 0.02	5.37± 0.02	8
*% increase of crystallite size of aged samples with respect to fresh samples							

Table 4.3 gives the information about the crystallite size, d-spacing and lattice constant of both fresh and aged samples of CZM, where the crystallite size of CZM was found to be varied from 2.7 to 3.6 nm. The FWHM of CZM samples was observed to be increased with dopant and it reached maximum when 50 % of Zr ions were replaced with Mn ions. The increase in crystallite size of CZM3 and CZM4 was due to the saturation of solubility limit of Mn in Ce - Zr structure and it led to the additional peaks corresponding to Mn ions. In case of $Ce_{0.6}Zr_{0.4}O_2$, the lattice constant was found to be 5.31 Å for (111) plane, which was less than that of pure ceria. i.e. 5.41 Å. It can be justified with the fact that the ionic radius of Zr^{4+} (0.84 Å) was less than that of Ce^{4+} (0.97 Å). The replacement of Zr ions by Mn ions led to increase the d-spacing of CZM. Although ionic radius of Mn is noted to be less than that of ceria, the d-spacing was found to be increased with Ce/Zr ratio, which was also supported by Hongmei et al. [2010]. The lattice constant was observed to be decreased in fresh CZM1 and CZM2 samples and increased in

CZM3 and CZM4 samples compared to fresh CZ3 samples. It is due to the solubility limit of Mn in CZ3 solid solutions, which led to the appearance of Mn_2O_3 peak. The peak shift, changes in d-spacing and the absence of ZrO_2 and Mn_2O_3 peak confirmed the formation of a solid solution in CZM1 and CZM2 with cubic structure. The crystallite size of aged CZM solid solutions was observed to be varied from 3.9 to 3.4 nm. The crystallite size of aged samples compared to fresh samples was found to be maximum, when 50 % of Zr ions were replaced by Mn ions. It was clearly noticed that the crystallite size of CZ3 was increased after ageing treatment due to the effect of sintering and crystal growth. However, this effect was reduced significantly after the replacement of Zr ions by Mn ions. It is noted from the results that the increase in d-spacing of fresh and aged samples was observed to be increased with Mn ions concentration. The lattice constant was found to be varied very marginally after the ageing treatment compared to that of fresh sample. It is confirmed from the above studies that the structural stability of CZM was maintained even at elevated temperature of 800 °C.

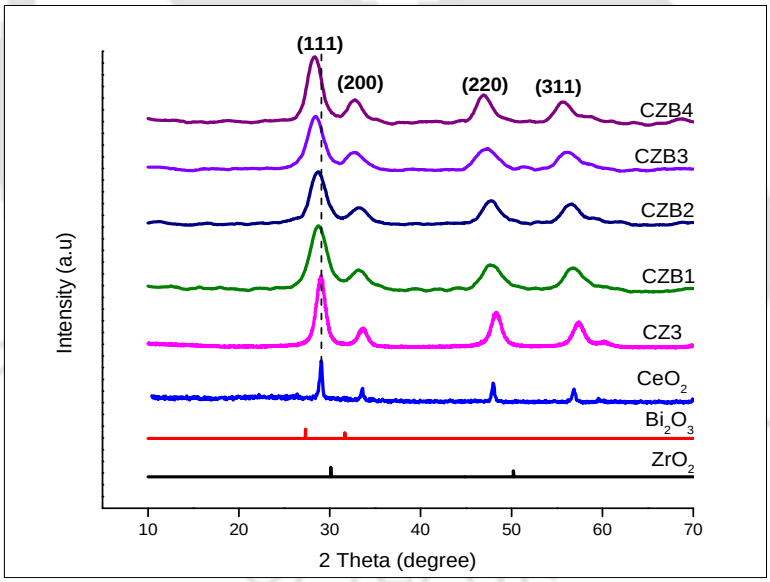

Figure 4.8 XRD patterns of fresh $Ce_{0.6}Zr_{0.4-x}Bi_{1.3x}O_2$ samples

Figure 4.8 depicts the XRD patterns of freshly prepared $Ce_{0.6}Zr_{0.4-x}Bi_{1.3x}O_2$ (CZB) ($0 \leq x \leq 0.4$) samples. In addition to those results, the peaks corresponding to ZrO_2 and Bi_2O_3 are also shown, which were obtained from JCPDS file 49-1642 and 77-0374, respectively, for the comparison purpose. Four major peaks were observed to be around 28, 32, 47 and 56˚ for the corresponding plane of (111), (200), (220) and (311), which confirmed the cubic fluorite structure according to

JCPDS file 34-0394. The absence of ZrO_2 and Bi_2O_3 peaks in CZB samples confirmed the formation of a homogeneous solid solution with the insertion of Zr and Bi ions in the ceria lattice. The ionic radius of Bi^{3+} was found to be 1.03 Å, which was and higher than Ce^{4+} (0.97 Å) Zr^{4+} (0.84 Å) and lower than Ce^{3+} (1.14 Å). A continuous shift in peak towards the lower angle side in CZB was due to the increase of Ce/Zr ratio and the strain induced due to the insertion of higher ionic radius of Bi ions.

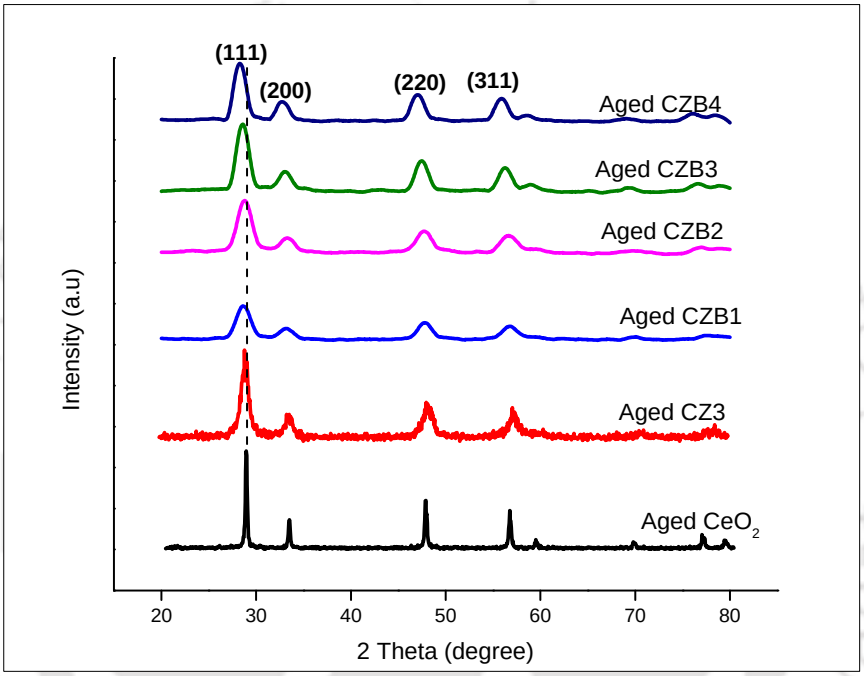

Figure 4.9 XRD patterns of aged $Ce_{0.6}Zr_{0.4-x}Bi_{1.3x}O_2$ samples

Figure 4.9 shows the XRD patterns of aged $Ce_{0.6}Zr_{0.4-x}Bi_{1.3x}O_2$ ($0 \leq x \leq 0.4$) (CZB) samples. The peaks were observed to be around 28, 32, 47 and 56˚ same as that of the fresh samples, which confirmed their cubic fluorite structure even after ageing the sample up to 800 °C. The FWHM was found to be decreased without any peak shift for the aged samples compared to that of the corresponding fresh samples, which was significant for higher particle size and it was reported in Table 4.4. However, the increase in crystallite size of aged CZB sample compared to that of the fresh sample was not found to be significant. The ageing process of the sample rearranged the crystal and its orientation, and it could be inferred from the decrease in FWHM compared to the fresh samples.

Table 4.4 shows the crystallite size, d-spacing and lattice constant of fresh and aged $Ce_{0.6}Zr_{0.4-x}Bi_{1.3x}O_2$ samples. The crystallite size of CZB samples was found to be varied around 2.72 ±0.06 nm, and the d-spacing was observed to be increased with Bi^{3+} concentration, which was also due to the strain present in the material. The increase in crystallite size due to ageing was not significant in all the CZB composition. The increase in lattice constant was due to the insertion of larger ionic radius of Bi^{3+} ions in the ceria lattice in both fresh and aged samples. The change in lattice constant and d-spacing of aged samples was not significantly influenced in comparison with that of fresh samples.

Table 4.4 Crystallite size, d-spacing and lattice constant of fresh and aged $Ce_{0.6}Zr_{0.4-x}Bi_{1.3x}O_2$ (CZB) solid solutions

Sample	Fresh samples			Aged samples			% increase of crysta -llite size*
	Crysta -llite size (nm)	d-spacing (Å)	Lattice constant (Å)	Crysta -llite size (nm)	d-spacing (Å)	Lattice constant (Å)	
$Ce_{0.6}Zr_{0.4}O_2$ - CZ3	7.5± 0.3	3.07± 0.03	5.31± 0.05	10.8± 0.9	3.09± 0.01	5.34± 0.04	45
$Ce_{0.6}Zr_{0.3}Bi_{0.13}O_2$ -CZB1	2.7± 0.5	3.07± 0.05	5.23± 0.03	2.8± 0.3	3.08± 0.05	5.26± 0.03	3.3
$Ce_{0.6}Zr_{0.2}Bi_{0.26}O_2$ -CZB2	2.8± 0.2	3.07± 0.04	5.31± 0.18	2.8± 0.1	3.08± 0.13	5.28± 0.02	1.7
$Ce_{0.6}Zr_{0.1}Bi_{0.39}O_2$ -CZB3	2.7± 0.7	3.08± 0.16	5.33± 0.05	2.8± 0.5	3.08± 0.02	5.33± 0.04	3.6
$Ce_{0.6}Bi_{0.52}O_2$ - CZB4	2.8± 0.9	3.12± 0.46	5.40± 0.15	2.8± 0.9	3.13± 0.02	5.42± 0.03	1.7
*% increase of crystallite size of aged samples with respect to fresh samples							

The XRD patterns of freshly prepared $Ce_{0.6}Zr_{0.4-x}La_{1.3x}O_2$ (CZL) ($0 \leq x \leq 0.4$) are shown in Figure 4.10. The peaks for ZrO_2 and La_2O_3 were also shown, which were obtained from JCPDS file 49-1642 and 22-0369, respectively, along with CZL samples in order to compare those peaks. Four major peaks were observed around 28, 33, 48 and 55˚ for the plane of (111), (200), (220) and (311), respectively. The crystallite size of fresh CZL samples was observed to be varied in the range of 2.80 to 2.95 nm. The XRD pattern of CZL samples confirmed their cubic fluorite structure according to JCPDS 34-0394 of cubic CeO_2. It was revealed that all the peaks in the pattern of CZL showed a slight shift towards lower angle with an increase of La and / or Zr ions substitution in the ceria lattice. The sequential change of the diffraction peaks confirmed the formation of a single-phase solid solution. As no XRD patterns corresponding to La_2O_3 and ZrO_2 were observed in CZL samples, it is suggested that the La and Zr ions were inserted in the ceria lattice and formed a homogenous solid solution of CZL.

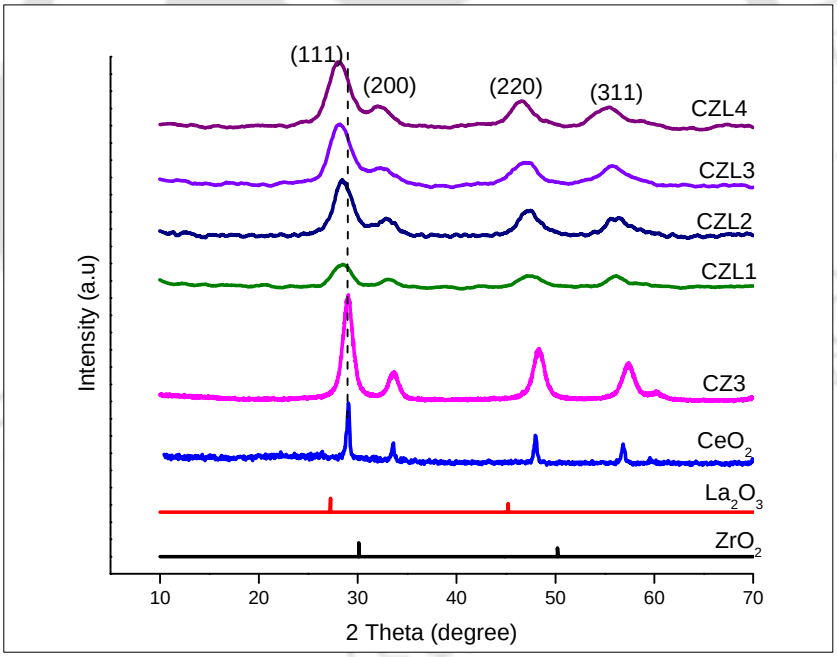

Figure 4.10 XRD patterns of fresh $Ce_{0.6}Zr_{0.4-x}La_{1.3x}O_2$ samples

The XRD patterns of aged $Ce_{0.6}Zr_{0.4-x}La_{1.3x}O_2$ ($0 \leq x \leq 0.4$) samples are shown in Figure 4.11. Aged CeO_2 and $Ce_{0.6}Zr_{0.4}O_2$ samples were also plotted for the comparison. Though the observed peaks of aged samples were similar to that of the fresh samples, the FWHM was found to be decreased confirming the increased crystallite size of CZL. A continuous peak shift towards the lower angle side was observed with the substitution of La^{3+} in place of Zr^{4+} in $Ce_{0.6}Zr_{0.4}O_2$. The

crystallite size of aged CZL was calculated and found to be varied in the range of 2.85 to 4.51 nm, which are shown in Table 4.5.

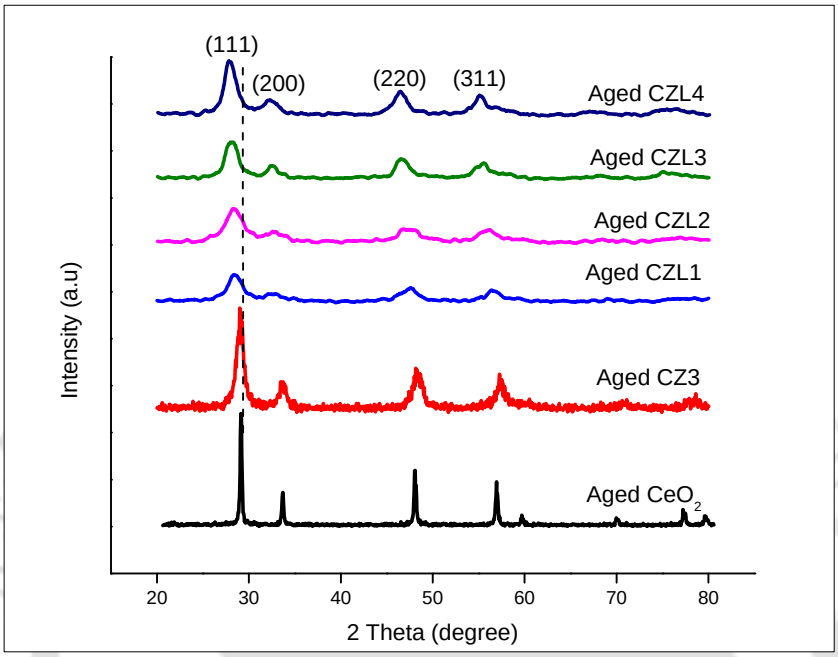

Figure 4.11 XRD patterns of aged $Ce_{0.6}Zr_{0.4-x}La_{1.3x}O_2$ samples

The crystallite size, d-spacing and lattice constant of fresh and aged samples of $Ce_{0.6}Zr_{0.4-x}La_{1.3x}O_2$ (CZL) were calculated from the XRD data and the results are presented in Table 4.5. It is observed that the crystallite size of CZL was strongly influenced by the substitution of La ions. The crystallite size of fresh CZL samples was in the range of 2.80 to 2.96 nm, when the Zr ions were replaced by La ions in $Ce_{0.6}Zr_{0.4}O_2$. In case of aged CZL samples, the crystallite size was found to be increased significantly compared to that of fresh samples. The increase in crystallite size of aged sample was found to be the highest for the CZL2 sample and the lowest for the CZL4 sample compared to that of CZL fresh samples. The lattice constant of aged CZL was observed to be varied from 5.31 to 5.41 Å, which was less than that of the CeO_2 of 5.410 Å. The doping of large ionic radius of La^{3+} (1.17 Å), Ikeda et al. [2005], in CZ3 lattice was expected to increase the lattice constant of CZL, where the same was observed to be increased in both fresh and aged samples.

Table 4.5 Crystallite size, d-spacing and lattice constant of fresh and aged $Ce_{0.6}Zr_{0.4-x}La_{1.3x}O_2$ (CZL) solid solutions

Sample	Fresh samples			Aged samples			% increase of crysta -llite size*
	Crysta -llite size (nm)	d-spacing (Å)	Lattice constant (Å)	Crysta -llite size (nm)	d-spacing (Å)	Lattice constant (Å)	
$Ce_{0.6}Zr_{0.4}O_2$ -CZ3	7.5± 0.3	3.07± 0.03	5.31± 0.05	10.8± 0.9	3.09± 0.01	5.34± 0.04	45
$Ce_{0.6}Zr_{0.3}La_{0.13}O_2$ -CZL1	2.8± 0.3	3.13± 0.06	5.32± 0.02	3.2± 0.5	3.11± 0.15	5.31± 0.17	12.0
$Ce_{0.6}Zr_{0.2}La_{0.26}O_2$ -CZL2	2.9± 0.7	3.12± 0.07	5.36± 0.05	4.5± 0.8	3.13± 0.10	5.35± 0.01	36.8
$Ce_{0.6}Zr_{0.1}La_{0.39}O_2$ -CZL3	3.0± 0.3	3.14± 0.04	5.39± 0.03	3.3± 0.6	3.16± 0.04	5.37± 0.01	9.1
$Ce_{0.6}La_{0.52}O_2$ - CZL4	2.8± 0.2	3.15± 0.11	5.39± 0.02	2.9± 0.5	3.18± 0.16	5.41± 0.03	1.7
*% increase of crystallite size of aged samples with respect to fresh samples							

Figure 4.12 shows the XRD pattern of the fresh $Ce_{0.6}Zr_{0.4-x}Nd_{1.3x}O_2$ (CZN) ($0 \leq x \leq 0.4$) solid solutions, where the peaks of ZrO_2 and Nd_2O_3 referred from JCPDS file 49-1642 and 83-1356, respectively, were also presented along with fresh CZN samples for the comparison purpose. The peaks were observed to be around 29, 33, 48 and 57˚ for the plane of (111), (200), (220) and (311), respectively in all the CZN samples, where peaks corresponding to Nd_2O_3 and ZrO_2 were not observed. The formation of a solid solution was confirmed with the peak shift in CZN1 and CZN2. Though the characteristic peaks for cubic fluorite structure of CeO_2 were found in all CZN samples, the peaks corresponding to Nd_2O_3 were observed in CZN3 and CZN4 confirming the presence of cubic Nd_2O_3. It might be due to the saturation limit of Nd^{3+} ions in ceria lattice.

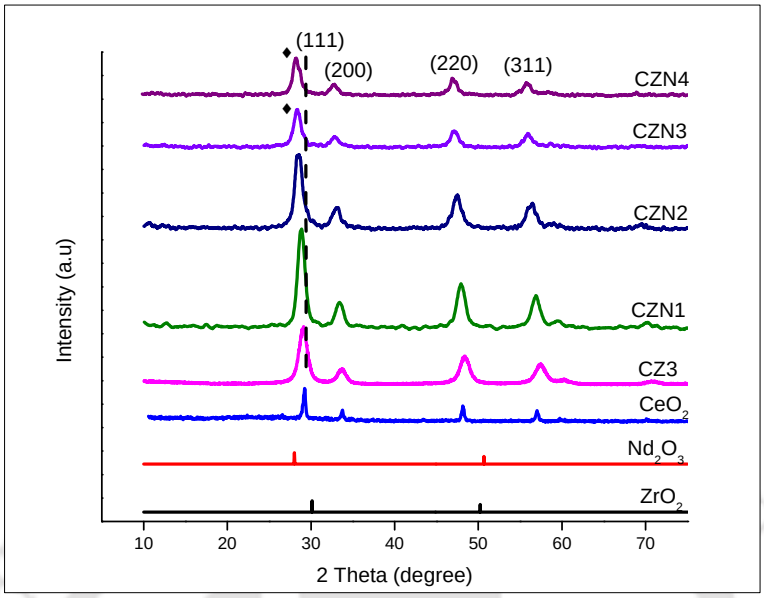

Figure 4.12 XRD patterns of fresh $Ce_{0.6}Zr_{0.4-x}Nd_{1.3x}O_2$ samples

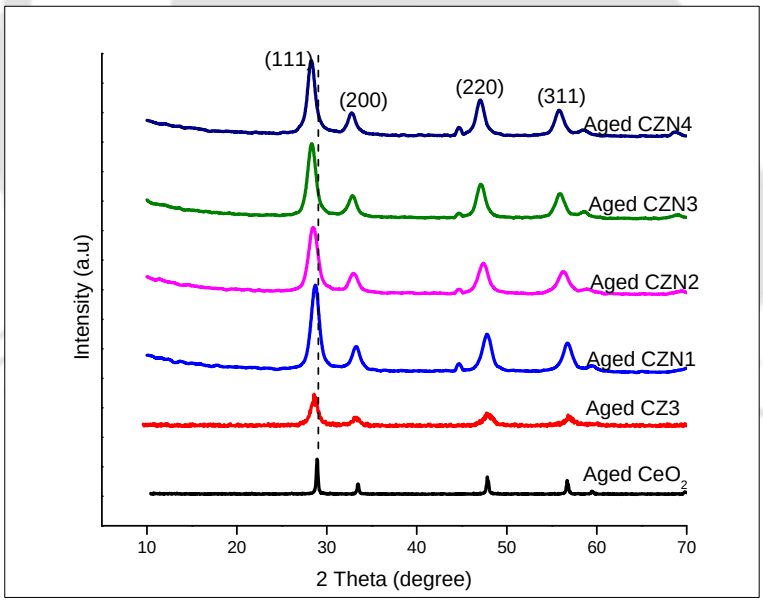

Figure 4.13 XRD patterns of aged $Ce_{0.6}Zr_{0.4-x}Nd_{1.3x}O_2$ samples

The X-ray diffractogram patterns of aged $Ce_{0.6}Zr_{0.4-x}Nd_{1.3x}O_2$ ($0 \leq x \leq 0.4$) solid solutions are shown in Figure 4.13 along with aged samples of CeO_2 and CZ3 for comparison purpose. It is observed that the FWHM was observed to be decreased, which resulted in higher crystallite size compared to that of fresh samples. The development of cubic Nd_2O_3 was evident after ageing in case of CZN3 and CZN4 as like that of fresh samples. The crystallite size of aged CZN was

found to be increased compared to that of fresh CZN samples and varied from 7.5 to 8.5 nm, which is about 10-19 % enhancement in comparison with fresh samples and it might be due to the sintering effect of the doping element present in CZN.

Table 4.6 Crystallite size, d-spacing and lattice constant of fresh and aged $Ce_{0.6}Zr_{0.4-x}Nd_{1.3x}O_2$ (CZN) solid solutions

Samples	Fresh samples			Aged samples			% increase of crysta-llite size*
	Crysta-llite size (nm)	d-spacing (Å)	Lattice constant (Å)	Crysta-llite size (nm)	d-spacing (Å)	Lattice constant (Å)	
$Ce_{0.6}Zr_{0.4}O_2$-CZ3	7.5± 0.3	3.07± 0.03	5.31± 0.05	10.8± 0.9	3.09± 0.01	5.34± 0.04	45
$Ce_{0.6}Zr_{0.3}Nd_{0.13}O_2$ -CZN1	6.5± 0.5	3.06± 0.07	5.30± 0.06	7.6± 0.7	3.16± 0.05	5.32± 0.02	18
$Ce_{0.6}Zr_{0.2}Nd_{0.26}O_2$ -CZN2	6.6± 0.6	3.11± 0.04	5.38± 0.04	7.5± 0.6	3.19± 0.07	5.37± 0.02	14
$Ce_{0.6}Zr_{0.1}Nd_{0.39}O_2$ -CZN3	7.7± 0.7	3.12± 0.07	5.40± 0.02	8.5± 0.5	3.20± 0.06	5.39± 0.03	10
$Ce_{0.6}Nd_{0.52}O_2$ -CZN4	6.6± 0.6	3.10± 0.03	5.37± 0.05	7.8± 0.4	3.22± 0.04	5.40± 0.03	19
*% increase of crystallite size of aged samples with respect to fresh samples							

Table 4.6 gives the crystallite size, d-spacing and lattice constant of fresh and aged samples of $Ce_{0.6}Zr_{0.4-x}Nd_{1.3x}O_2$ solid solutions. The crystallite size and d-spacing of aged CZN were calculated from their major peak (111). Lattice constant of CZN was found to be increased from 5.30 to 5.40 Å in fresh CZN samples with the replacement of Zr ions by Nd ions in ceria lattice. The lattice expansion was due to the higher ionic radius of Nd^{3+} (1.109 Å), Wu et al. [2007], compared to that of Ce^{4+} and Zr^{4+}. The phenomenon also was observed in aged CZN lattice.

4.1.3 Quantitative studies on oxygen storage capacity (OSC) of CZY and CZM solid solutions by thermogravimetric analysis

The solid solutions of $Ce_{0.6}Zr_{0.4-x}Y_{1.3x}O_2$ (CZY) and $Ce_{0.6}Zr_{0.4-x}Mn_xO_2$ (CZM) were heated from 30 to 800 °C and cooled down to 150 °C. Then the second heating cycle was followed up to 800 °C. Figure 4.14 a-e shows the weight loss pattern of the second heating cycle of CZY and CZM solid solutions and these data were used to calculate the OSC of the same, as described by Ozawa et al. [2000].

It is observed from Figure 4.14 (a-e) that the change in weight loss was found to be high in $Ce_{0.6}Zr_{0.2}Al_{0.26}O_2$ (CZA2), $Ce_{0.6}Zr_{0.2}Mn_{0.2}O_2$ (CZM2), $Ce_{0.6}Zr_{0.1}Bi_{0.39}O_2$ (CZB3), $Ce_{0.6}Zr_{0.2}La_{0.26}O_2$ (CZL2) and $Ce_{0.6}Zr_{0.3}Nd_{0.13}O_2$ (CZN1) from the composition of CZA, CZM, CZB, CZL and CZN solid solutions, respectively. It is also noted that the CZA2 has the highest weight loss compared to all the samples considered in the present study.

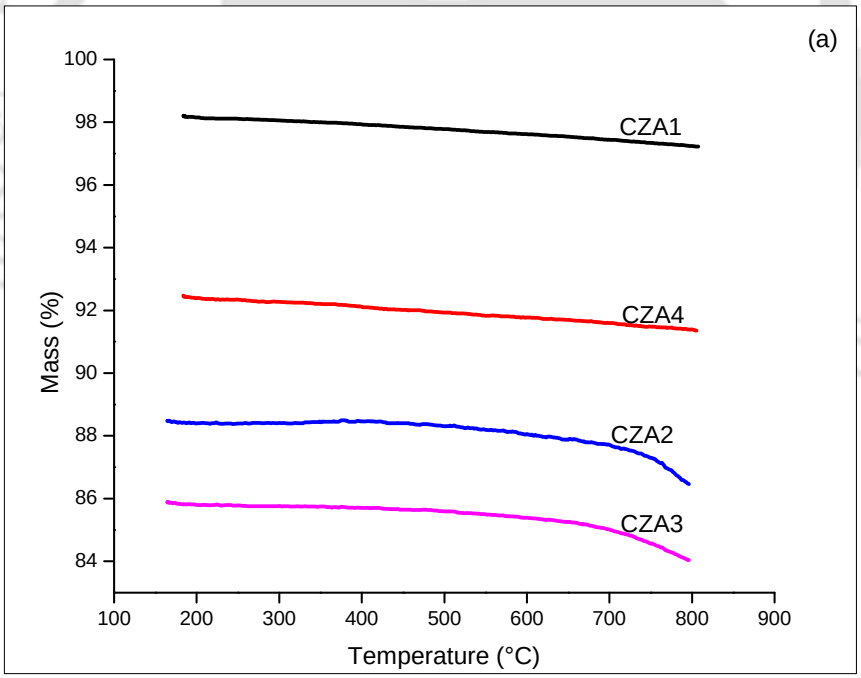

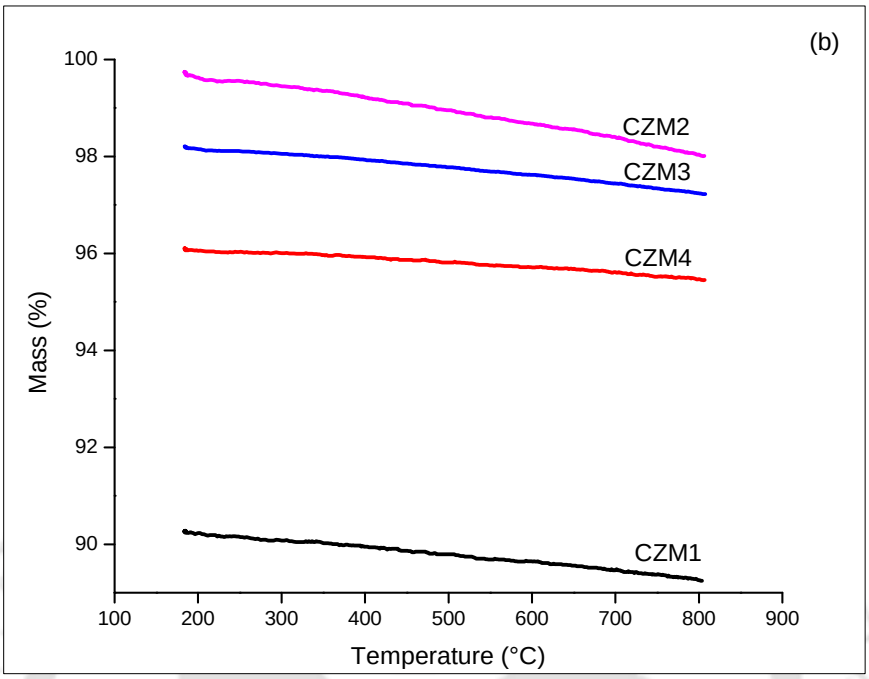
(b)
100
98
96
94
92
90
Mass (%)
CZM2
CZM3
CZM4
CZM1
100
200
300
400
500
600
700
800
900
Temperature (°C)

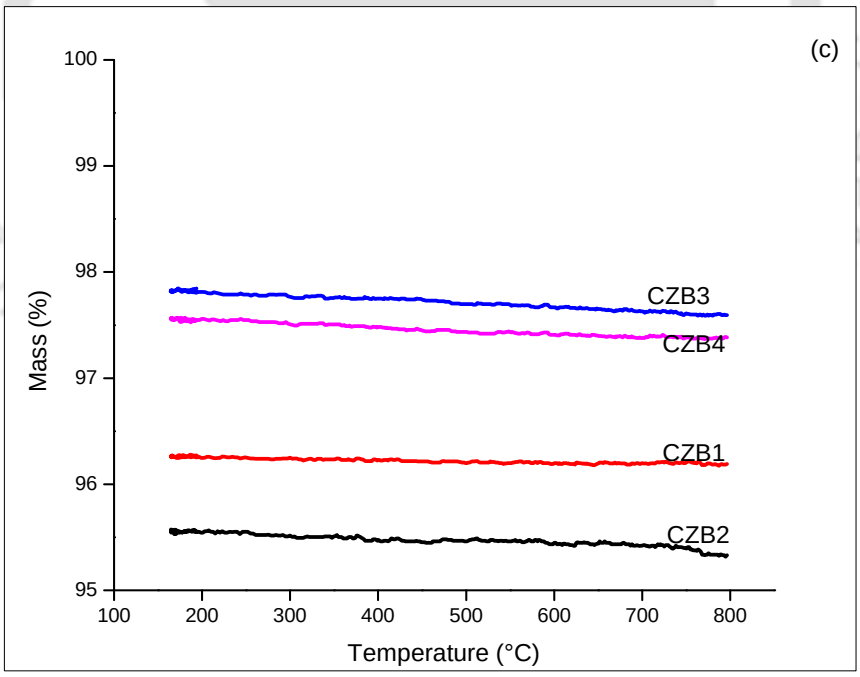
(c)
100
99
98
97
96
95
Mass (%)
CZB3
CZB4
CZB1
CZB2
100
200
300
400
500
600
700
800
Temperature (°C)

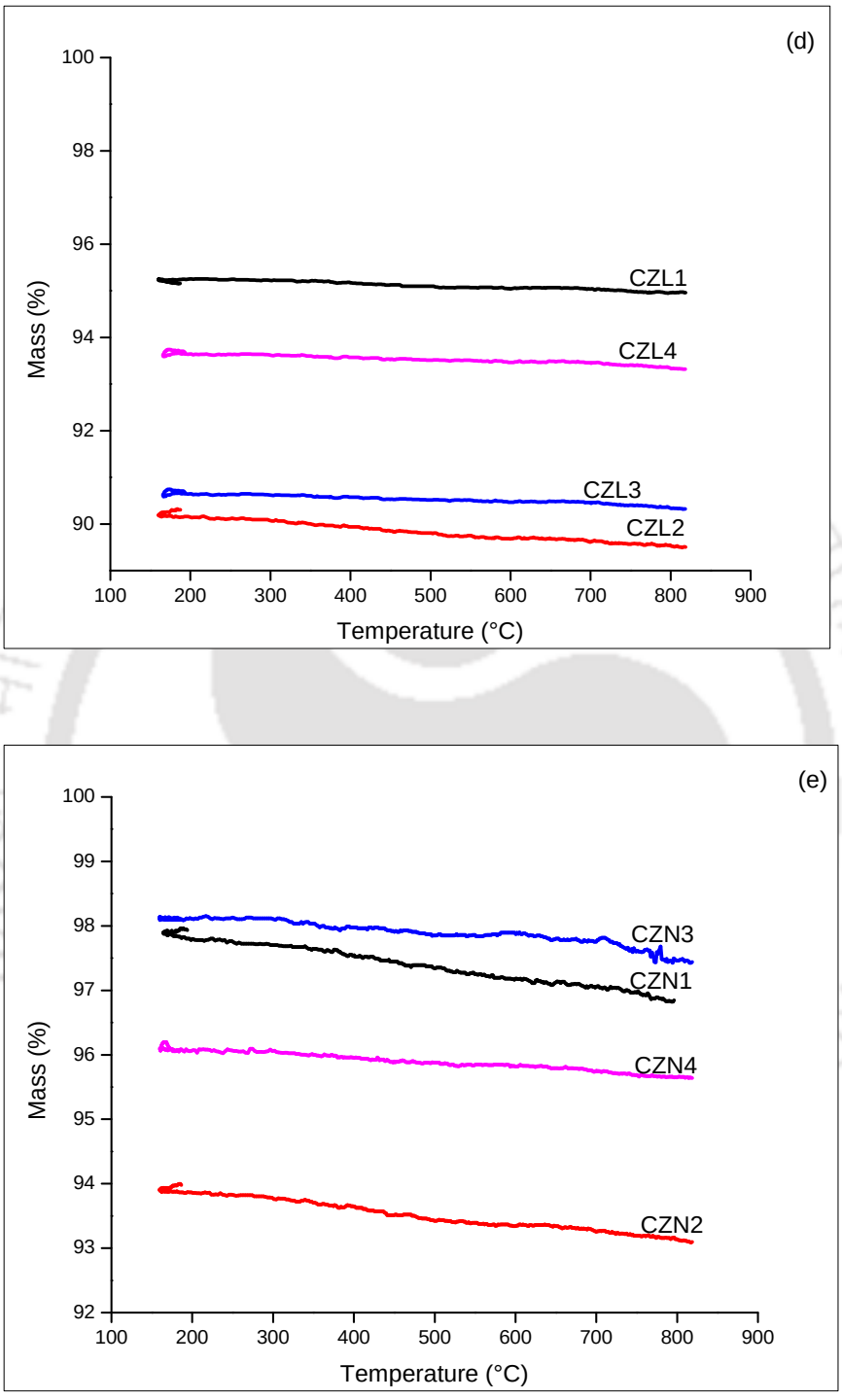

Figure 4.14 Weight loss of the CZY and CZM solid solutions during the second heating cycle: (a) $Ce_{0.6}Zr_{0.4-x}Al_{1.3x}O_2$, (b) $Ce_{0.6}Zr_{0.4-x}Mn_xO_2$, (c) $Ce_{0.6}Zr_{0.4-x}Bi_{1.3x}O_2$, (d) $Ce_{0.6}Zr_{0.4-x}La_{1.3x}O_2$, (e) $Ce_{0.6}Zr_{0.4-x}Nd_{1.3x}O_2$

The OSC data can be used to characterize the oxygen transfer capability of catalytic materials. The release and intake of oxygen in ceria occur owing to the following reversible reaction. Eq. 4.1 shows the conversion of Ce^{4+} to Ce^{3+} or vice versa.

$$2CeO_2 \rightarrow Ce_2O_3 + \frac{1}{2}O_2 \quad \text{... (4.1)}$$

The high OSC material can be chosen for the catalytic activity under reducing environment due to its oxygen releasing mechanism and the same for $Ce_xZr_{1-x}O_2$ is shown in Eq. 4.2

$$Ce_x^{4+}Zr_{1-x}O_2 \rightarrow (Ce_{1-2\delta}^{4+}Ce_{2\delta}^{3+})_x Zr_{1-x}O_{2-\delta} + \frac{\delta}{2}O_2 \quad \text{... (4.2)}$$

Since the value of vacancy content is very small, the reaction must be written as follows for the metal oxides having oxygen vacancy content with little structural change, Ozawa et al. [2000]. The substitution of third element (Al^{3+}, Mn^{2+}, Bi^{3+}, La^{3+} and Nd^{3+}) along with Zr^{4+} into the ceria lattice follows the oxygen releasing mechanism as described in Eq 4.3 to 4.7 for CZY and CZM solid solutions.

$$Ce_{0.6}Zr_{0.4-x}Al_{1.3x}O_2 \rightarrow (Ce_{1-2\delta}^{4+}Ce_{2\delta}^{3+})_{0.6} Zr_{0.4-x}Al_{1.3x}O_{2-\delta} + \frac{\delta}{2}O_2 \quad \text{... (4.3)}$$

$$Ce_{0.6}Zr_{0.4-x}Mn_xO_2 \rightarrow (Ce_{1-2\delta}^{4+}Ce_{2\delta}^{3+})_{0.6} Zr_{0.4-x}Mn_xO_{2-\delta} + \frac{\delta}{2}O_2 \quad \text{... (4.4)}$$

$$Ce_{0.6}Zr_{0.4-x}Bi_{1.3x}O_2 \rightarrow (Ce_{1-2\delta}^{4+}Ce_{2\delta}^{3+})_{0.6} Zr_{0.4-x}Bi_{1.3x}O_{2-\delta} + \frac{\delta}{2}O_2 \quad \text{... (4.5)}$$

$$Ce_{0.6}Zr_{0.4-x}La_{1.3x}O_2 \rightarrow (Ce_{1-2\delta}^{4+}Ce_{2\delta}^{3+})_{0.6} Zr_{0.4-x}La_{1.3x}O_{2-\delta} + \frac{\delta}{2}O_2 \quad \text{... (4.6)}$$

$$Ce_{0.6}Zr_{0.4-x}Nd_{1.3x}O_2 \rightarrow (Ce_{1-2\delta}^{4+}Ce_{2\delta}^{3+})_{0.6} Zr_{0.4-x}Nd_{1.3x}O_{2-\delta} + \frac{\delta}{2}O_2 \quad \text{... (4.7)}$$

The method of calculation of OSC from the weight loss data is discussed below in detail. Eq. (4.2) was used to calculate the OSC of CZ samples. In order to understand the methodology used to calculate the OSC, the weight loss and OSC values were referred from Ozawa et al. [2000] and the same was verified based on the procedure as cited below.

Composition of the sample $(Ce_{0.8}Zr_{0.2}O_2)_{0.3}/Al_2O_3$; Weight loss: 0.26 % and δ : 0.08, Ozawa et al. [2000].

Molecular weight of the individual element:

Ce = 140 g/mol, Zr =91 g/mol, Al =27 g/mol, O =16 g/mol,

Mn = 55 g/mol, La = 139 g /mol, Bi = 209 g/mol

Molecular weight of $(Ce_{0.8}Zr_{0.2}O_2)_{0.3}/Al_2O_3$ = 150.66 g/mol

In 150.66 g /mol of solid solution, it contains 48.66 g of $Ce_{0.8}Zr_{0.2}O_2$

It can be written as per gram, like 150.66 g of the sample contains 48.66 g of $Ce_{0.8}Zr_{0.2}O_2$

Then 100 gram of the sample contains (48.66/150.66)*100=32.3 g of $Ce_{0.8}Zr_{0.2}O_2$

The weight loss from 32.3 g of $Ce_{0.8}Zr_{0.2}O_2$ = 0.26 g of oxygen

According to Eq. (4.2) (δ/2)*(weight of $Ce_{0.8}Zr_{0.2}O_2$ / mol. weight of $Ce_{0.8}Zr_{0.2}O_2$)

= weight of O_2/ mol weight of O_2

δ/2 = (0.26/32)*(162.2/32.3)

δ = 0.08 mol of oxygen/mol of catalyst

As the calculation methodology followed was matched with rest of the samples, reported by Ozawa et al. [2000], the same procedure was followed for the CZY and CZM samples. The methodology adopted for $Ce_{0.6}Zr_xAl_{1.3x}O_2$ samples to calculate the OSC with respect to CeO_2 is given below:

The observed weight loss of $Ce_{0.6}Zr_{0.1}Al_{0.39}O_2$ (CZA3) was 1.726 %.

The molecular weight of $Ce_{0.6}Zr_{0.1}Al_{0.39}O_2$ (CZA3) = 133.2 g/mol

In 133.2 g/mol, the sample contains 116 g/mol of CeO_2

It can be written as

133.2 g of the solid solution contains 116 g of CeO_2

Then 100 g of the CZA3 sample contains = (116/133.2)*100 = 87.087 g of CeO_2

i.e., 87.087 g of CeO_2 lost 1.726 g of oxygen

As the doping elements such as Zr, Al, Mn, Bi, La and Nd were used to influence the redox process of Ce^{4+} in to Ce^{3+} or vice versa, the OSC was calculated against the concentration of CeO_2.

According to Eq. 4.3

$$(\delta/2)*(\text{weight of } CeO_2 / \text{ mol. weight of } CeO_2) = \text{weight of } O_2 / \text{ mol weight of } O_2$$

$$\delta/2 = (1.726/32)*(172/87.087)$$

$$\delta = 0.21305 \text{ mol of oxygen/mol of } CeO_2$$

The OSC of rest of the test samples was calculated using the Eq. 4.3, 4.4, 4.5, 4.6 and 4.7 for CZA, CZM, CZB, CZL and CZN solid solution, respectively and the results are reported and compared with OSC of CZ3 and it is shown in Figure 4.15, where the comparison of the respective OSC with CZ3 was also presented.

Figure 4.15 shows the OSC of $Ce_{0.6}Zr_{0.4}O_2$ (CZ3), $Ce_{0.6}Zr_{0.4-x}Y_{1.3x}O_2$ and $Ce_{0.6}Zr_{0.4-x}Mn_xO_2$ ($0 \leq x \leq 0.04$) solid solutions. The OSC data were arranged in an order of CZA, CZM, CZN, CZL and CZB composition and compared with each other and CZ3. It is observed that the OSC of solid solutions was influenced by the concentration of the doping elements in ceria. The OSC of $Ce_{0.6}Zr_{0.4}O_2$ was influenced by the replacement of Zr^{4+} by 3rd element which created more defects in the CeO_2 lattice. It is noted that the high OSC was observed in $Ce_{0.6}Zr_{0.2}Al_{0.26}O_2$ (CZA2), $Ce_{0.6}Zr_{0.2}Mn_{0.2}O_2$ (CZM2), $Ce_{0.6}Zr_{0.1}Nd_{0.13}O_2$ (CZN1), $Ce_{0.6}Zr_{0.2}La_{0.26}O_2$ (CZL2) and $Ce_{0.6}Zr_{0.1}Bi_{0.39}O_2$ (CZB3) among $Ce_{0.6}Zr_{0.4-x}Al_{1.3x}O_2$, $Ce_{0.6}Zr_{0.4-}Mn_xO_2$, $Ce_{0.6}Zr_{0.4-x}Nd_{1.3x}O_2$ $Ce_{0.6}Zr_{0.4-x}La_{1.3x}O_2$ and $Ce_{0.6}Zr_{0.4-x}Bi_{1.3x}O_2$ solid solutions, respectively. The possible reasoning for the enhancement of OSC is explained as follows: Two essential requirements for an efficient OSC material were the oxygen vacancies and high anion mobility, Cho. [1991]. Thus, the following effects on dopant concentration on the oxygen mobility are to be considered: 1) Oxygen mobility was increased with oxygen vacancy concentration, which was increased with the concentration of dopant; 2) The associative interaction between the dopant cation and the oxygen vacancy was increased with the concentration of dopant resulting to the reduced oxygen mobility. Thus, the high OSC was found at the optimum concentration of the dopant. The respective mechanisms were called as dopant vacancy compensation mechanism and dopant interstitial compensation mechanism, Bao et al. [2008]. The change in OSC with respect to the concentration of 3rd element in CZ3 was due to the above mechanism, where OSC of the CZY and CZM was increased and then decreased with doping element against its concentration.

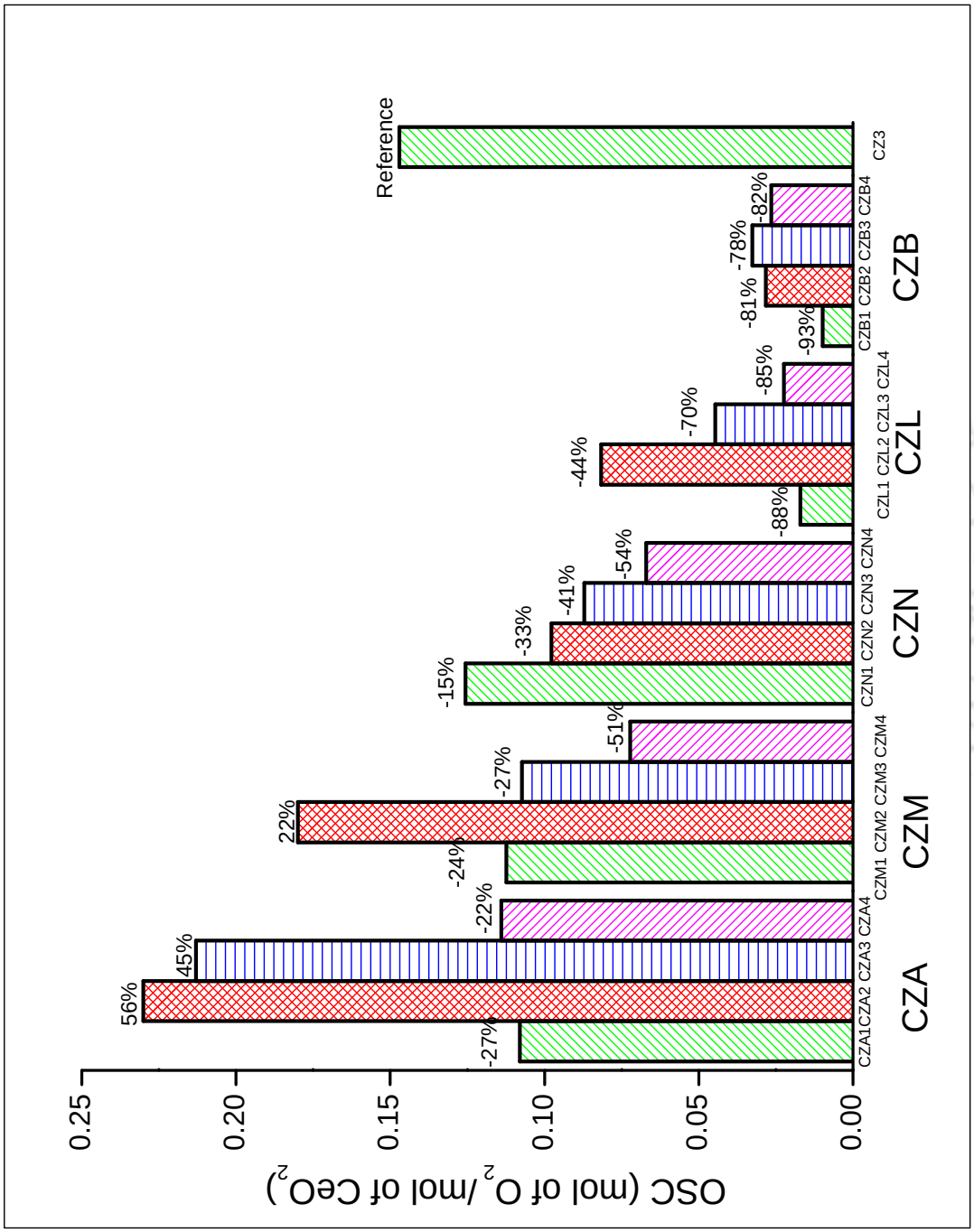

Figure 4.15 Comparison of the OSC of $Ce_{0.6}Zr_{0.4-x}Y_{1.3x}O_2$ and $Ce_{0.6}Zr_{0.4-x}Mn_xO_2$ (Y= Al, Nd, La, Bi; $0 \leq x \leq 0.04$) samples against CZ3

The OSC of $Ce_{0.6}Zr_{0.4-x}Bi_{1.3x}O_2$, $Ce_{0.6}Zr_{0.4-x}Nd_{1.3x}O_2$ and $Ce_{0.6}Zr_{0.4-x}La_{1.3x}O_2$ solid solutions was found to be less than that of $Ce_{0.6}Zr_{0.4}O_2$. In case of CZB solid solution, it might be due to the fact that the release of oxygen from the lattice could be below 300 °C which was also supported by Yasuda et al. [2010]. As the weight loss occurred during 300 to 800 °C was considered to calculate the OSC of a catalyst, Ozawa [2000], the OSC of CZB3 samples was observed to be less than 78 % in comparison to that of $Ce_{0.6}Zr_{0.4}O_2$. Since the oxygen released from the solid solution was proposed to be used to enhance the combustion in an internal combustion engine, the oxygen released from the CZB might not able to solve the purpose of using the same. In CZN composition, the reduced OSC might be due to the formation of Nd_2O_3 after 75 % of substitution of Nd ions, which was confirmed by XRD technique. The appearance of Nd_2O_3 peak in CZN3 and CZN4 prevented the formation of a solid solution, which was favored for higher OSC. In case of CZL, it was observed that the OSC of CZL2 was 44 % less that of CZ3 solid solution. The localized increase of lattice distance after the substitution of 2nd and 3rd element was the indication of lattice defects. In $Ce_{0.6}Zr_{0.4-x}La_{1.3x}O_2$ composition, the lattice expansion was observed to be increased with the concentration of La^{3+}. It was due to the doping of larger ionic radius of La ions in the ceria lattice along with Zr ions. However, the reduced OSC observed in CZB, CZN, and CZL compared to CZ3 was due their higher ionic radius compared to Ce^{4+}.

Figure 4.16 shows the comparison of OSC and specific surface area of $Ce_{0.6}Zr_{0.2}Al_{0.26}O_2$ (CZA2), $Ce_{0.6}Zr_{0.1}Al_{0.39}O_2$ (CZA3), $Ce_{0.6}Zr_{0.2}Mn_{0.2}O_2$ (CZM2), $Ce_{0.6}Zr_{0.2}Nd_{0.13}O_2$ (CZN1), $Ce_{0.6}Zr_{0.2}La_{0.26}O_2$ (CZL2) and $Ce_{0.6}Zr_{0.1}Bi_{0.39}O_2$ (CZB3) solid solutions with respect to $Ce_{0.6}Zr_{0.4}O_2$ (CZ3). The OSC of CZA2, CZA3 and CZM2 was 56, 45 and 22 % higher than that of CZ3, respectively, whereas the OSC of CZB3, CZL2 and CZN1 solid solutions was 78, 44 and 15 % less than that of CZ3, respectively. The lattice expansion was caused due to the doping of 2nd and 3rd element in the ceria lattice, where the 3rd elements were Al, Mn, Bi, La and Nd and the 2nd element was Zr^{4+}. The lattice expansion of CZB, CZL and CZN solid solutions was due to the higher ionic radius of Bi^{3+} (1.03 Å), La^{3+} (1.17 Å) and Nd^{3+} (1.109 Å), respectively, in comparison with pure Ce^{4+} (0.97 Å). Though the ionic radius of Al^{3+} (0.51 Å) and Mn^{2+} (0.83 Å) was less than that of CeO_2, the lattice expansion was due to the increase in concentration of Ce/Zr ratio. Thus, the lattice expansion in case of CZA and CZM was the indication of lattice defects, which were desirable to increase the OSC of a material, and it was present only in case

of $Ce_{0.6}Zr_{x-0.4}Al_{1.3x}O_2$ (CZA), $Ce_{0.6}Zr_{x-0.4}Mn_xO_2$ (CZM) solid solutions. The high OSC was found in CZA2 and CZM2 solid solutions among the CZA and CZM composition respectively, which was due to the vacancy compensation and dopant interstitial compensation mechanism, as discussed earlier.

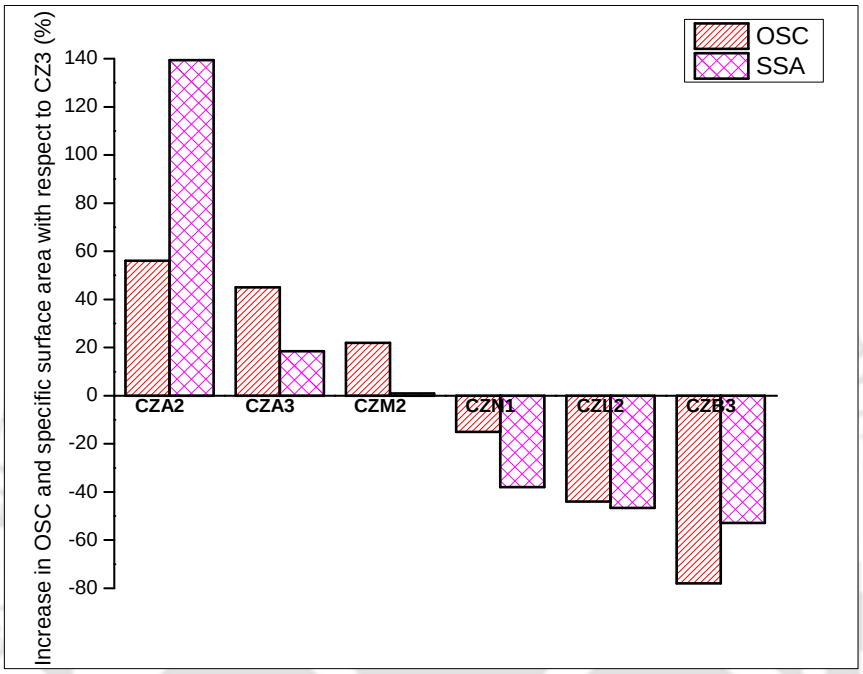

Figure 4.16 Comparison of OSC and specific surface area (SSA) of different solid solutions with respect to $Ce_{0.6}Zr_{0.4}O_2$

Table 4.7 gives the BET-specific surface area of high OSC nanoparticles. Since the OSC of CZA2, CZM2, CZB3, CZL2 and CZN1 was found to be the highest in CZA, CZM, CZB, CZL and CZN solid solutions, respectively, a study on specific surface area was focused only for those solid solutions. The specific surface area of CZA3 was also studied due to its positive improvement of OSC compared to CZ3. The specific surface area of ceria was observed to be increased with the substitution of Zr^{4+}, Al^{3+}, Mn^{2+}, Bi^{3+}, La^{3+} and Nd^3 in its lattice. It was found that the specific surface area of CZA2, CZA3 and CZM2 was 139, 18 and 1 % higher than that of CZ3 sample. However, the same for CZB3, CZL2 and CZN1 solid solution was noted to be 52, 46 and 38 % less compared to that of CZ3 samples. These results were also presented in Figure 4.16, where the reduction of OSC of CZB3, CZL2 and CZN1 in comparison to that of CZ3 was correlated with reduced specific surface area of the solid solution. It was also observed that CZA2, CZA3 and CZM2 had increased specific surface area leading to increased OSC

compared to CZ3. Among the best combination of CZA and CZM, the specific surface area and OSC of CZA2 were found to be the highest compared to that of CZA3 and CZM3.

Table 4.7 BET specific surface area for high OSC nanoparticles

Sl.No	Ceria based high OSC nanoparticles	Nomenclature	OSC (mol. of O_2/mol. of CeO_2)	Specific surface area (m^2/g)
1	CeO_2	CeO_2	-	3.676
2	$Ce_{0.6}Zr_{0.4}O_2$	CZ3	0.147	50.743
3	$Ce_{0.6}Zr_{0.2}Al_{0.26}O_2$	CZA2	0.2293	121.496
4	$Ce_{0.6}Zr_{0.1}Al_{0.39}O_2$	CZA3	0.2131	60.125
5	$Ce_{0.6}Zr_{0.2}Mn_{0.2}O_2$	CZM2	0.1799	51.199
6	$Ce_{0.6}Zr_{0.1}Bi_{0.39}O_2$	CZB3	0.0327	23.903
7	$Ce_{0.6}Zr_{0.2}La_{0.26}O_2$	CZL2	0.0817	27.106
8	$Ce_{0.6}Zr_{0.2}Nd_{0.13}O_2$	CZN1	0.1256	31.458

In order to increase the OSC of ceria, Al^{3+}, Mn^{2+}, Bi^{3+}, La^{3+} and Nd^{3+} were doped along with Zr^{4+} through the sol-gel preparation technique. From the OSC studies, it was found that the doping of Al^{3+} yielded a better solid solution which has the highest OSC compared to rest of the ions reported in the present study.

Since the OSC of CZA2, CZM2, CZB3, CZL2 and CZN1 was found to be highest in their respective solid solutions, the TEM images were obtained only for those samples.

4.1.4. TEM studies on high OSC solid solutions

TEM analysis provides information about the size and shape of primary particles and their state of agglomeration.

The TEM images of fresh $Ce_{0.6}Zr_{0.2}Al_{0.26}O_2$ (CZA2) sample are shown in Figure 4.17 (i-iv) at different magnification. The size of the crystals was observed to be less than 5 nm with and without agglomeration. The shape of the particles was observed to be spherical in nature. The

observation made from TEM images in connection with crystallite size was in good agreement with the XRD results.

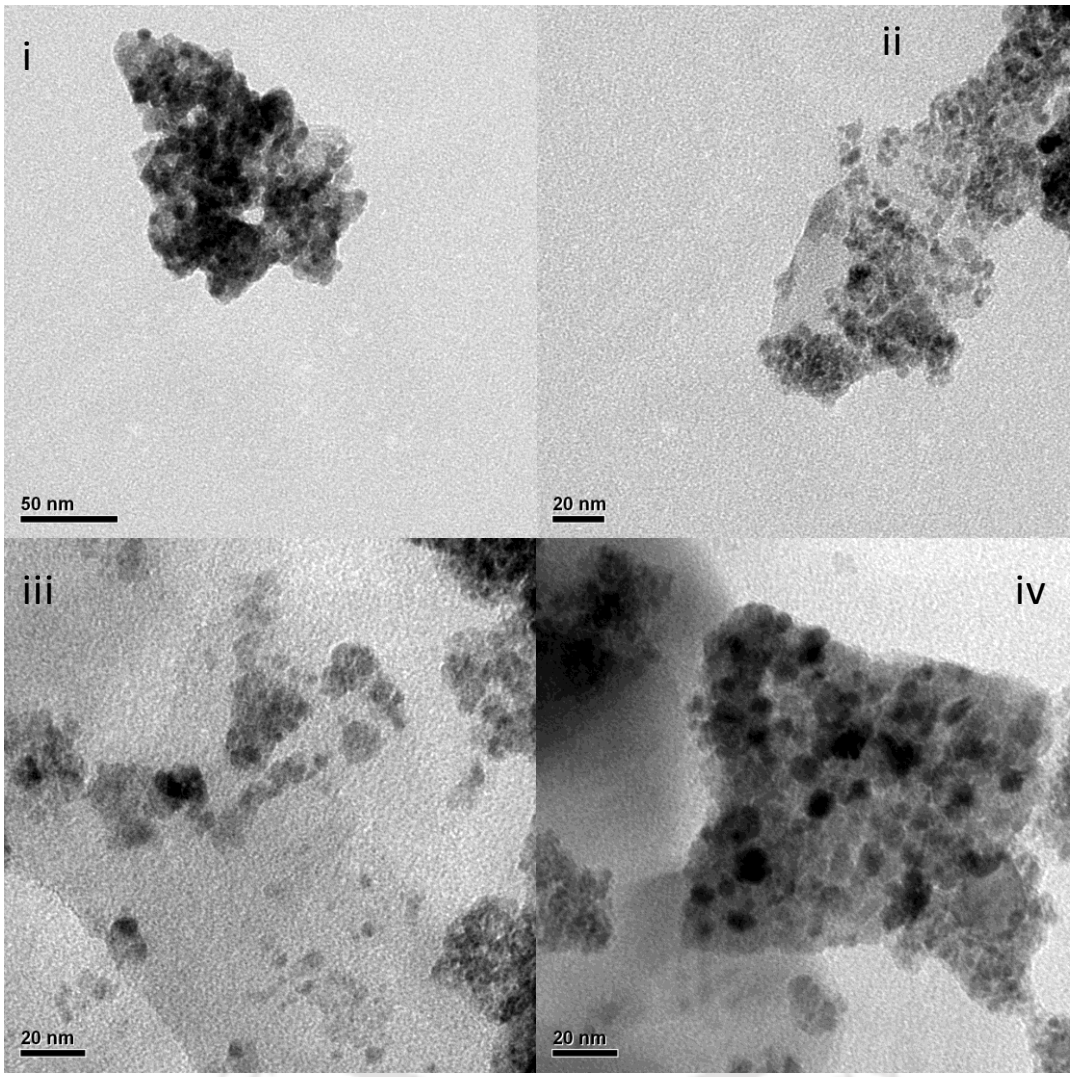

Figure 4.17 (i-iv) TEM images of fresh $Ce_{0.6}Zr_{0.2}Al_{0.26}O_2$ at different magnification

Figure 4.18 (i-iv) shows the TEM images of fresh $Ce_{0.6}Zr_{0.2}Mn_{0.2}O_2$ solid solutions in three different magnifications. The particles observed from the TEM images were in the average size of 4 nm and spherical in nature and the crystallite size was observed to be in good agreement with the results of XRD. The crystallites were observed to be uniform.

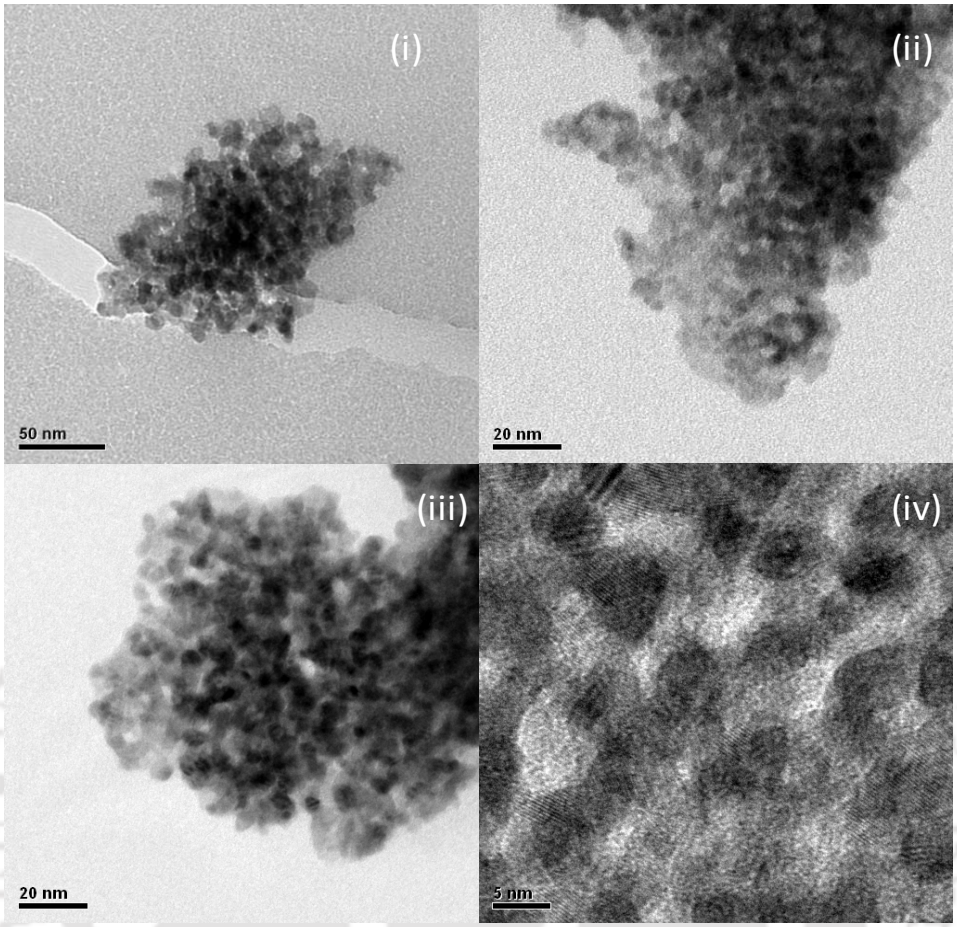

Figure 4.18 (i-iv) TEM images of fresh $Ce_{0.6}Zr_{0.2}Mn_{0.2}O_2$ at different magnification

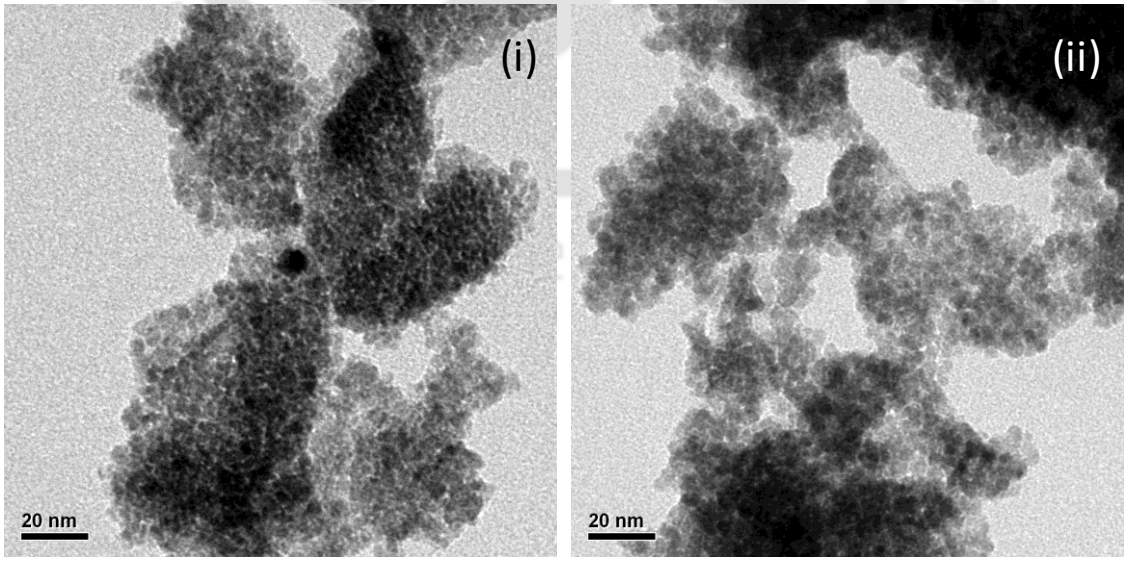

Figure 4.19 (i-ii) TEM images of fresh $Ce_{0.6}Zr_{0.2}Bi_{0.39}O_2$

Figure 4.19 (i-ii) shows the TEM images of fresh $Ce_{0.6}Zr_{0.2}Bi_{0.26}O_2$ solid solutions. The particles were observed to be uniform in size and shape. The crystallites were found to be equiaxed and spherical in shape with an approximate size of 4 nm.

Figure 4.20 shows the TEM image of fresh $Ce_{0.6}Zr_{0.2}La_{0.26}O_2$, where a densely packed crystallites along with agglomeration were observed. The crystallite size was observed to be less than 5 nm and well matched with the XRD results. The shape of the crystallites was found to be spherical.

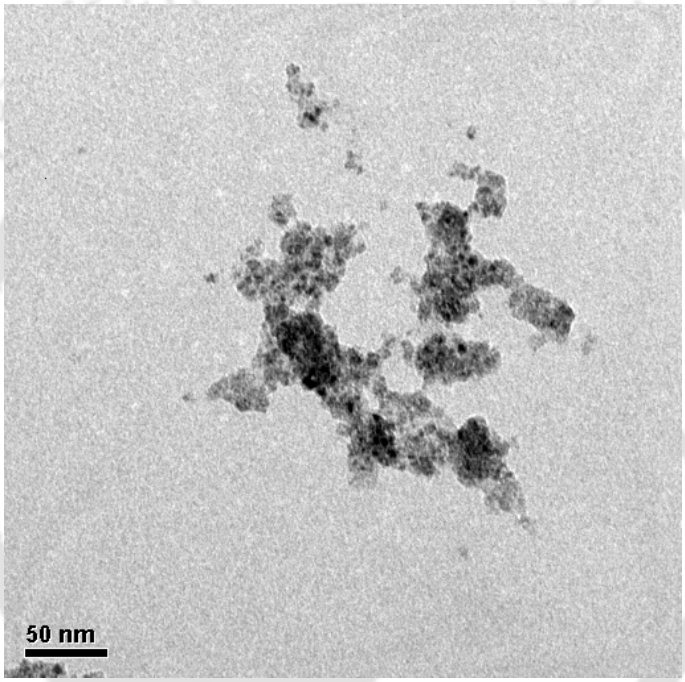

Figure 4.20 TEM image of fresh $Ce_{0.6}Zr_{0.2}La_{0.26}O_2$

Figure 4.21 shows the TEM image of fresh $Ce_{0.6}Zr_{0.2}Nd_{0.1}O_2$. It was observed that the shape and size of test sample were observed to be uniform. The size of the crystals was reported to be less than 10 nm and matched with XRD results.

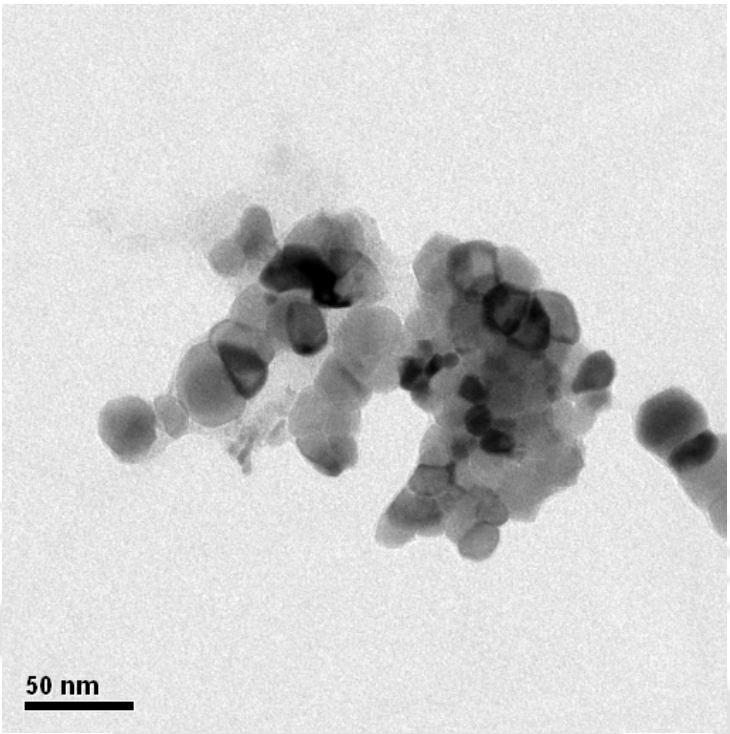

Figure 4.21 TEM image of fresh $Ce_{0.6}Zr_{0.2}Nd_{0.13}O_2$

4.1.5 Qualitative confirmation of OSC

Since the OSC of $Ce_{0.6}Zr_{0.2}Al_{0.26}O_2$ (CZA2), $Ce_{0.6}Zr_{0.1}Al_{0.39}O_2$ (CZA3) and $Ce_{0.6}Zr_{0.2}Mn_{0.2}O_2$ (CZM2) was found to be higher than that of $Ce_{0.6}Zr_{0.4}O_2$ (CZ3), the qualitative confirmation studies such as OSC band, coefficient of thermal expansion and lattice defects were carried out only for CZA and CZM samples using Raman spectroscopy, thermomechanical analyzer and HRTEM, respectively.

4.1.5.1. Lattice vibration studies

Since, the XRD pattern is generated by the cation sub-lattice, it showed no tetragonality. It exhibits an oxygen displacement from the ideal fluorite sites, whose structure was much closer to that of cubic structure. Raman spectroscopy is a potential tool to differentiate between t" (tetragonal) and cubic phase based on the oxygen lattice vibrations, which are sensitive to crystal symmetry, Zhang et al. [2009].

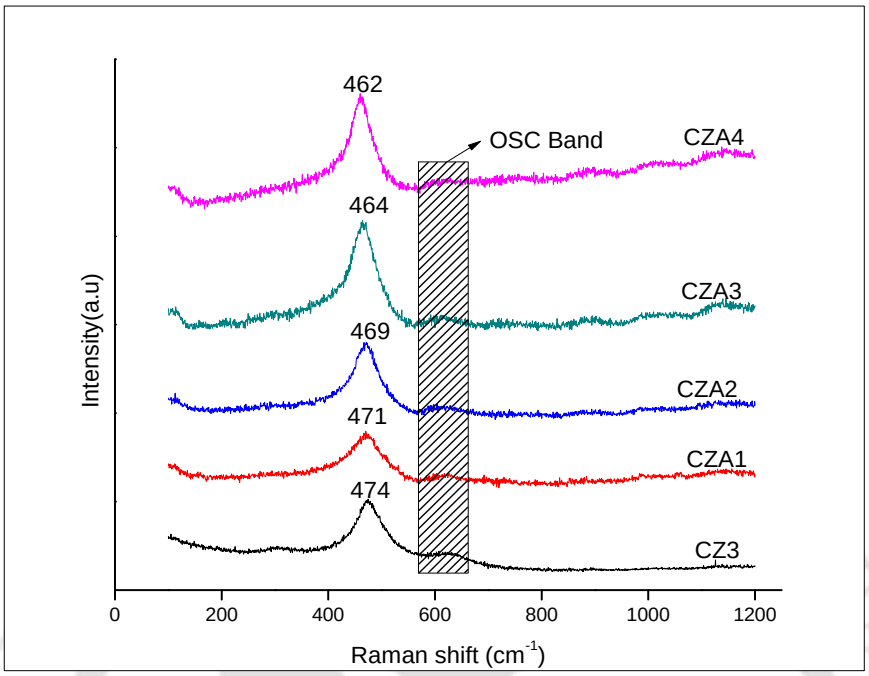

Figure 4.22 Raman spectra of fresh $Ce_{0.6}Zr_{0.4-x}Al_{1.3x}O_2$ solid solutions

The Raman spectra of the fresh $Ce_{0.6}Zr_{0.4-x}Al_{1.3x}O_2$ solid solutions are shown in Figure 4.22, where an intense peak around 470 cm^{-1} and a very small shoulder peak around 610 cm^{-1} were observed in all the samples. The peak at 474 cm^{-1} was attributed to the perfect CeO_2 based cubic fluorite lattice due to the vibration mode of F_{2g} symmetry and there was no sign of tetragonal modification, which was supported by Jia et al. [2008]. The peak observed at 610 cm^{-1} for fresh samples confirmed the presence of oxygen vacancies in the solid solution, which was also confirmed by Deshpande et al. [2004]. Thus, the improvement of oxygen mobility of $Ce_{0.6}Zr_{0.4}O_2$ was noticed due to the introduction of Al^{3+}. It is also observed that there were no distinctive peaks for the monoclinic and tetragonal phases of zirconia. A very small peak at 310 cm^{-1} in $Ce_{0.6}Zr_{0.4}O_2$ and 300 cm^{-1} in $Ce_{0.6}Zr_{0.1}Al_{0.39}O_2$ sample revealed the negligible presence of tetragonal phase (t″). It is also observed that the peaks were broadened and found to be asymmetric in comparison with $Ce_{0.6}Zr_{0.4}O_2$ confirming the presence of more defective structure in fresh CZA solid solution. A shift in the major peak observed for CZA samples compared to $Ce_{0.6}Zr_{0.4}O_2$ samples was due to distortion of the oxygen sublattice influenced by the sharing of O^{2-} anions with Al and compressive strain in the sample.

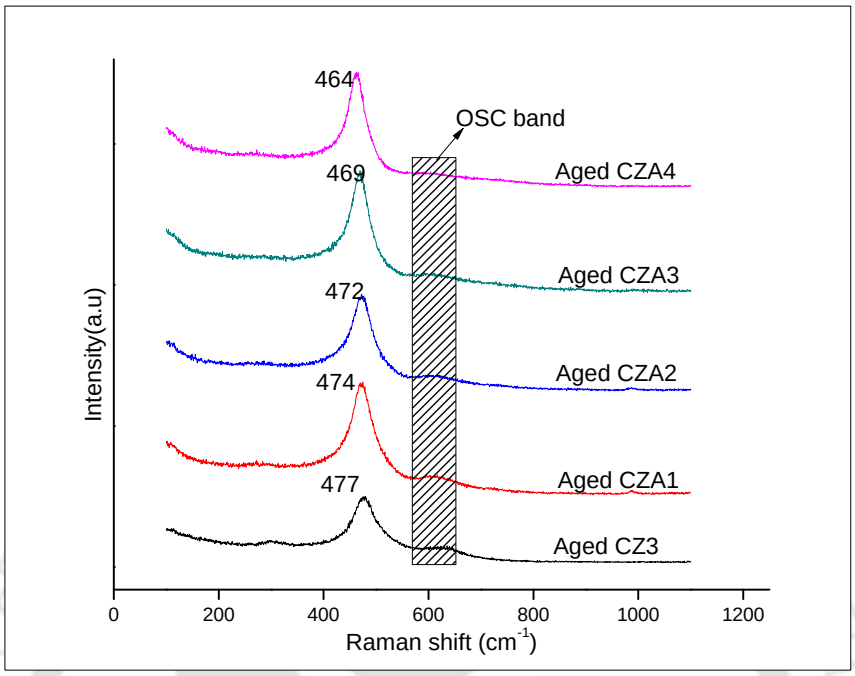

Figure 4.23 Raman spectra of aged $Ce_{0.6}Zr_{0.4-x}Al_{1.3x}O_2$ solid solution

The Raman spectra of aged $Ce_{0.6}Zr_{0.4-x}Al_{1.3x}O_2$ samples are shown in Figure 4.23, where a strong intense peak in the range of 464 to 477 cm^{-1} was observed. The OSC band was observed in all the aged samples of CZA. There was no phase separation of all CZA samples and no change in the presence of OSC peak observed around 600 and 610 cm^{-1} due to ageing. Thus, it is reasonable to state that the $Ce_{0.6}Zr_{0.4-x}Al_{1.3x}O_2$ formed a solid solution and it maintained the high oxygen mobility after the aging process.

Figure 4.24 depicts the Raman spectra of fresh $Ce_{0.6}Zr_{0.4-x}Mn_xO_2$ samples. It was observed that the Raman spectrum exhibited a strong band in the range of 474–459 cm^{-1} and a shoulder peak around 611–631 cm^{-1} in all the samples. The major peak observed about 465 cm^{-1} was assigned to F_{2g} vibration mode of a cubic fluorite CeO_2 like structure. The peak observed about 611 cm^{-1} might be due to the lattice distraction or oxygen vacancies. The same effect was observed in all CZM samples. The peaks observed around 460 and 621 cm^{-1} for $Ce_{0.6}Zr_{0.2}Mn_{0.2}O_2$ (CZM2) confirmed its cubic fluorite structure, which was also supported by Jia et al. [2008]. The peak observed around 600 cm^{-1}, Deshpande et al. [2004], 620 cm^{-1}, Prasad et al. [2009] and 570 cm^{-1}, Reddy and Khan [2005] confirmed the presence of oxygen vacancies or lattice defect in CZM compounds. It is noted that the band observed at around 462 cm^{-1} became broader and weaker

with an increase of Mn ions. The reasoning for band broadening is the presence of more oxygen vacancies, which is related to the changes in the structure of CeO_2 in the presence of Zr/ Mn ions, Hu et al. [2009]. A continuous shift in major peak towards the lower wave length for all the fresh samples was observed with an increase of Ce/Zr ratio and it was due the increase in lattice constant and lattice defects.

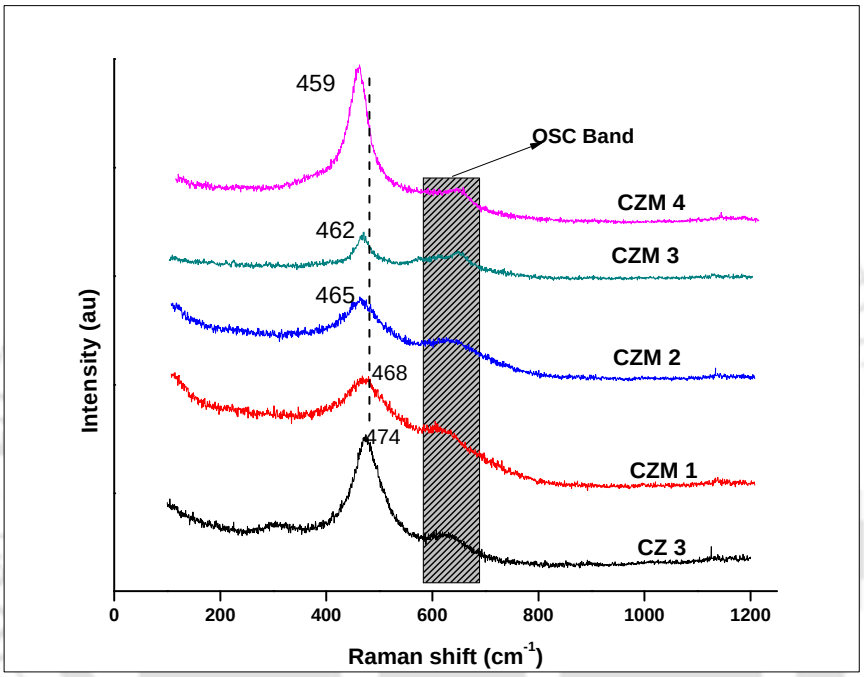

Figure 4.24 Raman spectra of fresh $Ce_{0.6}Zr_{0.4-x}Mn_xO_2$ samples

The Raman spectra of aged $Ce_{0.6}Zr_{0.4-x}Mn_xO_2$ samples are shown in Figure 4.25. It was observed that there were negligible peak shift in all the aged samples compared to that of fresh samples and the number of bands observed for all the spectra was observed to be the same. It was noted that the peaks observed for the aged samples were found to be weak compared to that of fresh samples. The peak broadening in aged $Ce_{0.6}Zr_{0.2}Mn_{0.2}O_2$ (CZM2) sample compared to fresh sample confirmed the presence of more defective sites, as supported by Zhang et al. [2009]. The peak shift observed in aged samples was increased with Ce/Zr ratio, lattice defects and the lattice constant. With the above observation, it is confirmed that the structure of $Ce_{0.6}Zr_{0.4-x}Mn_xO_2$ was not changed due to ageing.

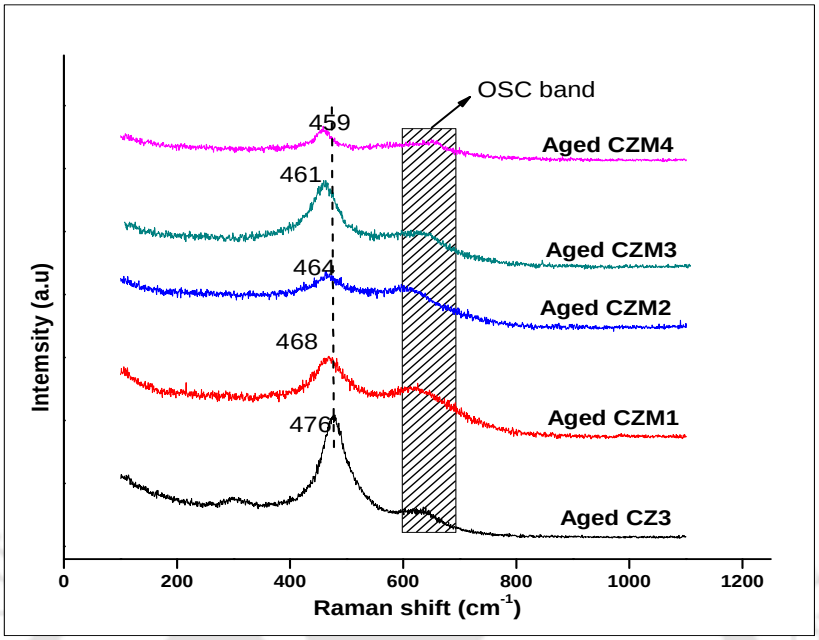

Figure 4.25 Raman spectra of aged $Ce_{0.6}Zr_{0.4-x}Mn_xO_2$ samples

4.1.5.2 Studies on thermal expansion

The thermal expansion of $Ce_{0.6}Zr_{0.4-x}Al_{1.3x}O_2$ samples against temperature is shown in Figure 4.26. It is observed that the thermal expansion of all the samples was increased non-linearly in the temperature range of 100 – 300 °C and linearly after 300 °C. It was also observed that the $Ce_{0.6}Zr_{0.4-x}Al_{1.3x}O_2$ samples showed negative and positive thermal expansion from room temperature to 200 °C and above 200 °C, respectively. Though metals have positive thermal expansion, some metal oxides contract upon heating during a particular temperature range and have negative thermal expansion (NTE), Govindaraj et al. [2007], which is expected to be caused by the vibration of the oxide structure of the sample. The phenomenon of the decrease of NTE is explained by considering the M–O–M bond (M = metal bonded with oxygen), which is schematically represented in Figure 4.27. Due to longitudinal vibration of oxygen, the distance between metal and oxygen bond was increased leading to reduced distance between the metal and metal bond, Evans et al. [1998]. The thermal expansion of the sample beyond 200 °C was increased with kinetic energy, which resulted to increase the equilibrium spacing of atoms. Due to the enhancement of anti-sintering characteristics, the thermal expansion of CZA was restricted with an increase of Al^{3+} concentration. It is observed that the thermal expansion of

$Ce_{0.6}Zr_{0.2}Al_{0.26}O_2$ (CZA2) was found to be the lowest compared to that of any other samples reported in $Ce_{0.6}Zr_{0.4-x}Al_{1.3x}O_2$ composition.

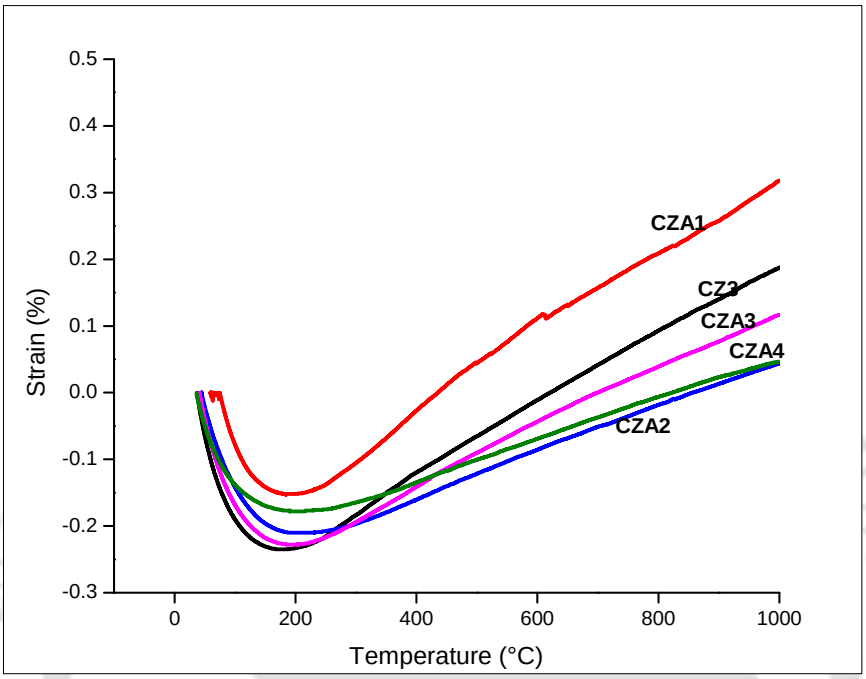

Figure 4.26 Thermal expansion behavior of $Ce_{0.6}Zr_{0.4-x}Al_{1.3x}O_2$ samples

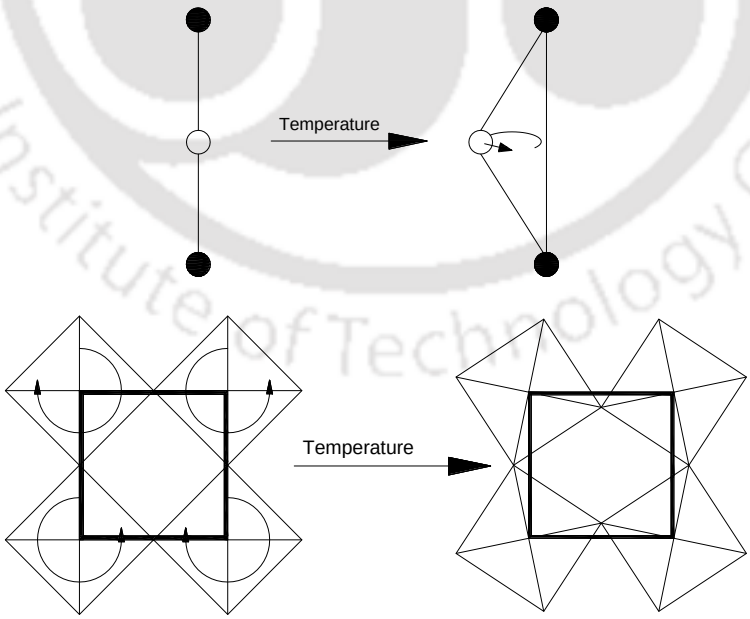

Figure 4.27 A schematic representation about transverse thermal vibration of M-O-M Bond, Evans et al. [1998]

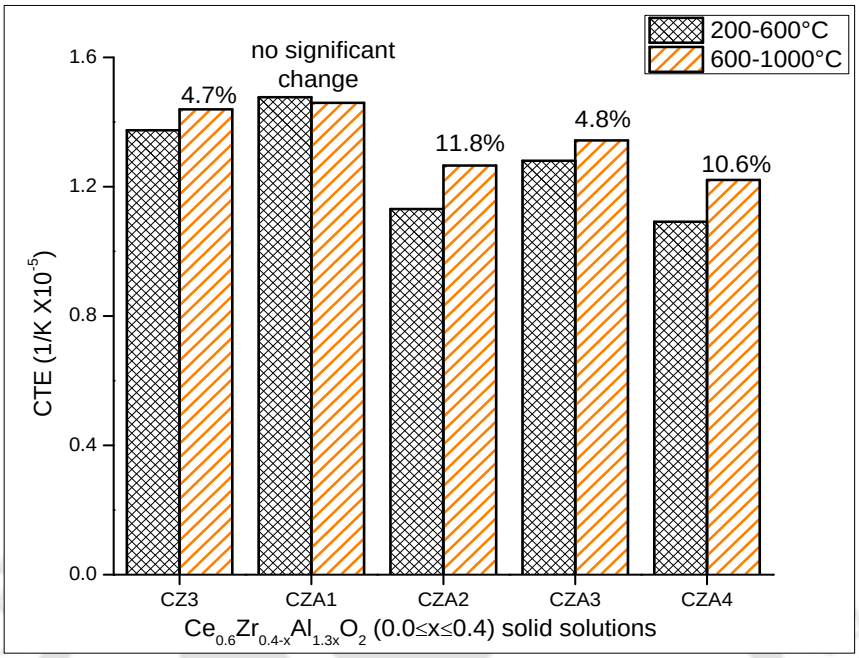

Figure 4.28 Coefficient of thermal expansion (CTE) of $Ce_{0.6}Zr_{0.4-x}Al_{1.3x}O_2$ at different temperature range

Figure 4.28 shows the CTE of $Ce_{0.6}Zr_{0.4-x}Al_{1.3x}O_2$ (CZA) samples in the temperature range of 200-600 °C and 600-1000 °C. It is noticed that the CTE of CZ3, CZA2, CZA3 and CZA4 was increased by 4.7, 11.9, 4.8 and 10.6 %, respectively, in the temperature range of 600-1000 °C compared to the range of 200-600 °C. Though CTE of CZA1 was observed to be decreased by 1.2 %, it is well within the experimental deviation. The enhancement of CTE of sample in the temperature range of 600-1000 °C was due to the loss of oxygen and the associated reduction of Ce^{4+} to Ce^{3+}. The change of valancy of cerium caused to increase the ionic radius of sample from 0.9 to 1.47 Å, thus the loss of oxygen led to the formation of anionic vacancy causing the increased CTE, Fagg et al. [2005]. An increase of CTE beyond 600 °C was due to enhanced oxygen vacancies leading to higher CTE for CZA2 compared to that of any other composition of $Ce_{0.6}Zr_{0.4-x}Al_{1.3x}O_2$.

The influence of Mn and Zr ion substitution in CeO_2 lattice on the thermal expansion of $Ce_{0.6}Zr_{0.4-x}Mn_xO_2$ is shown in Figure 4.29. The change in thickness of the sample with respect to temperature was recorded from 30 to 1000 °C. All the samples experienced the negative thermal expansion below 200 °C. Thermal expansion of $Ce_{0.6}Zr_{0.4-x}Mn_xO_2$ was increased linearly with

temperature beyond 200 °C. It is observed that the thermal expansion of CZM2 was found to be higher compared to that of any other $Ce_{0.6}Zr_{0.4-x}Mn_xO_2$ samples reported in the present study.

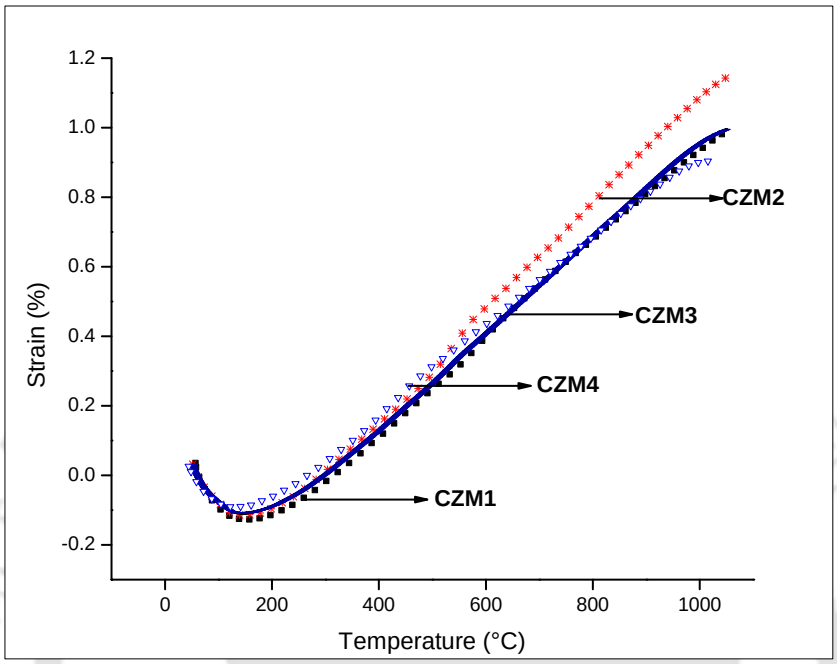

Figure 4.29 Thermal expansion behavior of $Ce_{0.6}Zr_{0.4-x}Mn_xO_2$ samples

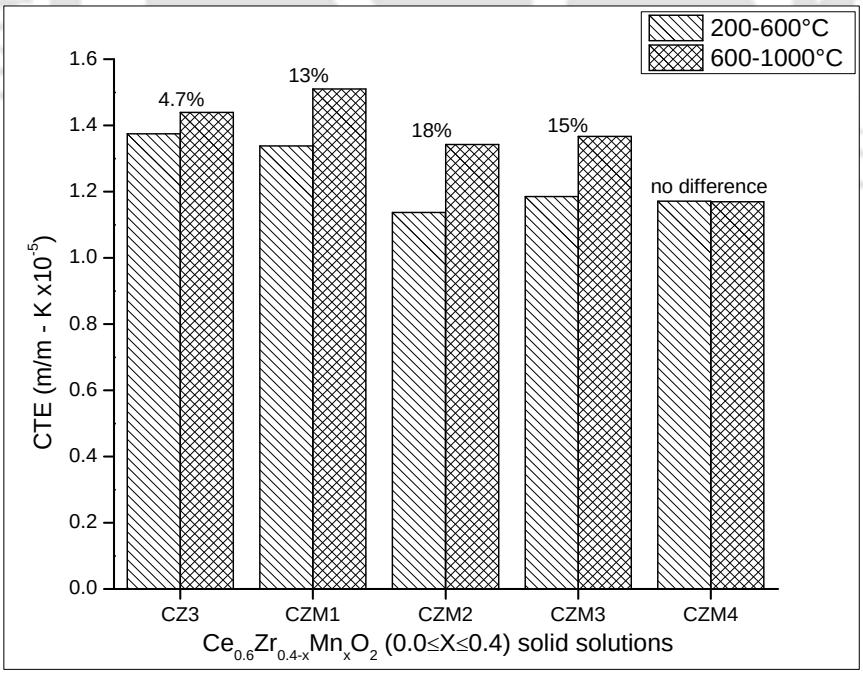

Figure 4.30 Coefficient of thermal expansion of $Ce_{0.6}Zr_{0.4-x}Mn_xO_2$ at different temperature range

Since the increase in thermal expansion of the sample beyond 600 °C was an indication of more oxygen vacancies, the coefficient of thermal expansion of $Ce_{0.6}Zr_{0.4-x}Mn_xO_2$ composition at a different temperature range was studied and the results are shown in Figure 4.30. The increase in CTE of the samples from 200 – 600 °C to 600 – 1000 °C was observed to be 4.7, 13, 18, 15 and 0 % for CZ3, CZM1, CZM2, CZM3 and CZM4, respectively. The increase in CTE of CZM2 in the above referred temperature range was found to be high due to the presence of high-oxygen vacancy.

4.1.5.3 Lattice defects confirmation

In order to study the influence of Zr, Al and Mn ions substitution in ceria lattice on its OSC, HRTEM images were obtained for CeO_2, $Ce_{0.6}Zr_{0.4}O_2$ (CZ3), $Ce_{0.6}Zr_{0.2}Al_{0.26}O_2$ (CZA2) and $Ce_{0.6}Zr_{0.2}Mn_{0.2}O_2$ (CZM2) and the results are compared.

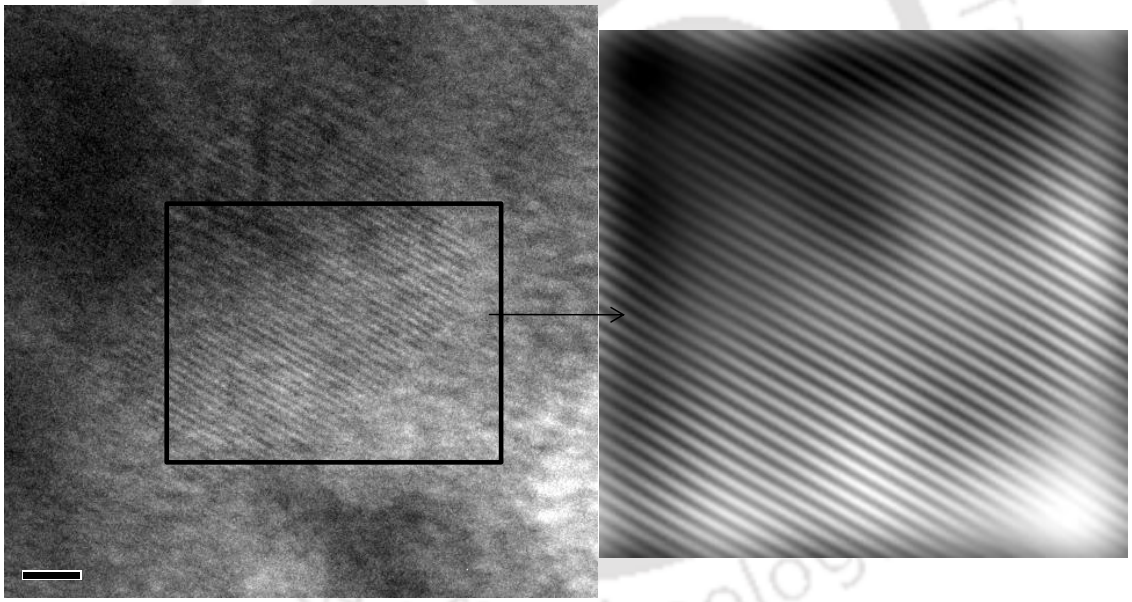

Figure 4.31 HRTEM image and filtered image of CeO_2 without significant lattice defect

Figure 4.31 shows the HRTEM image of CeO_2, where it showed the perfect lattice plane with the interplanar distance of 0.15 nm without any significant surface defects. The filtered image indicates the lattice fringes without any crystal defects. It is also observed that the lattice fringes were oriented uniformly in the same direction. It was clearly identified from the marked portion that CeO_2 lattice fringes were observed to have no significant defects.

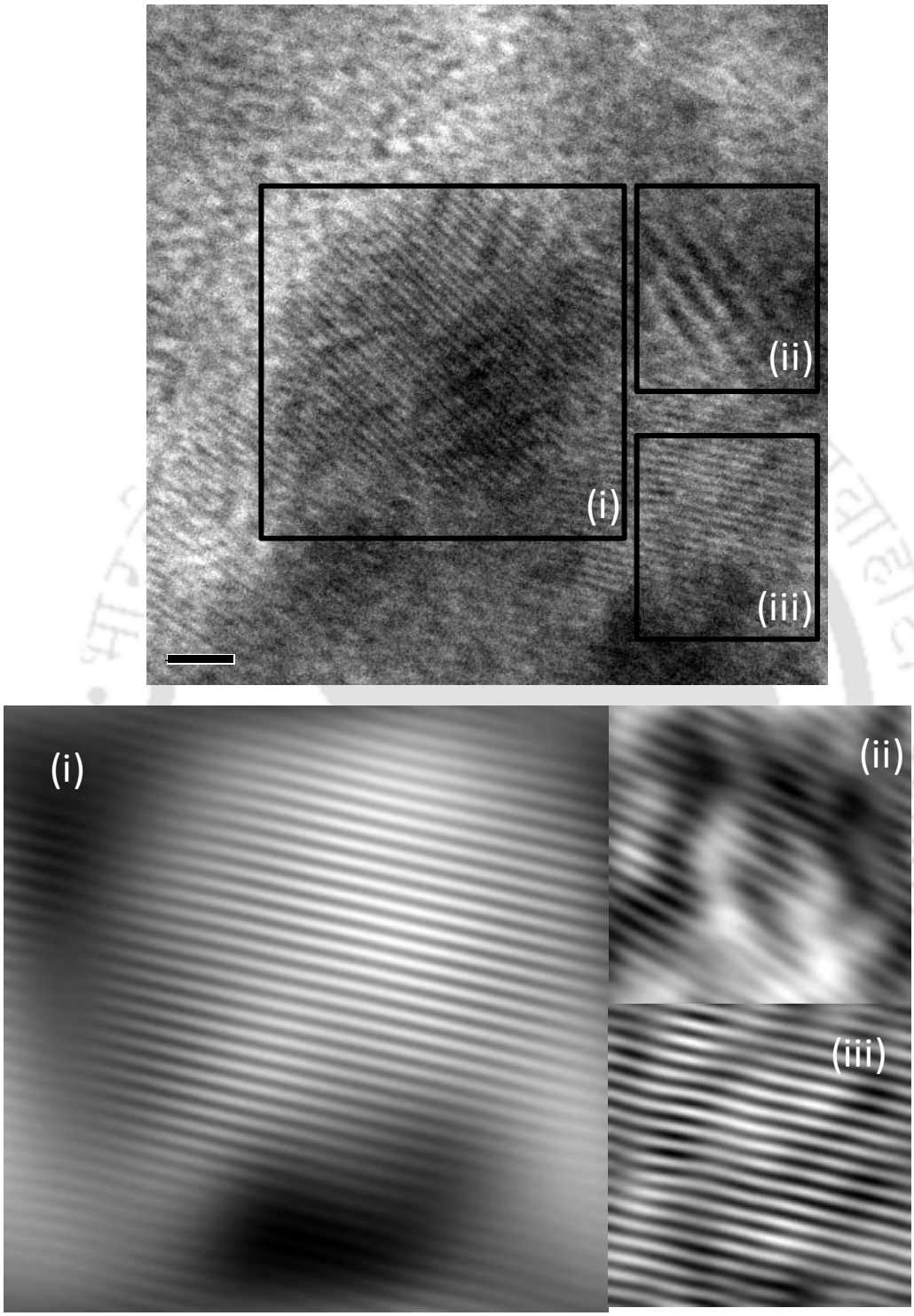

Figure 4.32 HRTEM images of $Ce_{0.6}Zr_{0.4}O_2$, (i) filtered image without lattice defect, (ii) Filtered image with lattice defect-edge dislocation and (iii) Filtered image with lattice defect- edge dislocation

Figure 4.32 shows the HRTEM image of $Ce_{0.6}Zr_{0.4}O_2$, where few defects were identified from the marked portions, which were due to the substitution of Zr ions in CeO_2 lattice. The marked portion in the image was filtered and represented separately, where the edge dislocation defects were noticed. In some cases, the non-defective fringes were also noted, which agrees well with the interplanar spacing corresponding to the (111) plane.

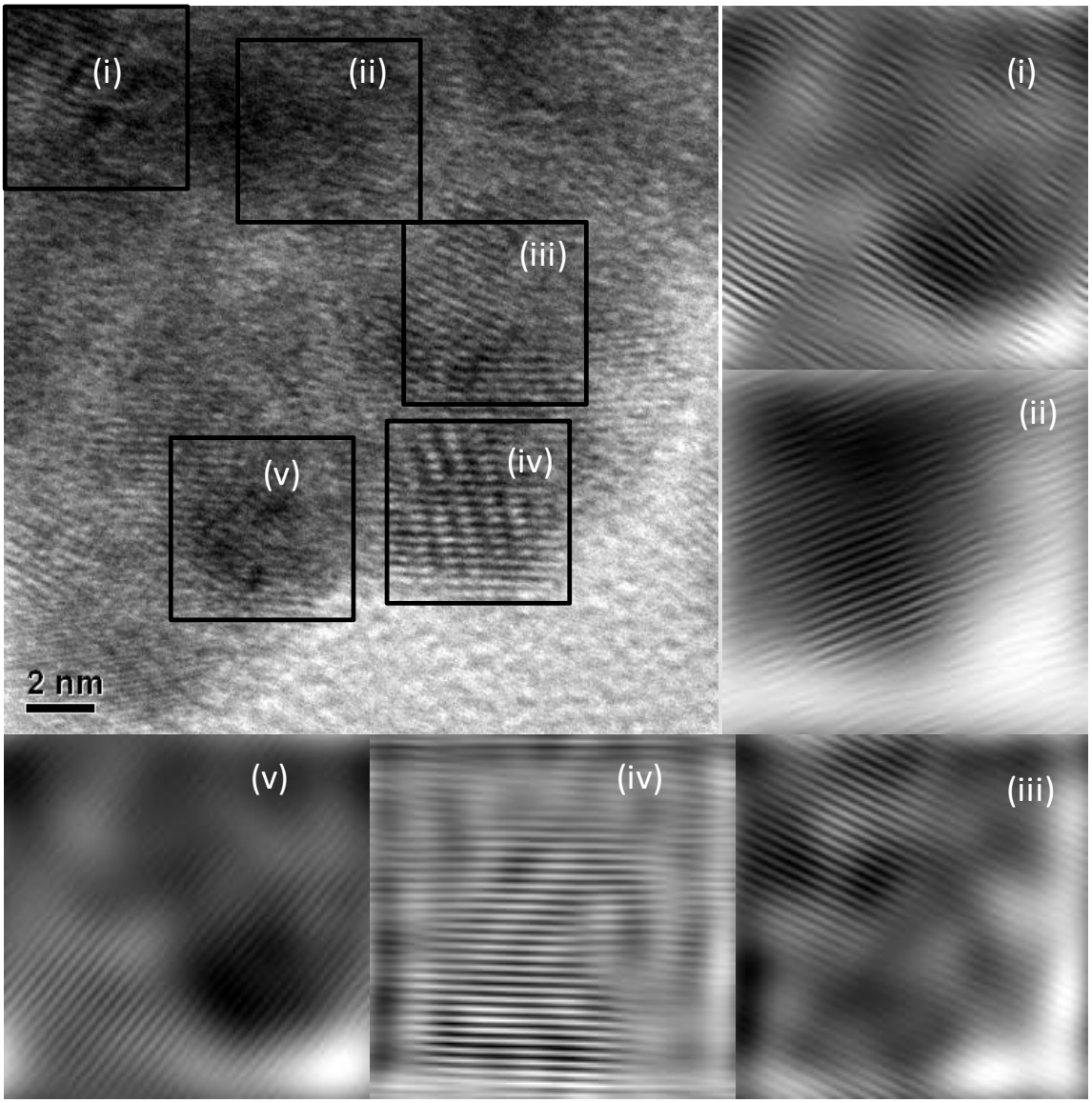

Figure 4.33 HRTEM images of $Ce_{0.6}Zr_{0.2}Al_{0.26}O_2$ (i) - (v) Filtered image with lattice defects

Figure 4.33 shows the HRTEM images of $Ce_{0.6}Zr_{0.2}Al_{0.26}O_2$, where many distinguished defects resulting to more oxygen vacancies were observed. The marked portions in the image were presented as corresponding filtered images (i-v), where the lattice defects in CZA2 were

identified to be the edge dislocation. The distorted lattice fringes were the indication of lattice defects. The interplanar spacing of CZA2 was observed to be around 0.28 nm. The increase in interplanar distance is due to the insertion of Al^{3+} ions resulting to the increase of Ce/Zr ratio.

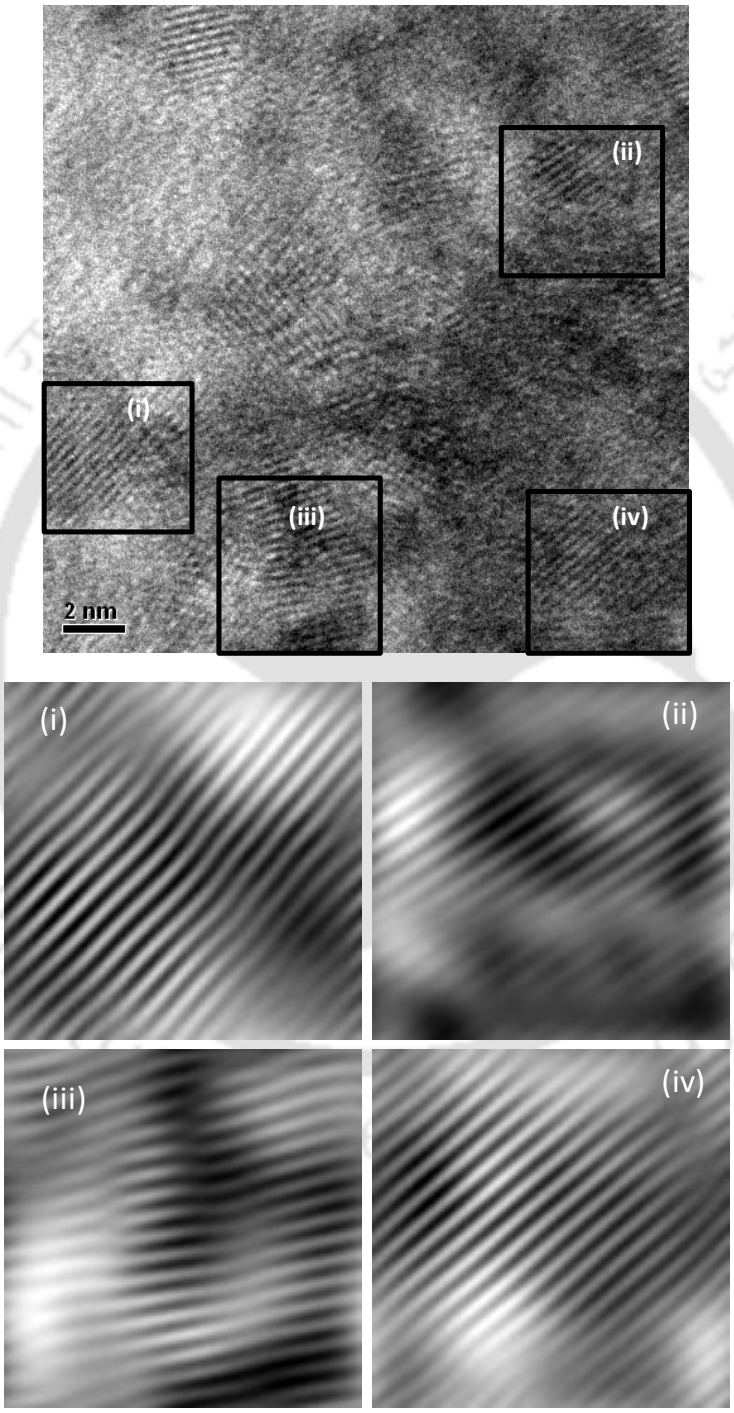

Figure 4.34 HRTEM image of $Ce_{0.6}Zr_{0.2}Mn_{0.2}O_2$ (i-iv) Filtered image with lattice defects

Figure 4.34 shows the HRTEM images of $Ce_{0.6}Zr_{0.2}Mn_{0.2}O_2$, where more number of defects, and the randomized orientation of lattice fringes were observed. It gave an impression that the particles were not coalesced. The marked portions in HRTEM image were filtered and represented separately with the indication of i-iv, where the defective and dislocated lattice fringes where identified, which were due to the substitution of Zr and Mn ions in ceria lattice. These lattice defects were expected to play a significant role for the improvement of OSC compared to other type of samples.

From the OSC and its confirmation studies, it was found that the doping of Al^{3+} yielded a solid solution which has the highest OSC compared to rest of the ions Mn^{2+}, Bi^{3+}, La^{3+} and Nd^{3+}. It was noted that the introduction of Zr^{4+} and Al^{3+} ions into ceria lattice led to considerable modification of its textural, structural and redox properties, which were confirmed by the different characterization techniques: (1) enhancement of BET specific surface area in CZA, (2) effective restraining of sintering the crystallite particles, stabilizing the pseudo-cubic *t″*-phase restricting the phase separation of CZA to form a homogeneous solid solution and high thermal stability, (3) creating more defective structure and enhancing the mobility of bulk oxygen which contributes to the increase of OSC and redox properties of CZA systems.

4.2 Optimization of surfactant and synthesis technique to prepare nanofuel

In order to prepare a highly stable nanofuel at least for a period of one week, it was synthesized using different surfactants and preparation techniques. Different surfactants according to their hydrophilic head charge namely anionic (SDS), cationic (CTAB) and nonionic (tween 20, oleic acid, tween 80) were used. Different types of nonionic category surfactants were selected based on their chain length. Tip sonication, magnetic stirring and combination of both were used to synthesize the nanofuel in order to select a suitable preparation technique for stable nanofuel.

4.2.1 Influence of surfactant on the stability of nanofuel

Figure 4.35 shows the comparison of relative stability of nanofuels having the concentration of 0.06 wt. % of CeO_2 with and without adding the surfactants. The nanofuels were prepared using tip sonication technique for 1 hr with different surfactants and the samples were observed for 7 hrs under static condition in order to select a suitable surfactant to prepare the nanofuel for further studies. It was observed that the nanofuel prepared without any surfactant was found to

have 80 and 55 % stability after 2 and 7 hrs, respectively. However, the nanofuel prepared with CTAB, SDS, tween 20, oleic acid and tween 80 surfactant was found to have 63, 65, 78, 84 and 89 % stability, respectively, at the end of 7 hrs. It was noted that the nanofuel prepared with tween 80 maintained 100 % stability for about 3 hrs. However, the same prepared with tween 20 and oleic acid as a surfactant was observed to be 100 % stable for about 1 hr only. Beyond 2 hrs of its preparation, the tween 20 based nanofuel showed the rapid sedimentation of nanoparticles compared to that of oleic acid. At the end of 7 hrs, the increase in stability of CTAB, SDS, tween 20, oleic acid and tween 80 based nanofuel was found to be 14, 17, 42, 53 and 63 %, respectively, compared to that of the nanofuel prepared without any surfactant. The surfactant was found to promote the physical stability of nanofuel and the stability enhancement of the same was observed to be low in anionic / cationic surfactants and high in non-ionic surfactants compared to that of the nanofuel prepared without any surfactants. It was due to the fact that the surfactant kept the particles dispersed in the base fluid by electrostatic repulsive forces among the particles and hydrophobic surface forces due to physical adsorption of surfactant by solid particles, and it was also supported by Murshed et al. [2005].

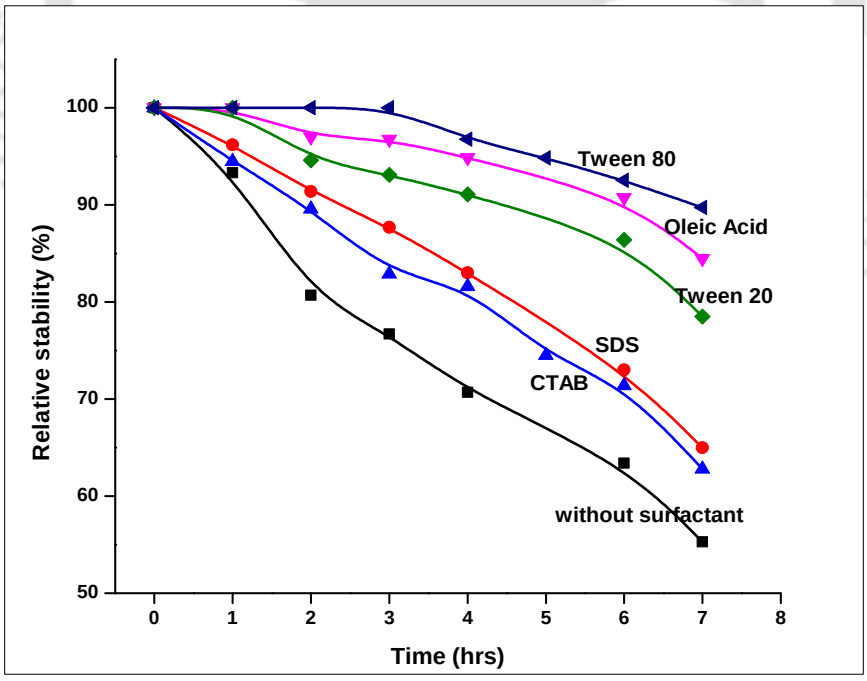

Figure 4.35 Influence of different surfactants on the relative stability of nanofuel having 0.06 wt. % of CeO_2

Ceria nanoparticles exhibited a tendency for aggregation and formation of the large entangled agglomerates due to their size and high surface energy in base fuel. The rate of sedimentation of nanoparticles was found to be high in nanofuel, when no surfactant was used, which was due to strong Van der Waals force of attraction among nanoparticles due to their size. The increase in stability of nanofuel with surfactant was due to the fact that the surfactant molecules get adsorbed over the ceria surface by their hydrophobic segments with hydrophilic head directed towards the base fluid, which was also confirmed by Lisunova et al. [2006]. The electrostatic stabilization achieved in ionic surfactants was due to the presence of negative and positive hydrophilic head charges in SDS and CTAB, respectively, Paria et al, [2004], and their respective schematic diagrams are shown in Figures 4.36a and 4.36b. The presence of single hydrocarbon chain in CTAB and SDS surfactants has the tendency to form micelles leading to higher rate of sedimentation of nanoparticles in base fluid, which was also supported by Tah et al. [2011]. Though the homogeneous dispersion of CTAB and SDS was ensured in nanofuel using a suitable synthesis technique, it was not advisable to use them in a CI engine where the fuel injectors and nozzle holes are expected to be blocked due to their size.

a)

b)

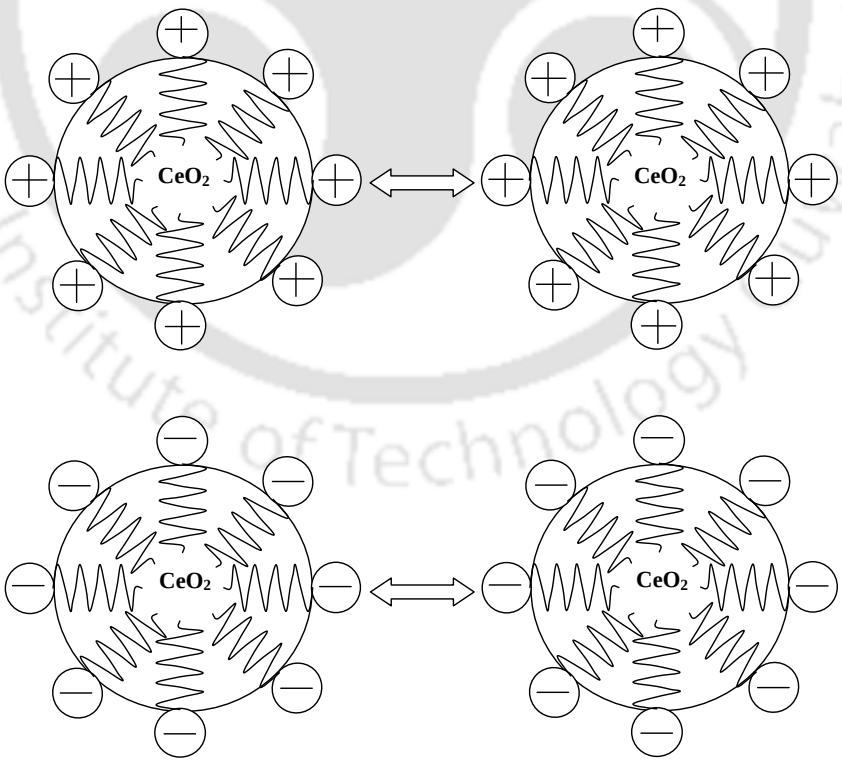

Figure 4.36 Electrostatic stabilization mechanism of (a) CTAB and (b) SDS surfactant on Nanofuel

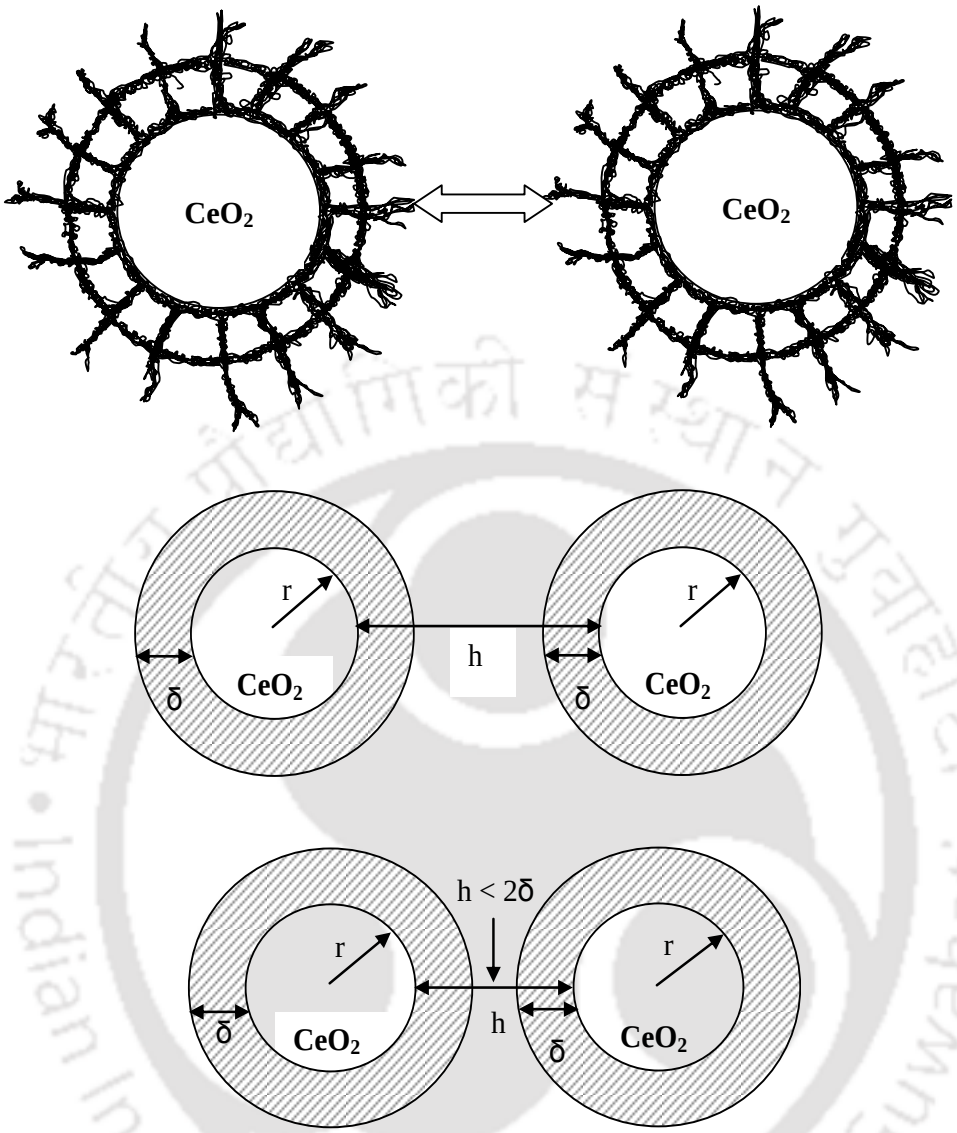

Figure 4.37 Steric stabilization mechanism of Non-ionic surfactant

In case of nonionic surfactants, the steric stabilization mechanism was observed in nanofuel. The long-chain molecules present in tween 20, tween 80 [Young et al. 2000] and oleic acid [Morales et al. 2005] were attached to the nanoparticles and they form a layer between the particle and the fluid molecules, where the thickness of adsorbed layer was noted to be δ. These layers increased the potential between the particles and imparted repulsive force between them. If two particles maintain the separation distance of h, which is smaller than 2δ, the adsorbed layers can overlap or become compressed, resulting the strong repulsion. The above mechanism is schematically shown in Figure 4.37. Though tween 20 and tween 80 belong to the same group of surfactant, both differs with hydrophobic compound attached with them. Tween 20 has lauric

acid and tween 80 has oleic acid as a hydrophobic structure, Lorenz et al. [1977]. Steric stabilization occurs due to the presence of steric barriers from the adsorbed nonionic molecules that prevent the particles coming close enough to dominate the Van der Waals force of attraction between the particles. Tween 80 contains the ethylene oxide and long hydrocarbon chain compared to oleic acid and it imparts both lipophilic and hydrophilic characteristics, Som et al. [2014], leading to increased stability of nanofuel compared to oleic acid and tween 20 based nanofuel.

By comparing all the results, the nanofuel with tween 80 was observed to show the improved stability, where the sedimentation was found to be nearly 0 % for at least 3 hrs and 10 % at the end of 7 hrs. Eventhough the nanofuel with oleic acid was observed to show the 100 % stability for 1 hr, the sedimentation was observed to be increased by around 33 % compared to that of the nanofuel having tween 80 at the end of 7 hrs. With respect to time, the reduction in nanofuel stability was due to the depletion of surfactant layer of nanoparticles caused by the frequent collision among them. Thus, the nanoparticles were observed to be stable during initial period after synthesis of nanofuel but started to settle with respect to time. However, the rate of sedimentation was found to be influenced by the nature of surfactant used to prepare the nanofuel. Hence, the nanofuel with tween 80 was used for further studies in order to suggest a suitable preparation technique with different concentration of nanofuel.

4.2.2 Influence of preparation technique on the relative stability of nanofuel

Figure 4.38 illustrates the relative stability of nanofuel with tween 80 as a surfactant prepared by magnetic stirrer for 2 hrs at different CeO_2 concentration for the period of 72 hrs. As the rapid sedimentation of nanoparticles was noted in all cases, the experiments were limited to 72 hrs. The samples were kept motionless till completion of the test. It was noted that the relative stability of nanofuel was observed to be 100 % in all the concentration for the period of 2 hrs. After 2 hrs period of the nanofuel preparation, the rate of settling of nanoparticles was observed to be high with an increase of the concentration of CeO_2. Due to lower concentration of CeO_2, the distance between the particles was sufficient enough to dominate both the repulsive and attractive forces acting against each other. With the absence of repulsive and attractive forces between the particles, the nanoparticles were subjected to continuous collision against each other due to the Brownian motion, which caused the sapping of adsorbed surfactant layer. In due

course of time, the nanoparticles started to aggregate and then agglomerate and thus the gravitational force influenced the rate of sedimentation of the particles even at lower concentration. When the particle concentration was increased, the minimum distance between the particles was decreased and it caused the domination of Van der Waals force of attraction leading to aggregation and sedimentation of them. Thus, the stability of nanofuel was decreased continuously. Due to the continuous stirring process, the temperature of nanofuel was also increased leading to depletion of the adsorbed surfactant layer of the nanoparticles. Thus, the agglomeration of nanoparticle was observed and it results the sedimentation of the particles. After 72 hrs of its preparation, the relative stability of nanofuel was observed to be 72.8, 71.3, 68, 64.8 and 61.5 % for 0.02, 0.04, 0.06, 0.08 and 0.1 wt. % of CeO_2, respectively.

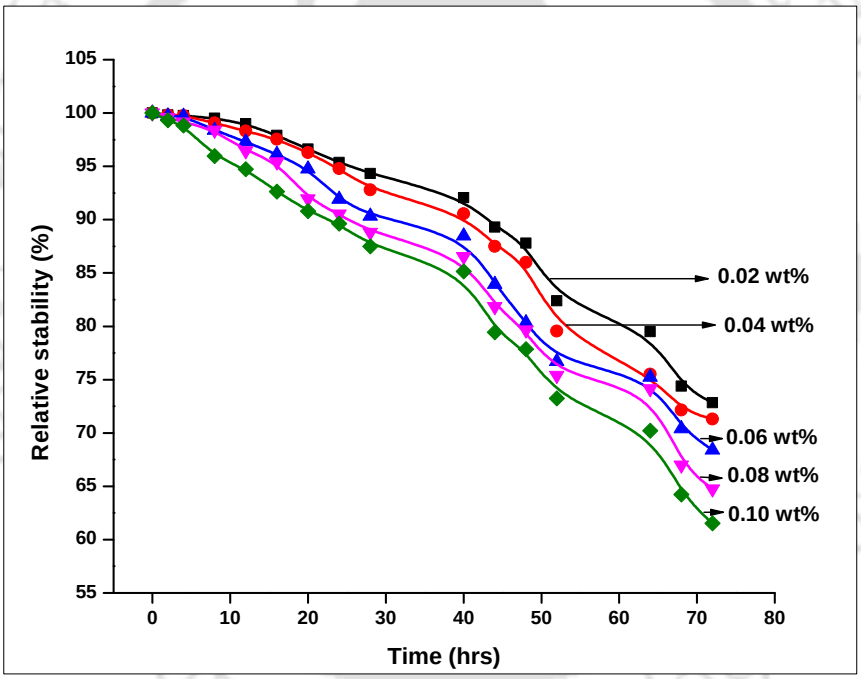

Figure 4.38 Relative stability of nanofuel prepared by magnetic stirrer for 72 hrs

Figure 4.39 shows the relative stability of nanofuel at different concentrations with tween 80 as a surfactant prepared using the tip sonicator for 2 hrs. During the sample preparation, the temperature of the nanofuel was maintained at 35 °C using an ice bath. It is observed that the relative stability of nanofuel was observed to be within 93 % after 72 hrs of ageing for all the concentration of CeO_2 dispersed nanofuel. The stability of nanofuel synthesized by the tip sonication technique was found to be high compared to that of the sample prepared through

magnetic stirring method. The relative stability of nanofuel at 0.02, 0.04, 0.06, 0.08 and 0.10 wt. % was observed to be 93.5, 91.4, 87.0, 86.0 and 84.6 %, respectively, at the end of 168 hrs, where the corresponding 100 % relative stability of the above was observed for the period of 4, 3, 3, 2 and 1 hr. The decrease in stability with time could be due to the damage on the adsorbed layer of the surfactant coating over the particles caused by the collision between the particles. Thus, the electrostatic repulsive forces and hydrophobic surface forces generated by the surfactant became less. The Van der Waals force of attraction between the particles is expected to overcome the hydrophobic surface forces leading to the formation of agglomeration, and the particle clusters started to settle due to gravitational force. In comparison with the results reported against Figure 4.35, it is noted that the sedimentation was noted to be 1 and 11 % for the sonication of nanofuel by 2 and 1 hr, respectively, at the end of 7 hrs.

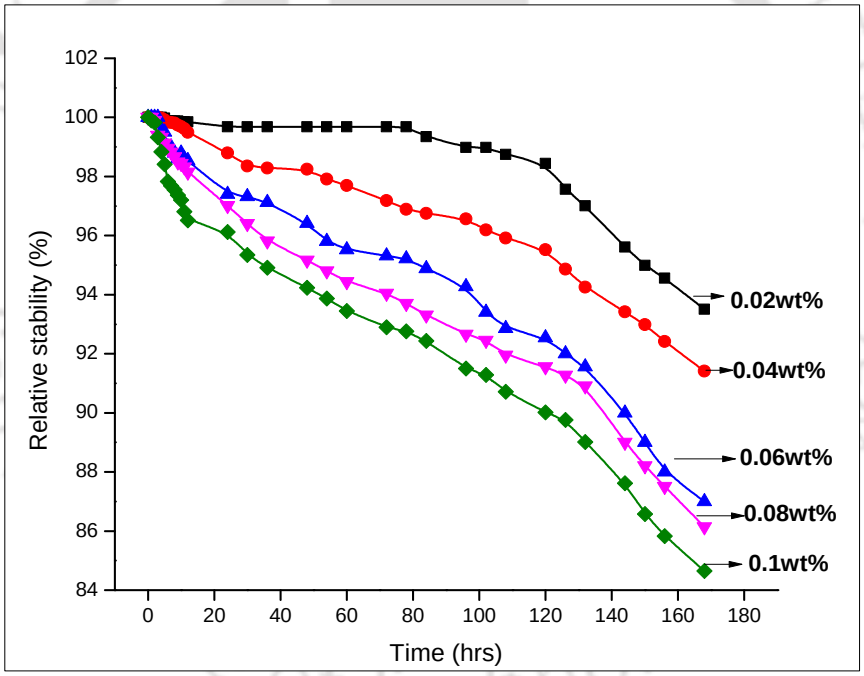

Figure 4.39 Relative stability of nanofuel prepared by tip sonicator for 168 hrs

Various forces such as gravitational force, electrostatic repulsive force and Van der Waals attractive force acting on the particles are playing an important role in the dispersion stability of the nanofuel. In both cases of sample preparation technique as discussed above, it is noted that a 0.02 wt. % nanofuel was found to be more stable for a longer period of time compared to rest of the sample. When particles became closer than the equilibrium distance during the Brownian motion of particles, the Van der Waals force of attraction dominates and these two particles are

attracted each other leading to increased size of agglomeration and thus the gravitational force influences the sedimentation. The above phenomenon is more significant when CeO_2 concentration was high. The ratio between volume of liquid and volume of particles was found to be 3.6 x 10^{10}, 1.8 x 10^{10}, 1.2 x 10^{10}, 0.9 x 10^{10} and 0.72 x 10^{10} for the concentration of 0.02, 0.04, 0.06, 0.08 and 0.1 wt. %, respectively. It is noted that the volumetric ratio of liquid to particles was observed to be decreased with an increase of concentration. The above observation was confirmed by the fact that the rate of sedimentation was proportional to the concentration of CeO_2. The effect of gravitational force, which favors the sedimentation, became dominant in the nanofuel even with less concentration of CeO_2 particles with time.

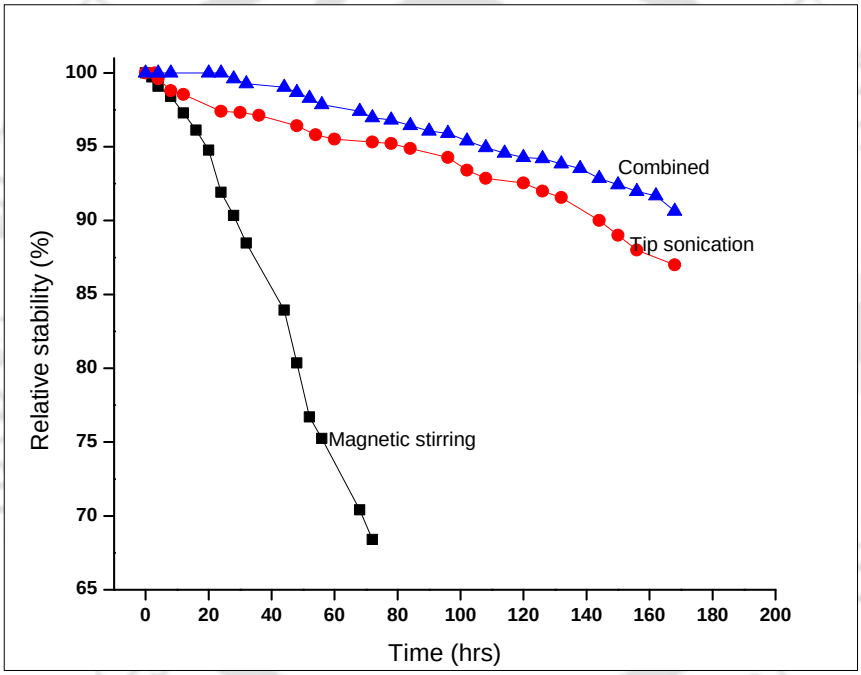

Figure 4.40 Comparison of relative stability of 0.06 wt. % nanofuel

Figure 4.40 shows the comparison of relative stability of nanofuel based on the preparation techniques namely magnetic stirring, tip sonication and combined technique of both. Due to high rate of sedimentation, the relative stability of nanofuel was studied up to 72 hrs in case of magnetic stirring method. However, the relative stability of nanofuel synthesized by tip sonication and combined technique was studied up to 168 hrs. It is observed that the nanofuel prepared by the magnetic stirring method showed the poor stability compared to rest of the techniques even within 72 hrs of its preparation. Overall, the combined technique of nanofuel

preparation showed the best results compared to that of individual techniques up to 168 hrs of sample preparation.

It is observed from Table 4.8 that the combined method produced more stable nanofuel than the rest of the methods, where the summary of the relative stability after 72 hrs and 168 hrs of ageing is given in addition to duration of 100 % relative stability. Since the probe sonicates for 30 min. followed by the magnetic stirring for 30 min. alternatively for the period of 2 hrs, it helped to maintain the surfactant coating over the nanoparticles. The density of the supernatant of nanofuel was also studied for the same testing period in order to support the above findings, where it was observed to be varied in the range of 0.838 to 0.843 g/cm^3 during the testing period. From the above studies, the homogeneous dispersion of the nanoparticles and the stability of nanofuel were confirmed to be superior, when the sample was prepared by the combined method.

Table 4. 8 Relative stability of nanofuel based on the synthesis technique

	Magnetic Stirring	Tip sonication	Combined Technique
After 72 hrs of ageing	68.4 % relative stability	95.3 % relative stability	97 % relative stability
After 168 hrs of ageing	Not applicable	87 % relative stability	91.6 % relative stability
100 % relative stability till	1 hr	3 hr	24 hr

The XRD patterns of (i) as received CeO_2 nanoparticles and (ii) CeO_2 nanoparticles derived from centrifuging the nanofuel prepared from magnetic stirring, tip sonication and combined technique were studied and the results are shown in Figure 4.41. The XRD profile confirmed the polycrystalline nature of cerium oxide nanoparticles. The high intensity peaks were observed at 28.6, 33.15, 47.55 and 56.45˚ for the lattice plane of (111), (200), (220) and (311), respectively. The observed peaks were matched with JCPDS-ICDD No: 81-0792 of CeO_2 crystal. The strain present in the nanoparticles was calculated using the FWHM of the main peak of XRD pattern of CeO_2 and it was found to be 0.351, 0.452 and 0.356 % for the preparation technique of magnetic stirring, tip sonication and combined method, respectively. The strain induced in the

nanoparticle by the centrifugal force during the particle separation from the nanofuel was considered to be the same irrespective of the processing technique followed to prepare the nanofuel. The process induced strain on the nanoparticles was calculated by subtracting the inherent strain present in the as received CeO_2 nanoparticle and it is observed to be 1.04, 8.14 and 1.56 % for the preparation technique of magnetic stirring, tip sonication and combined technique, respectively. The strain developed in the nanoparticle due to tip sonication process was observed to be the highest compared to other processing techniques and it might be one of the reasons for damaging the surfactant coating over the nanoparticles, which caused their sedimentation after the specific period. Though the strain developed in the nanoparticle by the combined technique and magnetic stirring method was found to be approximately same, the surfactant coating was removed in later case due to high rate of heat generation. The nanofuel prepared through the combined technique has the good stability for a long period of time while maintaining the surfactant coating over the CeO_2 nanoparticles.

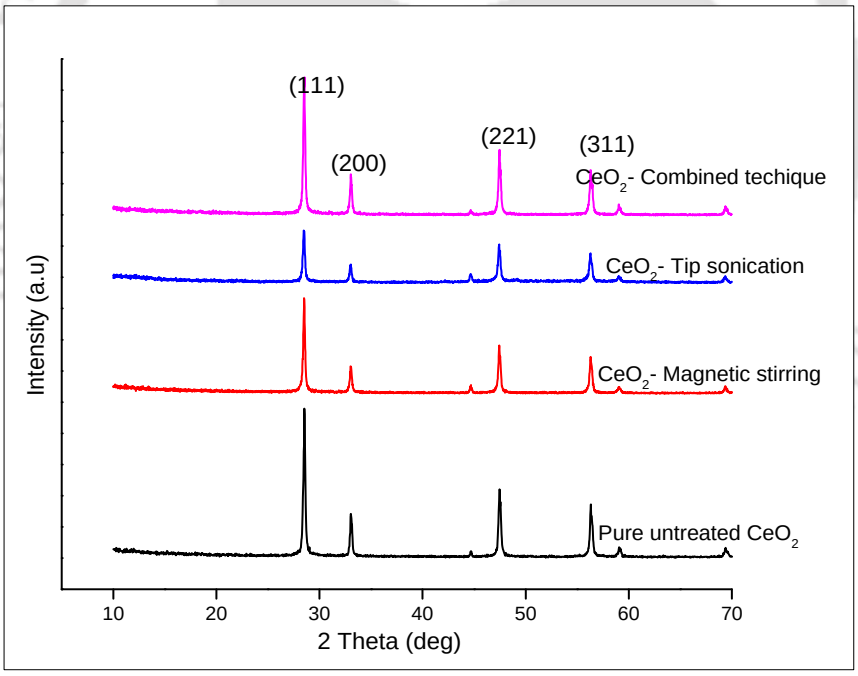

Figure 4.41 XRD patterns of derived CeO_2 nanoparticle from nanofuel

Figure 4.42 shows the TEM images of the nanofuel drop synthesized by the magnetic stirring, tip sonication method and combined technique at different magnifications. It is observed from Figure 4.42a that the particles were observed to be more agglomerated in the magnetic stirring preparation technique. In case of tip sonication technique, the particles were observed to be non-

uniform nature due to more strain present in the particles, which are shown in Figure 4.42b. However, a uniform size of nanoparticles is observed in Figure 4.42c and 4.42d, where the nanofuel was synthesized by the combined technique and it is expected that the inherent characteristics of the nanoparticles were maintained without any distortion.

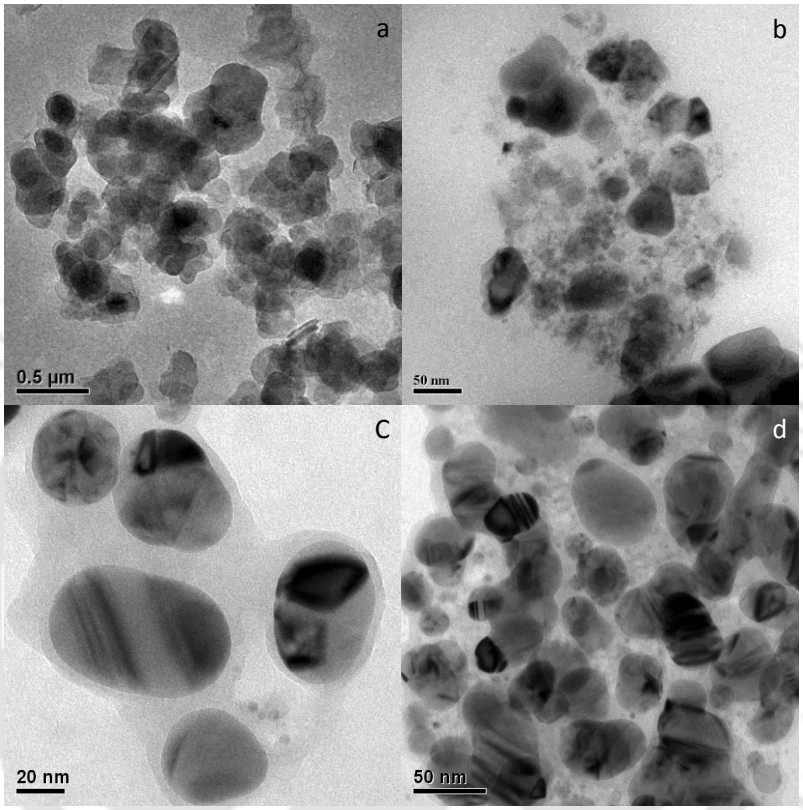

Figure 4.42 TEM images of nanofuel drop synthesized by the a) Magnetic stirring, b) Tip sonication, c) Combined technique in 20nm scale, d) Combined technique in 50nm scale

The above results indicated that the combination of tip sonication and magnetic stirring was a successful synthesis technique to prepare homogeneous dispersion of CeO_2 in diesel for a longer period of time.

4.2.3 Accelerated relative stability study

Figure 4.43 and 4.44 shows the relative stability of CeO_2 based nanofuel at 0.06 wt. % by the natural and accelerated sedimentation condition, respectively. The later was used to reduce the time consumption required for the stability studies and to predict the relative stability of the nanofuel against ageing. An accelerated ageing study using centrifuge was done at 1000 rpm for

the period of 5, 10, 15, 20, 25 and 30 min. and the relative stability studies were done. The relative stability of nanofuel under natural and accelerated ageing was compared and the following relation was obtained, which gives the correlation between the period of centrifuging and equivalent normal sedimentation period.

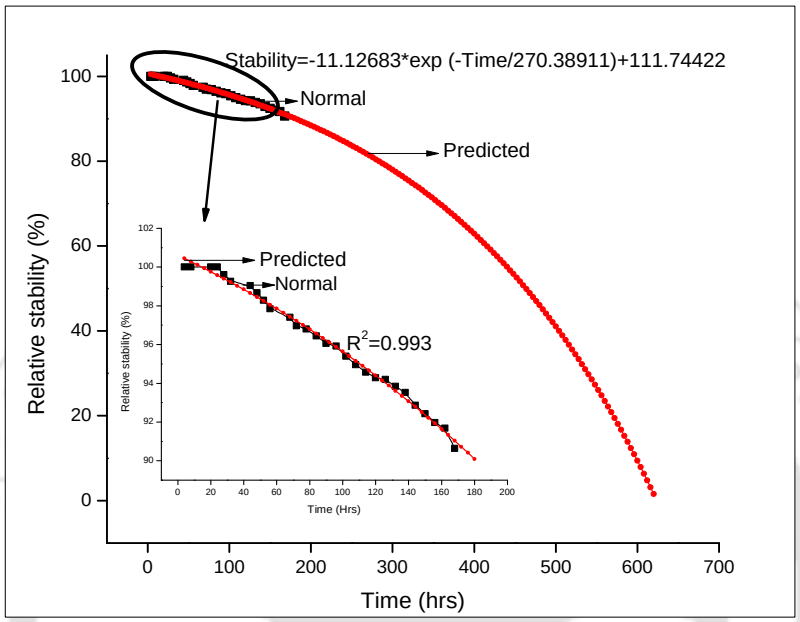

Figure 4.43 Predicted relative stability of nanofuel up to 620 hrs period of time- nanofuel synthesized by combined technique

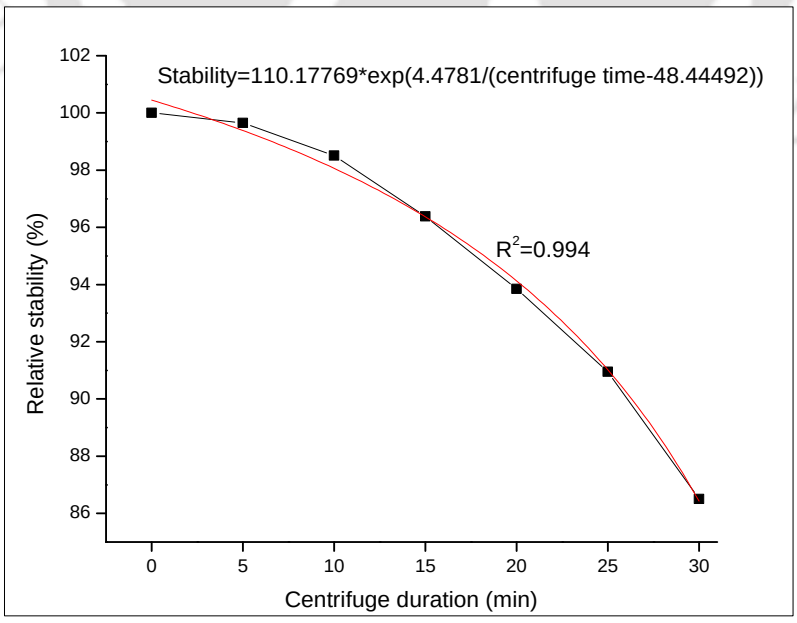

Figure 4.44 Accelerated relative stability with curve fitting for CeO_2 nanofuel at 0.06 wt. %

The relation between natural sedimentation timing and centrifuge timing is as follows:

$$AS = 110.1777 * e^{4.4781/(CT-48.4449)} \quad \text{... (4.8)}$$

$$NS = -11.12683 * e^{NT/27.38911} + 111.74422 \quad \text{... (4.9)}$$

where AS= Accelerated relative stability (%), CT= Centrifuge time (min), NS=Natural relative stability (%) and NT= Normal time (hrs). By equating the equation (4.8) and (4.9), the relation between centrifuge time and normal ageing time was obtained, which is given in equation (4.10).

$$CT = \frac{4.4781}{ln[-0.101046 * e^{NT/27.38911} + 1.014777]} + 48.44492 \quad \text{... (4.10)}$$

The equation (4.10) was validated for 168 hrs of normal ageing and presented as inset in Figure 4.43. The relative stability of 91.03 % was achieved for 168 hrs of normal ageing equivalent to 24.98 min. of centrifuge timing obtained using the above equation, whereas the experimental results showed the stability of 90.64 % for 168 hrs, where a close approximation between them was obtained. Since the deviation between experimental and predicted results was found to be significantly very less, the equation (4.10) was used to calculate the relative stability of nanofuel after 5, 10, 15, 20 and 25 days, where the respective dispersion stability was noted to be 94.4, 84.7, 69.6, 46.1 and 9.4 % and their equivalent centrifuge time was calculated to be 19.5, 31.4, 38.7, 43.3 and 46.6 min, respectively. It is also noted that the nanoparticles were found to be settled completely after 620 hrs.

4.3 Optimization of ceria concentration for the performance enhancement of an IC engine

Though tween 80 was found to be a suitable surfactant to prepare CeO_2 based nanofuel, it was found to be not appropriate for the synthesized samples such as CZA, CZM and others. As tween 80 has oleic acid as a hydrophobic structure and being a non-ionic surfactant, the oleic acid was chosen to prepare the nanofuel using different types of nanoparticles. As tween 80 has the ability to remove petroleum hydrocarbon, Lai et al. [2009], it might reduce the lubrication efficiency in an IC engine. As the surface tension of tween 80 was found to be 43.7 mN/m, which was higher than that of the oleic acid (32.12 mN/m), it is expected to influence the droplet formation of fuel and its penetration in the combustion chamber. By considering the application

of nanofuel in an IC engine, the relative stability of the nanofuel was compromised by 6 % at 7 hrs of stability, which is within the experimental deviation, and thus the oleic acid was selected as a surfactant for further studies.

Ceria concentration in diesel played an important role to reduce the concentration of toxic gases by influencing the complete combustion of the fuel in an IC engine, which is reflected in the performance of an IC engine, i.e. brake power (BP), brake specific fuel consumption (BSFC), brake thermal efficiency (BTE) and mechanical efficiency. In order to find the optimum concentration of CeO_2 in diesel, a nanofuel with oleic acid as a surfactant was synthesized at different concentrations such as 0.02, 0.04, 0.06, 0.08 and 0.1 wt. % of CeO_2 and tested in an IC engine.

Figure 4.45 shows the effect of concentration of CeO_2 in diesel and load on BTE of an IC engine. It was observed that the BTE was increased with loading. In an IC engine, the heat transfer process is mainly between the combustion chamber charge and the chamber wall. The temperature of the combustion chamber wall depends on the combustion deposit over it, which was influenced by the engine loading. Due to the reduction in temperature difference, the heat loss from the combustion charge to the cylinder wall was reduced with an increase of load. At 25 % loading, the temperature difference between the combustion charge and cylinder wall was comparatively higher than the other loading condition. Thus, the heat loss was the highest at no load condition, which was decreased with an increase of load. The trend of BTE of an engine against loading while using diesel and nanofuel was due to the reduced heat loss and increased brake power at higher loading in an IC engine, Ramadhas et al. [2005]. The BTE was observed to be high for nanofuels compared to that of diesel in all the loading condition and concentration of dispersed CeO_2 nanoparticles. The BTE was found to be increased with nanofuel having up to 0.06 wt. % of CeO_2 and then it was decreased. The nanofuel penetration depth was increased due to the improved momentum of nanofuel, which was also supported by Shafii et al. [2011]. If the fuel penetration reaches a zone, where the temperature of it is lower than the ignition temperature of fuel, it reduced the burning rate of fuel and increased the unburned and partially burned species. However, the under penetration of fuel resulted in poor air utilization leading to the formation of rich fuel mixture and incomplete combustion of fuel, which was also reported by Heywood [1988]. It was found that the BTE of 0.06 wt. % of CeO_2 nanofuel was high compared to all the test fuels. This might be due to fact that the under penetration and over

penetration were expected in the nanofuel having less than 0.06 wt. % and more than 0.06 wt. % of CeO_2, respectively. The optimum penetration depth was expected in 0.06 wt. % of nanofuel and thus the BTE was found to be high compared to the rest of the test fuel.

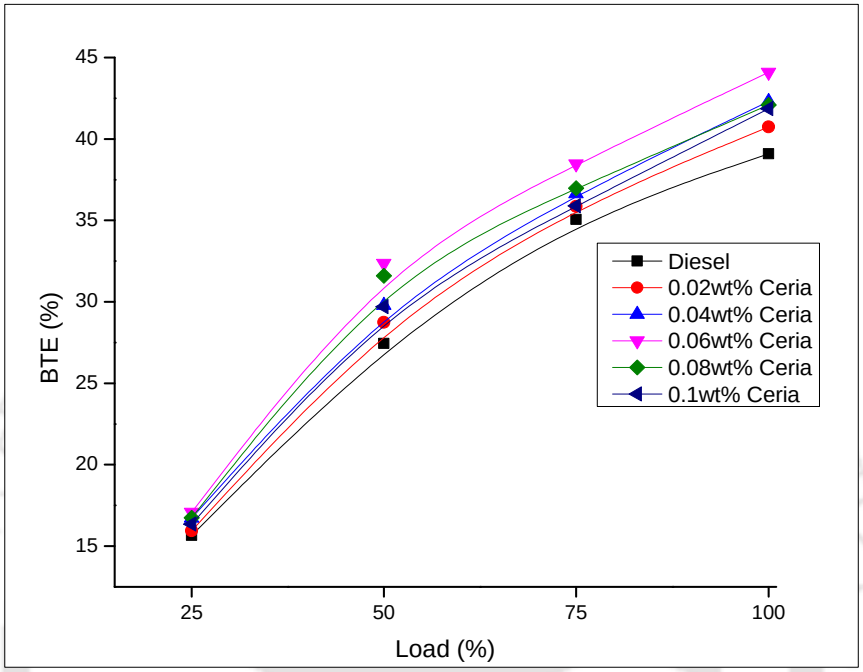

Figure 4.45 Effect of ceria concentration and load on BTE of an IC engine

Figure 4.46 shows the increase in brake thermal efficiency (BTE) of an engine against different concentrations of nanofuel usage compared to diesel and loading conditions. The BTE was observed to be increased in all types of nanofuels compared to diesel under all loading conditions. It was noticed that the maximum performance of an engine was observed at 50 % loading condition irrespective of the concentration of nanofuel. After 50 % loading condition, the trend was found to be decreased up to 75 % loading and then it was increased. It is noted that the maximum enhancement of BTE at 100 % loading was noted to be 13 %, which was less than that of the results observed at 50 % loading, i.e. 18 %. It was due to the fact that there was more rapid combustion at 50 % loading condition, which was also supported by Ajav et al. [1999]. The increase in BTE was observed to be high at 0.06 wt. % nanofuel irrespective of mechanical loading, where the enhancement of BTE was noted to be 9, 18, 10, and 13 % at 25, 50, 75 and 100 % loading, respectively. It is due to the optimum depth of fuel penetration at 0.06 wt. %, which reduced the problems of over and under penetration of fuel in the combustion chamber.

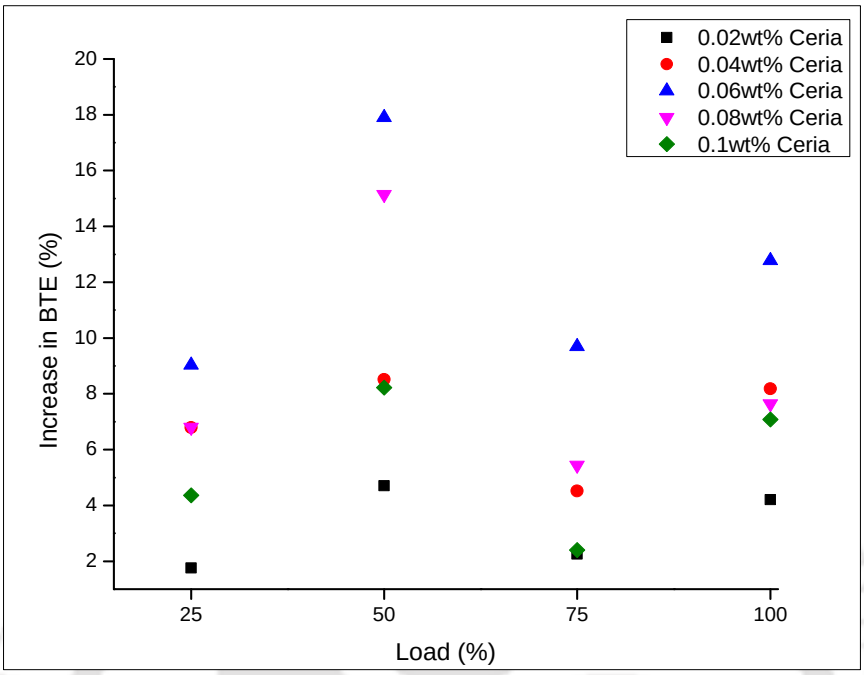

Figure 4.46 Increase in BTE while nanofuel usage compared to diesel in an IC engine at different concentration of CeO_2 nanoparticles

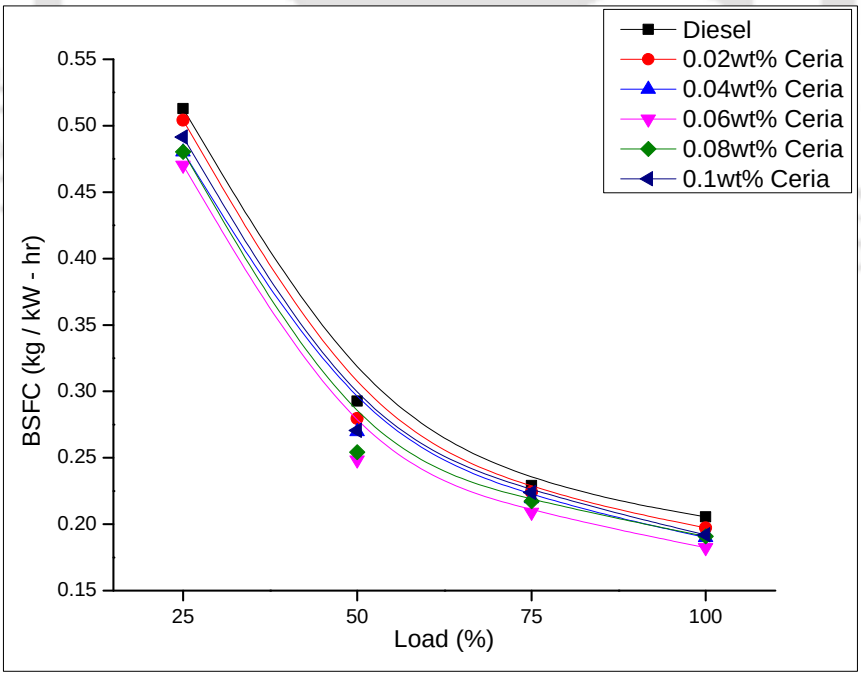

Figure 4.47 Effect of concentration of ceria nanoparticles on BSFC of an engine

Figure 4.47 shows the brake specific fuel consumption (BSFC) of nanofuel against different concentrations of CeO_2 and loading conditions. It was observed that the BSFC of an engine was decreased with an increase of load irrespective of type of fuel used. It was due to the fact that the fuel required to operate the engine was less than the increase of brake power due to relatively less portion of heat loss at higher loading conditions, Godiganur et al. [2010]. The BSFC of nanofuel was found to be significantly less compared to that of diesel in all concentrations of nanofuel and loads. It was due to that the CeO_2 promoted the fuel combustion by acting as a catalyst and the engine produced the required amount of power in order to maintain the speed by burning the less quantity of fuel, supported by Mandal et al. [2012]. The BSFC was found to be decreased with an increase of concentration till 0.06 wt. % and then it was started to increase, which was due to the under and over penetration of fuel. The nanofuel at 0.06 wt. % CeO_2 was found to have the lowest BSFC compared to all concentration tested in this study due to its optimum penetration depth of fuel.

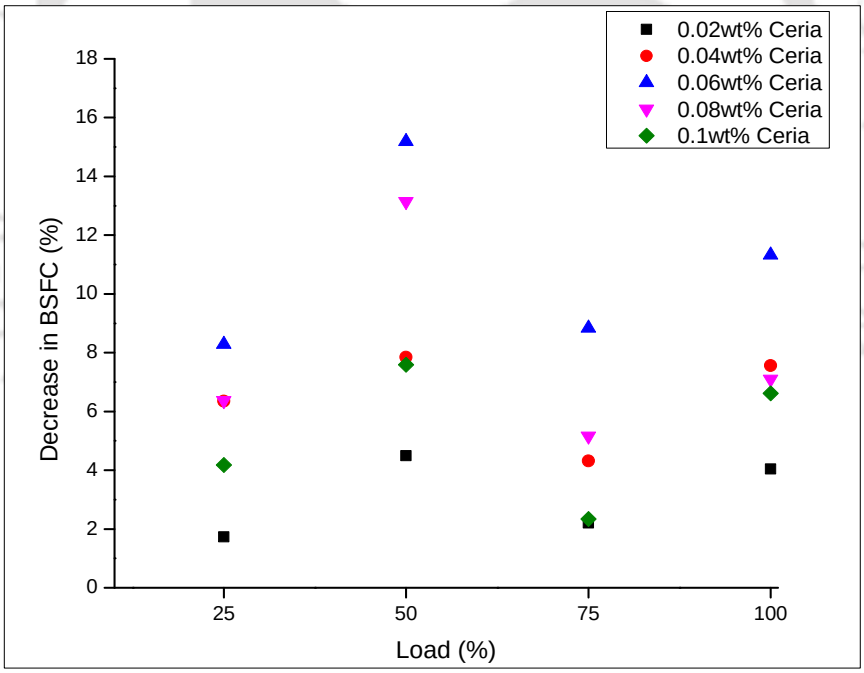

Figure 4.48 Decrease in BSFC compared to diesel with respect to CeO_2 concentration

Figure 4.48 shows the reduction of brake specific fuel consumption (BSFC) of nanofuel at different concentration of ceria and loading conditions. If the diesel system is replaced with nanofuel system, there was a reduction of BSFC irrespective of CeO_2 concentration. The oxygen stored in the ceria helped to have a complete combustion and encouraged for lower fuel

consumption. The maximum reduction of BSFC was observed to be 8.2, 15.1, 8.8 and 11.3 % at 25, 50, 75 and 100 % loading conditions, respectively, for 0.06 wt. % nanofuel compared to that of pure diesel. When nanofuel was used in the system, the BSFC was decreased by about 15.1 % at 50 % loading and the same was limited to only 11.3 % at full loading condition at 0.06 wt. % CeO_2 in diesel. Though the maximum reduction of BSFC was noted at 50 % loading condition for 0.06 wt. % CeO_2 in diesel, by considering the economic perspective, the maximum reduction of BSFC by 11.3 % was preferred. The increase in BSFC after 75 %, which was observed for all the CeO_2 concentration, was due to the rapid combustion in an engine, Ajav et al. [1999].

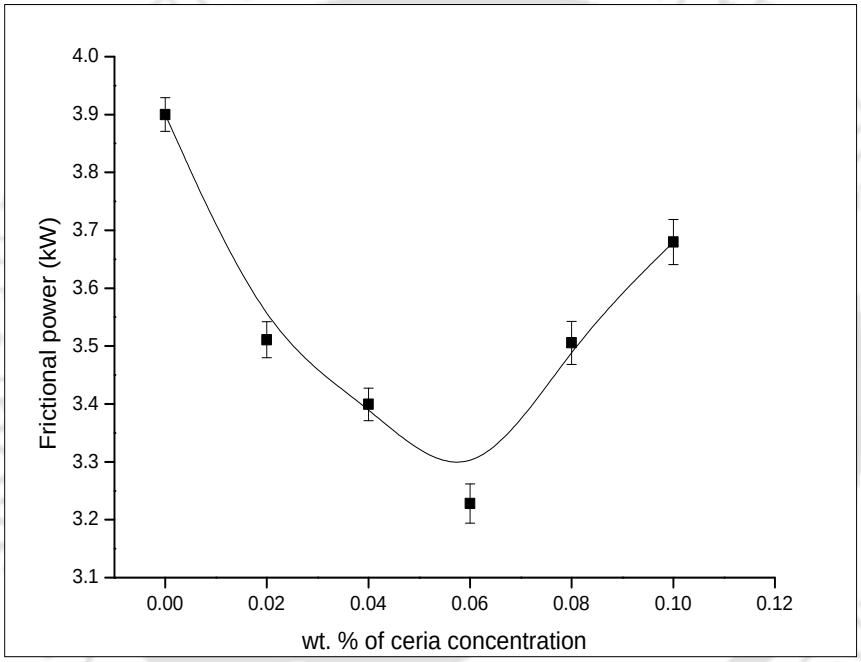

Figure 4.49 Effect of CeO_2 concentration on frictional power of an IC engine

Figure 4.49 shows the effect of CeO_2 concentration on frictional power of an engine, which was calculated by following the Willan's line method. It was observed that the frictional power was found to be decreased till 0.06 wt. % CeO_2 nanoparticles in diesel and then it was found to be increased. Since the friction power was less in case of nanofuel usage in all concentration compared to diesel, the nanoparticles in diesel acted as a solid lubricant and it reduced the friction between the contacting surfaces. It was due to the fact that the cerium oxide nanoparticles produced a layer between two contacting surfaces, which was also confirmed by Sharma et al. [2010]. As the higher nanoparticle concentration produced more pressure to adhere

the layer to sustain the abrasive contact between the surfaces, the frictional power was observed to be increased after 0.06 wt. % of CeO_2 in diesel.

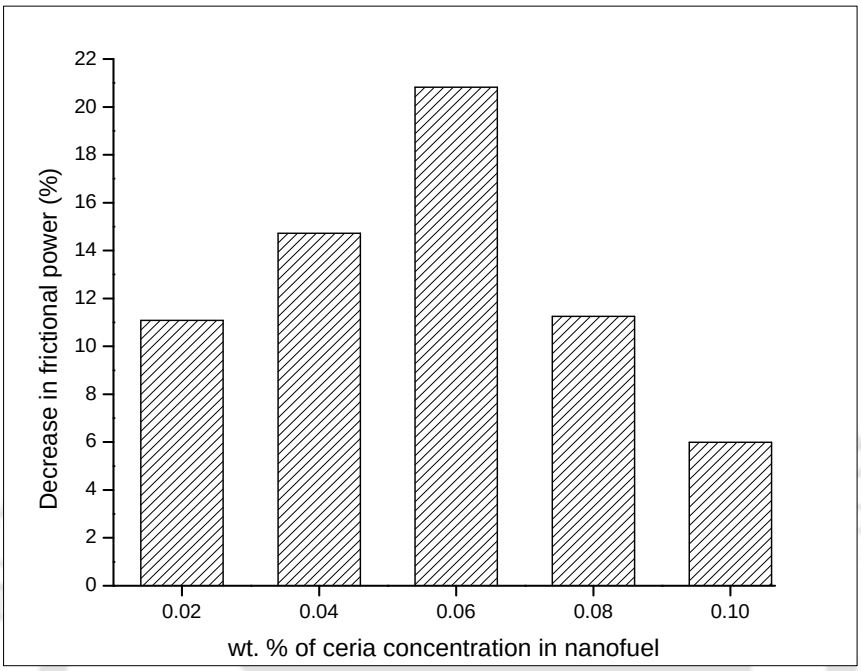

Figure 4.50 Decrease in frictional power of an engine with respect to diesel

Figure 4.50 shows the decrease in frictional power of an engine when nanofuel was used. It was calculated based on the diesel, which was observed to be increased till 0.06 wt. % CeO_2 nanoparticles in diesel and then it was found to be decreased. The high reduction of frictional power was observed in 0.06 wt. % loading of ceria nanoparticle in diesel.

Figure 4.51 shows the effect of ceria nanoparticle concentrations in diesel on mechanical efficiency of an engine against loading. It was observed that the mechanical efficiency of an engine was increased with loading irrespective of type of fuel used either diesel or nanofuel. Since the frictional power calculated through the Willian's line method was constant irrespective of loading, the mechanical efficiency was influenced by the brake power with respect to load. The increasing trend observed for the nanofuel and diesel was due to the generation of higher brake power against load. The mechanical efficiency was found to be high in case of ceria dispersed diesel in all the concentrations compared to that of diesel. It was due to that the nanoparticles in diesel acted as a solid lubricant and thus reducing the frictional power loss. The

nanofuel with 0.06 wt. % of ceria experienced high mechanical efficiency at all the loading conditions compared to any other nanofuel considered in the present study.

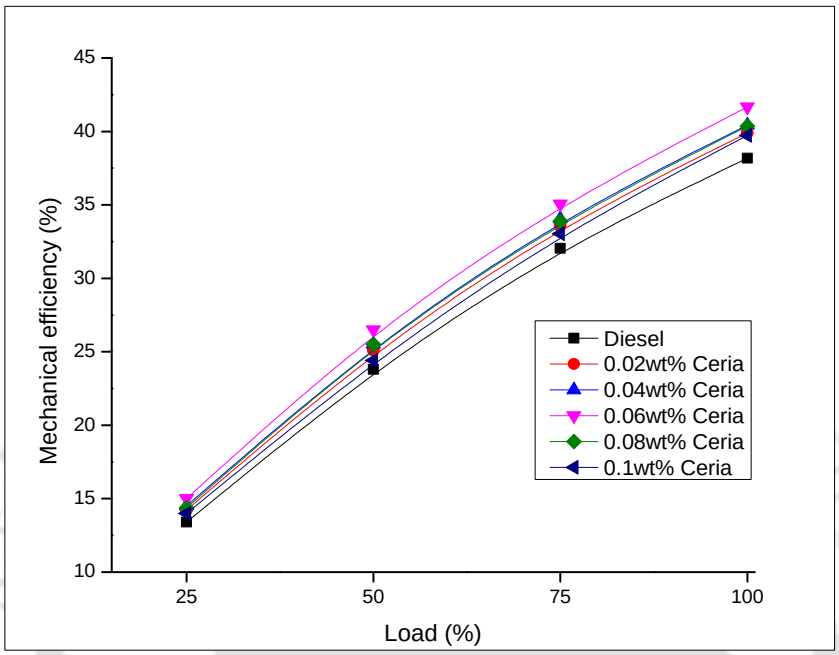

Figure 4.51 Effect of CeO_2 concentration on mechanical efficiency of an IC engine

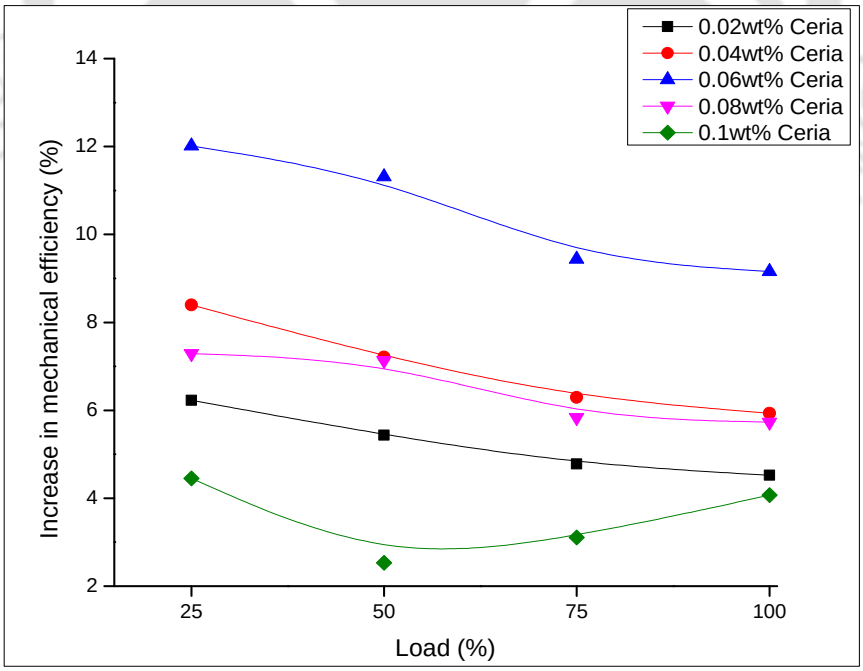

Figure 4.52 Increase in mechanical efficiency compared to diesel with respect to CeO_2 concentration

Figure 4.52 shows the increase in mechanical efficiency of nanofuel at different concentrations of CeO_2 compared to that of diesel. It was observed that the mechanical efficiency of an engine was found to be increased at all the loading conditions compared to diesel. Since the frictional power at 0.06 wt. % was found to be the minimum compared to the remaining concentration of nanofuel, the mechanical efficiency was found to be increased up to 0.06 wt. % and then it was decreased. The nanofuel containing 0.06 wt. % showed the maximum increase in mechanical efficiency, which was observed to be 12.0, 11.3, 9.4 and 9.2 % at 25, 50, 75 and 100 % load respectively, compared to pure diesel. It was due to the decrease in frictional power at 0.06 wt. % of CeO_2, as discussed above.

4.4 Studies on high OSC nanoparticles dispersed diesel

As the engine performance at 0.06 wt. % CeO_2 dispersed diesel was found to be the best, the relative stability studies and fuel characteristics were focused on 0.06 wt. % of nanoparticles dispersed diesel. The nanofuel with required concentration was prepared using the combination technique of tip sonication and magnetic stirring with oleic acid as a surfactant.

4.4.1 Studies on the dispersion stability of nanofuel

As the engine performance at 0.06 wt. % of CeO_2 based nanofuel was found to be superior compared to other types of concentration, further studies were focused on 0.06 wt. % of high OSC nanoparticles i.e. CZ3, CZA2, CZA3 and CZM2 dispersed diesel. In order to have a trend in the results, two more concentrations i.e. 0.05 and 0.07 wt. % in addition to 0.06 wt. % of respective nanoparticles were dispersed in diesel and their dispersion stability was studied up to 168 hrs. Figure 4.43(a-e) shows the relative stability of CeO_2, $Ce_{0.6}Zr_{0.4}O_2$ (CZ3), $Ce_{0.6}Zr_{0.2}Al_{0.26}O_2$ (CZA2), $Ce_{0.6}Zr_{0.1}Al_{0.39}O_2$ (CZA3) and $Ce_{0.6}Zr_{0.2}Mn_{0.2}O_2$ (CZM2) based nanofuel. It was observed from all type of nanofuel that the relative stability of 0.05 and 0.07 wt. % of nanoparticle dispersed diesel was found to have higher and lower stability than the 0.06 wt. % nanofuel, respectively. It was found that the dispersion stability of 0.06 wt. % of CeO_2, CZ3, CZA2, CZA3 and CZM2 based nanofuel was noted to be 87, 88, 88, 91 and 89 %, respectively at the end of 168 hrs.

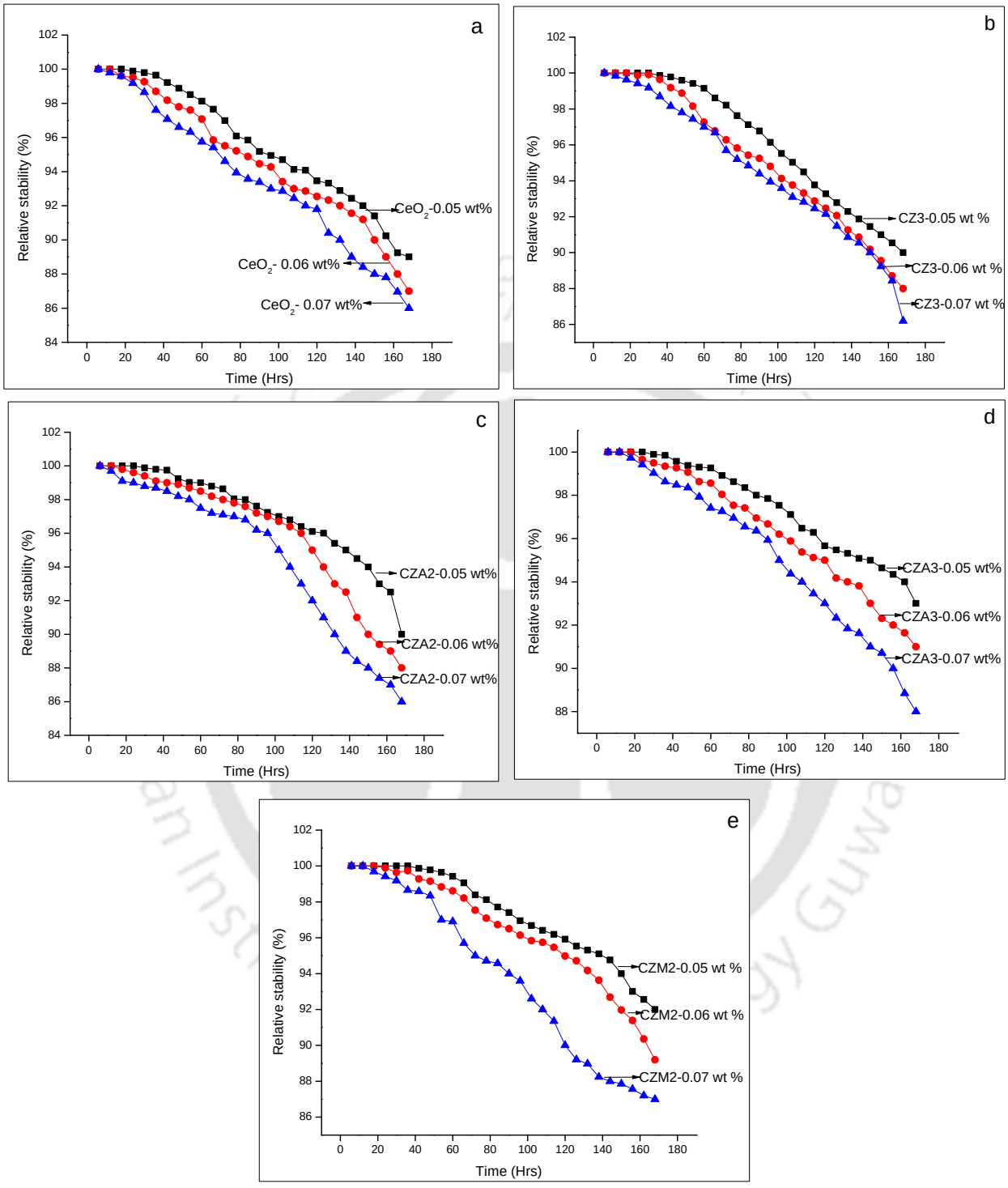

Figure 4.53 Relative stability studies on nanofuel based on (a) CeO_2, (b) $Ce_{0.6}Zr_{0.4}O_2$, (c) $Ce_{0.6}Zr_{0.2}Al_{0.26}O_2$, (d) $Ce_{0.6}Zr_{0.1}Al_{0.39}O_2$, (e) $Ce_{0.6}Zr_{0.2}Mn_{0.2}O_2$

The relative stability of CeO_2, CZ3, CZA2, CZA3 and CZM2 dispersed diesel after 40 hrs and 168 hrs is shown in Table 4.9. The sedimentation of nanoparticles irrespective of their type and size up to 40 hrs was found to be very less and then the sedimentation started to happen. Once the nanoparticles started to agglomerate, the gravitational force influenced to dominate leading to the settlement of nanoparticles quickly even at lower concentration. Since the stability of nanofuel was observed to be influenced by the particle size of nanoparticles, which was also supported by Gan et al. [2012], the stability of CeO_2 based nanofuel was found to be the lowest compared to that of rest of the nanofuel. The stability of CZA3 based nanofuel was observed to be the highest compared to rest of the nanofuels due to the size and density of CZA3 nanoparticles. It was proved from the above studies that the rate of sedimentation was influenced by the crystallite size and concentration of nanoparticles dispersed in diesel.

Table 4.9 One week relative stability studies on nanofuels

Type of nanoparticles dispersed in diesel	Crystallite size (nm)	Density (g/cc)	Relative stability of nanofuel (%)					
			0.05 wt. %		0.06 wt. %		0.07 wt. %	
			40 (hrs)	168 (hrs)	40 (hrs)	168 (hrs)	40 (hrs)	168 (hrs)
CeO_2	25	7.2	99	89	98	87	97	86
$Ce_{0.6}Zr_{0.4}O_2$ (CZ3)	7.8	6.77	99.7	90	99	88	98	86
$Ce_{0.6}Zr_{0.2}Al_{0.26}O_2$ (CZA2)	4.7	6.19	99.7	90	99	88	98.5	86
$Ce_{0.6}Zr_{0.1}Al_{0.39}O_2$ (CZA3)	2.6	5.96	99.5	93	99.2	91	98.4	88
$Ce_{0.6}Zr_{0.2}Mn_{0.2}O_2$ (CZM2)	2.7	6.10	99.8	92	99.2	89	98.6	87

Figure 4.54 shows the relative stability of CeO_2, CZ3, CZA2, CZA3 and CZM2 dispersed diesel having the concentration of 0.05, 0.06 and 0.07 wt. % after 40 and 168 hrs. It was observed that the relative stability of 0.05 wt. % nanofuel was found to be the highest compared to the remaining nanofuel after 40 hrs. In all the concentrations, the stability of CeO_2 type nanofuel was found to be the lowest compared to the remaining nanofuel.

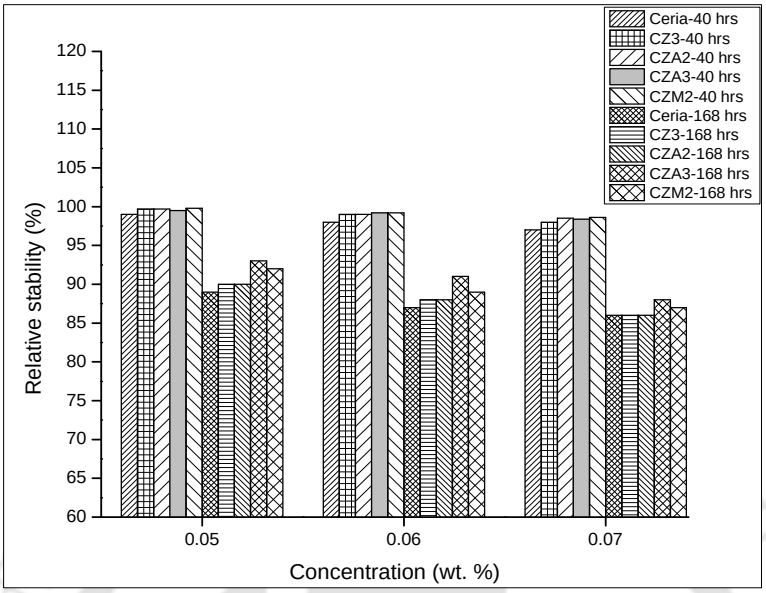

Figure 4.54 Effect of concentration and duration on relative stability of high OSC nanoparticle dispersed diesel

4.4.2 Characterization of nanofuel

The high OSC nanoparticles such as CeO_2, $Ce_{0.6}Zr_{0.4}O_2$ (CZ3), $Ce_{0.6}Zr_{0.2}Al_{0.26}O_2$ (CZA2), $Ce_{0.6}Zr_{0.1}Al_{0.39}O_2$ (CZA3) and $Ce_{0.6}Zr_{0.2}Mn_{0.2}O_2$ (CZM2) were dispersed in diesel at different concentrations such as 0.05, 0.06 and 0.07 wt. % with oleic acid as a surfactant and then the fuel characteristics such as surface tension, flash point and fire point temperature, thermal conductivity and viscosity were studied at room temperature and reported.

Figure 4.55 shows the surface tension of different types and concentration of nanoparticles dispersed diesel. It was observed that the surface tension of nanofuel was not varied significantly irrespective of the type of nanoparticles and their concentration. When the concentration of nanoparticles was increased from 0.05 to 0.07 wt. %, the surface tension of nanofuel was found to be increased within 4 %. Since the nanofuel was a heterogeneous mixture of nanoparticles dispersed in fuel, an increase of surface tension of nanofuel might be due to the homogenous presence of nanoparticles in the fuel. Though the addition of nanoparticles in diesel increased its surface tension, as reported by Moosavi et al. [2010], the steric stabilization of surfactant reduced the surface energy at the liquid-air interface leading to the reduction of surface tension of nanofuel, which was increased due to the addition of nanoparticles, and it is also supported by Tanvir et al. [2012]. As the long-chain nonionic oleic acid surfactant molecules attached on the

solid particles, they form a layer between the particles and the surrounding fluid molecules. Such layers increased the potential between particles and impart a repulsive force between them. This in turn caused a reduction in surface tension upon addition of surfactant, which was also documented by Khaleduzzaman et al. [2013]. However, the enhancement observed for the surface tension of diesel against dispersion of nanoparticles and their concentration was found to be within the limit of experimental deviation. Thus, it is suggested that the effect of adding nanoparticles on the surface tension of diesel was negligible, i.e. the atomization of diesel is not expected to be influenced with an addition of nanoparticles.

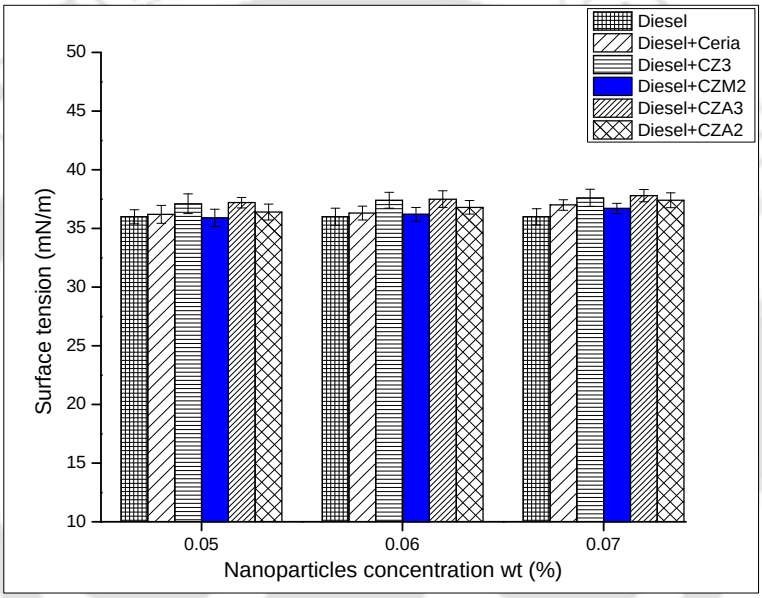

Figure 4.55 Effect of high OSC nanoparticles on the surface tension of diesel

As the flash point and fire point temperature of the fuel show the indication of its volatility, the influence of different types of nanoparticles and their concentration was studied and reported. Higher flash point temperature of nanofuel is preferred for safe handling of the fuel. The flash point and fire point temperature of nanofuel against the particle concentration with different nanofuel are shown in Figure 4.56 and 4.57, respectively. It is noted that both flash point and fire point temperature of diesel were found to be increased within 9 % irrespective of type of nanoparticles and their concentration, which was also observed by Prabu et al. [2012]. It was due to the increase in flammability and combustibility of fuel with the addition of nanoparticles, which was also supported by Karthik et al. [2013]. Thus, the fuel dispersed with cerium oxide based nanoparticles is inherently safer to handle than the base fuel. As the flash point and fire

point temperature of diesel obtained from different commercial outlets were observed to be varied within the experimental variation, the enhancement observed in case of nanofuel falls within the limit. The handling requirement of the nanofuel is same as that of diesel and the combustion behavior of the nanofuel in connection with above is also not expected to be influenced compared to that of pure diesel.

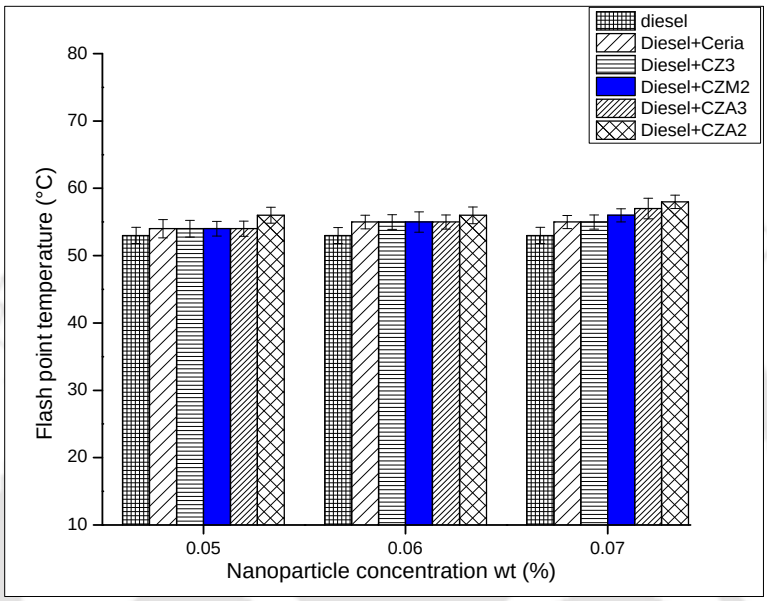

Figure 4.56 Effect of high OSC nanoparticles on the flash point temperature of diesel

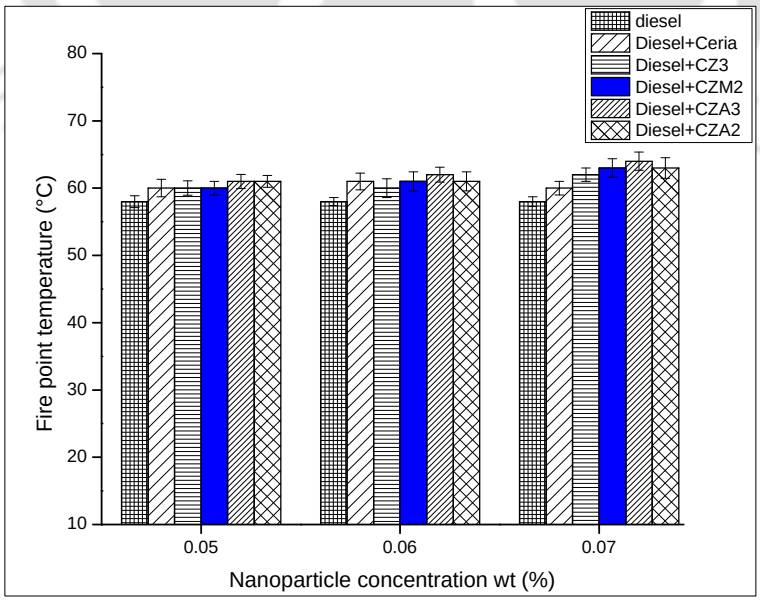

Figure 4.57 Effect of high OSC nanoparticles on the fire point temperature of diesel

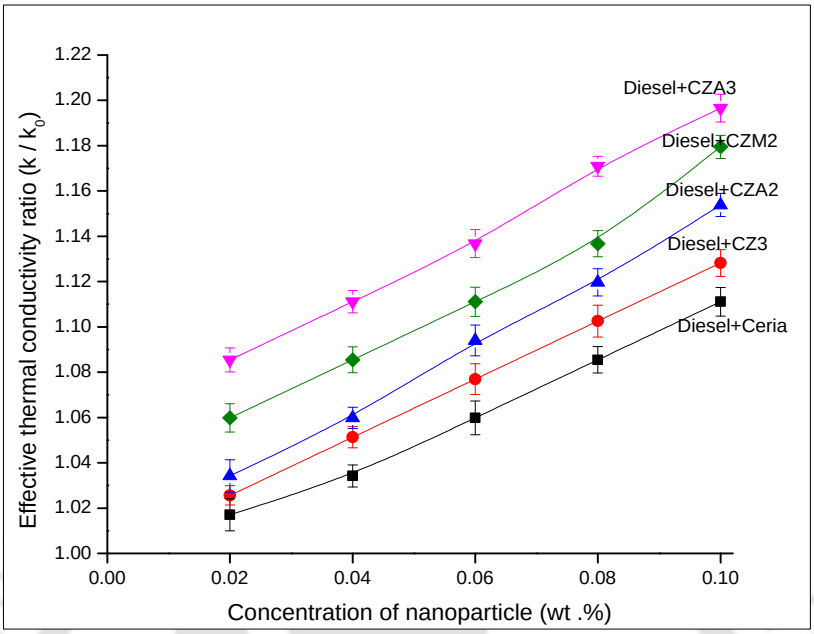

Figure 4.58 Effective thermal conductivity of nanofuel having different concentration of nanoparticles

Figure 4.58 shows the effective thermal conductivity of nanofuel having different concentrations of nanoparticles at room temperature. It is observed that the effective thermal conductivity of nanofuel was increased with concentration of high OSC nanoparticles and it is observed to be maximum at 0.1 wt. % nanoparticles, in this study. The increase in thermal conductivity of nanofuel was due to large specific surface area and enhanced specific heat capacity of nanocrystalline materials, as stated by Xuan et al. [2000]. The increase in thermal conductivity not only depends on the concentration of nanoparticles dispersed in diesel, but it also depends on the size and shape of the nanoparticles and temperature of nanofuel. Since the shape of nanoparticles and temperature of nanofuel are the constant factors for specific applications, the effective thermal conductivity of nanofuel depends on the concentration and size of the nanoparticles dispersed in diesel. Brownian motion of the nanoparticles in fluid is responsible for transporting energy through collision between the nanoparticles or liquid convection, which enhanced the transport of thermal energy causing the increase of thermal conductivity of nanofuel. The higher enhancement of effective thermal conductivity of nanofuel was expected to increase the heat transfer capability, Das et al. [2003b]. It is observed from Figure 4.58 that the rate of increase of thermal conductivity was found to be linear with respect to concentration and the slope of the curve was observed to be in the range 1.18 to 1.27, 1.30 to 1.28, 1.61 to 1.65,

1.31 to 1.49 and 1.25 to 1.97 for CeO_2, CZ3, CZA2, CZA3 and CZM2 based nanofuel, respectively. It was also observed that the effective thermal conductivity of CZA3 dispersed nanofuel was high compared to that of the remaining nanofuel, which is due to its lowest crystallite size of 2.6 nm, compared to the average crystallite size of CeO_2, CZ3, CZA2 and CZM2, and their respective values were 25, 7.8, 4.7 and 2.7 nm. Though the CZM2 crystallite size was approximately the same as CZA3, the high enhancement of effective thermal conductivity in CZA3 was due the presence of lower ionic radius of Al^{3+} in CZA3, which was also supported by Tada et al. [2010], where it was reported that the thermal conductivity of lower ionic radius element was higher compared to the higher ionic radius element. In case of CZA2, the particle size effect on thermal conductivity dominated the ionic radius effect leading to less effective thermal conductivity in comparison to that of CZA3.

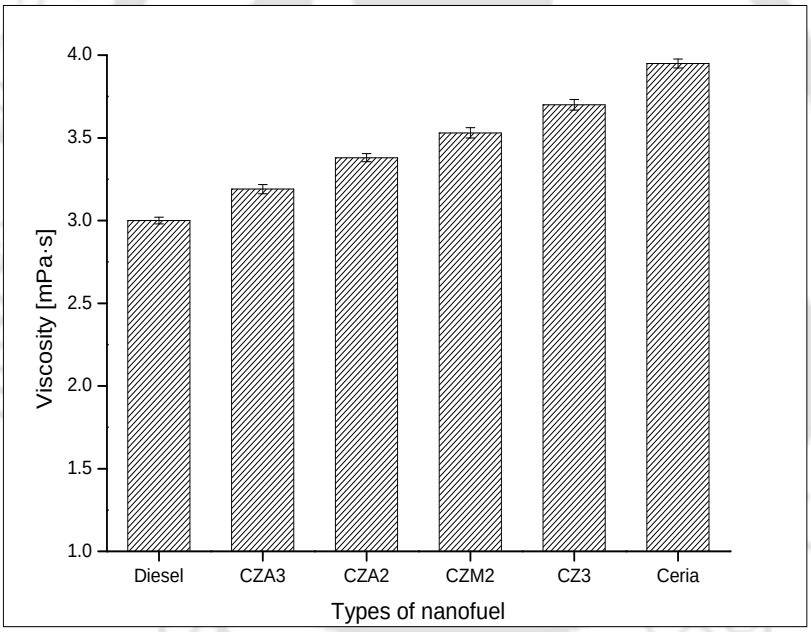

Figure 4.59 Effect of 0.06 wt. % OSC nanoparticles on viscosity of nanofuel at room temperature

Figure 4.59 shows the effect of 0.06 wt. % high OSC nanoparticles dispersed diesel on its viscosity at room temperature. The viscosity of nanofuel was observed to be high compared to that of diesel, which was also observed by Keblinski et al. [2005]. The addition of nanoparticles in the fuel increased the resistance between the fluid layers and hence increased the viscosity. The viscosity of CZA3 dispersed diesel was found to be less compared to that of CeO_2, CZ3,

CZA2 and CZM2 dispersed diesel, which is due less crystallite size of CZA3 compared to the rest of the nanoparticles. The increase in viscosity due to the nanoparticles dispersion in diesel was found to be in the range of 6.6 to 33.3 % in this study. As the change in viscosity of nanofuel was observed to be within the acceptable range of experimental variation in case of CeO_2, CZ3, CZA2, CZA3 and CZM2, the fuel injection pattern of those nanofuel in combustion chamber is expected to be the same.

4.5 Engine performance with high OSC nanoparticle (0.06 wt. %) dispersed diesel (Nanofuel) and emission studies

In order to find the influence of OSC of the nanoparticles, which were dispersed in diesel, the engine performance and emission analysis were studied. The engine performance parameters considered here are the brake specific fuel consumption (BSFC), brake thermal efficiency (BTE) and mechanical efficiency. During the performance studies at different loading condition, carbon monoxide (CO), hydrocarbon, oxides of nitrogen (NO_x) and carbon dioxide (CO_2) were measured. The nanofuel was prepared by dispersing high OSC nanoparticles such as CZA2, CZA3, CZM2 in diesel. CeO_2 and CZ3 based nanofuel was also considered for the comparison purpose.

4.5.1 Engine performance studies

Figure 4.60 shows the effect of high OSC nanoparticles dispersed diesel on brake specific fuel consumption (BSFC) of an engine against different loading conditions. It is noted that the BSFC was observed to be decreased exponentially for nanofuel and diesel up to 50 % loading condition. In the range of 50 to 100 % load, the decrease in BSFC was significantly less compared to 25 to 50 % loading condition. The mass of fuel required to operate the engine and brake power developed by the engine were increased with load. However, the BSFC was found to be decreased with an increase of load in both cases of diesel and nanofuel. The main reason was that the fuel required to operate the engine after its normalized condition was less than the brake power developed during the loading condition. Since the heat loss due to heat transfer between the combustion gas mixture to cylinder wall was found to be less during the higher loading conditions, the reduction in BSFC was found to be very less in the range of 50 to 100 % loading condition. The highest reduction of BSFC was found in case of CZA2 dispersed diesel compared to all types of nanofuel tested in this study, which was clearly indicated through the

inset of Figure 4.60. It is due to the fact that the complete combustion of nanofuel having the highest OSC nanoparticles was occurred leading to the reduced requirement of mass of the fuel used to run the engine to produce the same brake power. As the increase in oxygen concentration of the fuel was expected to reduce the ignition delay in the engine, as reported by Heywood [1988], it led to complete combustion of the fuel and reduced BSFC.

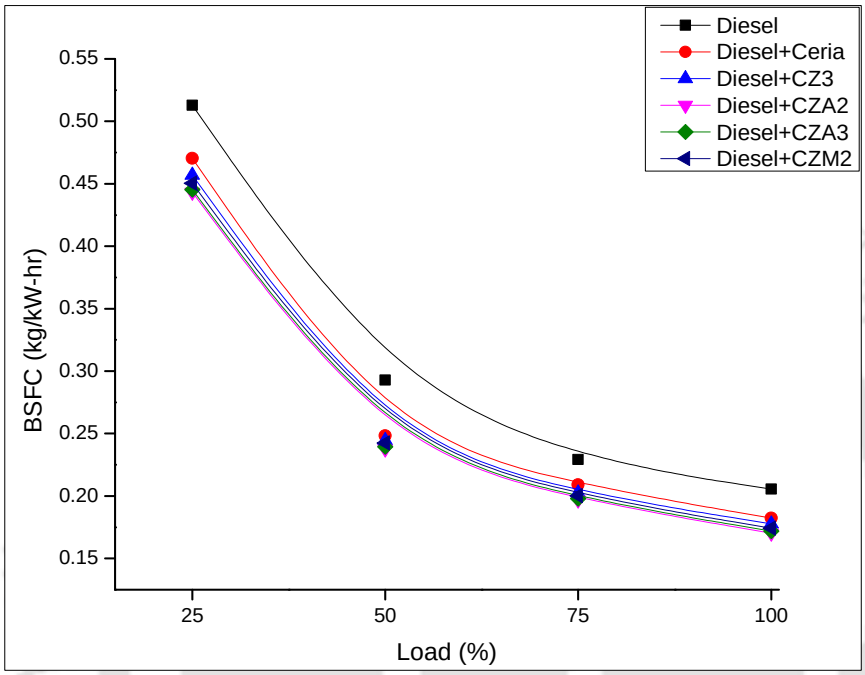

Figure 4.60 Effect of high OSC nanoparticles in diesel at 0.06 wt. % on BSFC

Figure 4.61 shows the effect of OSC nanoparticles dispersed diesel at 0.06 wt. % on decrease of the BSFC of an engine with respect to diesel against different loading conditions. The reduction of BSFC of nanofuel was observed to be high at 50 % loading condition compared to rest of the loads, where the BSFC was found to be decreased by 15.2, 16.5, 18.8, 18.2 and 17.2 % in case of CeO_2, CZ3, CZA2, CZA3 and CZM2 dispersed diesel, respectively, compared to diesel. Highest reduction was observed in CZA2 dispersed nanofuel, which was found to be 13.6, 18.8, 14.2 and 17.1 % in 25, 50, 75 and 100 % loading condition. The decrease in BSFC can be due to the positive effects of nanoparticles on physical properties, which was denoted as oxygen content of nanoparticle dispersed fuel and also the reduction of ignition delay, Tyagi et al.[2008], which might be helpful to have the complete combustion of nanofuel, Pivkina et al. [2004]. In addition, it can be due to the effects of nanoparticles on fuel propagation in the

combustion chamber. On the other hand, the nanoparticles dispersed diesel increased the mixture momentum and, consequently, the penetration depth in the cylinder, Kao et al. [2008], where indepth penetration increased the contact with air inside the combustion chamber. As a result, the combustion was improved, which was also observed by Shaffi et al. [2011]. Though BSFC was found to be decreased by 17.1 % in case of 100 % loading, the same was observed to be 18.8 % at 50 % loading. Based on the economical and industrial point of view, an engine is preferred to be run at 100 % loading and / or over loading up to certain extent when the engine is operated with nanofuel having 0.06 wt. % of CZA2 nanoparticles.

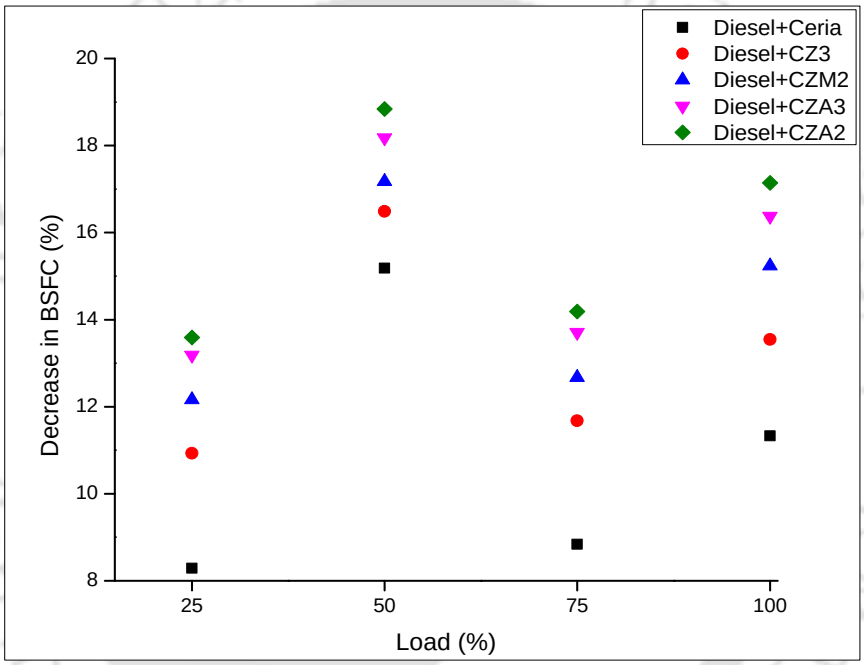

Figure 4.61 Decrease in BSFC of an engine using 0.06 wt. % nanofuel with respect to diesel

Figure 4.62 shows the brake thermal efficiency (BTE) of a diesel engine with respect to different loading conditions and types of nanoparticles at 0.06 wt. %. It is observed that the BTE of an engine was increased with load for all type of fuel, including the nanofuel and diesel. It was due to the reduction of heat loss and increase of power with an increase of load. It was observed that the BTE of nanofuel was higher than the diesel in all the loading conditions. It was due to the decrease in ignition delay for high OSC nanoparticle dispersed diesel. Since the ignition delay was decreased with respect to the oxygen concentration in diesel, the same was expected in CZA2 compared to any other nanofuel due to its high OSC. As the reduced ignition delay in the

CZA2 dispersed diesel was expected to burn completely, it led to complete combustion in high OSC dispersed diesel leading to have increased BTE.

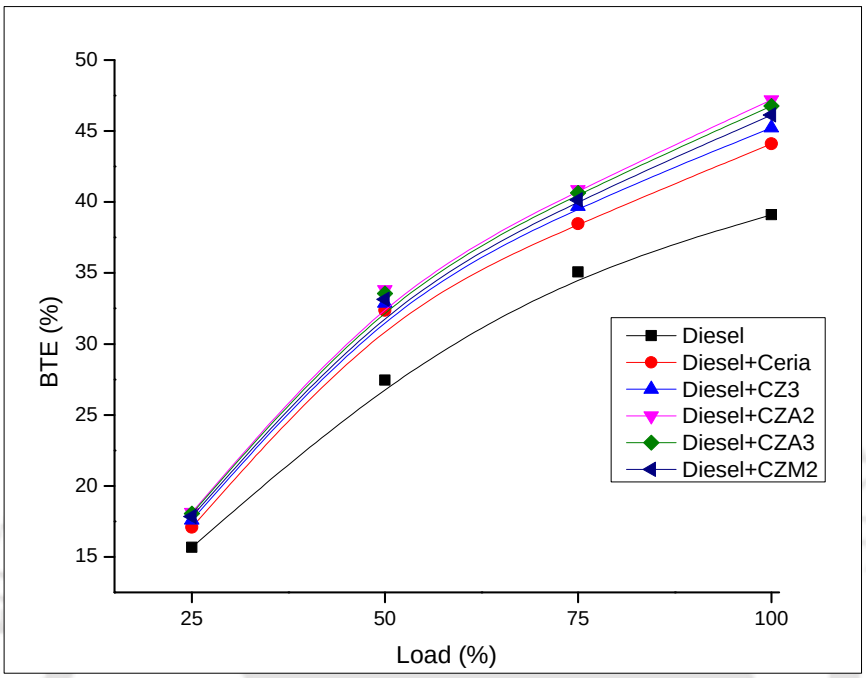

Figure 4.62 Effect of high OSC nanoparticles in diesel at 0.06 wt. % on BTE of an engine

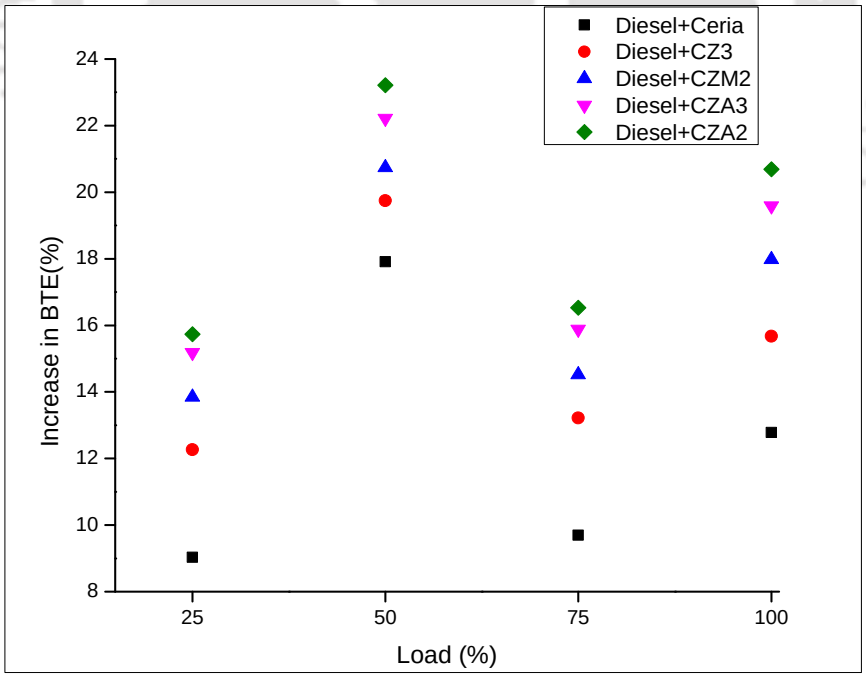

Figure 4.63 Increase in BTE of an engine using 0.06 wt. % nanofuel with respect to diesel

Figure 4.63 shows the increase in BTE of an engine with respect to diesel at different loading conditions, where a positive trend was observed in all loads. The maximum increase of BTE was found to be 17.9, 19.8, 23.2, 22.2 and 20.7 % for CeO_2, CZ3, CZA2, CAZ3 and CZM2 based nanofuel, respectively, at 50 % loading condition in comparison to that of diesel. The BTE of an engine was increased when nanofuel was used compared to diesel which was due to the increase in burning process of combustion. The increase in BTE of nanofuel was due to the overall heat transfer characteristics of the combustion gases produced by the nanofuel, which were significantly better than those of normal diesel. The maximum increase in BTE of CZA2 based nanofuel was observed in all the loads compared to other nanofuel, which was due to the dispersion of highest OSC nanoparticles in diesel compared to rest of the nanoparticles. Based on the economic consideration, it is recommended to operate an engine at 100 % loading though the efficiency difference at 50 % and 100 % loading was noted to be only 3 %.

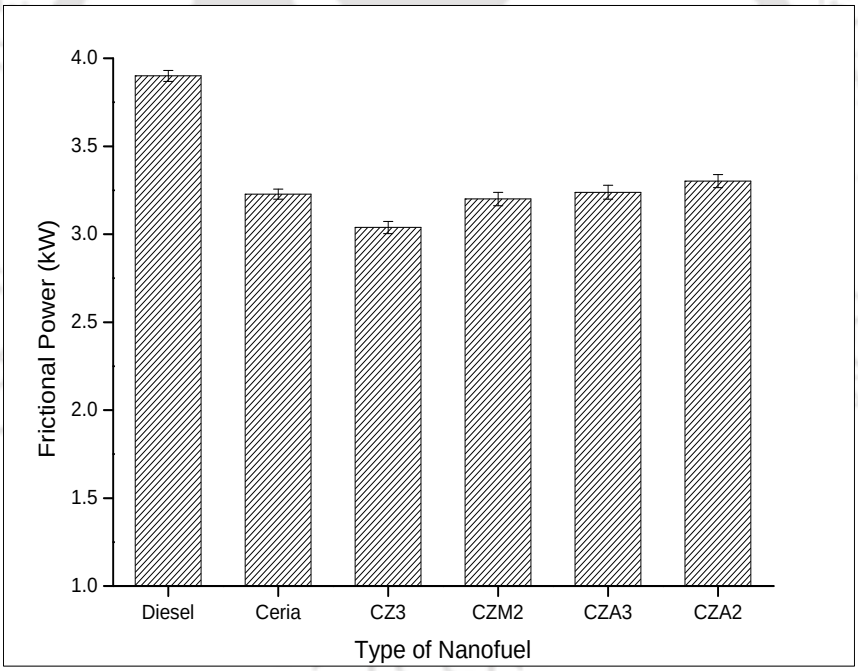

Figure 4.64 Effect of high OSC nanoparticles in diesel at 0.06 wt. % on frictional power of an engine

Figure 4.64 shows the effect of high OSC nanoparticles in diesel on frictional power of an engine and it was calculated using the Willian's line method. The frictional power of an engine was found to be less for all type of nanofuel compared to diesel. The decrease in frictional power of an engine with nanofuel proved that the nanoparticles in diesel acted as a solid lubricant. The

decrease in frictional power with respect to diesel was noted to be 17.2, 22.1, 17.9, 16.9 and 15.3 % for CeO_2, CZ3, CZM2, CZA3 and CZA2 based nanofuel, respectively. It was found that the frictional power of CZ3 based nanofuel was found to be the lowest compared to that of remaining nanofuel taken in the present study.

Figure 4.65 shows the effect of high OSC nanoparticles dispersed diesel on mechanical efficiency of an engine with respect to different types of high OSC nanoparticles and loading conditions. It was observed that the mechanical efficiency of an engine was increased with loading conditions. It was due to the increase in power generated by the engine against load. An increase of mechanical efficiency was observed when nanofuel was used compared to diesel. It was due to decrease in frictional power, when nanofuel was used. The mechanical efficiency of CZ3 nanoparticles dispersed diesel was found to be higher compared to that of rest of the nanofuel tested in this study, as the CZ3 based nanofuel showed the lowest frictional power.

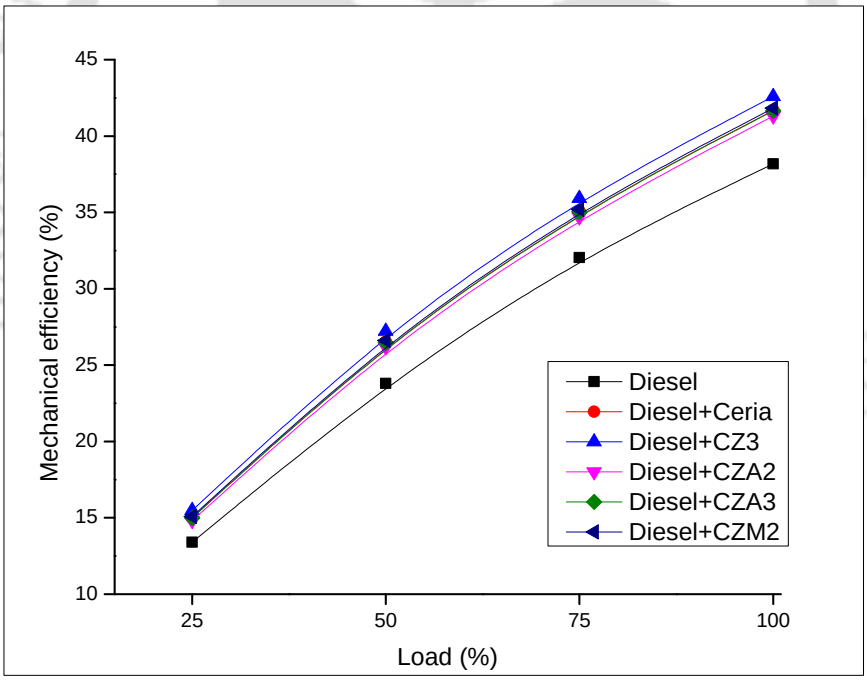

Figure 4.65 Effect of high OSC nanoparticles in diesel at 0.06 wt. % on mechanical efficiency of an engine

Figure 4.66 shows the effect of high OSC nanoparticle dispersed diesel at 0.06 wt. % on increase of mechanical efficiency of an engine with respect to diesel at different loading conditions. It was observed that the mechanical efficiency of an engine was found to be increased by 12.0,

15.6, 10.6, 11.9 and 12.6 % for CeO_2, CZ3, CZA2, CZA3 and CZM2, respectively, dispersed diesel at 25 % loading condition. Since the mechanical efficiency of an engine was influenced by the frictional power, the maximum increase in mechanical efficiency of an engine at 100 % loading was noted to be 11.6 % for CZ3 based nanofuel. Though the frictional power for CZ3 was found to be less leading to increase the mechanical efficiency, the brake thermal efficiency and BSFC of CZ3 based nanofuel were inferior to that of CZA2.

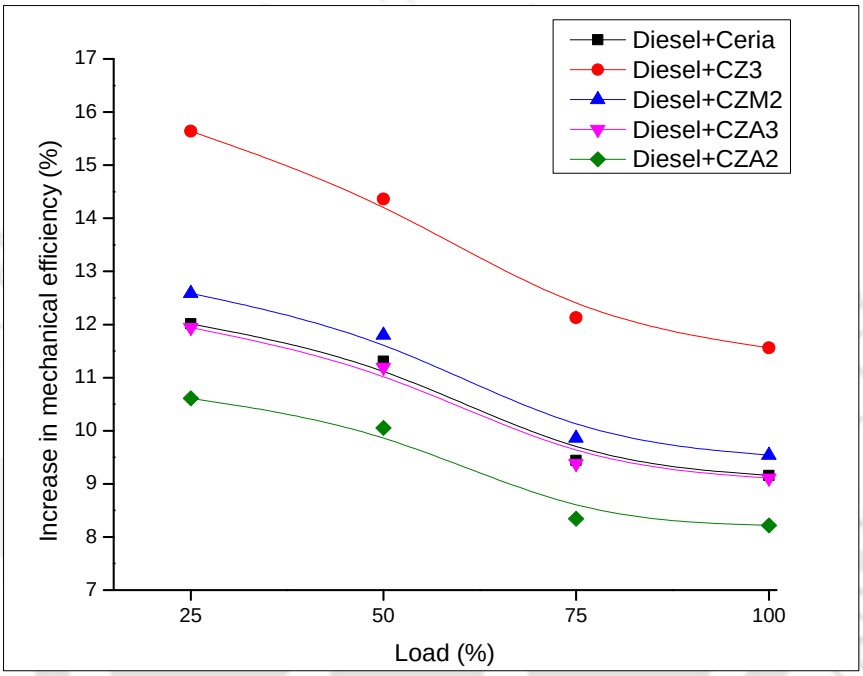

Figure 4.66 Increase in mechanical efficiency of an engine using 0.06 wt. % nanofuel with respect to diesel

Table 4.10 gives the comprehensive data on the performance parameters and their changes in an engine with respect to diesel using high OSC nanoparticles at 0.06 wt. %, where the influence of different types of nanoparticles against loading was reported.

Table 4.10 Engine performance parameters of an engine and their changes with respect to diesel using high OSC nanoparticles at 0.06 wt. %

		Level			% change		
		BTE (%)	BSFC (kg/kW-hr)	Mechanical efficiency (%)	BTE	BSFC	Mechanical efficiency
Diesel	25	15.7	0.51	13.4	-	-	-
	50	27.5	0.29	23.8	-	-	-
	75	35.1	0.23	32.0	-	-	-
	100	39.1	0.21	38.2	-	-	-
CeO_2 dispersed Diesel	25	17.1	0.47	15.0	9.0	8.3	12.0
	50	32.4	0.25	26.5	17.9	15.2	11.3
	75	38.5	0.21	35.1	9.7	8.9	9.4
	100	44.1	0.18	41.7	12.8	11.3	9.2
CZ3 dispersed Diesel	25	17.6	0.46	15.5	12.3	10.9	15.6
	50	32.9	0.24	27.2	19.8	16.5	14.4
	75	39.7	0.20	35.9	13.2	11.7	12.1
	100	45.2	0.18	42.6	15.7	13.6	11.6
CZM2 dispersed Diesel	25	17.8	0.45	15.1	13.9	12.2	12.6
	50	33.1	0.24	26.6	20.7	17.2	11.8
	75	40.2	0.20	35.2	14.5	12.7	9.9
	100	46.1	0.17	41.8	18.0	15.2	9.5
CZA3 dispersed Diesel	25	18.1	0.45	15.0	15.2	13.2	11.9
	50	33.6	0.24	26.5	22.2	18.2	11.2
	75	40.6	0.20	35.0	15.9	13.7	9.4
	100	46.8	0.17	41.7	19.6	16.4	9.1
CZA2 dispersed Diesel	25	18.1	0.44	14.8	15.7	13.6	10.6
	50	33.9	0.24	26.2	23.2	18.8	10.1
	75	40.9	0.20	34.7	16.5	14.2	8.3
	100	47.2	0.17	41.3	20.7	17.1	8.2

4.5.2 Exhaust gas analysis using high OSC nanoparticles (0.06 wt. %) dispersed diesel (Nanofuel)

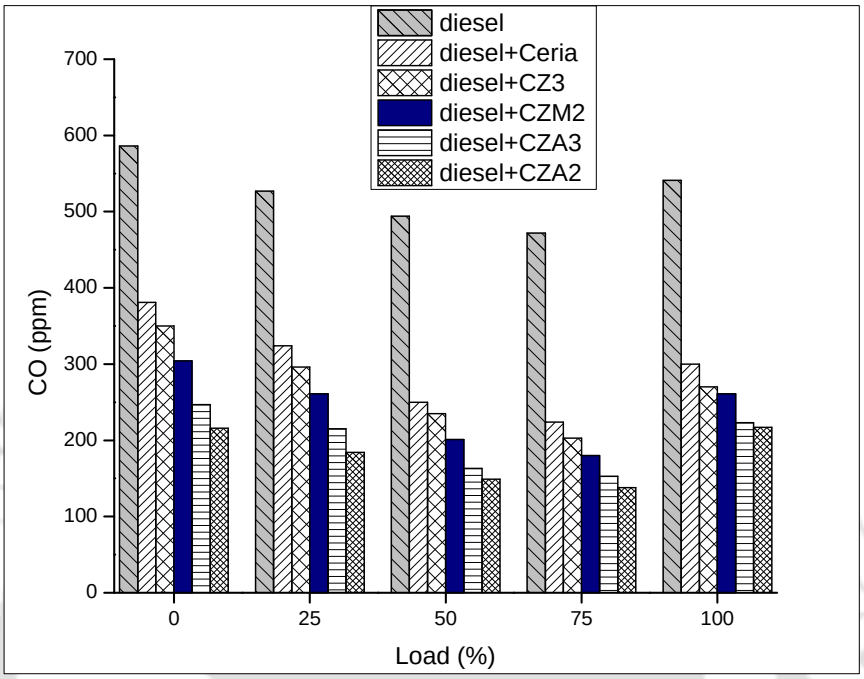

Figure 4.67 Effect of nanoparticles in diesel at 0.06 wt. % on CO emission

Figure 4.67 shows the CO emission using high OSC nanoparticles such as CeO_2, CZ3, CZA2, CZA3 and CZM2 dispersed diesel. It was found that the CO emission was observed to be decreased with an increase of loading conditions and after reaching its lowest value at 75 % loading, CO emission was increased again for the diesel and nanofuel. In all cases irrespective of load and fuel, the highest concentration of CO was observed at no load condition, where the rich fuel mixture was used in order to get the required combustion temperature and pressure. As the temperature inside the cylinder was increased with load, it resulted the reduction of CO emission up to 75 % loading condition and then it was increased. The CO emission was reduced from 586 to 472 ppm and 216 to 138 ppm for diesel and CZA2 based nanofuel, respectively at 75 % loading condition. The reason is as follows: the diesel engine is quality governed engines. The quantity of air supplied for each cycle irrespective of load on the engine is nearly constant. With an increase of load, the amount of fuel injected into the engine is increased while maintaining the constant supply of air. Thus, a lean fuel mixture is available at lower loading condition and rich fuel mixture is available at higher loading condition. It will result in increased CO emission

at higher loads. It was observed from the results that a significant reduction of CO was observed when the engine was operated using the nanofuel. The cerium based nanoparticles were acted as a chemically active component and it worked as an oxygen storage device by releasing the O_2 in the presence of reduced gas environment of CO and converting into CO_2 leading to the reduction of the concentration of CO.

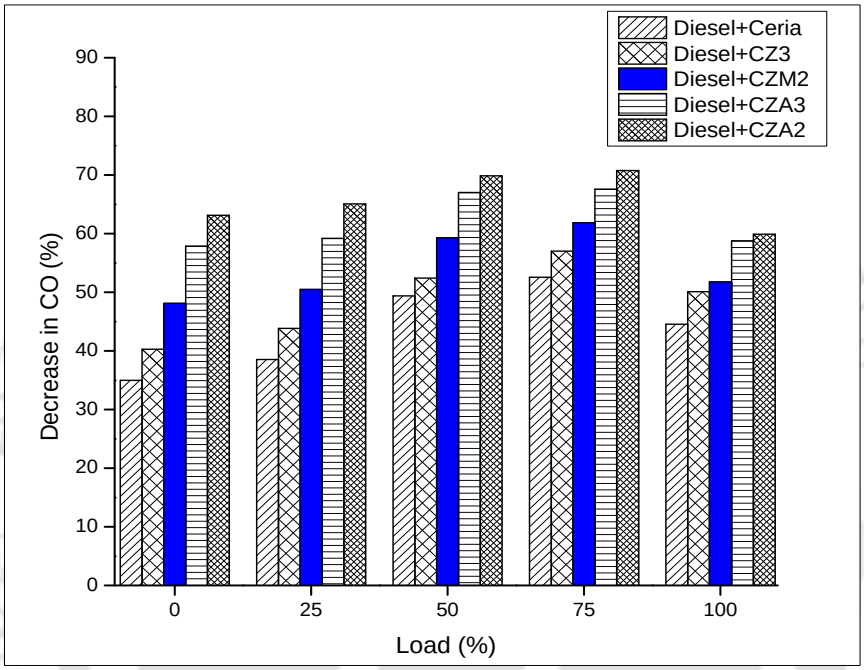

Figure 4.68 Decrease in CO emission with different types of nanofuel at 0.06 wt. % in comparison with diesel

Figure 4.68 shows the decrease in CO emission compared to diesel using high OSC nanoparticles CeO_2, CZ3, CZA2, CZA3 and CZM2 dispersed diesel against different loading conditions. It was observed that the decrease of CO concentration at no load condition was the lowest. However, the reduction of CO was increased with loading pattern and it reached the maximum reduction at 75 % loading condition. The same was noted to be 53, 57, 62, 68 and 71 % for CeO_2, CZ3, CZM2, CZA3 and CZA2 based nanofuel, respectively. At 100 % load, the decrease in CO was found to be less than that of 75 % load. The trend observed for all types of nanofuel against the reduction of CO was followed the same as that of the OSC of nanoparticles. The reduction of CO was found to be very high in case of CZA2 based nanofuel and less in case of CeO_2 based nanofuel in all the loading conditions, where the trend of OSC of the nanoparticle and quantity of oxygen liberation was reflected. When economic aspect of running the engine

was considered, the reduction of CO was noted to be 60 % when CZA2 based nanofuel was used at 100 % loading conditions. The oxygen content in nanofuel aided for complete combustion leading to reduced concentration of CO liberation.

Figure 4.69 shows the effect of high OSC nanoparticles dispersed diesel on hydrocarbon emission against different loading conditions. The trend observed for the emission level of hydrocarbon for the nanofuel and pure diesel with load variation was similar and it was same as that of CO emission. The emission level of hydrocarbon was higher at no load condition and it was gradually decreased till 75 % load, where it was reduced from 328 to 220 ppm and 141 to 117 ppm for pure diesel and CZA2 dispersed diesel, respectively. It was due to the fact that a rich fuel mixture was required to start the engine at low loading conditions to get the required combustion temperature and pressure and maintain the speed at higher loading condition. In all type of nanofuel, the hydrocarbon emission level was less compared to pure diesel. With further increase of load beyond 75 %, an increasing trend of hydrocarbon emission was observed.

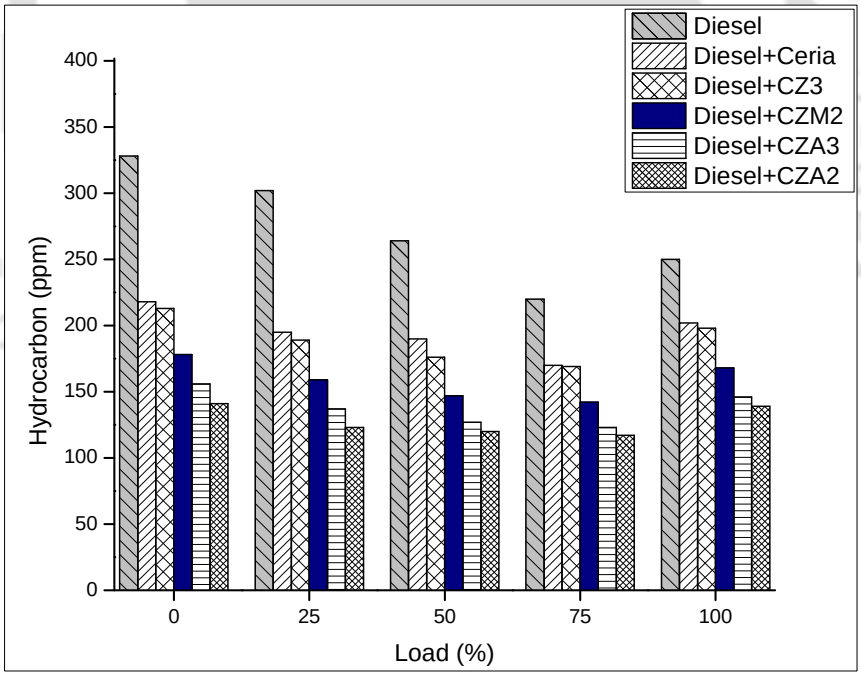

Figure 4.69 Effect of nanoparticles in diesel at 0.06 wt. % on hydrocarbon emission

Figure 4.70 shows the decrease in hydrocarbon emission using high OSC nanoparticles CeO_2, CZ3, CZA2, CZA3 and CZM2 dispersed diesel compared to pure diesel. The reduction of hydrocarbon was observed to be high in all type of nanofuel compared to diesel and it follows

the trend of OSC of the nanoparticles irrespective of loading. The presence of oxygen in the nanofuel reduced the activation temperature of carbon combustion, which promoted the complete combustion of fuel leading to decrease the hydrocarbon emission. A high reduction of unburned hydrocarbon was observed to be 57, 59, 55, 47 and 44 % at 0, 25, 50, 75 and 100 % load, respectively for CZA2 nanofuel, where it involved in complete combustion process due to its more oxygen content compared to the remaining nanofuel.

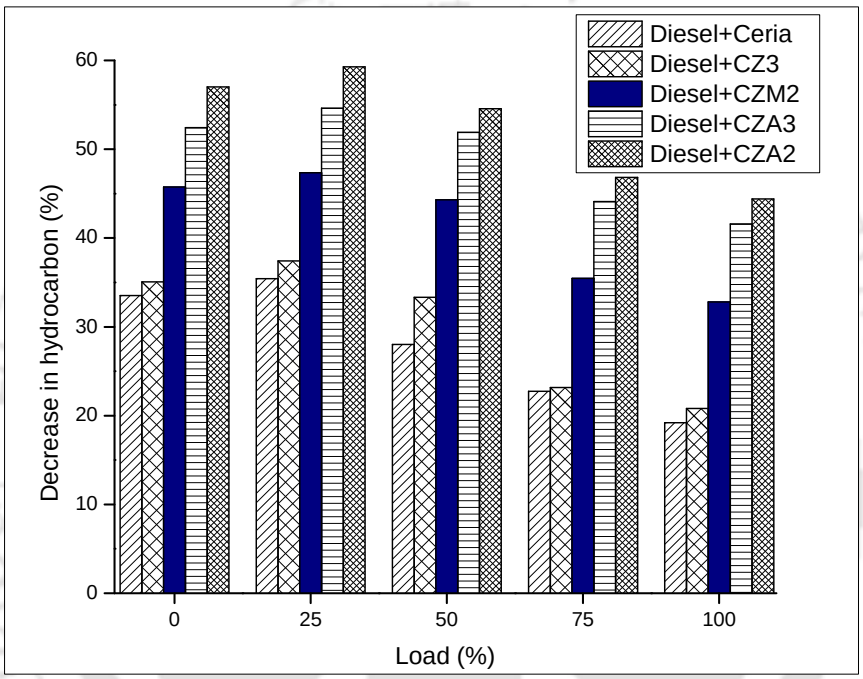

Figure 4.70 Decrease in hydrocarbon emission with different nanofuel at 0.06 wt. % in comparison with diesel

Cerium oxide provides necessary oxygen for the oxidation of CO or C_xH_y or it absorbs oxygen for the reduction of NO_x. Cerium oxide may store or release oxygen in the following reaction processes:

$$2CeO_2 \xrightarrow{\Delta} Ce_2O_3 + \frac{1}{2}O_2 \qquad ...(4.11)$$

The removal of oxygen from ceria was occurred when it was exposed to oxygen deficient atmosphere at high temperature, which led to the formation of several cerium oxide phases of the type of CeO_{2-x} with a range of possible compositions ($0 \leq x \leq 0.5$). Like CeO_2, the oxygen release

reactions for CZ3, CZA2, CZA3 and CZM2 were also given in equation (4.2), (4.3), (4.4) and (4.5), respectively. The amount of oxygen released / absorbed during oxygen reduction or rich environment by CZA2 was comparatively higher than the remaining nanoparticles. It was due to the high OSC and specific surface area of CZA2 compared to rest of the nanoparticles, which are given in Table 4.7. It helped to increase the area of contact between the fuel and the oxidizer to achieve the maximum possible combustion, which resulted in reduced CO and hydrocarbon emission.

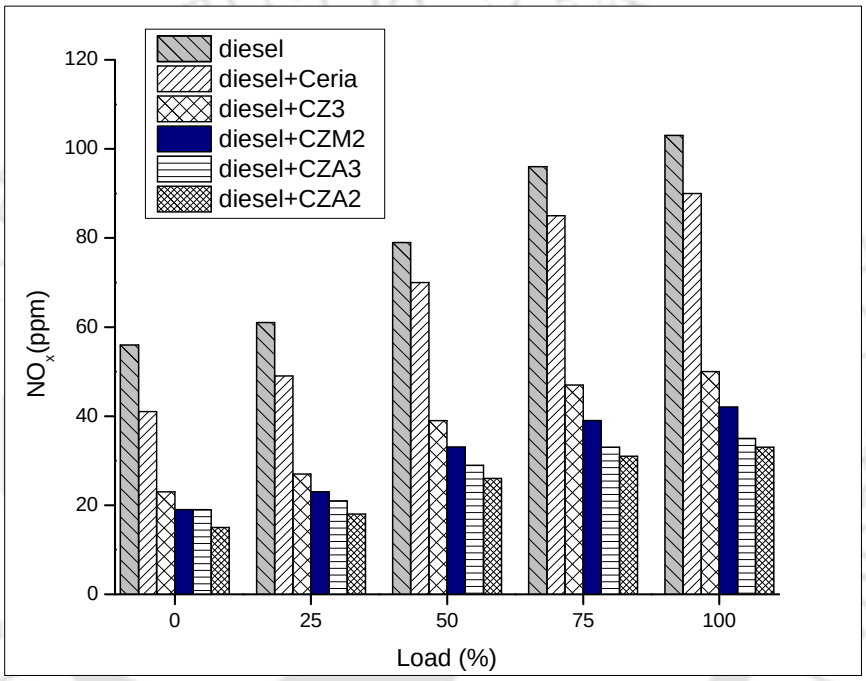

Figure 4.71 Effect of nanoparticles in diesel at 0.06 wt. % on NO_x emission

Figure 4.71 shows the effect of various high OSC nanoparticles dispersed diesel on NO_x emission at different loading conditions. It was observed that the emission level of NO_x was observed to be increased with loading for both nanofuel and diesel. The major source of NO_x during combustion is the presence of nitrogen in air and fuel. The quantity of NO and NO_x formation was observed to be directly influenced by the combustion temperature. NO_x comprises of different oxides of nitrogen formed during the combustion process by the oxidation of nitrogen. Initially, the amount of NO_x was less due to low combustion temperature at zero loading condition, which was gradually increased with loading. The NO_x content was increased from 58 to 100 ppm and 15 to 33 ppm for diesel and CZA2 nanofuel, respectively, when the

loading was increased from 0 to 100 %. The NO_x emission was observed to be high at higher loading condition due to higher gas temperature, Kumar et al. [2008]. Irrespective of loading condition, NO_x emission of an engine by nanofuel usage was observed to lower than that of diesel usage. It was due to the oxygen absorption characteristics of CeO_2, CZ3, CZA2, CZA3 and CZM2 in the oxygen rich environment. The reduction trend of NO_x content reflects the OSC of different nanoparticles.

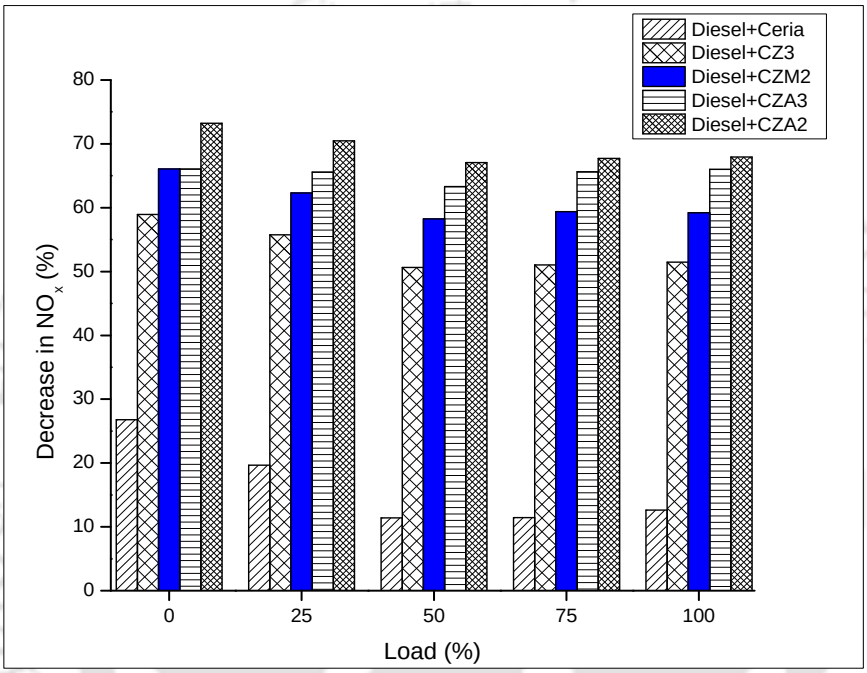

Figure 4.72 Decrease in NO_x emission with different types of nanofuel at 0.06 wt. % in comparison with diesel

Figure 4.72 shows the decrease in NO_x emission using high OSC nanoparticles CeO_2, CZ3, CZA2, CZA3 and CZM2 dispersed diesel at different loading conditions compared to that of diesel, where the reduction of NO_x emission was observed in all types of nanofuel and loading. Due to high OSC of the nanoparticles, a corresponding reduction in emission of NO_x was noted and the reduction was remarkable for nanoparticle dispersed diesel, where the trend of OSC was followed in the reduction of NO_x emission. It was observed that a higher reduction of NO_x was obtained for CZA2 nanofuel in all range of loading conditions, which was observed to be 73, 70, 67, 67.7 and 67.9 % for 0, 25, 50, 75 and 100 % of load, respectively. It is also observed that the quantity of NO_x emission at higher loading condition was less, when the nanofuel was used to

run the engine compared to pure diesel. It is due to the fact that the catalytic activity of nanoparticles became more influential after sufficient period of operation in an engine with nanofuel which promoted the possible chemical reactions as discussed by Chen et al. [2009]. A major factor contributing to NO_x emissions included the high combustion temperature and presence of oxygen during the combustion process, Zhuiykov et al. [2002]. The high OSC nanoparticle dispersed diesel reduced the ignition delay in an engine leading to decrease the combustion temperature, which resulted the reduced NO_x emission compared to that of diesel.

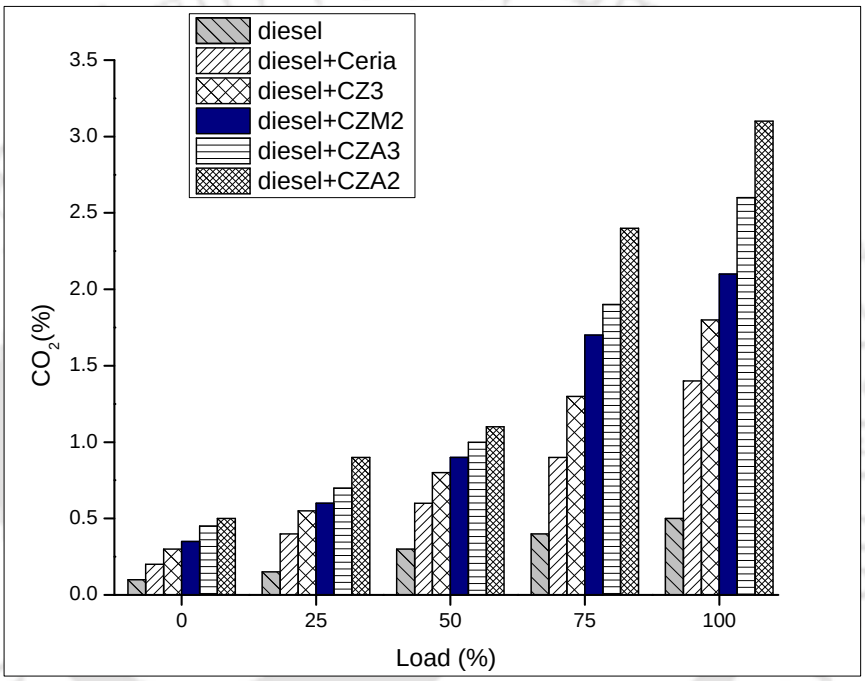

Figure 4.73 Effect of nanoparticles in diesel at 0.06 wt. % on CO_2 emission

Figure 4.73 shows the effect of high OSC nanoparticles on CO_2 emission with nanofuel at different loading conditions. It was observed that the quantity of CO_2 was increased for all types of nanofuel and diesel with an increase of load. The CO_2 level was observed to be high at 100 % loading. The CO_2 is considered to be the product of complete combustion of a hydrocarbon fuel, which results in the reduction of concentration of CO. It was observed that the CO_2 emission for nanofuel was higher than that of diesel. The rising trend of CO_2 emission with load is due to the higher fuel requirement with an increase of load. The CO_2 emission was increased from 0.1 to 0.5 % and 0.5 to 3.1 % for diesel and CZA2 based nanofuel, respectively, when the loading was increased from 0 to 100 %. In all cases, CZA2 dispersed nanofuel was observed to generate

more quantity of CO_2 compared to other fuel due to its high conversion rate of CO in to CO_2 in the presence of high OSC materials in diesel. The trend observed for the increase of CO_2 concentration is similar to that of OSC trend.

Figure 4.74 shows the increase in CO_2 emission with different nanofuel against loading conditions. It was observed that the increase in trend of CO_2 for all type of nanofuel was the same as that of OSC content of nanoparticles. It was found that the increase in CO_2 concentration at 100 % loading was noted to be 180, 260, 320, 420 and 520 % for CeO_2, CZ3, CZM2, CZA3 and CZA2 based nanofuel, respectively. The increase in CO_2 emission of CZA2 based nanofuel was found to be 400, 500, 266, 500 and 520 % at 0, 25, 50, 75 and 100 % of load, respectively. It is due the high OSC capacity of CZA2, which was used to oxidize the CO and converted into CO_2. The increase in CO_2 emission is due to the equivalent reduction of CO emission in addition to the oxidation of hydrocarbon.

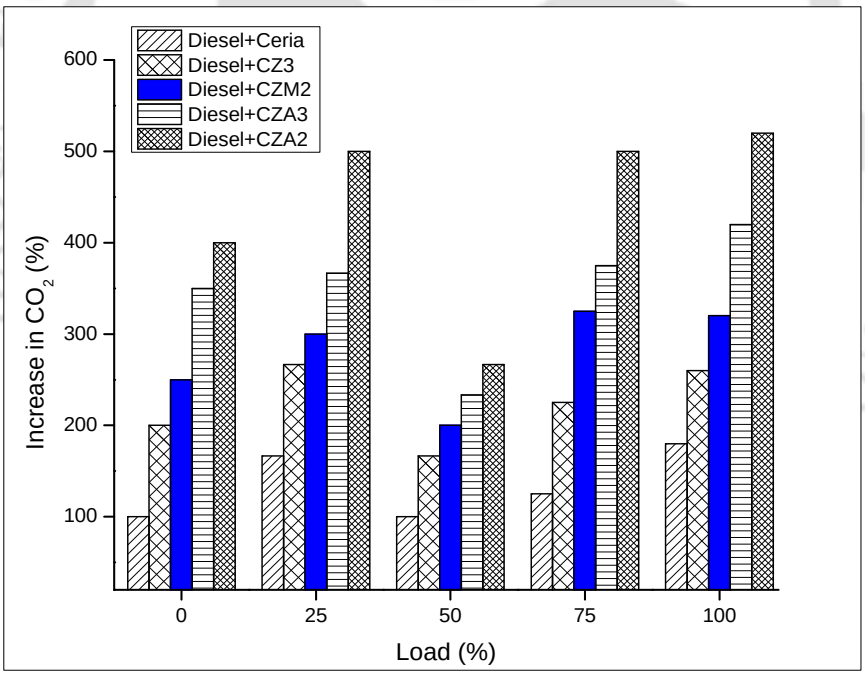

Figure 4.74 Increase in CO_2 emission with different types of nanofuel at 0.06 wt. % in comparison with diesel

The NO_x formation and reduction are explained with the help of following equation. Added to that the oxidation mechanism of hydrocarbon and CO emission is explained as follows for CeO_2

dispersed diesel, Sajith et al. [2010], and Mandal et al. [2012]. The oxidation process to obtain CO_2 is also shown here.

NO is formed by the combination of nitrogen present in air and oxygen. At high temperature, the diatomic nitrogen breaks to monoatomic nitrogen, which easily reacts with oxygen to form NO

$$N_2 \rightarrow 2N \quad \text{... (4.12)}$$

$$2N + O_2 \rightarrow 2NO \quad \text{... (4.13)}$$

$$2N + 2O_2 \rightarrow 2NO_2 \quad \text{... (4.14)}$$

This NO_2 reacts with cerium based high OSC nanoparticles to form cerium peroxide or super oxide

$$CeO_2 + NO_2 \rightarrow Ce(NO_2)O_2 \quad \text{... (4.15)}$$

The super oxide gets decomposed and contributes to the conversion of NO_x in to N_2 and oxidation of carbon

$$2Ce(NO_2)O_2 + 2C \rightarrow 2CeO_2 + N_2 + 2CO_2 \quad \text{... (4.16)}$$

$$2Ce(NO_2)O_2 + 4CO \rightarrow 2CeO_2 + N_2 + 4CO_2 \quad \text{... (4.17)}$$

The cerium based high OSC nanoparticles act as a catalyst to reduce the NO_x by influencing the reduction of NO or NO_2 by C and CO formed by combustion

$$2NO + C \rightarrow N_2 + CO_2 \quad \text{... (4.18)}$$

$$2NO_2 + 2C \rightarrow N_2 + 2CO_2 \quad \text{... (4.19)}$$

$$2NO + 2CO \rightarrow N_2 + 2CO_2 \quad \text{... (4.20)}$$

$$2NO_2 + 4CO \rightarrow N_2 + 4CO_2 \quad \text{... (4.21)}$$

In order to oxidize the hydrocarbon during the combustion process, the oxygen released from the ceria reacts with hydrocarbon and converts it in to CO_2 and H_2O as per the following reaction:

$$(2x+y)CeO_2 + C_xH_y \rightarrow \left[\frac{(2x+y)}{2}\right]Ce_2O_3 + xCO + \frac{y}{2}H_2O \quad \text{... (4.22)}$$

As cerium oxide has higher stability at Ce^{3+} ionic state, the CeO_2 converts into Ce_2O_3 after oxidizing the hydrocarbon and it remains active even after the initial stage of combustion and gets reduced into CeO_2 through the reduction of nitrogen oxide by the following reaction.

$$Ce_2O_3 + NO \rightarrow 2CeO_2 + \frac{1}{2}N_2 \quad \text{... (4.23)}$$

Table 4.11 summaries the details of engine exhaust emission using high OSC nanoparticle dispersed diesel against loading, where the influence of nanoparticles on the reduction of NO_x, hydrocarbon and CO and the increase of CO_2 against loading was noted.

Table 4.11 Engine exhaust emission of high OSC nanoparticles dispersed diesel against loading and different type of nanofuel

		Level				% change			
Engine Exhaust emission		CO (ppm)	HC (ppm)	NO_x (ppm)	CO_2 (%)	CO (%) (-)	HC (%) (-)	NO_x (%) (-)	CO_2 (%) (+)
Diesel	0	586	328	56	0.1	-	-	-	-
	25	527	302	61	0.15	-	-	-	-
	50	494	264	79	0.3	-	-	-	-
	75	472	220	96	0.4	-	-	-	-
	100	541	250	103	0.5	-	-	-	-
CeO_2 dispersed Diesel	0	381	218	41	0.2	35.0	33.5	26.8	100
	25	324	195	49	0.4	38.5	35.4	19.7	167
	50	250	190	70	0.6	49.4	28.0	11.4	100

	75	224	170	85	0.9	52.5	22.7	11.5	125
	100	300	202	90	1.4	44.6	19.2	12.6	180
CZ3 dispersed Diesel	0	350	213	23	0.3	40.3	35.1	58.9	200
	25	296	189	27	0.55	43.8	37.4	55.7	267
	50	235	176	39	0.8	52.4	33.3	50.6	167
	75	203	169	47	1.3	57.0	23.2	51.0	225
	100	270	198	50	1.8	50.1	20.8	51.5	260
CZM2 dispersed Diesel	0	304	178	19	0.35	48.1	45.7	66.1	250
	25	261	159	23	0.6	50.5	47.4	62.3	300
	50	201	147	33	0.9	59.3	44.3	58.2	200
	75	180	142	39	1.7	61.9	35.5	59.4	325
	100	261	168	42	2.1	51.8	32.8	59.2	320
CZA3 dispersed Diesel	0	247	156	19	0.45	57.9	52.4	66.1	350
	25	215	137	21	0.7	59.2	54.6	65.6	367
	50	163	127	29	1	67.0	51.9	63.3	233
	75	153	123	33	1.9	67.6	44.1	65.6	375
	100	223	146	35	2.6	58.8	41.6	66.0	420
CZA2 dispersed Diesel	0	216	141	15	0.5	63.1	57.0	73.2	400
	25	184	123	18	0.9	65.1	59.3	70.5	500
	50	149	120	26	1.1	69.8	54.6	67.1	267
	75	138	117	31	2.4	70.8	46.8	67.7	500
	100	217	139	33	3.1	59.9	44.4	68.0	520

4.6 Field trial on nanofuels

Field study was carried out in three different diesel generators having the capacity of 15, 25 and 30 kW. One liter of each type of nanofuel based on CeO_2, CZ3, CZA2, CZA3 and CZM2 nanoparticles was supplied and the testing was done under no load condition of the engine.

Figure 4.75 shows the running time of the diesel generators having different capacity. It was observed that the utilization period of nanofuel was high compared to diesel in all three diesel generators. It was also noted that the running period of diesel and nanofuel was decreased with

an increase of capacity of the generator. It was due to the fact that the higher capacity generator consumed more quantity fuel in order to meet the power output compared to that of lower capacity generator. The utilization time was increased with the OSC of the nanoparticles used in diesel in all three generators, where the lowest running time was observed in CeO_2 based nanofuel and the same was noted to be highest in case of CZA2 based nanofuel among the nanofuel category. The running time for the remaining CZ3, CZA3 and CZM2 based nanofuel was found to be in between CeO_2 and CZA2 results according to their OSC.

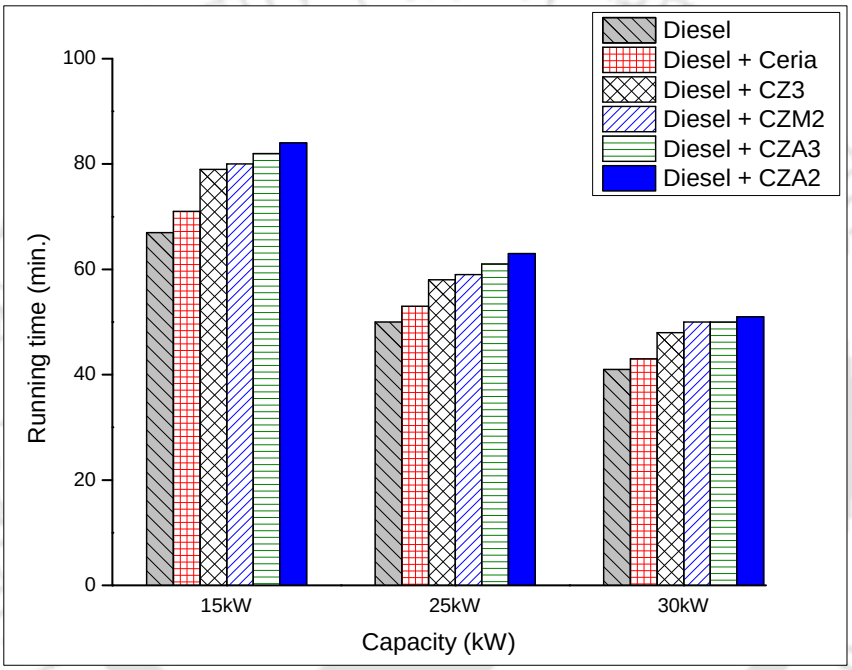

Figure 4.75 Effect of nanofuel at 0.06 wt. % on running time of different capacity of diesel generators at no load condition

Figure 4.76 shows the increase in utilization time of nanofuel compared to diesel usage. It is proved that a diesel generator can be adapted to run with nanofuel to generate increased utility. The increase in running time with respect to diesel showed the decrease in fuel consumption compared to that of diesel. It was observed that the increase in utilization time of CZA2 dispersed nanofuel was observed to be 25±1 % for all three generators compared to that of diesel usage. However, the enhancement was limited to 5±1 %, 17±1 %, 20±2 % and 22 % for CeO_2, CZ3, CZM2 and CZA3 based nanofuel, respectively. The high utilization period in CZA2 dispersed nanofuel was due its highest OSC compared to the remaining nanofuel. The

enhancement in utility period followed the same trend as that of OSC of different nanoparticles dispersed in diesel.

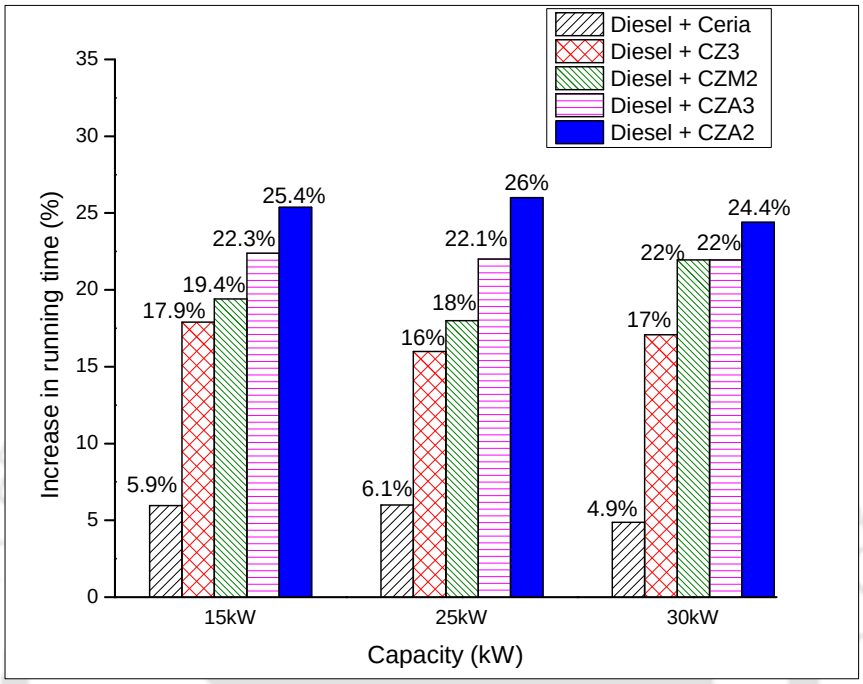

Figure 4.76 Increase in running time of different capacity of diesel generators using nanofuel at 0.06 wt. % compared to diesel

भारतीय प्रौद्योगिकी संस्थान गुवाहाटी
Indian Institute of Technology Guwahati

Chapter 5

Conclusions and future scope

5.1 Conclusions

Cerium based solid solutions of $Ce_xZr_{1-x}O_2$ (x = 0.4, 0.5, 0.6, 0.7, 0.8) were synthesized by sol-gel and co-precipitation technique, where the high OSC composition was found in the $Ce_{0.6}Zr_{0.4}O_2$ solid solution synthesized by the sol-gel technique. In order to increase the OSC of $Ce_{0.6}Zr_{0.4}O_2$ further, the Al^{3+}, Mn^{2+}, Bi^{3+}, La^{3+} and Nd^{3+} were doped by sol-gel synthesize technique and it formed the homogeneous solid solutions of $Ce_{0.6}Zr_{0.4-x}Y_{1.3x}O_2$ (Y= Al, Bi, La and Nd) and $Ce_{0.6}Zr_{0.4-x}Mn_xO_2$, which were characterized by different analytical techniques. Based on the OSC studies, the solid solutions of CeO_2, $Ce_{0.6}Zr_{0.4}O_2$, $Ce_{0.6}Zr_{0.2}Al_{0.26}O_2$, $Ce_{0.6}Zr_{0.1}Al_{0.39}O_2$ and $Ce_{0.6}Zr_{0.2}Mn_{0.2}O_2$ were used for engine performance and exhaust emission analysis and the same was used for field trial in order to explore them for potential commercial application. The summary of major results obtained under each sub-heading is given below:

A. Synthesize of ceria based high oxygen storage capacity (OSC) materials

- The crystallite size of $Ce_xZr_{1-x}O_2$ ($0.4 \leq x \leq 0.8$) solid solutions varied in the range of 5 to 7 nm and 5 to 10 nm in sol-gel and co-precipitation technique, respectively.
- The $Ce_{0.6}Zr_{0.4}O_2$ solid solution was observed to have the cubic fluorite structure and lattice defects in order to have the highest OSC among the $Ce_xZr_{1-x}O_2$ ($0.4 \leq x \leq 0.8$) solid solutions.
- The OSC of $Ce_{0.6}Zr_{0.4}O_2$ solid solution prepared by co-precipitation and sol-gel method was observed to be 0.140 and 0.147 mol of O_2/mol of CeO_2, respectively, and thus the sol-gel method was chosen to synthesize nanoparticles for further improvement of its OSC.
- The crystallite size of $Ce_{0.6}Zr_{0.4-x}Y_{1.3x}O_2$ (Y= Al, Bi, La and Nd) and $Ce_{0.6}Zr_{0.4-x}Mn_xO_2$ solid solutions was observed to be less than that of $Ce_{0.6}Zr_{0.4}O_2$.

- The qualitative confirmation of OSC of nanoparticles was done by Raman spectroscopy, Thermomechanical analyzer and HRTEM images.

- The OSC of $Ce_{0.6}Zr_{0.4}O_2$ solid solution was influenced by the ionic radius of doping element. When Al^{3+} and Mn^{2+} ions were doped, whose ionic radius is lower than that of Ce^{4+}, the OSC of $Ce_{0.6}Zr_{0.2}Al_{0.26}O_2$, $Ce_{0.6}Zr_{0.1}Al_{0.39}O_2$ and $Ce_{0.6}Zr_{0.2}Mn_{0.2}O_2$ was increased by 56, 45 and 22 %, respectively, in comparison to that of $Ce_{0.6}Zr_{0.4}O_2$ solid solution.

- When Bi^{3+}, La^{3+} and Nd^{3+} ions were doped in $Ce_{0.6}Zr_{0.4}O_2$, the OSC was decreased by 78, 44 and 15 %, respectively, where the ionic radius of the doped elements was higher than the Ce^{4+}.

- The specific surface area of nanoparticles is observed to be directly proportional to their oxygen storage capacity.

- The OSC of $Ce_{0.6}Zr_{0.2}Al_{0.26}O_2$ was observed to be the highest amongst all the tested samples.

B. Selection of suitable surfactant and synthesis technique to prepare nanofuel

- Tween 80 as a surfactant was observed to show the better dispersion stability in CeO_2 based nanofuel.

- Combination of tip sonication and magnetic stirring technique was observed to be the suitable processing technique to prepare highly stable nanofuel.

- Accelerated sedimentation technique was noted to be the suitable one to estimate the relative stability of nanofuel till the final sedimentation of nanoparticles in the fuel. In case of CeO_2 dispersed diesel at 0.06 wt. %, the total sedimentation time was calculated to be 620 hrs.

- Oleic acid was selected as a surfactant to prepare all types of nanoparticles (CeO_2, $Ce_{0.6}Zr_{0.4}O_2$, $Ce_{0.6}Zr_{0.2}Al_{0.26}O_2$, $Ce_{0.6}Zr_{0.2}Mn_{0.2}O_2$ and $Ce_{0.6}Zr_{0.1}Al_{0.39}O_2$) dispersed diesel to be tested for engine studies.

C. Optimization of ceria concentration for the performance of an IC engine

- The performance of an IC engine was observed to be increased when CeO_2 dispersed diesel was tested.
- The optimum concentration CeO_2 in diesel was found to be 0.06 wt. %, where the brake thermal efficiency and mechanical efficiency of an engine were increased by 12.8 and 9.2 %, respectively. In addition, the brake specific fuel consumption and frictional power of an engine were decreased by 11.3 and 20.8 %, respectively.

D. Studies on high OSC nanoparticles dispersed diesel

- Stability of nanofuel was observed to be influenced by the concentration and crystallite size of the nanoparticles.
- The rate of sedimentation of nanoparticles in diesel was observed to be inversely proportional to the exponential relation.
- The relative stability of 0.06 wt. % of CeO_2, $Ce_{0.6}Zr_{0.4}O_2$, $Ce_{0.6}Zr_{0.2}Al_{0.26}O_2$, $Ce_{0.6}Zr_{0.1}Al_{0.39}O_2$ and $Ce_{0.6}Zr_{0.2}Mn_{0.2}O_2$ dispersed diesel was found to be 87, 88, 88, 91 and 89 %, respectively, after 168 hrs.
- As the $Ce_{0.6}Zr_{0.1}Al_{0.39}O_2$ nanoparticles have the lowest crystallite size, the nanofuel prepared with the same showed the highest relative stability for the period of 168 hrs.
- Surface tension of nanofuel was increased by 4% for all types of nanoparticle dispersed diesel tested in the present study, which is within the limitation of experimental variation.
- Flash point and fire point temperature of all types of nanofuel were increased by 9 %.
- Viscosity of nanofuel was observed to be increased with crystallite size of nanoparticle dispersed in diesel.
- Effective thermal conductivity ratio of nanofuel at room temperature was observed to be 1.06, 1.08, 1.09, 1.14 and 1.11 for CeO_2, $Ce_{0.6}Zr_{0.4}O_2$, $Ce_{0.6}Zr_{0.2}Al_{0.26}O_2$, $Ce_{0.6}Zr_{0.1}Al_{0.39}O_2$ and $Ce_{0.6}Zr_{0.2}Mn_{0.2}O_2$ dispersed diesel, respectively, at 0.06 wt.%.

E. Engine performance with high OSC nanoparticle (0.06 wt. %) dispersed diesel (Nanofuel) and emission studies

- When $Ce_{0.6}Zr_{0.2}Al_{0.26}O_2$ nanoparticles dispersed diesel was tested, the brake thermal efficiency and mechanical efficiency of an engine were increased by 20.7 and 8.2 %, respectively and the BSFC and frictional power were decreased by 17.1 and 15.3 %, respectively, which were found to be the best among all types of nanofuel considered in the present study, as the $Ce_{0.6}Zr_{0.2}Al_{0.26}O_2$ has the OSC of 0.2293 mol of O_2/ mol of CeO_2, the highest among the other types of nanoparticles proposed in the present study.
- The highest reduction of friction power in an engine was observed in $Ce_{0.6}Zr_{0.4}O_2$ dispersed diesel and thus the mechanical efficiency of the same was high compared to other types of nanofuel.
- Emission level of hydrocarbon, CO and NO_x was observed to be decreased in all type of nanofuel compared to diesel.
- Highest emission reduction was obtained for $Ce_{0.6}Zr_{0.2}Al_{0.26}O_2$ nanofuel, where the emission level of NO_x, CO and hydrocarbon were reduced by 68, 60 and 44 %, respectively, compared to that of diesel emission.

F. Field trial on nanofuels

- Utilization time of the commercial diesel generators was increased with nanofuel compared to diesel. It was found to be increased by 5±1, 17±1, 20±2 and 22 % for CeO_2, $Ce_{0.6}Zr_{0.4}O_2$, $Ce_{0.6}Zr_{0.2}Mn_{0.2}O_2$ and $Ce_{0.6}Zr_{0.1}Al_{0.39}O_2$ dispersed diesel, respectively.
- The increase in utilization time of 25±1 % was observed for 15, 25 and 30 kW diesel generator, when $Ce_{0.6}Zr_{0.2}Al_{0.26}O_2$ nanoparticles dispersed diesel was tested.

5.2 Scope of future work

The work presented here opens up several avenues for further development of the high OSC nanoparticles for the application of an IC engine. The scope of the future work is outlined as follows:

- Cerium based four-metal combination can be synthesized in order to increase the OSC further.
- The high OSC nanoparticles may be prepared with magnetic characteristics in order to trap them after the catalytic application.
- Combustion studies on nanoparticles dispersed diesel may be carried out.
- Higher OSC nanoparticles can be used in biodiesel blends in order to reduce the CO_2 emissions.
- Accelerated sedimentation studies may be further extended for all types of nanofuel.
- The high OSC nanoparticles may be mixed with coal powder to increase the fuel combustion efficiency and reduce the emission level.
- Systematic field study can be carried out with respect to load and speed in order to find the effective utilization of nanofuel for the commercial applications.
- Nanofuel can be explored for stationary power production units such as steam turbine, where diesel is used as a heat source.

भारतीय प्रौद्योगिकी संस्थान गुवाहाटी
Indian Institute of Technology Guwahati

References

Ajav E. A, Singh B, Bhattacharya T K. Experimental study of some performance parameters of a constant speed stationary diesel engine using ethanol-diesel blends as fuel. Biomass and Bioenergy 17 (1999) 357–365.

Arias M, Garcia M F, Jues A I, Hungria A B, Anderson J A, Conesa J C, Soria J. Influence of thermal sintering on the activity for CO–O_2 and CO–O_2–NO stoichiometric reactions over Pd(Ce, Zr)O_x/Al_2O_3 catalysts. Applied Catalysis B: Environmental 38 (2002) 151–158.

Ashok M P, Saravannan C G. Performance and emission of the emulsified fuel in a DI diesel engine using additive diethyl ether with surfactant of Span 80. Energy and Fuels 21 (2007) 1878–1882.

Atkinson A, Ramos T M G M. Chemically induced stress in ceramic oxygen ion-conducting membranes. Solid state Ionics 129 (2000) 259–269.

Bao H, Chen X, Fang J, Jiang Z , Huang W. Structure-activity relation of Fe_2O_3–CeO_2 composite catalysts in CO oxidation. Catalysts Letter 125 (2008) 160–167.

Bazin P, Saura O, Meunier F C, Daturi M, Lavalley J C, Govic M A L, Harle V, Blanchard G. A thermogravimetric and FT-IR study of the reduction by H_2 of sulfated Pt/$Ce_xZr_{1-x}O_2$ solids. Applied Catalysis B: Environmental 90 (2009) 368–379.

Brook RD, Franklin B, Cascio W, Hong Y, Howard G, Lipsett M et al. Air pollution and cardiovascular disease: a statement for healthcare professionals from the expert panel on population and prevention science of the american heart association. Circulation 109 (2004). 2655–2671.

Cao CY, Cui ZM, Chen CQ, Song WG, Cai W. Ceria hollow nanospheres produced by a template-free microwave-assisted hydrothermal method for heavy metal Ion removal and catalysis. Journal of Physical Chemistry C 114 (2010) 9865–9870.

Cassee F R, Campbell A, Boere A J F, McLean S G, Duffin R, Krystek P, Gosens I, Miller M R. The biological effects of subacute inhalation of diesel exhaust following addition of cerium oxide nanoparticles in atherosclerosis-prone mice. Environmental Research 115 (2012) 1–10.

Chang Y, McCarty J G. Novel oxygen storage components for advanced catalysts for emission control in natural gas fueled vehicles. Catalysis Today 30 (1996) 163–170.

Changlin L, Xin G, Yanq W, Yaojun W, Yangang W, Xiaohui L, Guanzhong L. Synthesis and characterization of mesostructured ceria-zirconia solid solution. Journal of Rare Earths 27 (2009) 211–215.

Chen Y, Guo Z, Wang Z. Influence of CeO_2 on NO_x emission during iron ore sintering. Fuel Processing Technology 90 (2009) 933–938.

Cho B K. Chemical modification of catalyst support for enhancement of transient catalytic activity: nitric oxide reduction by carbon monoxide over rhodium. Journal of catalysis 131 (1991) 74–87.

Chong M K, Pita K, Kam C H. Photoluminescence of sol-gel-derived Y_2O_3: Eu^{3+} thin-film phosphors with Mg^{2+} and Al^{3+} co-doping. Applied Physics A, Materials Science & Processing 79 (2004) 433–437.

Chuang C C, Hsianga H I, Hwang J S, Wang T S. Synthesis and characterization of Al_2O_3-$Ce_{0.5}Zr_{0.5}O_2$ powders prepared by chemical co precipitation method. Journal of Alloys and Compounds 470 (2009) 387–392.

Crozier P, Wang R, Sharma R. In situ environmental TEM studies of dynamic changes in cerium-based oxides nanoparticles during redox processes. Ultramicroscopy 108 (2008) 1432–1440.

Das S K, Putra N, Thiesen P, Roetzel W. Temperature dependence of thermal conductivity enhancement for nanofluids. Journal of Heat Transfer 125 (2003a) 567–573.

Das S K, Narayan G, Baby A K. Survey on nucleate pool boiling of nanofluids: the effect of particle size relative to roughness. Journal of nanoparticle research 10 (2008) 1099–1108.

Das S K, Putra N, Roetzel W. Pool boiling characteristics of nano-fluids. International Journal of Heat and Mass Transfer 46 (2003b) 851–862.

Deshpande A S, Pinna N, Beato P, Antonietti M, Niederberger M. Synthesis and characterization of stable and crystalline $Ce_{1-x}Zr_xO_2$ nanoparticle sols. Chemistry of Materials 16 (2004) 2599–2604.

Dhage S.R, Gaikwad S P, Kumar P M, Ravi V. Synthesis of $Ce_{0.75}Zr_{0.25}O_2$ at 100°C. Ceramic International 31 (2004) 211–213.

Dong F, Tanabe T, Suda A, Takahashi N, Sobukawa H, Shinjoh H. Investigation of the OSC performance of $Pt/CeO_2ZrO_2Y_2O_3$ catalysts by CO oxidation and $^{18}O/^{16}O$isotopic exchange reaction. Chemical Engineering Science 63 (2008) 5020 – 5027.

Du Y, Shi S, He H, Dai H. Fabrication and characterization of $Ce_{0.7}Zr_{0.3}O_2$ nanorods having high specific surface area and large oxygen storage capacity. Particuology 9 (2011) 63–68.

Dutta G, Umesh V W, Baidya T, Hedge M S, Priolkar K R, Sarode P R. Reducibility of $Ce_{1-x}Zr_xO_2$: orgin of enhanced oxygen storage capacity. Catalytic Letters 108 (2006) 165–172.

Eguchi K, Setoguchi T, Inoue T, Arai H. Electrical properties of ceria-based oxides and their application to solid oxide fuel cells. Solid State Ionics 52 (1992) 165–72.

Evans J S O, Mary T A, Sleight A W. Negative thermal expansion materials. Physica B. 241-243 (1998) 311–316.

Fagg D P, Kharton V. V, Shaula A, Marozau I.P, Frade J R. Mixed conductivity, thermal expansion, and oxygen permeability of Ce (Pr, Zr) $O_{2-\delta}$. Solid State Ionics 176 (2005) 1723 – 1730.

Fitzsimmons M R, Eastman J A, Stach M M, Wallner G. Structural characterization of nanometer-sized crystalline Pd by x-ray-diffraction techniques. Physical Review B 44(6) (1991) 2454–2460.

Gan Y, Lim Y S, Qiao L. Combustion of nanofluid fuels with the addition of boron and iron particles at dilute and dense concentrations. Combustion and flame 159 4 (2012) 1732–1740.

Gan Y, Qiao L. Combustion characteristics of fuel droplets with addition of nano and micron sized aluminum particles. Combustion and flame 158 (2011a) 354–368.

Gan Y, Qiao L. Evaporation characteristics of fuel droplets with the addition of nanoparticles under natural and forced convection. International journal of Heat and Mass transfer 54 (2011b) 4913–4922.

Gan Y, Syuen Y, Lim Y S, Qiao L. Combustion of nanofluid fuels with the addition of boron and iron particles at dilute and dense concentrations. Combustion and flame 159 (2012) 1732–1740.

Ganesh D, Gowrishankar G. Effect of nano-fuel additive on emission reduction in a biodiesel fuelled CI engine. IEEE: International conference on electrical and control engineering (ICECE) (2011) 3453–3459.

Garg P, Alvarado J I, Marsh C, Carlson T A, Kessler D A, Annamalai K. An experimental study on the effect of ultrasonication on viscosity and heat transfer performance of multi-wall carbon nanotube-based aqueous nanofluids. International Journal of Heat and Mass Transfer 52 (2009) 5090–5101.

Gateshki, M Niederberger, A S Deshpande, Y Ren, V Petkov. Atomic-scale structure of nanocrystalline CeO_2–ZrO_2 oxides by total x-ray diffraction and pair distribution functional analysis. Journal of physics condensed Matter 19 (2007) 156205 1–12.

Ghom S A, Zamani C, Andreu T, Epifani M, Morante J R. Improvement of oxygen storage capacity using mesoporous ceria- zirconia solid solutions. Applied Catalysis B: Environmental 108– 109 (2011) 32–38.

Godiganur S, Murthy C S, Reddy R P. Performance and emission characteristics of a Kirloskar HA394 diesel engine operated on fish oil methyl esters. Renewable Energy 35 (2010) 355–359.

Golubovic M N, Hettiarachchi H D M, Worek W M , Minkowycz W J. Nanofluids and critical heat flux experimental and analytical study. Applied Thermal Engineering 29 (2009) 1281–1288.

Govindaraj R, Sundar C S, Arora A K. Atomic scale study of negative thermal expansion in zirconium tungsten. Physical Review B 76 (012104) (2007) 1–4.

Goyal K K. Renewable energy. Pinnacle technology (2009).

Guo J, Wu D , Zhang L, Gong M, Zhao M, Chen Y. Preparation of nanometric CeO_2–ZrO_2–Nd_2O_3 solid solution and its catalytic performances. Journal of Alloys and Compounds 460 (2008) 485–490.

Gupta A, Waghmare U V, Hegde M S. Correlation of oxygen storage capacity and structural distortion in transition-metel,, noble-metal, and rare-earth-ion-substituted CeO_2 from first principles calculation. Chemistry of Materials 22 (2010) 5184–5198.

He H, Dai H X, Wong K W, Au CT. $RE_{0.6}Zr_{0.4-x}Y_xO_2$ (RE = Ce, Pr; x = 0, 0.05) solid solutions: an investigation on defective structure, oxygen mobility, oxygen storage capacity, and redox properties. Applied Catalysis A: General 251 (2003) 61–74.

Heywood J B. Internal combustion engine fundamentals McGraw Hill, New York. (1988).

Hirano M, Fukuda Y, Iwata H, Hotta Y, Inagaki M. Preparation and spherical agglomeration of crystalline cerium (iv) oxide nanoparticles by thermal hydrolysis. Journal of American Ceramic Society 83 (2000) 5 1287–1289.

Hirano M, Hirai K. Effect of hydrolysis conditions on the direct formation of nanoparticles of ceria–zirconia solid solutions from acidic aqueous solutions. Journal of Nanoparticle Research 5 (2003) 147–156.

Hirano M, Kato E. Hydrothermal synthesis of nanocrystalline cerium (IV) oxide powders. Journal of American Ceramic Society 82 3 (1999) 786–88.

Hirano T. Dehydrogenation of ethylbenzene over potassium- promoted iron oxide containing cerium and molybdenum oxides. Applied Catalysis 28 (1986)119–132.

Hongmei L, Qingchao Z, Yile L, Maochu G, Yongdong C, Jianli W, Yaoqiang C. Effects of ceria/zirconia ratio on properties of mixed CeO_2 -ZrO_2 -Al_2O_3 compound. Journal of Rare Earths 28(1) (2010) 79–83.

Hori C E, Permana H, Ng K Y S, Brenner A, More K, Rahmoeller KM, Belton D. Thermal stability of oxygen storage properties in a mixed CeO_2-ZrO_2 system. Applied Catalysis B: Environmental 16 (1998) 105–117.

Hu C, Zhu Q, Jiang Z Nanosized CuO–$Zr_xCe_{1-x}O_y$ aerogel catalysts prepared by ethanol supercritical drying for catalytic deep oxidation of benzene. Powder Technology 194 (2009) 109–114.

Huang, Risha G A, Yang V, Yetter R A. Effect of particle size on combustion of aluminum particle dust in air. Combustion and flame. 156 (2009) 5–13.

Hwang Y, Lee J K, Lee C H, Jung Y M, Cheong S I, Lee C G, Ku B C, Jang S P. Stability and thermal conductivity characteristics of nanofluids. Thermochima Acta 455 (2007) 70–74.

Ikeda T, Hirata M, and Kimura T. Hydration structure of Y^{3+} and La^{3+} compared: An application of metadynamics. Journal of chemical physics. 122 (2005) 244507 1–5.

Jana M, Khojin A S, Zhong W H. Enhancement of fluid thermal conductivity by the addition of single and hybrid nano – additives. Thermochima Acta 462 (2007) 45–55.

Jia L, Shen M, Hao J, Rao T, Wang J. Dynamic oxygen storage and release over $Mn_{0.1}Ce_{0.9}O_x$ and $Mn_{0.1}Ce_{0.6}Zr_{0.3}O_x$ complex compounds and structural characterization. Journal of Alloys and compounds 454 (2008) 321–326.

Jung H Kittelson d B Zachariah R. The influence of a cerium additive on ultrafine diesel particle emissions and kinetics of oxidation. Combustion and Flame 142 (2005) 276–288.

Kao M. J, Ting C C, Lin B F, and Tsung T T. Aqueous aluminum nanofluid combustion in diesel fuel. Journal of Testing and Evaluation 36.2 (2008) 503 1–5.

Karthik R. Raja T S R, Madavan R. Enhancement of critical characteristics of transformer oiil using nanomaterials. Arab Journal of Science and Engineering 38 (2013) 2725–2733.

Kaspar J, Fornasiero P, Hickey N. Automotive catalytic converters: current status and some perspectives. Catalysis Today 77 (2003) 419–449.

Keblinski P, Eastman J A, and Cahill D G. Nanofluids for thermal transport Materials today 8 (2005) 36–44.

Keskin A, Guru M, Altiparmak D. Influence of tall biodiesel with Mg and Mo based fuel additives on diesel engine performance and emission. Bioresource Technology 99 (2008) 6434–6438.

Khaleduzzaman S S, Mahbubul I M, Shahrul I M., Saidur R. Effect of particle concentration, temperature and surfactant on surface tension of nanofluids. International Communications in Heat and Mass Transfer 49 (2013) 110–114.

Kim S J, Banf I C, Buongiorno J, Hu L W. Surface wettability change during pool boiling of nanofluids and its effect on critical heat flux. International Journal of Heat and Mass Transfer 50 (2007) 4105–4116.

Kondratenko E V, Sakamoto Y, Okumura K, Shinjoh H. Transient analysis of oxygen storage capacity of $Pt/CeO_2–ZrO_2$ materials with millisecond- and second-time resolution. Applied Catalysis B: Environmental 89 (2009) 476–483.

Kozlov A I, Kim D H, Yezerets A, Andersen P, Kung H H, Kung M C. Effect of preparation method and redox treatment on the reducibility and structure of supported ceria–zirconia mixed oxide. Journal of Catalysis. 209 (2002) 417–426.

Krause B, Mende M, Potschke P, Petzold G. Dispersability and particle size distribution of CNTs in an aqueous surfactant dispersion as a function of ultrasonic treatment time. Carbon 48 (2010) 2746–2754.

Kumar S A, Meenakshi K S, Narashimhan B R V, Srikanth S, Arthanareeswaran G. Synthesis and characterization of copper nanofluid by a novel one step method. Materials Chemistry and Physics 113 (2009) 57–62.

Kumar S K, Velraj R, Ganesan R. Performance and exhaust emission characteristics of a CI engine fuels with pongamia pinnata methyl ester (PPME) and its blends with diesel. 33 (2008) 2294–2302.

Lai C C, Huang Y C, Wei Y H, Chang J S. Biosurfactant enhanced removal of total petroleum hydrocarbons from contaminated soil. Journal of Hazardas materials 167 (2009) 609–614.

Letichevsky S, Claudio A. Tellez C A, Roberto R, Avillez R R D, Silva M I P D, Fraga M A, Appel L G. Obtaining $CeO_2–ZrO_2$ mixed oxides by co precipitation: role of preparation conditions. Applied Catalysis B: Environmental 58 (2005) 203–210.

Levasseur B, Kaliaguine S. Effect of iron and cerium in $La_{1-y}Ce_yCo_{1-x}Fe_xO_3$ perovskites as catalysts for VOC oxidation. Applied Catalysis B: Environmental 88 (2009) 305–314.

Li Y, Suzuki M, Ogawa H, Effect of ethyl tert-butyl ether addition to diesel fuel on characteristics of combustion and exhaust emissions of diesel engines. Fuel 88 (2009a) 2017–2024.

Li Y, Zhou J, Tung S, Schneider E, Xi S. A review on development of nanofluid preparation and characterization. Powder Technology 196 (2009b) 89–101.

Lima J F D, Martins R F, Neri C R, Serra O A. $ZnO:CeO_2$-based nanopowders with low catalytic activity as UV absorbers. Applied Surface Science 255 (2009) 9006–9009.

Lin C Y, Wang J C, Chen T C. Analysis of suspension and heat transfer characteristics of Al_2O_3 nanofluids prepared through ultrasonic vibration. Applied Energy 88 (2011) 4527–4533.

Lisunova M O, Lebovka N I, Melezhyk O V, Boiko Y P. Stability of the aqueous suspensions of nanotubes in the presence of nonionic surfactant. Journal of Colloid and Interface Science. 299 (2006) 740–746.

Lorenz W, Reimann H J, Schmal A, Dormann P, Schwarz B, Neugebauer E, et al. Histamine release in dogs by cremophor EI and its derivatives: oxethylated oleic acid is the most effective constituent. Agents actions 7-1 (1977) 63–67.

Luca L T D, Galfetti L, Severini F, Meda L, Marra G, Vorozhtsov A B, Meda L, Marra G, Sedoi, Babuk V A. Burning of nano-aluminized composite rocket propellants. Combustion, Explosion, and Shock Waves 41 (2005) 680–692.

Luo, Tok A I Y, Boey F Y C. Aqueous tape casting of 10 mol%- Gd_2O_3 doped CeO_2 nano-particles. Material Science and Engineering 429 (2006) 266–271.

Mandal S, Kanagaraj S. Reduction of emission in a diesel engine using nanofuel - ceria nanoparticle dispersed diesel. Journal of ASTM International 1567 (2012) 64–78.

Masui T, MinamiK, Koyabu K, Imanaka N. Synthesis and characterization of new promoters based on CeO_2–ZrO_2–Bi_2O_3 for automotive exhaust catalysts. Catalysis Today 117 (2006) 187–192.

Masui T, Ozaki T, Machida K I, Adachi H Y. Preparation of ceria–zirconia sub-catalysts for automotive exhaust cleaning. Journal of Alloys and Compounds 303–304 (2000) 49–55.

Medina C, M J, Martinez M J S, Radomski A, Corrigan O I and Radomski M W. Nanoparticles: pharmacological and toxicological significance. British Journal of Pharmacology 150 (2007), 552–558.

Meiqing S, Xinquan W, Yuan A, Duan W, Minwei Z, Jun W. Dynamic oxygen storage capacity measurements on ceria based material. Journal of rare earths 25 (2007) 48–52.

Meng, L., Liu, L., Zi, X., Dai, H., Zhao, Z., Wang, X., He, W., Preparation ceria-zirconia solid solution with enhanced oxygen storage capacity and redox performance. Front Environmental science Engineering China 24 (2010) 164–171.

Mikulova J, Rossignol S, Gerard F, Mesnard D, Kappenstei C, Duprez D. Properties of cerium–zirconium mixed oxides partially substituted by neodymium : Comparison with Zr–Ce–Pr–O ternary oxides. Journal of Solid State Chemistry 179 (2006) 2511–2520.

Ming Z, Yanling Y, Hairong W, Zhimin L, Maochu G, Yaoqiang C. Preparation and investigation of $Ce_{0.4}Zr_{0.5-x}Y_{0.1}Mn_xO_2$ oxygen-storage materials. Journal of Rare Earths 28 (2010) 260–214.

Modeshia D R, Wright C S, Payne J L, Sankar G, Fiddy S G, Walton R L. Low-temperature redox properties of nanocrystalline cerium (IV) oxides revealed by in situ XANES. The Journal of Physical Chemistry 111 (2007) 14035–14039.

Moosavi M, Goharshadi E K, Youssefi A. Fabrication, characterization, and measurement of some physicochemical properties of ZnO nanofluids. International Journal of Heat and Fluid Flow 31 (2010) 59–605.

Morales M A, Jain T K, Labhasetwar V, Pelecky D L L. Magnetic studies of iron oxide nanoparticles coated with oleic acid and pluronic block copolymer. Journal of applied physics 97 (10) (2005) 1–4.

Morikawa A, Suzuki T, Kanazawa T, Kikuta K, Suda A, Shinjo H. A new concept in high performance ceria–zirconia oxygen storage capacity material with Al2O3 as a diffusion barrier. Applied Catalysis B: Environmental 78 (2008) 210–221.

Murshed S M S, Leong K C, Yang C. Enhanced thermal conductivity of TiO_2–water based nanofluids. International Journal of Thermal Sciences 44(4) (2005) 367–73.

Ozawa M, Hattori M, Yamaguchi T. Thermal stability of ceria catalyst on alumina and its surface oxygen storage capacity. Journal of Alloys and Compounds 451 (2008) 621–623.

Ozawa M, Matuda K, Suzuki S. Microstructure and oxygen release properties of catalytic alumina-supported CeO_2–ZrO_2 powders. Journal of Alloys and Compounds 303–304 (2000) 56–59.

Paria S, Khilar K C. A review on experimental studies of surfactant adsorption at the hydrophilic solid-water interface. Advances in colloid and interface science 110 (3) (2004) 75-95.

Pavia D L, Lampman G M, Kriz G S. Introduction to spectroscopy, 3rd edition, Thomson, India Edition, (2007) 353–385.

Peng C T, Lia H K, Liaw B J, Chen Y Z. Removal of CO in excess hydrogen over CuO/ $Ce_{1-x}Mn_xO_2$ catalysts. Chemical Engineering Journal 172 (2011) 452–458.

Peters A, Pope III CA Cardiopulmonary mortality and air pollution. Lancet 360 (2002) 1184–1185.

Ping F, Jiqing L U, Xiaoyan X, Mengfei L. Catalytic combustion study of soot on $Ce_{0.7}Zr_{0.3}O_2$ solid solution. Journal of Rare Earths 26 (2008) 250–253.

Pivkina A, Ulyanova P, Frolov Y, Zavyalov S, Schoonman J. Nanomaterials for heterogeneous combustion. Propellants, explosives, pyrotechnics. 29 (2004) 39–49.

Pope CA Particulate air pollution, C-reactive protein, and cardiac risk. Eur Heart J 22 (2001) 1149–1150.

Prabhu S, Vinayagam B K. AFM investigation in grinding process with nanofluids using Taguchi analysis. International Journal of Advanced Manufacturing Technology 60 (2012) 149–160.

Prasad D H, Lee J H, Lee H W, Kim B K, Park J S. Chemical synthesis and characterization of $Ce_xZr_{1-x}O_2$ powders by a modified sol gel method. Journal of Ceramic Processing Research 10 (6) (2009) 748–752.

Ramadhas A. S, Muraleedharan C, Jayaraj S. Performance and emission evaluation of a diesel engine fueled with methyl esters of rubber seed oil. Renewable Energy 30 (2005) 1789–1800.

Rao R, Mishra B G. Structural redox and catalytic chemistry of ceria based materials. Bulletin of the Catalysis Society of India 3 (2003) 122–134.

Reddy B M, Katta L, Thrimurthulu G. Novel nanosized $Ce_xZr_{1-x}O_2$, $Ce_xHf_{1-x}O_2$ and $Ce_xTb_{1-x}O_{2-\delta}$ solid solutions: structural characteristics and catalytic performance. Catalysis Today 175 (2011) 585– 592.

Reddy B M, Khan A. Nanosized CeO_2-SiO_2, CeO_2-TiO_2, and CeO_2-ZrO_2 mixed oxides: influence of supporting oxide on thermal stability and oxygen storage properties of Ceria, Catalysis survey from Asia. 9-3 (2005) 155–171.

Rossignol S, Madier Y, Duprez D. Preparation of zirconia - ceria materials by soft chemistry. Catalysis Today 50 (1999) 261–270.

Rui R, Duan W, Xiaodong W, Jun F, Lei W, Xiaodi W. Structure and oxygen storage capacity of Pr-doped $Ce_{0.26}$ $Zr_{0.74}$ O_2 mixed oxides. Journal of Rare Earths 29 (2011) 1053–1059.

Sadri R, Ahmadi G, Togun H, Dahari M, Kazi S N, Sadeghinezhad E, Zubir N. An experimental study on thermal conductivity and viscosity of nanofluids containing carbon nanotubes. Nanoscale Research Letters 9:151 (2014) 1–16.

Sajith V, Sobhan C B, Peterson G P. Experimental investigation on the effects of cerium oxide nanoparticle fuel additives on biodiesel. Advances in Mechanical Engineering Article ID 581407 (2010) 1–6.

Sayle T X T, Parker S C, Sayle D C. Oxidising CO to CO_2 using ceria nanoparticles. Physical Chemistry Chemical Physics 7 (2005) 2936–2941.

Shafii M B, Daneshvar, Jahani N, Mobini. Effect of ferrofluid on the performance and emissions patterns a four-stroke diesel engine. Advances in Mechanical Engineering (2011) article ID 529049. 1–5.

Sharif S M, Fard F G, Khatibi E, Sarpoolaky H. Dispersion and stability of carbon black nanoparticles, studied by ultraviolet-visible spectroscopy. Journal of Taiwan institute of chemical engineers 40 (2009) 524–527.

Sharma S. K, Nirala A K, Kanagaraj S. Studies on the influence of cerium oxide nanoparticle as an anti wear lubricant additive. (2010) B.Tech thesis report, Indian Institute of Technology, Guwahati, India.

Shcherbakov A B, Ivanov V K, Zholobak N M, Ivanova O S , Krysanov Y E, Baranchikov A E, Spivak N Y, and Tretyakov Y D. Nanocrystalline. Ceria Based Materials-Perspectives for Biomedical Application. Biophysics 56 (2011) 1- 6.

Som I, Bhatia K Y, Asir M. Status of surfactants as penetration enhancers in transdermal drug delivery. Journal of Pharmacy and Bioallied sciences 4 (2012) 2–9.

Sonawane S S, Patankar K, Fogla A, Puranik B, Bhan U, Kumar S S. An experimental investigation of thermo-physical properties and heat transfer performance of Al_2O_3-aviation turbine fuel nanofluids. Applied Thermal Engineering 31 (2011) 2841–2849.

Suhonen S, Valden M, Hietikko M, Laitinen R, Savimaki A, Harkonen M. Effect of Ce–Zr mixed oxides on the chemical state of Rh in alumina supported automotive exhaust catalysts studied by XPS and XRD. Applied Catalysis A: General 218 (2001) 151–160.

Tada M, Yoshiya M, Yasuda H. Effect of ionic radius and resultant two-dimensionality of phonons on thermal conductivity in M_xCoO_2 (M = Li, Na, K) by perturbed molecular dynamics. Journal of Electronic materials 39-9 (2010) 1439–1445.

Tah B, Pal P, Mahato M, Talapatra G B. Aggregation behavior of SDS/CTAB catanionic surfactant mixture in aqueous solution and at the air/water interface. The journal of Physical Chemistry B 115 (2011) 8493–9.

Takatori K, Tani T, Watanabe N, Kamiya N. Preparation and characterization of nano-structured ceramic powders synthesized by emulsion combustion method. Journal of Nanoparticel Research 1 (1999) 197–201.

Tanvir S T, Qiao L. Surface tension of nanofluid-type fuels containing suspended nanomaterials. Nanoscale research letters 7 (2012) 226 1–10.

Trovarelli A, Boaro M, Rocchini E, Leitenburg C D, Dolcetti G. Some recent developments in the characterization of ceria-based catalysts. Journal of alloys and compounds. 323-324 (2001) 584–591.

Trovarelli. A Structural and oxygen storage/release properties of CeO_2-based solid solutions comments on inorganic Chemistry. A Journal of Critical Discussion of the Current Literature, 20 4-6 (1999) 263 –284.

Tyagi H, Patrick E. Phelan, Prasher R, Peck R, Lee T, Jose R. Pacheco, Arentzen P,. Increased hot plate ignition probability for Nanoparticle -laden Diesel fuel. Nanoletters 8 (2008) 1410–1416.

Vlaic G, Fornasiero P, Geremia G, Kaspar J, Graziani M. Relationship between the zirconia-promoted reduction in the Rh-loaded $Ce_{0.5}Zr_{0.5}O_2$ mixed oxide and the Zr–O local structure. Journal of catalysis 168 (1997) 386–392.

Vlaic G, Monte R D, Fornasiero P, Fonda E, Kaspar J, Graziani M. Redox property–local structure relationships in the Rh-loaded CeO_2–ZrO_2 mixed oxides. Journal of Catalysis 182 (1999) 378–389.

Wang Q, Li G, Zhao B Zhou R. The effect of Nd on the properties of ceria–zirconia solid solution and the catalytic performance of its supported Pd-only three-way catalyst for gasoline engine exhaust reduction. Journal of Hazardous Materials 189 (2011a) 150–157.

Wang Q, Li G, Zhao B, Zhou R. The effect of Nd on the properties of ceria–zirconia solid solution and the catalytic performance of its supported Pd-only three-way catalyst for gasoline engine exhaust reduction. Journal of Hazardous Materials. 189 (2011b) 150–157.

Wang Q, Li Z, Zhao B, Li G, Zhou R. Effect of synthesis method on the properties of ceria–zirconia modified alumina and the catalytic performance of its supported Pd-only three-way catalyst. Journal of Molecular Catalysis A: Chemical. 344 (2011c) 132– 137.

Wang X, Rodriguez J A, Jonathan, Hanson J C, Gamarra D, Arias A M, Garcıa M F. In situ studies of the active sites for the water gas shift reaction over Cu-CeO_2 catalysts: complex interaction between metallic copper and oxygen vacancies of ceria. Journal of Physical Chemistry B 110 (2006) 428–434.

Wei Z, Li H, Zhang X, Yan S, Lv Z, Chen Y, Gang M. Preparation and property investigation of CeO_2–ZrO_2–Al_2O_3 oxygen-storage compounds. Journal of Alloy and Compounds 455 (2008) 322–326.

Wu X, Wu X, Liang Q, Fan J, Weng D, Xie Z, Wei S. Structure and oxygen storage capacity of Pr/Nd doped CeO_2-ZrO_2 mixed oxides. Solid state science 9 (2007) 636–643.

Xiaodong W, Qing L, Duan W. Effect of manganese doping on oxygen storage capacity of ceria-zirconia mixed oxides. Journal of Rare Earths 24 (2006) 549–553.

Xiaodong W, Qing L, Xiaodi W, Duan W. Role of surface adsorption in fast oxygen storage and release of CeO_2-ZrO_2 mixed oxides. Journal of Rare Earths 25 (2007) 416–421.

Xuan Y, Li Q. Heat transfer enhancement of nanofluids. International Journal of Heat and Fluid Flow 21 (2000) 58–64.

Yang H H, Lee W J, Mi H H Wong C H. PAH emissions influenced by Mn-based additive and turbocharging from a heavy duty diesel engine Environment International 24 (1998) 389–403.

Yasuda K, Nobu M, Masui T, Imanaka N. Complete oxidation of acetaldehyde on Pt/CeO_2–ZrO_2–Bi_2O_3 catalysts Materials Research Bulletin 45 (2010) 1278–1282.

Yetter R A, Risha G A, Son S F. Metal particle combustion and nanotechnology. Proceedings of the combustion Institute 32 (2009)1819–1838.

Young T J, Mawson S, Johnston K P. Rapid expansion from supercritical to aqueous solution to produce submicron suspensions of water-insoluble drugs. Biotechnology progress 16 (2000) 402–407.

Zhang X, Long E, Li Y, Guo J, Zhang L, Gong M ,Wang M, Chen Y. CeO_2-ZrO_2-La_2O_3-Al_2O_3 composite oxide and its supported palladium catalyst for the treatment of exhaust of natural gas engined vehicles. Journal of Natural and Gas Chemistry 18 (2009) 139–144.

Zhang Z, Zhang Y, Mu Z, Yu P, Ni X, Wang S, Zheng L. Synthesis and catalytic properties of $Ce_{0.6}Zr_{0.4}O_2$ solid solutions in the oxidation of soluble organic fraction from diesel engines. Applied Catalysis B: Environmental 76 (2007) 335–347.

Zhu H, Zhang C, Tang Y, Wang J, Ren B, Yin Y. Preparation and thermal conductivity of suspension of graphite nanoparticle. Carbon 45 (2007) 226–268.

Zhu M, Ma Y, Zhang D. An experimental study of the effect of a homogenous combustion catalyst on fuel consumption and smoke emission in a diesel engine. Energy 36 (2011) 6004–6009.

Zhu M, Ma Y, Zhang D. Effect of a homogeneous combustion catalyst on the combustion characteristics and fuel efficiency in a diesel engine. Applied Energy 91 (2012) 166–172.

Zhu, Li X, Wang N, Wang X, Gao J, Li H. Dispersion behavior and thermal conductivity characteristics of Al_2O_3 - H_2O nanofluids. Current Applied Physics 9 (2009) 131–139.

Zhuiykov S, Ono T, Yamazoe N, Miura N. High-temperature NO_x sensors using zirconia solid electrolyte and zinc-family oxide sensing electrode, Solid State Ionics 152– 153 (2002) 801–807.

List of Publications

Papers published in Journals

1. N. Shanmugapriya, M. Bala Subramaniam, Chandramohan Somayaji, S. Kanagaraj.Influence of surfactants and synthesis techniques on the dispersion stability of Nanofuel. Physics and Chemistry of Liquids (accepted with minor revision)
2. N. Shanmugapriya, Chandramohan Somayaji, S. Kanagaraj. Synthesis and characterization of Nd^{3+} doped $Ce_{0.6}Zr_{0.4}O_2$ and its doping significance on oxygen storage capacity. Rare Metals (accepted for publication)
3. N. Shanmugapriya, Chandramohan Somayaji, S. Kanagaraj. Optimization of $Ce_{0.6}Zr_{0.4-x}Al_{1.3x}O_2$ solid solution based on oxygen storage capacity. Journal of Nanoparticle research 16 (2014) 21-10.
4. N. Shanmugapriya, Chandramohan Somayaji, S. Kanagaraj. Characterization and optimization of $Ce_{0.6}Zr_{0.4-x}Mn_xO_2$ ($x \leq 0.4$). Journal of Nanoparticle research 16 (2014) 2660 1-10.
5. N. Shanmugapriya, Chandramohan Somayaji, S. Kanagaraj. Optimization of ceria-zirconia solid solution based on OSC measurement by cyclic heating process. Journal of Procedia Engineering 64 (2013) 1235-1241.
6. N. Shanmugapriya, Chandramohan Somayaji, S. Kanagaraj. Oxygen storage capacity of $Ce_xZr_{1-x}O_2$ ($0.4 \leq x \leq 0.8$) solid solution using thermogravimetric analysis. Advanced Materials Research 747 (2013) 579-582.

Conference Proceeding

1. N. Shanmugapriya, Chandramohan Somayaji, S. Kanagaraj. Comparative studies on characteristics of $Ce_xZr_{1-x}O_2$ nanoparticles prepared by sol-gel and co-precipitation technique. Proceedings of 21st International Symposium on Processing and Fabrication of Advanced Materials, Edited by P.S. Robi, N. Bhatnagar and T.S. Srivatsan, (2012) 285-290.

Submitted

1. N. Shanmugapriya, M. Bala Subramaniam, Chandramohan Somayaji and S. Kanagaraj. Influence of surfactants and preparation methods on the dispersion stability of nanofuel. Energy, 2014.

Under preparation

1. N. Shanmugapriya, Chandramohan Somayaji and S. Kanagaraj. Performance enhancement of CZA and CZM dispersed diesel in an IC engine.

2. N. Shanmugapriya, Chandramohan Somayaji and S. Kanagaraj. Influence of ionic radius of doping element on the oxygen storage capacity studies on $Ce_{0.6}Zr_{0.4}O_2$.

Papers presented in International Conference

1. N. Shanmugapriya, K. Konanki Hareesh Naidu, Chandramohan Somayaji and S. Kanagaraj. Validation of thermodynamic two-zone combustion model for ceria dispersed diesel. International Conference on Environment and Energy 25^{th}-17^{th} Dec-2014, Jawaharlal Nehru Technological University, Hyderabad.

2. N. Shanmugapriya, M. Bala Subramaniam, Chandramohan Somayaji and S. Kanagaraj. Dispersion stability of surfactant coated ceria in nanofuel, 22^{nd} National and 11^{th} ISHMT-ASME Heat and Mass Transfer Conference, ISHMT-2013, Indian Institute of Technology. Kharagpur, India. December 28-31, 2013.

3. N. Shanmugapriya, Chandramohan Somayaji and S. Kanagaraj. Oxygen storage capacity of nanostructured ceria-zirconia solid solution prepared by sol-gel technique using Thermogravimetric studies, International conference on Design and Manufacturing, IConDM-2013, Indian Institute of Information Technology, Design and Manufacturing, Kancheepuram Chennai. July 18-20, 2013.

4. N. Shanmugapriya, Chandramohan Somayaji and S. Kanagaraj. Oxygen storage capacity of $Ce_xZr_{1-x}O_2$ ($0.4 \leq x \leq 0.8$) solid solution using Thermogravimetric Analysis, Multi-functional materials and structures, Bangkok, Thailand, July 14-17, 2013.

5. N. Shanmugapriya, Swapnita Kakati, Chandramohan Somayaji and S. Kanagaraj. Performance enhancement of conventional stove using a new class of fuel: Nanofuel. Rural Technology Action Group North East, Trade Centre, Guwahati, January 23 - 25, 2013.

6. N. Shanmugapriya, Mantuala Basumatary, Saptarshi Mandal, Chandramohan Somayaji and S. Kanagaraj. Enhanced performance of environmental friendly nanofuel for internal combustion engine. Rural Technology Action Group North East, Trade Centre, Guwahati, January 23 - 25, 2013.

7. N. Shanmugapriya, Chandramohan Somayaji and S. Kanagaraj. Comparative studies on characteristics of $Ce_xZr_{1-x}O_2$ nanoparticles prepared by sol-gel and co-precipitation technique. Processing and Fabrication of Advanced Materials XXI. Indian Institute of Technology Guwahati, India, December 10-13, 2012.

8. N. Shanmugapriya, M. Petchimmal, Chandramohan Somayaji and S. Kanagaraj, Synthesis of ultrafine $Ce_{0.4}Zr_{0.6}O_2.xAl_2O_3$ nanostructure using controlled flow rate of precursor. 4th International conference on Advanced nanomaterials. Indian Institute of Technology Madras, Chennai, October 17-19, 2012.

Annexure-I

Molar ratio calculation

Requirement of 5 grams of $Ce_{0.6}Zr_{0.4}O_2$

$0.6Ce(NO_3)_3.6H_2O+0.4ZrO(NO_3)_3.H_2O+3\ C_6H_8O_7 \rightarrow Ce_{0.6}Zr_{0.4}O_2+3NO_2+16H_2O+18CO_2$

One mole of $Ce_{0.6}Zr_{0.4}O_2$ = 152.4 grams

5 grams of $Ce_{0.6}Zr_{0.4}O_2$ = 0.032809 mole

The required amount of $Ce(NO_3)_3.6H_2O$

= 0.6*molecular weight of $Ce(NO_3)_3.6H_2O$ * mole of 5 grams of $Ce_{0.6}Zr_{0.4}O_2$

= 0.6*434.22*0.0332809

= 8.5478 grams

The required amount of $ZrO(NO_3)_3.H_2O$

= 0.4*molecular weight of $ZrO(NO_3)_3.H_2O$ * mole of 5 grams of $Ce_{0.6}Zr_{0.4}O_2$

= 0.4*231*0. 0332809=3.03155 grams

The required amount of $C_6H_8O_7$

= 3*molecular weight of $C_6H_8O_7$ * mole of 5 grams of $Ce_{0.6}Zr_{0.4}O_2$

= 3*320*0.033280

= 31.49664 grams